Doctoral theses at NTNU, 2024:265

Mika Okuhara

# Phased Array Radio System Navigation of Unmanned Aerial Vehicles

Doctoral thesis

NTNU
Norwegian University of Science and Technology
Thesis for the Degree of Philosophiae Doctor
Faculty of Information Technology and Electrical Engineering
Department of Engineering Cybernetics

NTNU
Norwegian University of Science and Technology

Mika Okuhara

# Phased Array Radio System Navigation of Unmanned Aerial Vehicles

Thesis for the Degree of Philosophiae Doctor

Trondheim, June 2024

Norwegian University of Science and Technology
Faculty of Information Technology and Electrical Engineering
Department of Engineering Cybernetics

NTNU
Norwegian University of
Science and Technology

**NTNU**
Norwegian University of Science and Technology

Thesis for the Degree of Philosophiae Doctor

Faculty of Information Technology and Electrical Engineering
Department of Engineering Cybernetics



ISBN 978-82-326-8122-8 (printed ver.)
ISBN 978-82-326-8121-1 (electronic ver.)
ISSN 1503-8181 (printed ver.)
ISSN 2703-8084 (online ver.)

Doctoral theses at NTNU, 2024:265

Printed by NTNU Grafisk senter

# Summary

While global navigation satellite system (GNSS) provides accurate positioning and wide coverage for unmanned aerial vehicle (UAV) navigation, it is prone to threats like jamming and spoofing because of weak signal strength. Phased array radio system (PARS) emerge as a promising alternative or backup system, offering higher signal-to-noise ratio (SNR), narrow beam-directed communication, and robust encryption to counter these vulnerabilities.

This thesis focuses on refining navigation techniques for UAVs independent or complementary to GNSS through the application of PARS. Our investigation centers on three main objectives: developing a calibration algorithm for accurately estimating the orientation of PARSs ground antennas, devising strategies to lessen the impact of multipath errors in vertical measurements from PARS, and creating a GNSS jamming detection algorithm for automatic handover or switching between GNSS- and PARS-aided inertial navigation system (INS).

The initial segment of our research introduces a calibration algorithm for PARS ground antennas. Obtaining the precise estimate of the PARS ground antennas orientation is critical for PARS-based positioning, as the UAV position is measured with respect to the PARS ground antenna position and in the local PARS coordinate frame. Since the error in the estimation of the ground antenna orientation induces more error as the range between the UAV and the ground antenna becomes longer, the calibration algorithm is essential to achieve long-distance beyond-bine-of-sight (BLOS) flight.

The calibration algorithm is based on multiplicative extended Kalman filter (MEKF) which estimates the ground antenna orientation using PARS and GNSS measurements, and enables in-flight calibration whenever reliable GNSS measurements are available. We evaluated the effectiveness of this algorithm, and the results underscored the algorithm's capacity to significantly improve the positioning accuracy of UAVs by ensuring that the orientation of PARS antennas is pinpointed with a high degree of accuracy.

Furthermore, we tackle the persistent issue of noise in PARS vertical measurements. Accurate vertical positioning is needed for the optimal operation of UAVs, and multipath interference, particularly over water, can significantly distort this data. Our research proposes methods utilizing barometric data to aid the vertical position or computing alternative elevation angle with incorporating the Earth's curvature into consideration, aiming to mitigate these inaccuracies. The proposed solutions have shown potential in decreasing the errors caused by signal reflections, thereby enhancing the UAVs' performance in various environmental conditions.

Additionally, the threat of GNSS jamming to UAV navigation is addressed through the development of a jamming detection algorithm. Given the increasing prevalence of GNSS jamming and its potential to disrupt UAV navigation, this

algorithm's integration with the conventional PARS/barometer-aided INS represents a significant stride towards safeguarding UAV operations. This detection algorithm enables UAVs to identify jamming attempts in real-time, allowing for an adaptive response that maintains navigation accuracy even in compromised GNSS conditions.

Throughout this study, we've tackled these challenges with a focus on careful exploration and understanding by combining theory with full-scale field experiments. By looking into how we can better calibrate PARS antennas, decrease noise in vertical measurements, and create a system to detect jamming, this thesis aims to contribute towards making UAV navigation more accurate and secure.

# *Preface*

This thesis is submitted in partial fulfillment of the requirements for the degree of philosophiae doctor (PhD) at the Norwegian University of Science and Technology (NTNU). The work that forms the foundation of this thesis has been carried out at the Department of Engineering Cybernetics and the NTNU Centre for Autonomous Marine Operations and Systems (NTNU AMOS). Associate Professor Torleiv Håland Bryne has been the main supervisor of this work, while Professor Tor Arne Johansen and Dr. Kristoffer Gryte has been the co-supervisors. This research was funded by the Research Council of Norway, Radionor Communications and Andøya Space through the BIA program's UAAFA project number 309370, and through the Centre for Autonomous Marine Operations and Systems, project number 223254.

## Acknowledgements

This thesis has benefited from the contributions and support of several individuals. I would like to extend my thanks to my main supervisor, Torleiv Håland Bryne, for his guidance and insights throughout this research process. His expertise has been a valuable resource. Likewise, appreciation is due to my co-supervisor, Tor Arne Johansen, for his supervision and the perspectives he provided, which have enriched this work.

Gratitude is also extended to Kristoffer Gryte for his role in conducting field tests, preparing datasets, and sharing knowledge about the experimental equipment, all of which have been critical to the research. I am thankful to Oliver Hasler for his efforts in post-processing the jammed GNSS data, a task essential for addressing one of the research challenges. Additionally, I would like to thank Pål Kvaløy at NTNU's UAVlab for his expertise in setting up and safely operating the UAV for these tests.

Moreover, I am deeply thankful to my supervisors for allowing me a degree of autonomy in my work. This freedom to shape my own working days has been invaluable, providing me with the space to engage in introspection and to ponder life more deeply and calmly than ever before. This period has led me to encounter new ideas, broaden my interests beyond my field of expertise, and, more importantly, to understand that I do not need to prove my worth. This experience has undoubtedly transformed my outlook on life.

I would also like to thank my colleagues for taking me out into nature and giving me unforgettable new experiences. Having grown up in big cities, stepping into nature was a new and transformative experience. Their willingness to share their insights gave me new perspectives on life and enriched my personal and professional growth in unexpected ways.

Lastly, I want to acknowledge the support of my partner, Boris Yanchev, whose continuous support has been significant throughout this journey. I could not have come this far without his support.

To all mentioned, your contributions have been instrumental in the completion of this thesis.

# Contents

# *Abbreviations*

**ACC** accelerometer

**ADC** analogue-to-digital converter

**AGC** automatic gain control

**ARS** angular rate sensor

**BLOS** beyond-bine-of-sight

**C/N0** carrier-to-noise ratio

**CDF** cumulative distribution function

**CW** continuous wave

**DoA** direction of arrival

**ECEF** Earth Centered Earth Fixed

**ECI** Earth Centered Inertial

**GNSS** global navigation satellite system

**GPS** Global Positioning System

**IMU** inertial measurement unit

**INS** inertial navigation system

**KF** Kalman filter

**LRT** likelihood ratio test

**MEKF** multiplicative extended Kalman filter

**MRP** modified Rodrigues parameters

**MSL** mean sea level

**NED** North East Down

**NLOS** non-line-of-sight

**NP** Neyman-Pearson

**PARS** phased array radio system

**PDAF** probabilistic data association filter

**PDF** probability density function

**PGA** programmable gain amplifier

**PNT** position, navigation, and timing

**PRN** pseudorandom noise

**RFI** radio frequency interference

**RTK** real time kinematic

**SLAM** simultaneous localisation and mapping

**SNR** signal-to-noise ratio

**UAV** unmanned aerial vehicle

**UWB** ultra wideband

**VO** visual odometry

# *Nomenclature*

$\{i\}$ Inertial coordinate frame

$\{e\}$ Earth Centered Earth Fixed coordinate frame

$\{n\}$ North East Down coordinate frame

$\{b\}$ BODY coordinate frame

$\{r\}$ Radio coordinate frame

$\{n_j\}$ $j^{\text{th}}$ North East Down coordinate frame

$\{r_j\}$ $j^{\text{th}}$ Radio coordinate frame

$\mu$ Latitude on the WGS-84 ellipse

$\lambda$ Longitude on the WGS-84 ellipse

$h$ Height over the WGS-84 ellipse

$\rho_u$ PARS range

$\psi_u$ PARS azimuth angle

$\theta_u$ PARS elevation angle

$S$ Earth Centered Earth Fixed (ECEF) position of the geoid below the UAV position

$T_s$ Sampling time or step length in numerical integration methods

# 1 Introduction

## 1.1 Background

The deactivation of selective availability pseudorandom errors in the Global Positioning System (GPS) in 2000 significantly enhanced the capabilities and applications of GNSS [1]. Offering global coverage through its position, navigation, and timing (PNT) services, GNSS has become integral to the operation of both manned and unmanned vehicles, favored for its high accuracy, low cost, and lightweight receivers. Coupled with an inertial measurement unit (IMU), GNSS achieves high precision and frequency in position estimates, benefiting numerous applications [2, 3].

Despite its strengths, GNSS is not without vulnerabilities. Its low signal power is susceptible to radio frequency interference (RFI), from natural occurrences like ionospheric scintillations [4] to human-made threats such as jamming [5] and spoofing [6, 7]. These vulnerabilities can lead to significant problems, including loss of signal integrity, misleading information, and complete system failure. For instance, jamming can drown out the GNSS signals, making it impossible for the receiver to determine its location, while spoofing can deceive the receiver with false signals, leading to incorrect positioning. The potential for GNSS disruption was starkly illustrated by the 2011 incident where Iranian forces captured a US RQ-170 UAV through spoofing [8]. Furthermore, GNSS's dependency on intricate satellite systems, governed by international entities, raises concerns about availability during global conflicts, exemplified by the Galileo system outage in July 2019 [9].

### Alternatives of GNSS

The vulnerabilities of GNSS highlight the critical need for alternative, GNSS-independent navigation solutions, especially for safety-critical operations of UAVs. To address this need, various technologies have been explored, including visual odometry, visual simultaneous localisation and mapping (SLAM), terrain/map matching, and ground-based radio positioning. These alternatives aim to provide reliable navigation solutions that do not rely on GNSS, thus enhancing the safety and robustness of UAV operations in environments where GNSS may be compromised. The basic principles of these GNSS-free navigation techniques and their advantages and disadvantages are presented below.

### Visual Odometry

Visual odometry (VO) estimates the motion of an agent (e.g., UAV) by analysing changes in images taken from onboard cameras [10, 11, 12, 13].

One of the primary advantages of VO is its ability to provide high precision in pose estimation, particularly in environments that are rich in visual features. Additionally, VO operates independently of external infrastructure, which allows for greater flexibility in exploration and indoor navigation tasks.

However, VO is predominantly suited for local navigation due to its reliance on sequential image processing, which can be a limitation for long-distance UAV operations. The technique's performance may also degrade in environments lacking distinct textures or under conditions of rapid motion, posing challenges in maintaining accuracy. Furthermore, VO demands significant computational resources for real-time processing, which can be a constraint for systems with limited onboard computing capabilities.

**SLAM (Simultaneous Localisation and Mapping)**

SLAM techniques create a map of the environment while tracking the UAV location within it [14, 15, 16, 17].

The primary advantage of SLAM lies in its ability to facilitate navigation by simultaneously mapping and localising, making it especially useful in environments where GNSS signals are denied or unavailable. This includes a variety of settings, from indoor spaces to complex urban landscapes, showcasing the versatility of SLAM to adapt to different environmental conditions. Reliance on visual or LiDAR input allows SLAM systems to operate independently of external infrastructure, further enhancing their utility in GNSS-denied areas.

However, the implementation of SLAM systems is not without its challenges. These systems can be complex to implement and may require substantial computational resources, limiting their application to local navigation tasks. Dynamic environments, characterised by frequent movements or changes, can pose additional challenges, potentially affecting the system's ability to maintain accurate mapping and localisation. Over time, the accumulation of small errors can degrade the accuracy of both the generated map and pose estimation, impacting the overall reliability of the SLAM system. Furthermore, while SLAM is adept at navigating unknown environments, long-distance navigation often necessitates a pre-existing global map, which may not always be feasible or available, thereby limiting the scope of SLAM's applicability for extended operations.

**Terrain/Map Matching**

Terrain/Map Matching aligns observed geographical features with a pre-existing map to estimate location [18].

This method proves invaluable in areas characterised by well-defined physical features or distinct landmarks, as it leverages these elements to improve navigation accuracy. The primary advantage of Terrain/Map Matching lies in its ability to offer improved reliability and accuracy over GNSS alone, especially in challenging or GNSS-denied environments.

However, the application of Terrain/Map Matching comes with its set of limitations. The technique's effectiveness is contingent upon the availability of a detailed and up-to-date global map, which poses a significant challenge in uncharted territories or regions where such maps are unavailable or outdated. The performance of Terrain/Map Matching systems is also highly dependent on the quality and resolution of the underlying map data; in instances where the map lacks detail or is not current, the system's accuracy and reliability can substantially degrade. Moreover, Terrain/Map Matching requires extensive computational resources to align observed data with map characteristics effectively, necessitating robust processing capabilities for real-time data matching. This dependence on high-quality map data and significant computational power can limit the applicability of the technique in dynamic or resource-constrained scenarios.

#### Ground-based Radio Positioning

Ground-based Radio Positioning, including technologies like ultra wideband (UWB) and ranging radios, provides accurate positioning through the use of ground-based transmitters and receivers [19, 20, 21].

This method is particularly effective in indoor or cluttered environments where GNSS signals may be obstructed or unavailable, making it an essential tool for applications requiring precise indoor navigation, asset tracking, and collision avoidance. One of the key advantages of ground-based radio positioning is its high accuracy and reliability, which are not contingent upon visual features or lighting conditions, thereby ensuring consistent performance across a variety of settings.

However, the implementation of ground-based radio positioning systems comes with its challenges. The requirement for specific infrastructure, including the installation of multiple transmitters or receivers, can render these systems costly and logistically complex, potentially limiting their applicability in large-scale or remote operations. Furthermore, while UWB technology offers exceptional precision, it is inherently limited to relatively short ranges due to its low-power emission and susceptibility to high-frequency signal attenuation. The effectiveness of ground-based radio positioning can also be compromised by environmental factors such as obstacles, multipath propagation, and electronic interference, which may adversely affect the system's range and accuracy. These limitations necessitate careful consideration of the operational context and objectives when deploying ground-based radio positioning technologies.

#### UWB vs. PARS

While UWB offers high-precision positioning over short distances, PARS can achieve long-range communication by focusing signal beams. The limitation of

UWB to short ranges is due to its low power emission and wide bandwidth, which leads to rapid signal attenuation. In contrast, PARS utilizes beamforming to direct signals efficiently over longer distances, making it more suitable for applications requiring extended coverage [20].

For UAVs operating over long distances without a global map, Ground-based Radio Positioning with PARS technology emerges as a more suitable option due to its long-range capabilities and flexibility in beam direction.

### Phased Array Radio System (PARS)

Recent studies [22, 23, 24, 25, 26] have demonstrated PARS's versatility in both high-bandwidth communication and accurate positioning capabilities. Originally designed for telemetry and live video streaming from UAVs [27], PARS has been adapted for precise 3D positioning using a directed, narrow transmission beam, achievable with a single ground antenna [24, 23]. This innovation offers a robust alternative to GNSS solutions, addressing security concerns through encrypted communication and a higher SNR.

The exploration of PARS as a navigation system for small UAVs has been motivated by the need for GNSS-independent solutions, with early research employing nonlinear observers for PARS-aided INS [23], and later integrating spoofing detection with GNSS- and PARS-aided INS [24]. Recent advancements have utilized the multiplicative extended Kalman filter (MEKF) for PARS-aided INS, allowing for more effective fusion of INS estimations with PARS measurements by accounting for cross-covariance [28, 29, 25, 26].

However, despite the promising capabilities of the PARS in enhancing UAV navigation, it encounters several critical challenges:

- As PARS measures the UAV position relative to the local ground antenna frame, calibration of the PARS ground antenna's orientation becomes necessary each time it is relocated. Previous approaches, relying on manual measurements with a GNSS receiver and a compass, or manual alignment with GNSS positions, become increasingly inaccurate over longer distances from the ground radio, highlighting the need for an automated pose estimation method.

- The issue of multipath interference arises when the PARS elevation angle measurements are distorted by noise resulting from radio signal reflections off water surfaces. This interference compromises the accuracy of positional determinations made through the direction-of-arrival (DOA) algorithm [22].

- The transition from GNSS-aided to PARS-aided positioning in scenarios of GNSS RFI is critical, necessitating an early detection mechanism for a reliable system handover. The degradation in the PNT solution just before complete signal loss makes early jamming detection critical for operational safety.

## 1.2 Contributions

This thesis addresses the challenges through several key contributions:

- Introducing a novel calibration algorithm for the PARS ground antenna orientation, leveraging GNSS data for enhanced UAV positioning accuracy. This development automates the antenna's pose estimation and ensures greater accuracy, especially beneficial for long-distance operations between the UAV and the ground station. (⇒ **Chapter 6**)
- Proposing solutions to the multipath problem by employing a non-linear update of barometer altitude, utilizing probabilistic data association filter (PDAF) to discern true signals from noise, and seeking alternative methods to improve elevation angle measurement reliability. (⇒ **Chapter 7**)
- Developing a novel approach to GNSS jamming detection using a Kalman filter (KF) and hypothesis testing, validated through real-world experimental data. This ensures a seamless transition to PARS-aided navigation, enhancing UAV navigational resilience against jamming attacks. (⇒ **Chapter 8**)

All contributions are validated through experimental UAV flights using the Radionor PARS for navigation. Notably, in some flights, the PARS-aided navigation is used in closed loop with the autopilot, including actual GNSS jamming.

## 1.3 Publications

This thesis is based on the following articles published in peer-review international journals and conferences.

### Journal publications

- Mika Okuhara, Torleiv Håland Bryne, Kristoffer Gryte, and Tor Arne Johansen. Phased array radio navigation system on UAVs: In-flight calibration. *Journal of Intelligent & Robotic Systems*, 109(3):51, 2023
- Mika Okuhara, Torleiv Håland Bryne, Kristoffer Gryte, Oliver Hasler, and Tor Arne Johansen. UAV navigation during active GNSS jamming using phased-array-radio positioning. *NAVIGATION: Journal of the Institute of Navigation*, 2024. Submitted

### Conference publications

- Mika Okuhara, Torleiv Håland Bryne, Kristoffer Gryte, and Tor Arne Johansen. Phased array radio navigation system on UAVs: GNSS-based calibration in the field. In *2021 International Conference on Unmanned Aircraft Systems (ICUAS)*, pages 210–218, 2021

- Mika Okuhara, Torleiv Håland Bryne, Kristoffer Gryte, and Tor Arne Johansen. Phased array radio navigation system on UAVs: Real-time implementation of in-flight calibration. *IFAC-PapersOnLine*, 56(2):1152–1159, 2023. 22nd IFAC World Congress
- Mika Okuhara, Torleiv Håland Bryne, Kristoffer Gryte, and Tor Arne Johansen. Elevation angle redundancy from barometric altitude in multipath-affected phased array radio navigation of UAVs. In *2024 International Conference on Unmanned Aircraft Systems (ICUAS)*, 2024. Submitted

**Internal reports**

- Mika Okuhara, Torleiv Håland Bryne, Kristoffer Gryte, and Tor Arne Johansen. Phased array radio and barometric navigation system for UAVs: A nonlinear measurement update approach. Internal Report, 2021
- Mika Okuhara, Torleiv Håland Bryne, Kristoffer Gryte, and Tor Arne Johansen. Phased array radio navigation system on UAVs: Multi hypothesis filter for noise mitigation. Internal Report, 2023

## 1.4 Outline

This thesis begins with mathematical preliminaries (**Chapter 2**) and positioning techniques (**Chapter 3**) used in our navigation system (**Chapter 4**). The system architecture of the UAV we used for field tests and the collected datasets are summarised in **Chapter 5**.

The main body of this thesis begins from **Chapter 6**, presenting the calibration algorithm of the PARS ground antenna orientation and its integration with our navigation system and its implementation for real-time operation, based on the following publications:

- Mika Okuhara, Torleiv Håland Bryne, Kristoffer Gryte, and Tor Arne Johansen. Phased array radio navigation system on UAVs: GNSS-based calibration in the field. In *2021 International Conference on Unmanned Aircraft Systems (ICUAS)*, pages 210–218, 2021
- Mika Okuhara, Torleiv Håland Bryne, Kristoffer Gryte, and Tor Arne Johansen. Phased array radio navigation system on UAVs: In-flight calibration. *Journal of Intelligent & Robotic Systems*, 109(3):51, 2023
- Mika Okuhara, Torleiv Håland Bryne, Kristoffer Gryte, and Tor Arne Johansen. Phased array radio navigation system on UAVs: Real-time implementation of in-flight calibration. *IFAC-PapersOnLine*, 56(2):1152–1159, 2023. 22nd IFAC World Congress

**Chapter 7** presents multiple solutions to mitigate the noise in the PARS elevation measurement using an external barometer measurement incorporating the curvature of the Earth, based on the following publications:

- Mika Okuhara, Torleiv Håland Bryne, Kristoffer Gryte, and Tor Arne Johansen. Phased array radio and barometric navigation system for UAVs: A nonlinear measurement update approach. Internal Report, 2021

- Mika Okuhara, Torleiv Håland Bryne, Kristoffer Gryte, and Tor Arne Johansen. Phased array radio navigation system on UAVs: Multi hypothesis filter for noise mitigation. Internal Report, 2023

- Mika Okuhara, Torleiv Håland Bryne, Kristoffer Gryte, and Tor Arne Johansen. Elevation angle redundancy from barometric altitude in multipath-affected phased array radio navigation of UAVs. In *2024 International Conference on Unmanned Aircraft Systems (ICUAS)*, 2024. Submitted

**Chapter 8** presents the jamming detection algorithm and its integration with our navigation system to enable switching from jammed GNSS to either jamming-free GNSS or PARS for UAV operation in a jamming-active environment, based on the following publication:

- Mika Okuhara, Torleiv Håland Bryne, Kristoffer Gryte, Oliver Hasler, and Tor Arne Johansen. UAV navigation during active GNSS jamming using phased-array-radio positioning. *NAVIGATION: Journal of the Institute of Navigation*, 2024. Submitted

Finally, **Chapter 9** provides conclusions and suggests future work.

# 2 Preliminaries

This section describes mathematical preliminaries before presenting positioning techniques and the navigation system.

## 2.1 Notations

Throughout this thesis, the following notations are used.

| Notation | Explanation |
|---|---|
| $\|\| \cdot \|\|_2$ | Euclidean vector norm |
| $\boldsymbol{I}_n$ | $n \times n$ identity matrix |
| $(\cdot)^\intercal$ | Transpose of a vector or a matrix |
| $\{\cdot\}$ | Coordinate frame |
| $\boldsymbol{z}_{bc}^{a} \in \mathbb{R}^3$ | Vector $\boldsymbol{z}$ from frame $\{b\}$ to $\{c\}$, resolved in $\{a\}$ |
| $\boldsymbol{S}(\cdot) \in SS(3)$ | Skew symmetric matrix, $\boldsymbol{S}(\boldsymbol{z}_1)\boldsymbol{z}_2 = \boldsymbol{z}_1 \times \boldsymbol{z}_2$ |
| $\boldsymbol{z}_1 \cdot \boldsymbol{z}_2$ | Dot product for two vectors $\boldsymbol{z}_1, \boldsymbol{z}_2 \in \mathbb{R}^3$ |
| $\boldsymbol{z} = (\boldsymbol{z}_1; \boldsymbol{z}_2; \ldots; \boldsymbol{z}_n)$ | Vector of stacked column vectors |
| $\text{diag}(\star_1, ..., \star_n)$ | Diagonal matrix with $n$ arguments diagonally |
| $\delta\star$ | Error variables represented by $\delta$ followed by a variable |
| $\partial \star_a / \partial \star_b$ | Partial derivatives |
| $\varepsilon_\star \sim \mathcal{N}(0, \sigma_\star^2)$ | Zero-mean Gaussian noise with standard deviation $\sigma_\star$ |
| $\mathbb{E}[\cdot]$ | Expected value |
| $\mu, \lambda, h$ | Latitude, longitude, and height above the WGS-84 ellipsoid |
| $T_s$ | the sampling time or step length in numerical integration methods |

Table 2.1: Summary of Notations

## 2.2 Attitude Representation

The rotation vector

$$\boldsymbol{a}_\phi \equiv \phi \boldsymbol{e} \tag{2.1}$$

is a general class of three-parameter attitude representations of a rigid body with one point fixed whose rotation is denoted by the angle $\phi$ about some axis, which we specify by a unit vector $\boldsymbol{e}$.

In this thesis, attitudes are represented as unit quaternions, using the Hamiltonian representation. For a rotation from some frame $\{a\}$ to another frame $\{b\}$, the unit quaternion is given as

$$\boldsymbol{q}_a^b = \begin{pmatrix} q_s \\ \boldsymbol{q}_v \end{pmatrix} = \begin{pmatrix} \cos(\frac{\phi}{2}) \\ \boldsymbol{e}\ \sin(\frac{\phi}{2}) \end{pmatrix}. \tag{2.2}$$

The unit quaternion contains the *real* or *scalar* part referred to as $q_s$, and the *imaginary* or *vector* part as $\boldsymbol{q}_v = (q_x, q_y, q_z)^\top$.

The rotation matrix, $\boldsymbol{R}_{ba} \in SO(3)$, represents the rotation between $\{a\}$ and $\{b\}$ frames. The quaternion can be used to calculate the rotation matrix, $\boldsymbol{R}_{ba} \in SO(3)$,

$$\boldsymbol{R}_{ba}(\boldsymbol{q}_a^b) = \left(q_s^2 - \boldsymbol{q}_v^\top \boldsymbol{q}_v\right) \boldsymbol{I}_3 + 2q_s \boldsymbol{S}(\boldsymbol{q}_v) + 2\boldsymbol{q}_v \boldsymbol{q}_v^\top \tag{2.3}$$

as in e.g. [29, Eq. (4)], [28, Eq. (117)], and [37, App. D.2].

The Hamiltonian quaternion product, denoted $\otimes$, is given as follows

$$\boldsymbol{q}_3 = \boldsymbol{q}_1 \otimes \boldsymbol{q}_2 \tag{2.4}$$

$$= \begin{pmatrix} q_{1_s} q_{2_s} - \boldsymbol{q}_{1_v}^\top \boldsymbol{q}_{2_v} \\ q_{1_s} \boldsymbol{q}_{2_v} + q_{2_s} \boldsymbol{q}_{1_v} + \boldsymbol{S}\left(\boldsymbol{q}_{1_v}\right) \boldsymbol{q}_{2_v} \end{pmatrix} \tag{2.5}$$

as in [28, Eq. (13)] and [37, App. D.2].

Furthermore, the conjugate of the quaternion is denoted by

$$(\boldsymbol{q}_a^b)^* = \begin{pmatrix} q_s \\ -\boldsymbol{q}_v \end{pmatrix}^\top \tag{2.6}$$

and has a relation

$$(\boldsymbol{q}_3)^* = (\boldsymbol{q}_1 \otimes \boldsymbol{q}_2)^* \tag{2.7}$$

$$= (\boldsymbol{q}_2)^* \otimes (\boldsymbol{q}_1)^* \tag{2.8}$$

and

$$(\boldsymbol{q}_a^b)^* = (\boldsymbol{q}_a^b)^{-1} \tag{2.9}$$

as $\boldsymbol{q}_a^b$ is a unit quaternion.

The attitude error is denoted $\delta\boldsymbol{q}$ and relates to the true quaternion $\boldsymbol{q}$ by

$$\boldsymbol{q} = \hat{\boldsymbol{q}} \otimes \delta\boldsymbol{q}(\delta\boldsymbol{a}) \tag{2.10}$$

where $\hat{\boldsymbol{q}}$ is the nominal estimated unit quaternion. The three dimensional attitude error in the state of the MEKF, $\delta\boldsymbol{a}$ is parameterized using four times the modified Rodrigues parameters (MRP)s, $\delta\boldsymbol{a}_{\text{mrp}}$, where

$$\delta\boldsymbol{a}_{\text{mrp}} \equiv \frac{\delta\boldsymbol{q}_v}{1 + \delta q_s} = \boldsymbol{e}\,\tan\left(\frac{\phi}{4}\right) \equiv \frac{\delta\boldsymbol{a}}{4}, \tag{2.11}$$

as given in [29, Eq. (10)]. The last two terms ensure that $a_p = \|\delta\boldsymbol{a}\|_2$ is approximately equal to $\phi$ for small rotations. As given in [29, Eq. (18c)], the error quaternion is calculated as

$$\delta\boldsymbol{q}(\delta\boldsymbol{a}) = \frac{1}{16 + a_p^2} \begin{pmatrix} 16 - a_p^2 \\ 8\delta\boldsymbol{a} \end{pmatrix}. \tag{2.12}$$

Moreover, the kinematic equation of a unit quaternion $\boldsymbol{q}_c^b$ can be given as

$$\dot{\boldsymbol{q}}_c^b = \frac{1}{2}\boldsymbol{q}_c^b \otimes \bar{\boldsymbol{\omega}}_{ac}^c - \frac{1}{2}\bar{\boldsymbol{\omega}}_{ab}^b \otimes \boldsymbol{q}_c^b = \frac{1}{2}\boldsymbol{\Omega}(\boldsymbol{\omega}_{ac}^c)\boldsymbol{q}_c^b - \frac{1}{2}\boldsymbol{\Gamma}(\boldsymbol{\omega}_{ab}^b)\boldsymbol{q}_c^b \tag{2.13}$$

where $\bar{\boldsymbol{\omega}}_\bullet^\bullet = (0, (\boldsymbol{\omega}_\bullet^\bullet)^\top)^\top$ and $\boldsymbol{\omega}$ is an angular velocity vector, and

$$\boldsymbol{\Omega}(\boldsymbol{\omega}) = \begin{pmatrix} 0 & -\boldsymbol{\omega}^\top \\ \boldsymbol{\omega} & -\boldsymbol{S}(\boldsymbol{\omega}) \end{pmatrix}, \quad \boldsymbol{\Gamma}(\boldsymbol{\omega}) = \begin{pmatrix} 0 & -\boldsymbol{\omega}^\top \\ \boldsymbol{\omega} & \boldsymbol{S}(\boldsymbol{\omega}) \end{pmatrix}. \tag{2.14}$$

Additionally, the Euler angles (roll, pitch and yaw) are represented as

$$\boldsymbol{\Theta} = \begin{pmatrix} \phi, & \theta, & \psi \end{pmatrix}^\top, \tag{2.15}$$

and relate to rotation matrix using

$$\boldsymbol{R}(\Theta) = \begin{pmatrix} c\theta c\psi & -c\phi s\psi + s\phi s\theta c\psi & s\phi s\psi + c\phi s\theta c\psi \\ c\theta s\psi & c\phi c\psi + s\phi s\theta s\psi & -s\phi c\psi + c\phi s\theta s\psi \\ -s\theta & s\phi c\theta & c\phi c\theta \end{pmatrix} \tag{2.16}$$

where $c\star$ denotes $\cos(\star)$ and $s\star$ denotes $\sin(\star)$.

## 2.3 Coordinate Frames

We consider $4 + 2m$ coordinate frames, where $m$ is the number of PARS ground antennas in use. The first four are the Earth Centered Inertial (ECI) frame, the ECEF frame, the North East Down (NED) frame and the BODY reference frame of the UAV, denoted $\{i\}$, $\{e\}$, $\{n\}$ and $\{b\}$ respectively, as indicated in Figure 2.1.

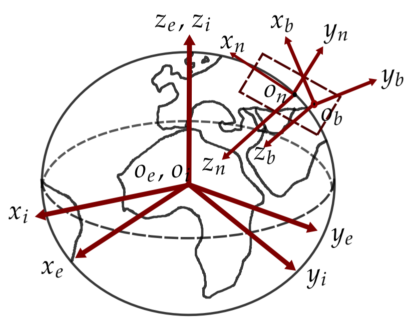


Figure 2.1: Definitions of the ECEF, the NED and the BODY coordinate frames

The remaining $2m$ coordinate frames are the local PARS coordinate frames and the local NED frames, denoted $\{r_j\}$ and $\{n_j\}$, where $j$ is the PARS index (i.e. $j = 1 \ldots m$). The PARS coordinate system resembles the local NED frame with coincided origins (i.e. $O_{n_j} = O_{r_j}$), however, it is rotated with respect to the local NED frame to be aligned with NED with the PARS ground antennas, as indicated in Figure 2.2.

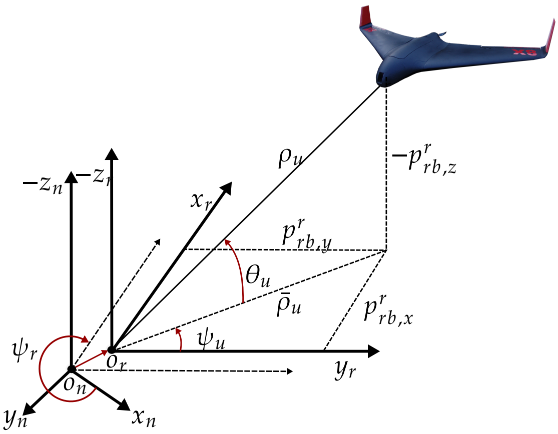


Figure 2.2: Range/azimuth/elevation measurements in PARS.[1]

Please note that:

* $\{n\}$ and $\{n_j\}$ are different frames, where the origin of $\{n\}$ is on the UAV while the origin of the $\{n_j\}$ is located in the center of the respective PARS ground radio antenna. Thus totaling 1+$m$ NED frames.

* when a single PARS ground antenna was used (i.e. $m = 1$), the index $j$ is omitted for convenience (i.e. $\{n_j\}$ is written as $\{n\}$).

* this research resolves navigation equations in the $\{e\}$-frame, while the previous work [25, 26] used a Earth-fixed $\{n\}$-frame instead (i.e. $\{n_j\}$-frame).

* the rotation between the $\{n_j\}$ and $\{r_j\}$ frames is the PARS antenna orientation estimated by the calibration algorithm presented in [32, 30, 33] [2].

[1] $\psi_r$ denotes the yaw angle between $\{n_j\}$ and $\{r_j\}$ (the index $j$is omitted in the figure). Range is represented with $\rho_u$ and the azimuth and elevation angles are represented with $\psi_u$ and $\theta_u$.

[2] The yaw angle of the rotation between the $\{n_j\}$ and $\{r_j\}$ frames is denoted $\psi_r$ as shown in Figure 2.2. This is the angle measured by a compass in [32, 30, 33] as an initial estimate. More detail is in Chapter 6.

# 3 Navigation Systems and Sensors

This chapter presents four navigation sensors or systems used in this thesis:

1. Inertial navigation system (INS)
2. Real time kinematic (RTK) global navigation satellite system (GNSS)
3. Phased array radio system (PARS)
4. Barometer

## 3.1 Inertial Navigation System

Inertial navigation system (INS) are autonomous navigation tools that calculate an object's position, velocity, and orientation using IMU. Typically IMU includes accelerometers, which measure specific force, and gyroscopes, which gauge angular rates.

An INS starts with a known location and then uses sensor data to compute subsequent movement. Accelerometers detect linear acceleration, whereas gyroscopes detect rotational motion. The INS integrates acceleration to obtain velocity and then integrates velocity to deduce position. Orientation is determined by integrating angular rates provided by gyroscopes[38, Ch. 5][39].

### 3.1.1 Inertial measurement unit

A simplified measurement model of IMU, providing specific force ($\boldsymbol{f}^b_{\mathrm{IMU}}$) and angular rate sensor (ARS) measurements ($\boldsymbol{\omega}^b_{\mathrm{IMU}}$) is given as

$$\boldsymbol{f}^b_{\mathrm{IMU}} = \boldsymbol{f}^b_{ib} + \boldsymbol{b}^b_{acc} + \varepsilon^b_{acc} \tag{3.1}$$

$$\boldsymbol{\omega}^b_{\mathrm{IMU}} = \boldsymbol{\omega}^b_{ib} + \boldsymbol{b}^b_{ars} + \varepsilon^b_{ars} \tag{3.2}$$

where $\boldsymbol{b}^b_\star$ is the accelerometer (ACC) and the ARS biases, and $\varepsilon^b_\star$ is zero-mean noise. The biases are modeled as Gauss-Markov processes

$$\dot{\boldsymbol{b}}^b_\star = -\boldsymbol{T}^{-1}_\star \boldsymbol{b}^b_\star + \varepsilon_{b_\star} \tag{3.3}$$

where $\varepsilon_{b_\star}$ assumed to be is zero-mean white noise, and $\boldsymbol{T}_\star$ represents the time constant matrices of the two processes.

### 3.1.2 Strapdown Equations

The position and velocity of the UAV with respect to the $\{e\}$-frame are denoted as $\boldsymbol{p}^e_{eb} \in \mathbb{R}^3$ and $\boldsymbol{v}^e_{eb} \in \mathbb{R}^3$. The attitude and the angular rate of the UAV relative to the $\{e\}$-frame are given as the unit quaternion $\boldsymbol{q}^e_b$ and as $\boldsymbol{\omega}^b_{eb} = \boldsymbol{\omega}^b_{ib} - \boldsymbol{R}^\top_{eb}\boldsymbol{\omega}^e_{ie} \in \mathbb{R}^3$. The gravity vector is given as $\boldsymbol{g}_b^e(\boldsymbol{p}_{eb}^e)$ and can be calculated using [38, Ch. 2.4.6]. The strapdown equation results in

$$\dot{\boldsymbol{p}}_{eb}^e = \boldsymbol{v}_{eb}^e \tag{3.4}$$

$$\dot{\boldsymbol{v}}_{eb}^e = -2\boldsymbol{S}(\boldsymbol{\omega}_{ie}^e)\boldsymbol{v}_{eb}^e + \boldsymbol{R}_{eb}\boldsymbol{f}_{ib}^b + \boldsymbol{g}_b^e \tag{3.5}$$

$$\dot{\boldsymbol{q}}_b^e = \frac{1}{2}\boldsymbol{\Omega}(\boldsymbol{\omega}_{ib}^b)\boldsymbol{q}_b^e - \frac{1}{2}\boldsymbol{\Gamma}(\boldsymbol{\omega}_{ie}^e)\boldsymbol{q}_b^e \tag{3.6}$$

where $\boldsymbol{\omega}_{ie}^e = (0, 0, \omega_{ie})^\intercal$ is the angular rate of the Earth rotation.

### 3.1.3 Challenges in INS

The integration process intrinsic to INS operation is subject to error accumulation over time, which can result in significant drift from the true position and orientation. This phenomenon, inherent in the use of accelerometers and gyroscopes, leads to a gradual degradation of system accuracy the longer the INS operates independently. To counteract this drift, integration with external position measurements from other navigation systems proves highly effective. Such augmentation can come from systems like GPS, PARS and barometer in this thesis. This hybrid approach, commonly referred to as sensor fusion, harnesses the strengths of multiple systems to maintain the precision and reliability of the INS, ensuring its continued efficacy in navigation tasks [38].

## 3.2 Real-time kinematic GNSS positioning

Real time kinematic (RTK) GNSS is a sophisticated satellite navigation technology that refines the accuracy of location data derived from GNSS, such as GPS, GLONASS, Galileo, or BeiDou. RTK improves upon the meter-level precision typical of standard GNSS receivers, attaining accuracies as precise as a few centimeters by harnessing high-frequency signals and real-time correction data from a fixed base station [40, 41, 42].

#### Functional Mechanics

The RTK GNSS system operates using two key components: a stationary base station and a mobile rover. The base station's role is to monitor GNSS signals from its fixed location, generating correction information that accounts for various potential signal distortions, such as atmospheric interference, satellite orbital discrepancies, and timing errors. The correction data are transmitted instantaneously to the rover, allowing it to calculate its position with remarkable precision relative to the base station.

The efficacy of RTK lies in its ability to mitigate common GNSS signal errors through real-time differential correction. By contrasting the signal phase received by the rover against the base station's known phase data, RTK GNSS can effectively neutralize error sources. This capability is pivotal in achieving its hallmark centimeter-level positioning accuracy, making it indispensable for applications requiring meticulous location data [43].

## 3.3 Phased Array Radio System positioning

The PARS determines a vehicle (in this case, a UAV) position in the radio coordinate system $\{r\}$ as

$$\boldsymbol{p}^r_{\text{PARS}} = \begin{pmatrix} p^r_{rb,x} \\ p^r_{rb,y} \\ p^r_{rb,z} \end{pmatrix} = \begin{pmatrix} \rho_u \cos(\psi_u)\cos(\theta_u) \\ \rho_u \sin(\psi_u)\cos(\theta_u) \\ -\rho_u \sin(\theta_u)) \end{pmatrix} \tag{3.7}$$

from the distance $\rho_u$, the azimuth angle $\psi_u$ and the elevation angle $\theta_u$. The concept is illustrated in Fig. 2.2. The distance $\rho_u$ from the PARS ground antenna to the UAV is determined by precisely measuring the signal's transmission time. The azimuth $\psi_u$ and the elevation $\theta_u$ are determined through the phase discrepancy observed in the incoming signals between the antenna elements of the ground radio. This is known as the direction-of-arrival (DOA) problem [44, 45]. Appendix A.1 illustrates the basis principle of the DoA problem.

The PARS solution is used to aid the INS with a MEKF in a loosely coupled integration. Assuming zero-mean Gaussian noise $\varepsilon_\star \sim \mathcal{N}(0, \sigma_\star^2)$, the measurements provided from PARS are expressed as

$$\rho_y = \rho_u + \varepsilon_\rho, \tag{3.8}$$

$$\psi_y = \psi_u + \varepsilon_\psi, \tag{3.9}$$

$$\theta_y = \theta_u + \varepsilon_\theta. \tag{3.10}$$

The PARS position can be converted from the $\{r\}$-frame to the $\{n\}$-frame using

$$\boldsymbol{p}^n_{\text{PARS}} = \boldsymbol{R}^n_r(\boldsymbol{q}^n_r)\boldsymbol{p}^r_{\text{PARS}} \tag{3.11}$$

where the unit quaternion $\boldsymbol{q}^n_r$ represents the rotation from $\{r\}$ to $\{n\}$, which is obtained by the calibration of the mounting of the PARS ground antenna explained in Chapter 6 [1].

As presented in [22], the vertical measurement of PARS is sometimes very noisy, as the elevation angle is prone to multipath errors due to the reflections from water surfaces. To avoid this issue, the vertical measurement in Eq. (3.7) was replaced by an altitude measurement based on barometer [2].

[1] Mentioned in Section 5.1.2.

[2] See Section 4.2.

## 3.4 Barometer altitude

A barometer measures the air pressure and then uses a standard atmospheric model to determine the height. Barometer-based altitude measurement was used for vertical aiding to mitigate errors in PARS elevation angle measurements in [35, 30, 33, 34, 31].

The altitude measurement $\gamma_y$ is modelled by assuming the barometer altitude bias $b_\gamma$ [3] and zero-mean Gaussian noise $\varepsilon_\gamma \sim \mathcal{N}(0, \sigma_\gamma^2)$ on the measured altitude over the Earth, $\gamma_u$, i.e.

$$\gamma_y = \gamma_u + b_\gamma + \varepsilon_\gamma. \tag{3.12}$$

where $\gamma_u$ is equivalent to the vertical position of the UAV in Figure 2.2 and $\gamma_u$ has the following relationship to the UAV's position $\boldsymbol{p}_{eb}^e$ and the Earth's specific radius $r_b$

$$\gamma_u = \|\boldsymbol{p}_{eb}^e\|_2 - r_b(\boldsymbol{p}_{eS}^e) \tag{3.13}$$

$$r_b = \|\boldsymbol{p}_{eS}^e(\mu_b, \lambda_b, h_{\mathrm{MSL}})\|_2 \tag{3.14}$$

with $S$ denoting the ECEF position of the geoid (approximate Earth's surface or the mean sea level (MSL)) below the UAV position $(\mu_b, \lambda_b)$. If assuming spherical Earth, $r_b = r_0$ where $r_0 = 6\,378\,137\,\mathrm{m}$ where $r_0$ is the WGS-84 Equatorial radius [38, Ch. 2.4.1].

Another formulation of Eq. (3.13) is simply

$$\gamma_u = \|\boldsymbol{p}_{eb}^e - \boldsymbol{p}_{eS}^e\|_2. \tag{3.15}$$

The rationale behind Eq. (3.15) is that the altitude is the distance between the geoid (or MSL) and the UAV.

### 3.4.1 Position on the geoid

The vector $\boldsymbol{p}_{eS}^e$ can be calculated in two stages. First, the geodetic height, $h_{\mathrm{s}}$ can be calculated from the estimated latitude, $\mu_b$, and longitude, $\lambda_b$, of the UAV using e.g. Earth Gravity Model (EGM) 96 or 2008. In the second stage $\boldsymbol{p}_{eS}^e$ is calculated using

$$\boldsymbol{p}_{eS}^e = \begin{pmatrix} (R_N + h_s)\cos(\mu_b)\cos(\lambda_b) \\ (R_N + h_s)\cos(\mu_b)\sin(\lambda_b) \\ (R_N(1 - e^2) + h_s)\sin(\mu_b) \end{pmatrix} \tag{3.16}$$

where $R_N = a(1 - e^2\sin^2(\mu_b))^{-1/2}$ is the WGS84 ellipsoid's semi major axis and $e$ is the ellipsoid's eccentricity.

[3] The barometer bias can be compensated from pre-flight, but can also be estimated real-time when GNSS is available [38, Ch. 16.2.2].

### 3.4.2 Measurement

Atmospheric pressure measurements from barometer can be converted to the altitude of UAV from sea level using [38, Eq. (6.19)]

$$\gamma_y = \frac{T_0}{K_t}[(\frac{P_b}{P_0})^{-(\frac{RK_t}{g_0})} - 1] \tag{3.17}$$

where

$P_0$: sea level surface pressure

$T_0$: sea level surface temperature

$P_b$: ambient air pressure measured by barometer

$R$: gas constant

$K_t$: atmospheric temperature gradient

$g_0$: average surface acceleration due to gravity.

The numerical values for these constants are in Appendix C.3.

# 4 Navigation System

This chapter introduces the foundational navigation system that serves as the basis for all the research documented in this thesis, as detailed in Section 1.3. The navigation system discussed in this thesis is essentially an aided INS. The system dynamics is propagated using IMU measurements (i.e. INS), and MEKF applies corrections to the INS-based system dynamics [46]:

As mentioned in Section 3.1, INS is prone to drift due to the cumulative errors inherent in its operation. Over time, the integration process employed by the INS, based on accelerometers and gyroscopes, inevitably leads to a deviation from the true position and orientation, a challenge known as drift.

To mitigate this problem, the INS is augmented with external position measurements from various sensors. This integration, which uses additional data from navigation systems such as GNSS, PARS and barometers, significantly improves the accuracy and reliability of INS. By adopting this hybrid strategy, often referred to as sensor fusion, the system effectively counteracts the drift problem. This method capitalises on the combined strengths of multiple sensing technologies to ensure the navigational integrity and performance of INS over long periods [38].

Looking more closely at the specifics of this sensor fusion strategy, MEKF plays a key role. The MEKF achieves this by adopting the INS as the system model and integrating measurements from other sensors (GNSS, PARS and barometer) as measurement models. The main feature of MEKF is that it estimates the error between the nominal state and the true state rather than estimating the full state. The error state $\delta\boldsymbol{x}$ is estimated as a correction to the nominal state estimate $\hat{\boldsymbol{x}}$ to get closer to the true state $\boldsymbol{x}$:

$$\boldsymbol{x} = \hat{\boldsymbol{x}} \otimes \delta\boldsymbol{x}. \tag{4.1}$$

Here, the $\oplus$ operator represents the + or the $\otimes$ operator (Hamiltonian quaternion product) depending on the state. [1].

## 4.1 System Model

The system model of the MEKF is essentially the dynamics of the INS. Please note that the system dynamics was propagated in $\{e\}$-frame instead of $\{n_j\}$-frame, unlike the previous work [22, 23, 24, 25, 26]. These changes were made to include the effect of the curvature of the earth.

[1] The estimates from the aided-INS (position, velocity and attitude) were compared with GNSS position and Pixhawk velocity and attitude for validation in Chapters 6 to 8

### 4.1.1 Nominal system kinematics

The nominal state estimate was given as

$$\hat{\boldsymbol{x}} = (\hat{\boldsymbol{p}}_{eb}^{e},\ \hat{\boldsymbol{v}}_{eb}^{e},\ \hat{\boldsymbol{q}}_{b}^{e},\ \hat{\boldsymbol{b}}_{\text{acc}}^{b},\ \hat{\boldsymbol{b}}_{\text{ars}}^{b})^{\top} \in \mathbb{R}^{16}, \tag{4.2}$$

The nominal state is updated using the following kinematic model based on the strapdown equations presented in Section 3.1:

$$\dot{\hat{\boldsymbol{p}}}_{eb}^{e} = \hat{\boldsymbol{v}}_{eb}^{e} \tag{4.3a}$$
$$\dot{\hat{\boldsymbol{v}}}_{eb}^{e} = -2\boldsymbol{S}(\boldsymbol{\omega}_{ie}^{e})\hat{\boldsymbol{v}}_{eb}^{e} + \hat{\boldsymbol{R}}_{eb}\hat{\boldsymbol{f}}_{ib}^{b} + \boldsymbol{g}_{b}^{e}(\hat{\boldsymbol{p}}_{eb}^{e}) \tag{4.3b}$$
$$\dot{\hat{\boldsymbol{q}}}_{b}^{e} = \frac{1}{2}\boldsymbol{\Omega}(\hat{\boldsymbol{\omega}}_{ib}^{b})\hat{\boldsymbol{q}}_{b}^{e} - \frac{1}{2}\boldsymbol{\Gamma}(\boldsymbol{\omega}_{ie}^{e})\hat{\boldsymbol{q}}_{b}^{e} \tag{4.3c}$$
$$\dot{\hat{\boldsymbol{b}}}_{\text{acc}}^{b} = -\boldsymbol{T}_{\text{acc}}^{-1}\hat{\boldsymbol{b}}_{\text{acc}}^{b} \tag{4.3d}$$
$$\dot{\hat{\boldsymbol{b}}}_{\text{ars}}^{b} = -\boldsymbol{T}_{\text{ars}}^{-1}\hat{\boldsymbol{b}}_{\text{ars}}^{b} \tag{4.3e}$$
$$\hat{\boldsymbol{f}}_{ib}^{b} = \boldsymbol{f}_{\text{IMU}}^{b} - \hat{\boldsymbol{b}}_{\text{acc}}^{b} \tag{4.3f}$$
$$\hat{\boldsymbol{\omega}}_{ib}^{b} = \boldsymbol{\omega}_{\text{IMU}}^{b} - \hat{\boldsymbol{b}}_{\text{ars}}^{b}, \tag{4.3g}$$

The equations Eq. (4.3) can be computed in discrete time using any integration methods. The exact integration methods that are in concert with the integration of quaternions can be found in [37].

### 4.1.2 Error-state system kinematics

The error state was given as

$$\delta\boldsymbol{x} = (\delta\boldsymbol{p}_{eb}^{e},\ \delta\boldsymbol{v}_{eb}^{e},\ \delta\boldsymbol{a}_{b}^{e},\ \delta\boldsymbol{b}_{\text{acc}}^{b},\ \delta\boldsymbol{b}_{\text{ars}}^{b})^{\top} \in \mathbb{R}^{15}. \tag{4.4}$$

Please note that the 3D attitude error states $\delta\boldsymbol{a}_{\star}^{\star}$, paramatrized as four times MRPs rather than rotation matrices or quaternions, are used to update the INS's states when correcting the nominal state using Eq. (2.10) and Eq. (2.12).

The continuous-time linearized error state system model

$$\delta\dot{\boldsymbol{x}} = \boldsymbol{F}(t)\delta\boldsymbol{x} + \boldsymbol{G}(t)\boldsymbol{w}, \tag{4.5}$$

where $\boldsymbol{w} = (\varepsilon_{\text{acc}}^{\top}, \varepsilon_{\text{ars}}^{\top}, \varepsilon_{b_{\text{acc}}}^{\top}, \varepsilon_{b_{\text{ars}}}^{\top})^{\top}$ is the process noise with spectral density $\boldsymbol{Q}$ given by $\mathbb{E}[\boldsymbol{w}(t)\boldsymbol{w}^{\top}(\tau)] = \boldsymbol{Q}\delta(t-\tau) \in \mathbb{R}^{(12+3m)\times(12+3m)}$. The derivation of the error-states is in Appendix B.1. The Jacobian matrices $\boldsymbol{F}(t)$ and $\boldsymbol{G}(t)$, and the spectral density matrix $\boldsymbol{Q}$ are given in Appendix B.2.

## 4.2 Measurement Model

We formulate the measurement models of the MEKF for GNSS, PARS and Barometer. The PARS and barometer measurements can be used either independently or in combination.

### 4.2.1 GNSS

The GNSS measures the position of the UAV in the $\{e\}$-frame. The measurement can be expressed as

$$\boldsymbol{y}^e_{\text{GNSS}} = \boldsymbol{p}^e_{\text{GNSS}} + \varepsilon_{\text{GNSS}}. \tag{4.6}$$

The measurement can be expressed as follows

$$\boldsymbol{y}^e_{\text{GNSS}} = \hat{\boldsymbol{p}}^e_{eb} + \delta\boldsymbol{p} + \varepsilon_{\text{GNSS}} \tag{4.7}$$

therefore, the measurement estimate becomes

$$\hat{\boldsymbol{y}}^e_{\text{GNSS}} = \hat{\boldsymbol{p}}^e_{eb}. \tag{4.8}$$

Therefore, the measurement matrix is trivially

$$\boldsymbol{H}_{\text{GNSS}} = \begin{pmatrix} \boldsymbol{I}_3 & \mathbf{0}_{3\times 12} \end{pmatrix} \in \mathbb{R}^{3\times 15}. \tag{4.9}$$

The measurement covariance matrix is given as

$$\boldsymbol{\mathcal{R}}^e_{\text{GNSS}} = \hat{\boldsymbol{R}}_{en}\text{diag}(\mathbb{E}[\varepsilon^2_{\text{GNSS},N}], \mathbb{E}[\varepsilon^2_{\text{GNSS},E}], \mathbb{E}[\varepsilon^2_{\text{GNSS},D}])\hat{\boldsymbol{R}}^\top_{en}. \tag{4.10}$$

where $N$, $E$ and $D$ represents the NED components, respectively. $\hat{\boldsymbol{R}}_{en}$ is calculated based on the position $\hat{\boldsymbol{p}}^e_{eb}$ via estimated latitude, $\hat{\mu}$, and longitude, $\hat{\lambda}$.

### 4.2.2 PARS

The range $\rho_y$, azimuth $\psi_y$ and elevation $\theta_y$ measurement can be related to a Cartesian position measurement in the radio coordinate system $\{r\}$ using

$$\boldsymbol{y}^r_{\text{PARS}} = \begin{pmatrix} \rho_y \cos(\psi_y)\cos(\theta_y) \\ \rho_y \sin(\psi_y)\cos(\theta_y) \\ -\rho_y \sin(\theta_y)) \end{pmatrix}. \tag{4.11}$$

The measurement Eq. (4.11) can be mathematically represented from the UAV position $\boldsymbol{p}^e_{eb} = \hat{\boldsymbol{p}}^e_{eb} + \delta\boldsymbol{p}^e_{eb}$:

$$\begin{aligned} \boldsymbol{y}^r_{\text{PARS}} &= \hat{\boldsymbol{R}}^\top_{nr}\boldsymbol{R}^\top_{en}\left(\hat{\boldsymbol{p}}^e_{eb} + \delta\boldsymbol{p}^e_{eb} - \boldsymbol{p}^e_{er}\right) + \varepsilon_{\text{PARS}} \\ &= \underbrace{\hat{\boldsymbol{R}}^\top_{nr}\boldsymbol{R}^\top_{en}\left(\hat{\boldsymbol{p}}^e_{eb} - \boldsymbol{p}^e_{er}\right)}_{\hat{\boldsymbol{y}}^r_{\text{PARS}}} + \underbrace{\hat{\boldsymbol{R}}^\top_{nr}\boldsymbol{R}^\top_{en}}_{\boldsymbol{H}_{\text{PARS}}}\delta\boldsymbol{p}^e_{eb} + \varepsilon_{\text{PARS}} \end{aligned} \tag{4.12}$$

where $\boldsymbol{p}^e_{er}$ is the known ground radio position, $\boldsymbol{R}^\top_{en}$ is a rotation matrix from $\{e\}$-frame to $\{n\}$-frame, $\hat{\boldsymbol{R}}^\top_{nr}$ is obtained from Chapter 6 and is an estimated rotation matrix from $\{n\}$-frame to $\{r\}$-frame representing the ground radio mounting attitude calibration, and $\varepsilon_{\text{PARS}} \sim \mathcal{N}(0, \boldsymbol{\mathcal{R}}^r_{\text{PARS}})$. The matrix $\boldsymbol{\mathcal{R}}^r_{\text{PARS}}$ is the covariance of the PARS measurement $\rho_y$, $\psi_y$ and $\theta_y$ converted into Cartesian coordinates.

Thus, the measurement estimate is

$$\hat{\boldsymbol{y}}^r_{\text{PARS}} = \hat{\boldsymbol{R}}^\intercal_{nr}\boldsymbol{R}^\intercal_{en}\left(\hat{\boldsymbol{p}}^e_{eb} - \boldsymbol{p}^e_{er}\right) \tag{4.13}$$

and the measurement matrix becomes

$$\boldsymbol{H}_{\text{PARS}} = \begin{pmatrix}\hat{\boldsymbol{R}}^\intercal_{nr}\boldsymbol{R}^\intercal_{en} & \mathbf{0}_{3\times12}\end{pmatrix} \in \mathbb{R}^{3\times15}. \tag{4.14}$$

The measurement covariance matrix in cylindrical coordinates is given by

$$\boldsymbol{\mathcal{R}}_{\text{PARS}} = \text{diag}(\mathbb{E}[\varepsilon^2_\rho], \mathbb{E}[\varepsilon^2_\psi], \mathbb{E}[\varepsilon^2_\theta]) \tag{4.15}$$

and can be converted into in Cartesian coordinates

$$\boldsymbol{\mathcal{R}}^r_{\text{PARS}} = \boldsymbol{M}_{\text{PARS}}\boldsymbol{\mathcal{R}}_{\text{PARS}}\boldsymbol{M}^\intercal_{\text{PARS}} \tag{4.16}$$

as shown in [47, Ch. 1.6] and [25], where $\boldsymbol{M}$ is a Jacobian matrix of $\boldsymbol{p}^r_{\text{PARS}}$ with respect to the noise $\boldsymbol{\varepsilon} = (\varepsilon_\rho, \varepsilon_\psi, \varepsilon_\theta)^\intercal$:

$$\boldsymbol{M}_{\text{PARS}} = \frac{\partial \boldsymbol{p}^r_{\text{PARS}}}{\partial \boldsymbol{\varepsilon}} = \begin{pmatrix} m_{11} & m_{12} & m_{13} \\ m_{21} & m_{22} & m_{23} \\ m_{31} & m_{32} & m_{33} \end{pmatrix} \tag{4.17}$$

with

$$\begin{aligned}
m_{11} &= \cos(\psi_y)\cos(\theta_y) \\
m_{12} &= -\rho_y\cos(\theta_y)\sin(\psi_y) \\
m_{13} &= -\rho_y\cos(\psi_y)\sin(\theta_y) \\
m_{21} &= \cos(\theta_y)\sin(\psi_y) \\
m_{22} &= \rho_y\cos(\psi_y)\cos(\theta_y) \\
m_{23} &= -\rho_y\sin(\psi_y)\sin(\theta_y) \\
m_{31} &= -\sin(\theta_y) \\
m_{32} &= 0 \\
m_{33} &= -\rho_y\cos(\theta_y).
\end{aligned}$$

### 4.2.3 PARS + Barometer

As mentioned in Section 3.3, the PARS vertical measurement is sometimes noisy as the elevation angle is prone to multipath errors due to the reflections from water surfaces. To avoid this issue, the vertical measurement in Eq. (3.7) was replaced by a barometer-based altitude measurement Eq. (3.12), and a measurement of the horizontal range ($\bar{\rho}_m$) was computed in *either* of the following ways to prevent the noise in elevation angle measurement from affecting the horizontal positioning

$$\bar{\rho}_y = \sqrt{\rho_y^2 - \gamma_y^2} \tag{4.18}$$

$$\bar{\rho}_y \approx \rho_y \underbrace{\frac{\hat{\boldsymbol{p}}^e_{eb} \cdot \boldsymbol{p}^e_{er}}{\|\hat{\boldsymbol{p}}^e_{eb}\|_2 \|\boldsymbol{p}^e_{er}\|_2}}_{\cos\alpha} \tag{4.19}$$

where Eq. (4.18) simply uses Pitagoras formula, and Eq. (4.19) uses a trigonometric relation as shown in Figure 4.1.

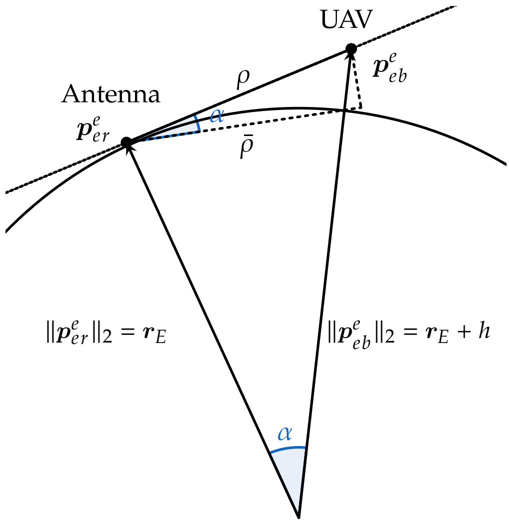


Figure 4.1: Approximation of the elevation angle. $r_E$ and $h$ are the earth radius and a height from the earth surface.

The resulting Cartesian PARS position measurement becomes

$$\boldsymbol{y}^r_{\text{PARS,Alt}} = \begin{pmatrix} \bar{\rho}_y \cos(\psi_y) \\ \bar{\rho}_y \sin(\psi_y) \\ -\gamma_y \end{pmatrix} \tag{4.20}$$

by combining the horizontal components of PARS and barometer measurements. This position measurement ($\boldsymbol{y}^r_{\text{PARS,Alt}}$) can be related to the UAV position ($\boldsymbol{p}^e_{eb}$) by

$$\boldsymbol{y}^r_{\text{PARS,Alt}} = \boldsymbol{R}^\intercal_{nr} \boldsymbol{R}^\intercal_{en} (\boldsymbol{p}^e_{eb} - \boldsymbol{p}^e_{er}). \tag{4.21}$$

Considering the relation $\boldsymbol{p}^e_{eb} = \hat{\boldsymbol{p}}^e_{eb} + \delta\boldsymbol{p}^e_{eb}$, the estimate measurement is given as

$$\hat{\boldsymbol{y}}^r_{\text{PARS,Alt}} = \boldsymbol{R}^\intercal_{nr} \boldsymbol{R}^\intercal_{en} (\hat{\boldsymbol{p}}^e_{eb} - \boldsymbol{p}^e_{er}), \tag{4.22}$$

and the Jacobean matrix of $\boldsymbol{y}^r_{\text{PARS,Alt}}$ with respect to $\delta\boldsymbol{p}^e_{eb}$ is found by differentiating Eq. (4.21)

$$\left.\frac{\partial \boldsymbol{y}^r_{\text{PARS,Alt}}}{\partial \delta\boldsymbol{p}^e_{eb}}\right|_{\delta\boldsymbol{p}^e_{eb} = \boldsymbol{0}_{3\times1}} = \underbrace{\boldsymbol{R}^\intercal_{nr} \boldsymbol{R}^\intercal_{en}}_{\boldsymbol{R}^\intercal_{er}} \in \mathbb{R}^{3\times3}. \tag{4.23}$$

Thus, the measurement matrix becomes

$$\boldsymbol{H}_{\text{PARS,Alt}} = (\boldsymbol{R}_{er}^{\intercal}\ \boldsymbol{0}_{3\times3}\ \boldsymbol{0}_{3\times3}\ \boldsymbol{0}_{3\times3}\ \boldsymbol{0}_{3\times3}) \in \mathbb{R}^{3\times15}. \tag{4.24}$$

Finally, the measurement covariance matrix

$$\mathcal{R}_{\text{PARS,Alt}} = \text{diag}(\mathbb{E}[\varepsilon_\rho^2], \mathbb{E}[\varepsilon_\psi^2], \mathbb{E}[\varepsilon_{Alt}^2]) \tag{4.25}$$

is mapped from spherical coordinates to Cartesian coordinates

$$\mathcal{R}_{\text{PARS,Alt}}^{r} = \boldsymbol{M}_{\text{PARS,Alt}}\mathcal{R}_{\text{PARS,Alt}}\boldsymbol{M}_{\text{PARS,Alt}}{}^{\intercal} \tag{4.26}$$

using the Jacobean matrix $\boldsymbol{M}_{\text{PARS,Alt}}$ of $\boldsymbol{y}_{\text{PARS,Alt}}^{r}$ with respect to the measurement noise $\boldsymbol{\varepsilon}_{\text{PARS,Alt}} = (\varepsilon_\rho, \varepsilon_\psi, \varepsilon_{Alt})^{\intercal}$ [47, Ch. 1.6]

$$\boldsymbol{M}_{\text{PARS,Alt}} = \frac{\partial \boldsymbol{y}_{\text{PARS,Alt}}^{r}}{\partial \boldsymbol{\varepsilon}_{\text{PARS,Alt}}} = \begin{pmatrix} m_{11} & m_{12} & m_{13} \\ m_{21} & m_{22} & m_{23} \\ 0 & 0 & 1 \end{pmatrix}, \tag{4.27}$$

with

$$\begin{aligned} m_{11} &= \frac{\cos(\psi_y)\rho_y}{\bar{\rho_y}} & m_{12} &= -\sin(\psi_y)\bar{\rho_y} \\ m_{13} &= -\frac{\cos(\psi_y)\gamma_y}{\bar{\rho_y}} & m_{21} &= \frac{\sin(\psi_y)\rho_y}{\bar{\rho_y}} \\ m_{22} &= \cos(\psi_y)\bar{\rho_y} & m_{23} &= -\frac{\sin(\psi_y)\gamma_y}{\bar{\rho_y}}. \end{aligned}$$

In addition, the measurement and its covariance can be transformed from $\{r\}$ frame to $\{n\}$ frame by taking

$$\boldsymbol{y}_{\text{PARS},Alt}^{n} = \boldsymbol{R}_{nr}\ \boldsymbol{y}_{\text{PARS},Alt}^{r} \tag{4.28}$$

$$\mathcal{R}_{\text{PARS,Alt}}^{n} = \boldsymbol{R}_{nr}\mathcal{R}_{\text{PARS,Alt}}^{r}\boldsymbol{R}_{nr}^{\intercal}. \tag{4.29}$$

### 4.2.4 Barometer

From Section 3.4, the barometer measurement is

$$\boldsymbol{y}_{\text{baro}} = \gamma_y. \tag{4.30}$$

Using Eq. (3.12) and Eq. (3.15), the altitude measurement ($y_{\text{baro}}$) can then be related to the UAV position ($\boldsymbol{p}_{eb}^{e}$)

$$y_{\text{baro}} = \|\boldsymbol{p}_{eb}^{e} - \boldsymbol{p}_{eS}^{e}\|_2 + b_\gamma + \varepsilon_\gamma \tag{4.31}$$

Considering the relation $\boldsymbol{p}^e_{eb} = \hat{\boldsymbol{p}}^e_{eb} + \delta\boldsymbol{p}^e_{eb}$, the estimated measurement becomes

$$\hat{y}_{\text{baro}} = \|\hat{\boldsymbol{p}}^e_{eb} - \boldsymbol{p}^e_{eS}\|_2 + b_\gamma \tag{4.32}$$

The Jacobian matrix of $y_{\text{baro}}$ with respect to $\delta\boldsymbol{p}^e_{eb}$ can be computed by differentiating Eq. (4.31)

$$\left.\frac{\partial y_{\text{baro}}}{\partial \delta\boldsymbol{p}^e_{eb}}\right|_{\delta\boldsymbol{p}^e_{eb}=\boldsymbol{0}_{3\times1}} = \frac{(\hat{\boldsymbol{p}}^e_{eb} - \boldsymbol{p}^e_{eS})^\intercal}{\|\hat{\boldsymbol{p}}^e_{eb} - \boldsymbol{p}^e_{eS}\|_2} \in \mathbb{R}^{1\times3} \tag{4.33}$$

such that the measurement matrix becomes

$$\boldsymbol{H}_{\text{baro}} = \begin{pmatrix} \frac{(\hat{\boldsymbol{p}}^e_{eb} - \boldsymbol{p}^e_{eS})^\intercal}{\|\hat{\boldsymbol{p}}^e_{eb} - \boldsymbol{p}^e_{eS}\|_2} & \boldsymbol{0}_{1\times12} \end{pmatrix} \in \mathbb{R}^{1\times15}. \tag{4.34}$$

The measurement covariance matrix is trivially

$$\mathcal{R}_{\text{baro}} = \mathbb{E}[\varepsilon_\gamma^2]. \tag{4.35}$$

## 4.3 Pre-launch calibration

### 4.3.1 Accelerometer

We can use the information that the linear and angular velocities are zero pre-launch to estimate the ACC bias and the initial roll and pitch angles. The accelerometer measures only the gravity and the ACC bias and noise when the UAV is at rest. From Eq. (3.1),

$$\boldsymbol{f}^b_{\text{IMU}} \approx -\boldsymbol{R}^\intercal_{eb}\boldsymbol{g}^e_b + \boldsymbol{b}^b_{\text{acc}} + \boldsymbol{\varepsilon}^b_{\text{acc}} \tag{4.36}$$

This result in

$$\boldsymbol{y}_{\text{acc}} = \boldsymbol{f}^b_{\text{IMU}} \tag{4.37}$$

$$\hat{\boldsymbol{y}}_{\text{acc}} = -\hat{\boldsymbol{R}}^\intercal_{eb}\boldsymbol{g}^e_b + \hat{\boldsymbol{b}}^b_{\text{acc}} \tag{4.38}$$

$$\boldsymbol{H}_{\text{acc}} = \begin{bmatrix} \boldsymbol{0}_{3\times3} & \boldsymbol{0}_{3\times3} & -\boldsymbol{S}(\hat{\boldsymbol{R}}^\intercal_{eb}\boldsymbol{g}^e_b) & \boldsymbol{I}_3 & \boldsymbol{0}_{3\times3} \end{bmatrix}. \tag{4.39}$$

The derivation is is in Appendix B.3.1.
The measurement covariance matrix is given by

$$\mathcal{R}_{\text{acc}} = \text{diag}(\mathbb{E}[\varepsilon^2_{\text{acc},x}], \mathbb{E}[\varepsilon^2_{\text{acc},y}], \mathbb{E}[\varepsilon^2_{\text{acc},z}]) \tag{4.40}$$

### 4.3.2 Angular rate sensor

Similarly, as we know that the UAV has zero angular rate pre-launch, We can use this to estimate the ARS bias. The angular rate sensor only measures the Earth's rotation, the ARS bias and noise when the UAV is at rest. From Eq. (3.2),

$$\boldsymbol{\omega}^b_{\text{IMU}} \approx \boldsymbol{R}^\intercal_{eb}\boldsymbol{\omega}^e_{ie} + \boldsymbol{b}^b_{\text{ars}} + \boldsymbol{\varepsilon}^b_{\text{ars}}. \tag{4.41}$$

This result in

$$\boldsymbol{y}_{\text{ars}} = \boldsymbol{\omega}^b_{\text{IMU}} \tag{4.42}$$

$$\hat{\boldsymbol{y}}_{\text{ars}} = \hat{\boldsymbol{R}}^\intercal_{eb}\boldsymbol{\omega}^e_{ie} + \hat{\boldsymbol{b}}^b_{\text{ars}} \tag{4.43}$$

$$\boldsymbol{H}_{\text{ars}} = \begin{bmatrix}\boldsymbol{0}_{3\times3} & \boldsymbol{0}_{3\times3} & \boldsymbol{0}_{3\times3} & \boldsymbol{0}_{3\times3} & \boldsymbol{I}_3\end{bmatrix} \tag{4.44}$$

The derivation is is in Appendix B.3.2.
The measurement covariance matrix is given by

$$\mathcal{R}_{\text{ars}} = \text{diag}(\mathbb{E}[\varepsilon^2_{\text{ars},x}], \mathbb{E}[\varepsilon^2_{\text{ars},y}], \mathbb{E}[\varepsilon^2_{\text{ars},z}]) \tag{4.45}$$

### 4.3.3 Virtual velocity

Similarly, we know that the UAV has no linear velocity when it is standing still. The initial velocity can be estimated using virtual zero velocity measurement

$$\boldsymbol{y}_{\text{vel}} = \boldsymbol{0}_{3\times3} \tag{4.46}$$

$$\hat{\boldsymbol{y}}_{\text{vel}} = \hat{\boldsymbol{v}}^e_{eb} \tag{4.47}$$

$$\boldsymbol{H}_{\text{vel}} = \begin{bmatrix}\boldsymbol{0}_{3\times3} & \boldsymbol{I}_3 & \boldsymbol{0}_{3\times3} & \boldsymbol{0}_{3\times3} & \boldsymbol{0}_{3\times3}\end{bmatrix}. \tag{4.48}$$

The measurement covariance matrix is simply given by

$$\mathcal{R}_{\text{vel}} = 10^{-5} \cdot \boldsymbol{I}_3. \tag{4.49}$$

## 4.4 Outlier rejection

Outlier rejection was implemented to prevent bad PARS measurements from degrading the estimation. If the test statistic

$$T(\boldsymbol{y}_\star) = (\boldsymbol{y}_\star - \hat{\boldsymbol{y}}_\star)^\intercal(\boldsymbol{H}_\star\hat{\boldsymbol{P}}\boldsymbol{H}^\intercal_\star + \mathcal{R}_\star)^{-1}(\boldsymbol{y}_\star - \hat{\boldsymbol{y}}_\star) \sim \chi^2_1 \tag{4.50}$$

is above some limit $\chi^2_\alpha$, the measurement is discarded as outlier [48, Section 7.6.1].

## 4.5 Multiplicative extended Kalman Filter

Using the motion model, the measurement models and the outlier rejection presented in this chapter, the MEKF is propagated. Please note that the pre-launch calibration models discussed in Section 4.3 were used before launch. After launch, the measurement models described in Section 4.2 were used.
The MEKF at time $k$ is computed in the following order:

1. Update nominal state using a discrete-time implementation of Eq. (4.3).

2. Propagate the covariance $\mathcal{P}[k]$ of $\delta\boldsymbol{x}[k] \sim \mathcal{N}(0, \mathcal{P}[k])$

$$\hat{\mathcal{P}}[k] = \boldsymbol{F}_d[k-1]\mathcal{P}[k-1]\boldsymbol{F}_d[k-1]^\intercal + \boldsymbol{Q}_d[k-1] \tag{4.51}$$

where $\boldsymbol{F}_d[k]$ and $\boldsymbol{Q}_d[k]$ can be calculated or approximated using van Loan [49] based on $\boldsymbol{F}(t)$, $\boldsymbol{G}(t)$ and $\boldsymbol{Q}_d(t)$ matrices (See Appendix B.4).

3. If any measurements are available,

   a) Compute the Kalman gain

   $$\boldsymbol{K}[k] = \hat{\mathcal{P}}[k]\boldsymbol{H}_\star^\intercal[k](\boldsymbol{H}_\star[k]\hat{\mathcal{P}}[k]\boldsymbol{H}_\star^\intercal[k] + \mathcal{R}_\star[k])^{-1}. \tag{4.52}$$

   b) Calculate the estimated error

   $$\delta\boldsymbol{x}[k] = \boldsymbol{K}[k](\boldsymbol{y}_\star[k] - \hat{\boldsymbol{y}}_\star[k]). \tag{4.53}$$

   c) Correct the nominal state using Eq. (4.1).

   d) Update the estimation error covariance.

   $$\mathcal{P}[k] = (\boldsymbol{I} - \boldsymbol{K}[k]\boldsymbol{H}_\star[k])\hat{\mathcal{P}}[k](\boldsymbol{I} - \boldsymbol{K}[k]\boldsymbol{H}_\star[k])^\intercal + \boldsymbol{K}[k]\boldsymbol{R}_\star[k]\boldsymbol{K}[k]^\intercal. \tag{4.54}$$

   e) Set the error state to zero.

   $$\delta\boldsymbol{x} = \mathbf{0}_{(15+3m)\times 1}. \tag{4.55}$$

Here, the prediction step corresponds to 1) and 2), and the correction step corresponds to 3).

## 4.6 Overview

An overview of the foundational navigation system is given in Fig. 4.2.

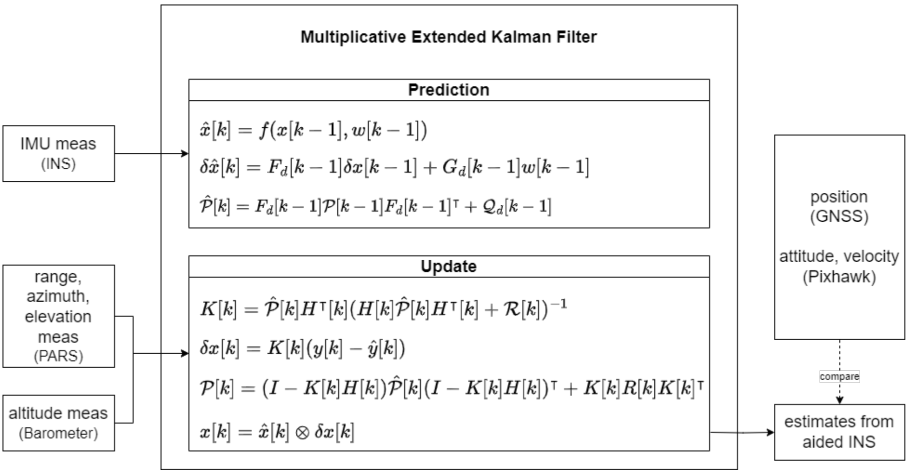

Figure 4.2: Foundational navigation system overview

# 5 Field Tests

During this research, we conducted field tests and collected real-world data to test and validate our navigation system. This chapter begins with an explanation of the general architecture of our experimental setup and provides details of the dataset collected from the field tests, indicating which dataset was used in which publication.

## 5.1 General Architecture

### 5.1.1 Payload

The UAV avionics contained a Pixhawk autopilot [50] running ArduPlane flight control software [51] with a 3DR GPS module, Honeywell HMC5883L 3-axis digital compass IC used in AHRS [52], MS5611-01BA03 barometric pressure sensor [53], and an internal IMU/INS.

In addition to the Pixhawk autopilot, the payload was also equipped with a tactical grade IMU, the Sensonor STIM 300 [54] and a Ublox F9P-ZED GNSS receiver to provide accurate RTK GNSS measurements. To synchronise the timestamps of the IMU and GNSS measurements, a SenTiBoard [55] was used. This synchronization can ease the integration of the measurements to an Odroid XU4 [56] on-board computer.

Furthermore, the Radionor Communications CRE2 144-LW PARS (Fig. 5.1a) was used to send telemetry data to the ground station and to receive commands and PARS measurements. To satisfy the redundancy requirements of beyond visual-line-of-sight flight, a 433 MHz 3DR radio was used as a redundant telemetry link. References [26, 24] provide further details about the payload.

### 5.1.2 Ground station

The ground station consisted of a Radionor Communications CRE2-189 PARS ground antenna (Fig. 5.1b), a uBlox ZED-F9P GNSS receiver to identify the location of the PARS ground antenna, and a laptop computer to remotely pilot the UAV, to log RTK GNSS data and process PARS positioning data.

The CRE2-189 is a ground radio with 8x8 antenna elements with a resolution of 3.75 m, and covering a 90° frustum both in elevation and in azimuth with a root mean square error of 0.1° on each axis.

In addition to providing the link between the UAV and the ground station, the UAV PARS also acts as a relay for communications from other nodes in the network that do not necessarily have radio line-of-sight to the ground station. This combination of ground and UAV radios allows ranges of up to 114 km when transmission rates are limited to 0.5 Mbit/s.

The position of the ground antenna, $\boldsymbol{p}^e_{er}$, was measured using GNSS before field tests.

**Antenna orientation**

As shown in Section 3.3, the PARS provides a position measurement in the local radio frame, $\{r\}$. Thus, it is essential to know the ground antenna location and the relative orientation of the $\{r\}$-frame and the local $\{n\}$-frame accurately. Although we have previously used a compass to measure orientation, a compass only gives an approximate angle because the compass reading changes when it is close to a metal antenna. Therefore, we developed an algorithm to estimate the precise orientation of the ground antenna in Chapter 6.

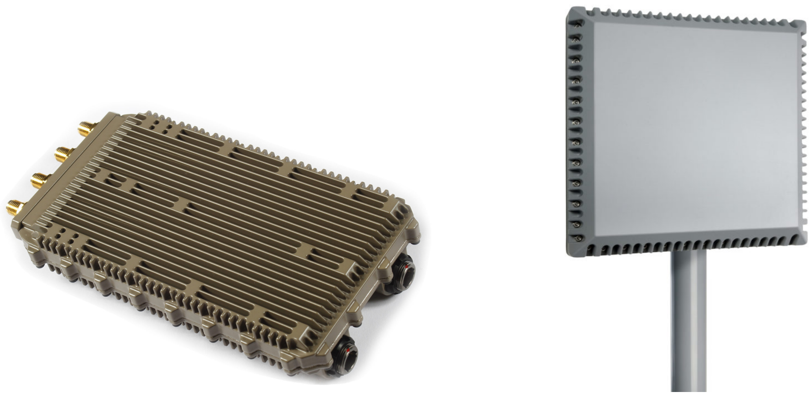

(a) CRE2-144-M2-SMA radio module (b) CRE2-189 ground station antenna

Figure 5.1: Radionor equipment

### 5.1.3 Software

When we want to test/operate our PARS/GNSS/barometer-aided INS in real life, we implemented the aided INS in DUNE Unified Navigation Environment [57, 58, 59], which is a robotic middleware written in C++. DUNE also supports the playback of previously recorded data to simplify the tuning process and to allow the testing of new features without the need for new flight time. This runs in Ubuntu Mate Linux on the onboard computer. [1]

[1] Please note that in Raudstein 2020 in Section 5.2.2, the UAV flew just using the Pixhawk autopilot and recorded sensor data (PARS, GNSS, IMU, barometer, etc.). This means that the UAV did not run our aided INS implemented in DUNE onboard during flights.

### 5.1.4 Overview

An overview of the hardware system used in this field test is given in Fig. 5.2.

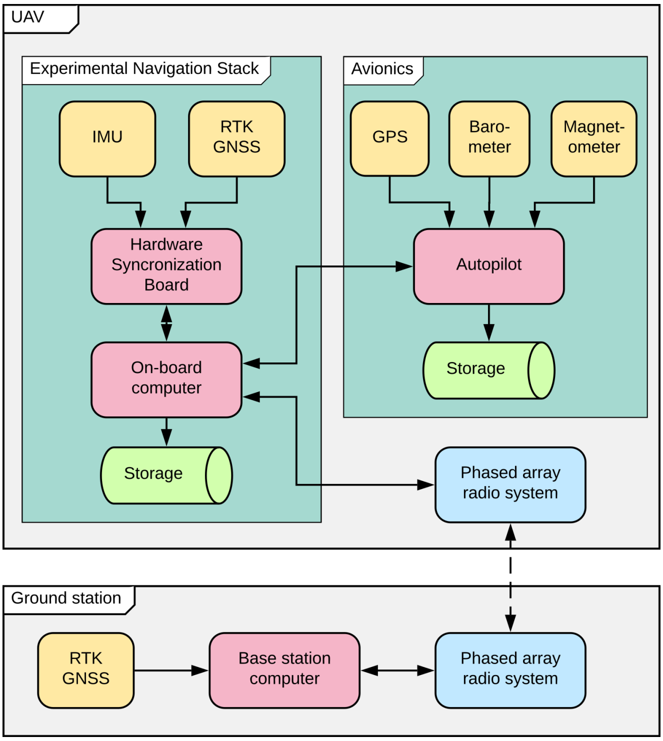


Figure 5.2: System overview

## 5.2 Datasets

We conducted multiple field tests and collected data using the equipment described in Section 5.1. During the field tests, we recorded IMU, RTK-GNSS, and PARS measurements with corresponding timestamps in addition to multiple sensor measurements (including a barometer) from a Pixhawk autopilot. Before conducting the flights, we measured the PARS ground antenna's position and orientation using GNSS and a compass.

### 5.2.1 Dataset 1: Raudtsein 2019

We conducted a field test on the 28$^{\text{th}}$ November 2019 at Raudstein in the north of Agdenes outside Trondheim. We performed test flights using a Skywalker X8 UAV with a **single** PARS ground antenna. Please see [26] for more details about the details of this field test.

#### Publication

The data from this field test was used in

- Mika Okuhara, Torleiv Håland Bryne, Kristoffer Gryte, and Tor Arne Johansen. Phased array radio navigation system on UAVs: Real-time implementation of in-flight calibration. *IFAC-PapersOnLine*, 56(2):1152–1159, 2023. 22nd IFAC World Congress

### 5.2.2 Dataset 2: Raudtsein 2020

A field test was carried out on October 8$^{\text{th}}$ 2020 under good weather conditions in the north of Agdenes outside of Trondheim, Norway. Multiple flights with a Skywalker X8 UAV were performed using **two** ground antennas for PARS.

The general architecture of the experimental equipment was as usual and the first ground antenna was located at the ground station as described in Section 5.1. The second antenna was set approximately perpendicular to the first antenna with a 2.6 km separation between the two antennas. The PARS was set to a 2 Mbit/s mode with a maximum distance of up to 60 km. The PARS modules communicate in the 5 GHz band.

#### Flight path

The flight path and the location of the ground antennas are indicated in Fig. 5.3.

#### Publication

The data from this field test was used in

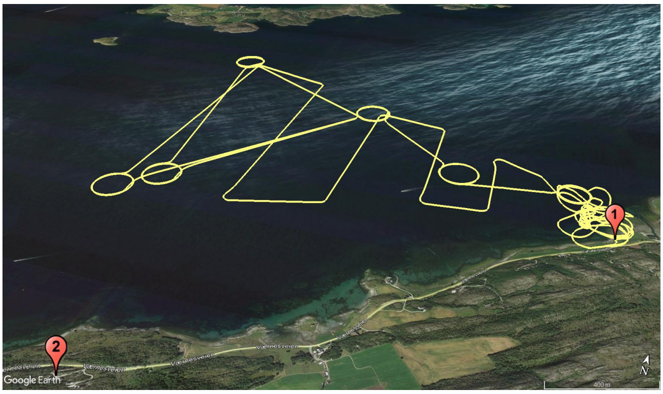


Figure 5.3: Flight path (Raudstein 2020)

- Mika Okuhara, Torleiv Håland Bryne, Kristoffer Gryte, and Tor Arne Johansen. Phased array radio navigation system on UAVs: GNSS-based calibration in the field. In *2021 International Conference on Unmanned Aircraft Systems (ICUAS)*, pages 210–218, 2021
- Mika Okuhara, Torleiv Håland Bryne, Kristoffer Gryte, and Tor Arne Johansen. Phased array radio and barometric navigation system for UAVs: A nonlinear measurement update approach. Internal Report, 2021
- Mika Okuhara, Torleiv Håland Bryne, Kristoffer Gryte, and Tor Arne Johansen. Phased array radio navigation system on UAVs: In-flight calibration. *Journal of Intelligent & Robotic Systems*, 109(3):51, 2023
- Mika Okuhara, Torleiv Håland Bryne, Kristoffer Gryte, and Tor Arne Johansen. Phased array radio navigation system on UAVs: Multi hypothesis filter for noise mitigation. Internal Report, 2023
- Mika Okuhara, Torleiv Håland Bryne, Kristoffer Gryte, and Tor Arne Johansen. Elevation angle redundancy from barometric altitude in multipath-affected phased array radio navigation of UAVs. In *2024 International Conference on Unmanned Aircraft Systems (ICUAS)*, 2024. Submitted

### 5.2.3 Dataset 3: Bleik 2022

An open GNSS jamming event was arranged by the Norwegian Communications Authority (Nkom), the Norwegian Public Roads Administration (NPRA), and the Norwegian Defense Research Establishment (FFI) at Bleik, Andøya, Norway on 19$^{\text{th}}$-23$^{\text{rd}}$ September 2022.

In addition to the usual equipment described in Section 5.1 during this event, we also recorded data from GNSS receivers fixed on the ground. When GNSS jamming is active, the UAV ran the PARS-aided INS implemented in DUNE unified navigation environment [57] on the onboard computer, and used the position reference from the PARS-aided INS in a closed-loop feedback. When GNSS jamming is NOT active, the UAV operated as usual using the Pixhawk autopilot. More details about this jamming event is given in Chapter 8.

**Publication**

A dataset recorded **when jamming is NOT active** on the 20$^{th}$ September 2022 was used in

- Mika Okuhara, Torleiv Håland Bryne, Kristoffer Gryte, and Tor Arne Johansen. Phased array radio navigation system on UAVs: Real-time implementation of in-flight calibration. *IFAC-PapersOnLine*, 56(2):1152–1159, 2023. 22nd IFAC World Congress

Multiple datasets recorded **when jamming is active** on the 20$^{th}$ September 2022 were used in

- Mika Okuhara, Torleiv Håland Bryne, Kristoffer Gryte, Oliver Hasler, and Tor Arne Johansen. UAV navigation during active GNSS jamming using phased-array-radio positioning. *NAVIGATION: Journal of the Institute of Navigation*, 2024. Submitted.

# 6 Calibration of ground antenna orientation

One of the critical points of PARS is that each time the ground radio antenna is moved, its full pose needs to be determined. This was done manually in the previous work, either by measuring the position and the attitude using a GNSS receiver and a compass, or by manually aligning PARS with the GNSS position. However, as the range from the ground radio becomes larger, a small error in antenna orientation induces large errors in measured PARS position. Thus, automatic estimation of the pose is an ideal method to achieve more accurate calibration results.

A similar problem setting can be seen in the area of vision-aided inertial navigation systems (V-INS's). The V-INS provides state estimates with combination of visual and inertial sensors. Its precision depends on a precise calibration of the rigid body transform between sensors, and one of the major methods is a Kalman filter to estimate relative rotation and translation recursively [60, 61, 62]. Strapdown inertial navigation system (SINS) also uses a similar method. The SINS performance depends on the accuracy and speed of initial alignment process, which is one of the key technologies in SINS. The KF is widely used in the initial alignment [63] with the information from an external sensor device such as GNSS [64], odometer [65] and Doppler velocity log (DVL) [66]. Optimisation-based initial alignment is also suggested as obtaining a roughly known initial estimate required for KF is hard for an in-motion vehicle [67, 68]. However, as we are aiming to run the calibration algorithm online in parallel the system operation, and the PARS ground radio antenna orientation can be roughly estimated using a compass [25], and with more practical treatment of noise, Kalman filter is suitable for the antenna orientation calibration.

The main idea of this chapter is formulating the calibration algorithm for the PARS ground antenna orientation (Section 6.1), integrating the algorithm with our navigation system to enable in-flight calibration (Section 6.2), and implementing the extended navigation system for real-time UAV operation (Section 6.3). The calibration algorithm uses GNSS data as ground truth, and the accuracy of the calibration should benefit both from a long calibration period, and from a long range between the UAV and the ground station. If GNSS is not available, this method cannot be used, and less accurate PARS navigation must be accepted.

This chapter is based on on the papers

- Mika Okuhara, Torleiv Håland Bryne, Kristoffer Gryte, and Tor Arne Johansen. Phased array radio navigation system on UAVs: GNSS-based calibration in the field. In *2021 International Conference on Unmanned Aircraft Systems (ICUAS)*, pages 210–218, 2021

- Mika Okuhara, Torleiv Håland Bryne, Kristoffer Gryte, and Tor Arne Johansen. Phased array radio navigation system on UAVs: In-flight calibration.

*Journal of Intelligent & Robotic Systems*, 109(3):51, 2023

- Mika Okuhara, Torleiv Håland Bryne, Kristoffer Gryte, and Tor Arne Johansen. Phased array radio navigation system on UAVs: Real-time implementation of in-flight calibration. *IFAC-PapersOnLine*, 56(2):1152–1159, 2023. 22nd IFAC World Congress

## 6.1 Calibration of the PARS ground antenna mounting

### 6.1.1 Introduction

In this work, an automatic estimation of the PARS antenna orientation was implemented using MEKF. This filter fuses PARS and GNSS measurements and estimates the optimal antenna orientation.

### 6.1.2 The Calibration Algorithm

The PARS antenna calibration problem is essentially to estimate the relative orientation of the PARS coordinate frame $\{r\}$ and the navigation frame $\{n\}$ [1]. The calibration algorithm that we developed to estimate the PARS ground antenna mounting is essentially a MEKF which uses the PARS position as a measurement ($\boldsymbol{y}$) and the GNSS position as an estimate of the measurement ($\hat{\boldsymbol{y}}$) in the measurement model. The MEKF then applies corrections to the state accordingly, to get close to the true state, resulting the estimation of the antenna attitude:

In other words, the estimated error state $\delta \boldsymbol{q}_r^n$ is used as a correction to the nominal state $\hat{\boldsymbol{q}}_r^n$ to get closer to the true state $\boldsymbol{q}_r^n$, being a unit quaternion representing the rotation between the $\{r\}$ and the $\{n\}$:

$$\boldsymbol{q}_r^n = \hat{\boldsymbol{q}}_r^n \otimes \delta \boldsymbol{q}_r^n(\delta \boldsymbol{a}). \tag{6.1}$$

Please note that the state vector contains only the attitude of the PARS ground antenna ( $\boldsymbol{q}_r^n$ or $\delta \boldsymbol{a}$ ) in this work, and Sections 4.1–4.3 in Chapter 4 were not used in this work. The outlier rejection from Section 4.4 was used. The general explanation of MEKF is in Section 4.5. The system and measurement models fed into the MEKF is presented below.

#### System model

**Nominal system model** As the PARS antenna is still on the ground, the system model is simply

$$\dot{\boldsymbol{q}}_r^n = 0. \tag{6.2}$$

The discrete version is

$$\hat{\boldsymbol{q}}_r^n[k] = \boldsymbol{q}_r^n[k-1]. \tag{6.3}$$

[1] The subscript $j$ is omitted here.

**Error-state model** The error state is computed in four times the MRPs $\delta\boldsymbol{a}$ other than rotation matrix or quaternion, and converted to $\delta\boldsymbol{q}_r^n$ when correcting the nominal state.

The continuous-time linearized error state system model

$$\delta\dot{\boldsymbol{a}} = \boldsymbol{F}(t)\delta\boldsymbol{a} + \boldsymbol{G}(t)\boldsymbol{\varepsilon}_{\delta\boldsymbol{a}} \tag{6.4}$$

where $\boldsymbol{\varepsilon}_{\delta\boldsymbol{a}}$ is the process noise with spectral density $\boldsymbol{Q}$ given by $\mathbb{E}[\boldsymbol{\varepsilon}_{\delta\boldsymbol{a}}(t)\boldsymbol{\varepsilon}_{\delta\boldsymbol{a}}^\top(\tau)] = \boldsymbol{Q}\delta(t-\tau) \in \mathbb{R}^{3\times3}$. As the PARS ground antenna is still, we can assume

$$\boldsymbol{F}(t) = \boldsymbol{0}_{3\times3} \tag{6.5}$$

$$\boldsymbol{G}(t) = \boldsymbol{I}_{3\times3} \tag{6.6}$$

$$\boldsymbol{Q} \approx \boldsymbol{0}_{3\times3} \tag{6.7}$$

the discretized system matrices are

$$\boldsymbol{F}_d = \boldsymbol{I}_{3\times3} \tag{6.8}$$

$$\boldsymbol{Q}_d \approx \boldsymbol{0}_{3\times3} \tag{6.9}$$

using van Loan in Appendix B.4.

**Measurement model**

The measurement model is formulated based on the following relationship between the UAV position ($\boldsymbol{p}_{eb}^e$), the ground station position ($\boldsymbol{p}_{er}^e$) and UAV PARS position relative to the ground radio ($\boldsymbol{p}_{rb}^r$):

$$\boldsymbol{p}_{eb}^e = \boldsymbol{p}_{er}^e + \boldsymbol{R}_{en}\boldsymbol{R}_{nr}\boldsymbol{p}_{rb}^r. \tag{6.10}$$

Firstly, moving $\boldsymbol{p}_{er}^e$ from RHS to LHS yields

$$\boldsymbol{p}_{eb}^e - \boldsymbol{p}_{er}^e = \boldsymbol{R}_{en}\boldsymbol{R}_{nr}\boldsymbol{p}_{rb}^r. \tag{6.11}$$

By multiplying both sides by $\boldsymbol{R}_n^{e\top}$ and using $\boldsymbol{R}_{nr} = \hat{\boldsymbol{R}}_{nr}(\boldsymbol{I}_3 + \boldsymbol{S}(\delta\boldsymbol{a}))$,

$$\boldsymbol{R}_{en}^\top(\boldsymbol{p}_{eb}^e - \boldsymbol{p}_{er}^e) = \boldsymbol{R}_{en}^\top\boldsymbol{R}_{en}\boldsymbol{R}_{nr}\boldsymbol{p}_{rb}^r \tag{6.12}$$

$$= \hat{\boldsymbol{R}}_{nr}(\boldsymbol{I}_3 + \boldsymbol{S}(\delta\boldsymbol{a}))\boldsymbol{p}_{rb}^r \tag{6.13}$$

$$= \hat{\boldsymbol{R}}_{nr}\boldsymbol{p}_{rb}^r + \hat{\boldsymbol{R}}_{nr}\boldsymbol{S}(\delta\boldsymbol{a})\boldsymbol{p}_{rb}^r. \tag{6.14}$$

Swapping cross product between $\boldsymbol{p}_{rb}^r$ and $\delta\boldsymbol{a}$ yields

$$\boldsymbol{R}_{en}^\top(\boldsymbol{p}_{eb}^e - \boldsymbol{p}_{er}^e) = \hat{\boldsymbol{R}}_{nr}\boldsymbol{p}_{rb}^r - \hat{\boldsymbol{R}}_{nr}\boldsymbol{S}(\boldsymbol{p}_{rb}^r). \tag{6.15}$$

Finally, by rearranging the order

$$\underbrace{\hat{\boldsymbol{R}}_{nr}\boldsymbol{p}_{rb}^r}_{\boldsymbol{y}} = \underbrace{\boldsymbol{R}_{en}^\top(\boldsymbol{p}_{eb}^e - \boldsymbol{p}_{er}^e)}_{\hat{\boldsymbol{y}}} + \underbrace{\hat{\boldsymbol{R}}_{nr}\boldsymbol{S}(\boldsymbol{p}_{rb}^r)}_{\boldsymbol{H}}\,\delta\boldsymbol{a}. \tag{6.16}$$

Thus,

$$\boldsymbol{y} = \hat{\boldsymbol{R}}_{nr}\boldsymbol{p}^r_{rb} \tag{6.17}$$
$$\hat{\boldsymbol{y}} = \boldsymbol{R}^\top_{en}(\boldsymbol{p}^e_{eb} - \boldsymbol{p}^e_{er}) \tag{6.18}$$
$$\boldsymbol{H} = \hat{\boldsymbol{R}}_{nr}\boldsymbol{S}(\boldsymbol{p}^r_{rb}). \tag{6.19}$$

GNSS and PARS measurements correspond to $\boldsymbol{p}^e_{eb}$ and $\boldsymbol{p}^r_{rb}$, respectively. $\boldsymbol{R}^\top_{en}$ and $\boldsymbol{p}^e_{er}$ are considered to be known since these can be computed from the surveyed ground antenna location. These measurements are injected into the correction step of the MEKF, where $\mathcal{R} = \mathcal{R}^n_{\text{GNSS}} + \mathcal{R}^n_{\text{PARS}}$ is a sum of RTK-GNSS and PARS measurement noise matrices, and where $\mathcal{R}^n_{\text{GNSS}} = \boldsymbol{R}^\top_{en}\mathcal{R}^e_{\text{GNSS}}\boldsymbol{R}_{en}$.

### Noise mitigation

In addition to the outlier rejection (described in Section 4.4), some practical modifications were made to mitigate noise effects in PARS measurements.

Firstly, as the elevation angles of PARS measurements are especially noisy, the PARS measurement equation was reformulated.

Secondly, as the PARS measurement, $\boldsymbol{p}^r_{rb}$ in the skew matrix of $\boldsymbol{H}$ was still noisy even though replacing the elevation angles by altitudes, $\boldsymbol{p}^r_{rb}$ was expressed by less noisy RTK-GNSS measurement of UAV, $\boldsymbol{p}^e_{eb}$ and antenna locations, $\boldsymbol{p}^e_{er}$ by arranging Eq. (6.11),

$$\boldsymbol{p}^r_{rb} = \hat{\boldsymbol{R}}^\top_{nr}\boldsymbol{R}^\top_{en}(\boldsymbol{p}^e_{eb} - \boldsymbol{p}^e_{er}) \tag{6.20}$$

and the equation (6.20) was substituted into the skew matrix of $\boldsymbol{H}$ in equation (6.19) to reduce the noise effect in the $\boldsymbol{H}$ matrix:

$$\boldsymbol{H} = -\hat{\boldsymbol{R}}_{nr}\boldsymbol{S}(\hat{\boldsymbol{R}}^\top_{nr}\boldsymbol{R}^\top_{en}(\boldsymbol{p}^e_{eb} - \boldsymbol{p}^e_{er})). \tag{6.21}$$

Here, the risk of this modification is the nominal state of antenna orientation $\hat{\boldsymbol{R}}_{nr}$. If this estimate is too far from the true state, this modification induces error in computation of $\boldsymbol{H}$ compared to using the measured $\boldsymbol{p}^r_{rb}$ vector.

### Validation

The estimated antenna orientation is validated by evaluating the residual between PARS and RTK-GNSS measurements,

$$\boldsymbol{p}^n_{nb\text{PARS}} - \boldsymbol{p}^n_{nb\text{RTK}}. \tag{6.22}$$

The RTK-GNSS measurement in $\{n\}$ frame was computed as[2]

$$\boldsymbol{p}^n_{nbRTK} = \boldsymbol{R}^\top_{en}(\boldsymbol{p}^e_{eb} - \boldsymbol{p}^e_{er}), \tag{6.23}$$

[2] $\boldsymbol{p}^e_{er} = \boldsymbol{p}^e_{en}$ since the origins of $\{n\}$ frame and $\{r\}$ frame coincide

and the position based on PARS measurements in $\{n\}$ frame was calculated using[3]

$$\boldsymbol{p}^{n}_{nb\mathrm{PARS}} = \boldsymbol{R}_{n*r}\boldsymbol{p}^{r}_{rb}, \tag{6.24}$$

where

$$\boldsymbol{R}_{n*r} = \begin{pmatrix} r_{11} & r_{12} & 0 \\ r_{21} & r_{22} & 0 \\ 0 & 0 & 1 \end{pmatrix}, \tag{6.25}$$

whereas $r_{11}$–$r_{22}$ are elements taken from the estimated matrix $\boldsymbol{R}_{nr}$.

$\boldsymbol{R}_{nr}$ was modified as RTK-GNSS altitude was used instead of PARS elevation angle. This modification might induce some biases in $x$- and $y$-components of $\boldsymbol{p}^{n}_{nb\mathrm{PARS}}$, since the effect of non-zero roll and pitch angles were ignored. If the roll and pitch angles are zero and only yaw angle affects the rotation between $\{r\}$ frame and $\{n\}$ frame, the $z$-component of $\boldsymbol{p}^{r}_{nb}$ does not affect $x$- and $y$-components. However, when the roll and pitch angles are not exactly zero, the contribution of the $z$-component has an effect.

### 6.1.3 Overview

An overview of the calibration algorithm is given in Fig. 6.1.

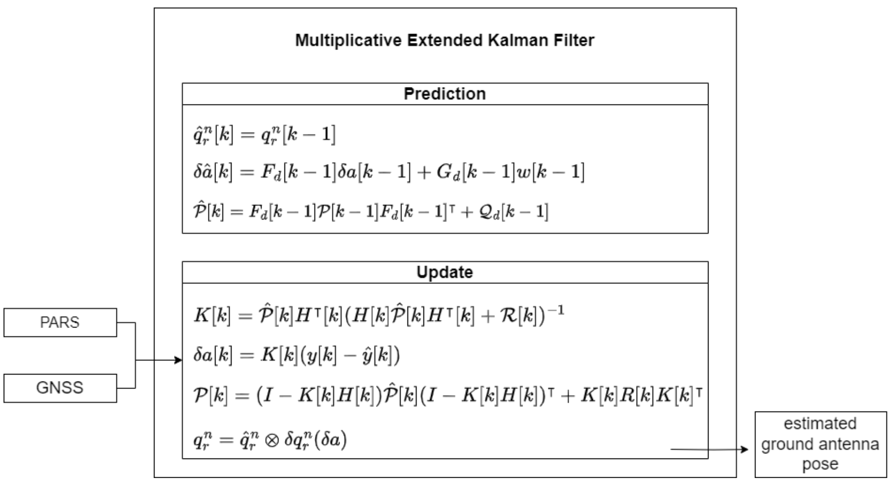


Figure 6.1: Calibration algorithm overview

### 6.1.4 Practical Aspects

In this work, we used the field test data from Raudstein 2020 (described in Section 5.2.2). Please note that the data from *multiple flights* and *only the first* PARS

[3] $\boldsymbol{p}^{r}_{nb} = \boldsymbol{p}^{r}_{rb}$ since the origins of $\{n\}$ frame and $\{r\}$ frame coincide

ground antenna was used. The tracks of the first and second UAV flights, named "flight 1" and "flight 2", are given in Fig. 6.2. The details of the UAV equipment used for the field test are the same as Section 5.1.

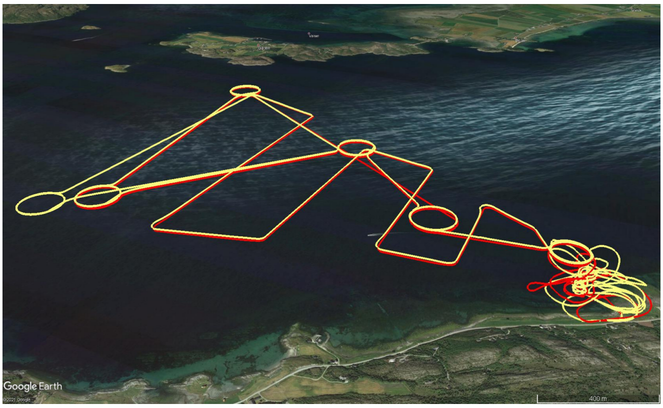


Figure 6.2: Flight paths of the UAV based on RTK-GNSS (flight 1 is yellow, flight 2 is red)

#### Initial calibration

As the algorithm shown in the Section 6.1.2 requires reasonably accurate initial estimates, the antenna orientation angles were measured using a compass. However, the compass gave only a crudely known angle as the compass measurement changes when it is close to a metal antenna. While the full orientation consists of the roll, pitch and yaw angles, only the yaw angle was measured, since the roll and pitch angles are close enough to zero, and were considered to be reasonable for the initial estimates. The PARS ground antenna position was identified using a GNSS receiver.

### 6.1.5 Results and Discussion

Offline calculations were carried out using the data obtained from the field test to verify the calibration algorithm presented in Section 6.1.2. The calibration algorithm was applied to the data from flight 1 and flight 2 with an identical ground antenna position and the results were compared between the two flights. In the offline calculations, rough estimates of the antenna orientation measured by a compass were used as an initial state:

$$\mathbf{\Theta}_{\text{PARS}} = (\phi_r\,, \theta_r\,, \psi_r) = (0\,, 0\,, -65.5^\circ).$$

The initial $\boldsymbol{P}$, $\boldsymbol{Q}$, and $\boldsymbol{R}_\star$ matrices were set as follows:

$$\begin{aligned}\boldsymbol{P}_0 &= \text{diag}((3°)^2, (3°)^2, (50°)^2)\\ \boldsymbol{Q} &= \boldsymbol{0}_{3\times3}\\ \boldsymbol{R}_{\text{PARS}} &= \text{diag}((15\,\text{m})^2, (2°)^2, (5\,\text{m})^2)\\ \boldsymbol{R}_{\text{RTK}} &= \text{diag}((0.2\,\text{m})^2, (0.2\,\text{m})^2, (0.4\,\text{m})^2).\end{aligned}$$

$\boldsymbol{Q}$ was set to 0, as the ground antenna is stationary. The $\chi^2_\alpha = 7.815$ was chosen as the outlier rejection threshold.

Figure 6.3 shows the antenna orientation estimates from flight 1 and flight 2 in Euler angles. In addition to the compass measurement, extreme initial conditions were also considered by setting the initial yaw angle to $-52°$ and $-97°$. Even though the initial estimates contain a relatively large variance, both $\psi_r = -52°$ and $\psi_r = -97°$ cases converged.

In the situation when GNSS is not available initially but available only a short period at some point, it corrects the estimation fairly quickly, as Fig. 6.4 shows. Here, 1 min of RTK-GNSS was made available for correction at mid-point in flight 2. Comparing with Fig. 6.3, applying calibration when the UAV is further might require shorter GNSS flight duration.

Table 6.1 shows the Euler angle estimates averaged over the last 100 iterations when $\psi_r = -65.5°$. Pitch gave the minimum and yaw gave maximum variance, since the PARS measurements have better accuracy in range and elevation than azimuth due to the aid of RTK-GNSS altitude. The difference in yaw angles between flight 1 and flight 2 was 0.144 50° which gives 7.6164 m error at the furthest point where the maximum ranges for flight 1 and flight 2 were 3.0225km and 3.0263km.

Table 6.2 shows the Euler angles averaged over last 100 iterations and means of residuals in flight 2 when $\psi_r = -65.5°$, where the antenna position has an error of 0.1m, 1m, and 10m. As the error becomes bigger, the induced errors in estimation increase. However, it still converges and gives relatively reasonable estimations even when the position error is 10m.

The estimated antenna orientation when $\psi_r = -65.5°$ was validated by the residual between the calibrated PARS and RTK-GNSS measurements, as shown in Fig. 6.5. Apart from small biases due to Eq. (6.24), the residual gave reasonable results, which indicates that the estimated antenna orientation is promising.

| | Flight 1 | Flight 2 |
|---|---|---|
| Roll [°] | 0.0042313 | 0.0039529 |
| Pitch [°] | -0.0014450 | -0.0013951 |
| Yaw [°] | -74.592 | -74.736 |

Table 6.1: Estimated antenna orientation in Euler angles

| Errors | 0.1 m | 1 m | 10 m |
|---|---|---|---|
| Roll [°] | 0.0037511 | 0.0019389 | -0.015739 |
| Pitch [°] | -0.0026741 | -0.014184 | -0.12920 |
| Yaw [°] | -74.733 | -74.702 | -74.396 |
| x [m] | 0.64061 | 1.5273 | 10.362 |
| y [m] | 1.9636 | 2.2236 | 4.8465 |

Table 6.2: Sensitivity of PARS antenna position in flight 2

### 6.1.6 Conclusion

In this paper, a MEKF-based calibration algorithm was implemented that automatically estimates the orientation of the ground antenna for the PARS. The calibration algorithm was applied to data obtained from a field test which involves multiple flights with an identical position of a ground antenna. The antenna orientations estimated from two independent flights coincided, and the suggested algorithm was proved to be robust and able to calibrate the antenna orientation based on RTK-GNSS measurements. As a future work, calibration using INS or additional PARS instead of GNSS is in the interest to achieve a fully GNSS-free navigation system.

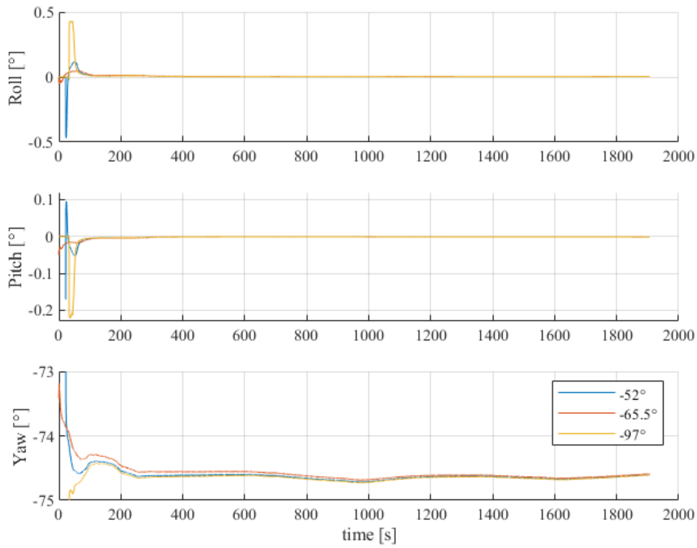


(a) flight 1

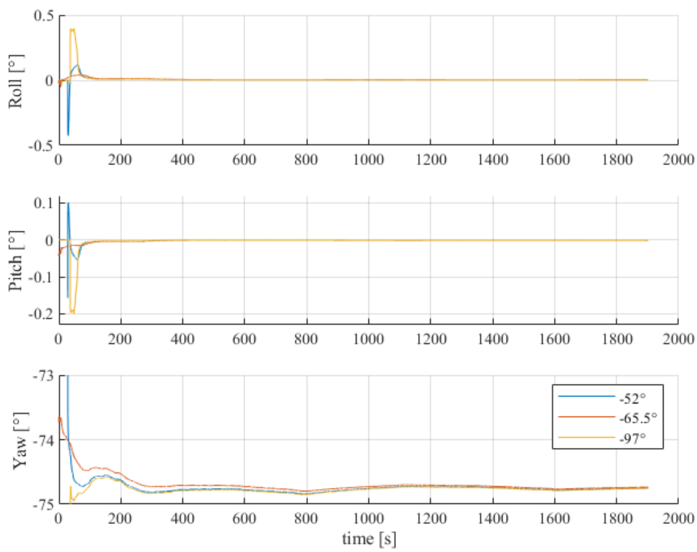


(b) flight 2

Figure 6.3: Euler angles of antenna orientations

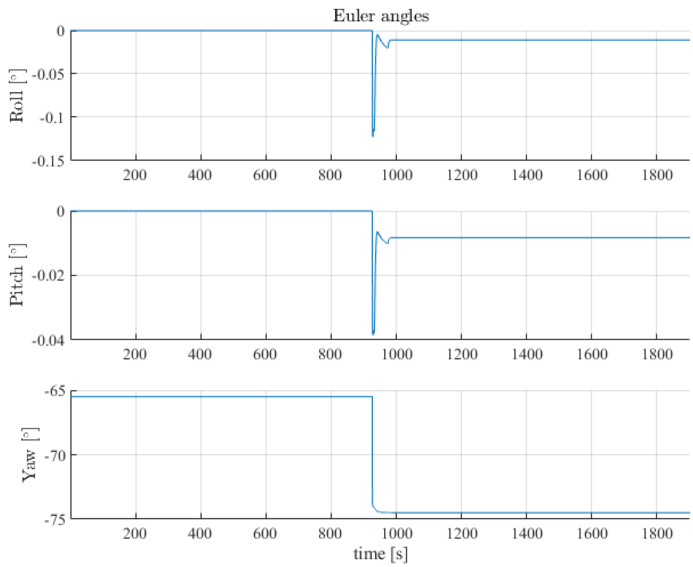


Figure 6.4: Euler angles of antenna orientation in flight 2 when GNSS is available only 1 min

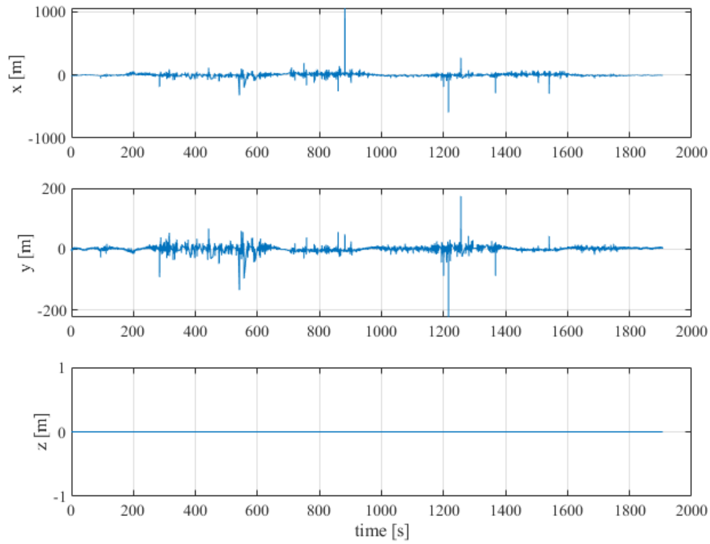


(a) flight 1

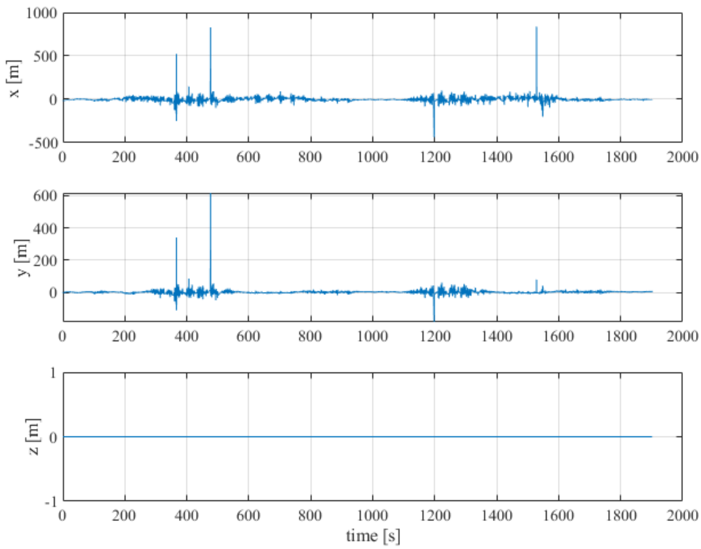


(b) flight 2

Figure 6.5: Residual between calibrated PARS and RTK-GNSS

## 6.2 Aided INS with in-flight calibration

### 6.2.1 Introduction

The main idea of this work is to enhance the calibration algorithm developed in Chapter 6.1. The major improvements are the following:

- The standalone calibration algorithm was integrated in the MEKF-based aided-INS such that we can perform the calibration online whenever GNSS measurements are available during flights.
- The algorithm integrated with the aided-INS enabled it to estimate the full poses of *multiple* PARS ground radios. We achieved this by including the ground antennas' orientation and its kinematics in extended state vector and the matrices of the MEKF.
- Further improvements to the entire aided-INS system were also made. The navigation equations were propagated in ECEF frame instead of NED frame, unlike the previous work [23, 24, 25, 26]. Using the ECEF frame as the navigation frame eases the calibration of multiple ground antennas by having a common reference frame. It also improves the use of PARS-aided INS in long-duration flight since this formulation considers the curvature of the Earth, and the navigation system directly outputs an unambiguous global position estimate.

This method enables refinement of the PARS-based navigation accuracy during a flight, even in the situation of GNSS unavailability at the initial stage of flight. Furthermore, considering that the calibration accuracy benefits from a long calibration period and a long-range between the UAV and the ground station, it gives a large extent of flexibility.

Moreover, this work also takes advantage of a direct barometer measurement providing altitude aiding to the INS independent of any other external altitude measurements as in [23, 24, 25, 26]. Data obtained from a field test using a fixed wing UAV and two ground antennas was used to verify the proposed method.

### 6.2.2 Positioning

The positioning techniques that formulate the navigation system in this work are INS (Section 3.1), RTK GNSS (Section 3.2), PARS (Section 3.3) and barometer (Section 3.4). The RTK GNSS measurements were also used as ground truth to examine the performance of the PARS and barometer-aided INS.

### 6.2.3 Navigation System

The navigation system in this work is the extended version of the one in Chapter 4. The differences are:

1. the system model (Section 4.1) was extended to include attitude states of $m$ ground antennas (i.e. the state vector was extended).
2. the calibration algorithm from Chapter 6.1 was added to the measurement models (Section 4.2). The measurement matrices were extended accordingly to the expansion of the state vector.
3. the measurement matrices for pre-launch calibration (Section 4.3) were also extended accordingly to the expansion of state vector.

The outlier rejection (Section 4.4) andMEKF (Section 4.5) are the same as Chapter 4.

Fundamentally, the INS was aided in two modes: The first mode is GNSS and PARS-aided INS so that the calibration algorithm from Chapter 6.1 can run simultaneously to estimate the PARS ground antenna orientations, and the second mode is PARS and barometer-aided INS, as shown in Figure 6.6. The navigation system switches between the two modes depending on the availability of GNSS measurements.

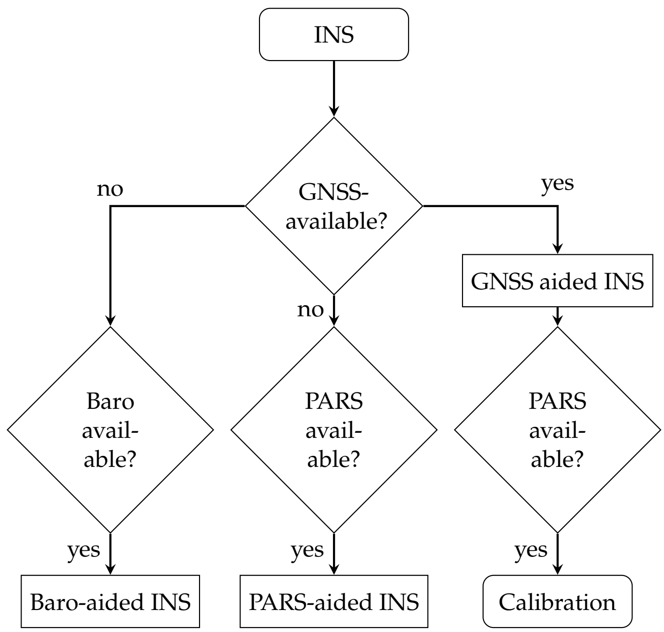


Figure 6.6: Flowchart of the navigation system

### 6.2.4 Navigation system model

The system model in Section 4.1 was extended to include attitude states of $m$ ground antennas (i.e. the state vector was extended).

### Nominal system kinematics

The nominal state estimate was given as

$$\hat{\boldsymbol{x}} = (\hat{\boldsymbol{p}}^e_{eb},\ \hat{\boldsymbol{v}}^e_{eb},\ \hat{\boldsymbol{q}}^e_b,\ \hat{\boldsymbol{b}}^b_{\text{acc}},\ \hat{\boldsymbol{b}}^b_{\text{ars}},\ \boldsymbol{q}^{n_1}_{r_1},\ \dots,\ \boldsymbol{q}^{n_m}_{r_m})^\intercal \in \mathbb{R}^{16+4m} \tag{6.26}$$

where $\boldsymbol{q}^{n_j}_{r_j}$ is the PARS ground antenna orientation, which is essentially the relative orientation of the PARS coordinate frame $\{r_j\}$ and the navigation frame $\{n_j\}$ for ground antenna $j \in [1, m]$.

The nominal state is updated using the following kinematic model based on the strapdown equations presented in Section 3.1

$$\dot{\hat{\boldsymbol{p}}}^e_{eb} = \hat{\boldsymbol{v}}^e_{eb} \tag{6.27a}$$

$$\dot{\hat{\boldsymbol{v}}}^e_{eb} = -2\boldsymbol{S}(\boldsymbol{\omega}^e_{ie})\hat{\boldsymbol{v}}^e_{eb} + \hat{\boldsymbol{R}}_{eb}\hat{\boldsymbol{f}}^b_{ib} + \boldsymbol{g}^e_b(\hat{\boldsymbol{p}}^e_{eb}) \tag{6.27b}$$

$$\dot{\hat{\boldsymbol{q}}}^e_b = \frac{1}{2}\boldsymbol{\Omega}(\hat{\boldsymbol{\omega}}^b_{ib})\boldsymbol{q}^e_b - \frac{1}{2}\boldsymbol{\Gamma}(\boldsymbol{\omega}^e_{ie})\boldsymbol{q}^e_b \tag{6.27c}$$

$$\dot{\hat{\boldsymbol{b}}}^b_{\text{acc}} = -\boldsymbol{T}^{-1}_{\text{acc}}\hat{\boldsymbol{b}}^b_{\text{acc}} \tag{6.27d}$$

$$\dot{\hat{\boldsymbol{b}}}^b_{ars} = -\boldsymbol{T}^{-1}_{\text{ars}}\hat{\boldsymbol{b}}^b_{\text{ars}} \tag{6.27e}$$

$$\dot{\hat{\boldsymbol{q}}}^{n_1}_{r_1} = 0 \tag{6.27f}$$

$$\vdots$$

$$\dot{\hat{\boldsymbol{q}}}^{n_m}_{r_m} = 0 \tag{6.27g}$$

$$\hat{\boldsymbol{f}}^b_{ib} = \boldsymbol{f}^b_{\text{IMU}} - \hat{\boldsymbol{b}}^b_{\text{acc}} \tag{6.27h}$$

$$\hat{\boldsymbol{\omega}}^b_{ib} = \boldsymbol{\omega}^b_{\text{IMU}} - \hat{\boldsymbol{b}}^b_{\text{ars}} \tag{6.27i}$$

The derivatives of $\boldsymbol{q}^{n_j}_{r_j}$ of are zero, as the ground antennas are stationary. The equations Eq. (6.27) can be computed in discrete time using any integration methods. Exact integration methods concerting the quaternion integration can be found in [37].

### Error-state system kinematics

The error state was given as

$$\delta\boldsymbol{x} = (\delta\boldsymbol{p}^e_{eb},\ \delta\boldsymbol{v}^e_{eb},\ \delta\boldsymbol{a}^e_b,\ \delta\boldsymbol{b}^b_{acc},\ \delta\boldsymbol{b}^b_{ars},\ \delta\boldsymbol{a}^{n_1}_{r_1},\ \dots\delta\boldsymbol{a}^{n_m}_{r_m})^\intercal \in \mathbb{R}^{15+3m}. \tag{6.28}$$

Please note that the 3D attitude error states $\delta\boldsymbol{a}^\star_\star$ (UAV and ground radio) paramatrized as four times MRPs rather than rotation matrices or quaternions, are used to update the INS's states when correcting the nominal state using Eq. (2.10) and Eq. (2.12).

The continuous-time linearized error state system model

$$\delta\dot{\boldsymbol{x}} = \boldsymbol{F}(t)\delta\boldsymbol{x} + \boldsymbol{G}(t)\boldsymbol{w} \tag{6.29}$$

where $\boldsymbol{w} = (\varepsilon_{\mathrm{acc}}^\intercal, \varepsilon_{\mathrm{ars}}^\intercal, \varepsilon_{b_{\mathrm{acc}}}^\intercal, \varepsilon_{b_{\mathrm{ars}}}^\intercal, \varepsilon_{\delta a_1}^\intercal, \dots, \varepsilon_{\delta a_m}^\intercal)^\intercal$ is the process noise with spectral density $\boldsymbol{Q}$ given by $\mathbb{E}[\boldsymbol{w}(t)\boldsymbol{w}^\intercal(\tau)] = \boldsymbol{Q}\delta(t-\tau) \in \mathbb{R}^{(12+3m)\times(12+3m)}$. The Jacobian matrices $\boldsymbol{F}$ and $\boldsymbol{G}$, and the spectral density matrix $\boldsymbol{Q}$ are given in Appendix C.1.

### 6.2.5 Measurement model (mode 1: PARS calibration)

When GNSS measurements are available, the navigation system uses GNSS to aid the INS while running the PARS ground radio system mounting calibration update presented in Chapter 6.1 simultaneously. The measurement matrices were extended accordingly to the expansion of the state vector.

#### GNSS

This is the extended version of the GNSS measurement model in Section 4.2.1:

The GNSS measures the position of the UAV in the $\{e\}$-frame

$$\boldsymbol{y}_{\mathrm{GNSS}}^e = \boldsymbol{p}_{\mathrm{GNSS}}^e + \varepsilon_{\mathrm{GNSS}}. \tag{6.30}$$

The measurement can be expressed as follows, therefore

$$\boldsymbol{y}_{\mathrm{GNSS}}^e = \hat{\boldsymbol{p}}_{eb}^e + \delta \boldsymbol{p} + \varepsilon_{\mathrm{GNSS}} \tag{6.31}$$

$$\Rightarrow \hat{\boldsymbol{y}}_{\mathrm{GNSS}}^e = \hat{\boldsymbol{p}}_{eb}^e \tag{6.32}$$

such that a linear measurement matrix

$$\boldsymbol{H}_{\mathrm{GNSS}} = \begin{pmatrix} \boldsymbol{I}_3 & \mathbf{0}_{3\times 12} & \mathbf{0}_{3\times 3m} \end{pmatrix} \in \mathbb{R}^{3\times(15+3m)} \tag{6.33}$$

can be applied in the MEKF. The measurement covariance matrix is given as

$$\mathcal{R}_{\mathrm{GNSS}}^e = \boldsymbol{R}_{en} \operatorname{diag}(\mathbb{E}[\varepsilon_{\mathrm{GNSS},N}^2], \mathbb{E}[\varepsilon_{\mathrm{GNSS},E}^2], \mathbb{E}[\varepsilon_{\mathrm{GNSS},D}^2]) \boldsymbol{R}_{en}^\intercal \tag{6.34}$$

where $\varepsilon_{\mathrm{GNSS}}$ is zero-mean Gaussian white noise.

#### PARS: Calibration

To mitigate the noise in the PARS elevation angle, the vertical measurement in Eq. (3.7) was replaced by utilizing an exogenous altitude measurement: [4]

$$\gamma_{y_j} = \gamma_{u_j} + b_{\gamma_j} + \varepsilon_{\gamma_j}. \tag{6.35}$$

The PARS range was also arranged, similarly to Eq. (4.18)

$$\bar{\rho}_{y_j} = \sqrt{\rho_{y_j}^2 - \gamma_{y_j}^2}. \tag{6.36}$$

[4] $\boldsymbol{p}_{r_j b}^{n_j} = \boldsymbol{p}_{n_j b}^{n_j}$ since the origins of $\{n_j\}$ frame and $\{r_j\}$ coincide.

Based on this, the resulting Cartesian position measurement becomes similar to Eq. (4.20)

$$\boldsymbol{p}^{r_j}_{\mathrm{PARS,Alt}} = \begin{pmatrix} \bar{\rho}_{y_j}\cos(\psi_{y_j}) \\ \bar{\rho}_{y_j}\sin(\psi_{y_j}) \\ -\gamma_{y_j} \end{pmatrix} \tag{6.37}$$

The measurement model is formulated based on the following relationship between the UAV position ($\boldsymbol{p}^e_{eb}$), the ground station position ($\boldsymbol{p}^e_{er_j}$) and UAV PARS position relative to the ground radio ($\boldsymbol{p}^{r_j}_{r_jb}$):

$$\boldsymbol{p}^e_{eb} = \boldsymbol{p}^e_{er_j} + \boldsymbol{R}_{en_j}\boldsymbol{R}_{n_jr_j}\boldsymbol{p}^{r_j}_{r_jb}. \tag{6.38}$$

By arranging Eq. (6.38) as shown in [32], the equation results in the form suitable for calibration,

$$\underbrace{\hat{\boldsymbol{R}}_{n_jr_j}\boldsymbol{p}^{r_j}_{r_jb}}_{\boldsymbol{y}_{\mathrm{pars}_j}} = \underbrace{\boldsymbol{R}^{\intercal}_{en_j}\left(\hat{\boldsymbol{p}}^e_{eb} - \boldsymbol{p}^e_{er_j}\right)}_{\hat{\boldsymbol{y}}_{\mathrm{pars}_j}} + \underbrace{\boldsymbol{R}^{\intercal}_{en_j}}_{\boldsymbol{H}_{\mathrm{pos}_j}}\delta\boldsymbol{p} + \underbrace{\hat{\boldsymbol{R}}_{n_jr_j}\boldsymbol{S}\left(\boldsymbol{p}^{r_j}_{r_jb}\right)}_{\boldsymbol{H}_{\mathrm{calib}_j}}\delta\boldsymbol{a}^{n_j}_{r_j} \tag{6.39}$$

where the measurement, the measurement estimate, and the measurement matrices are respectively

$$\boldsymbol{y}_{\mathrm{pars}_j} = \hat{\boldsymbol{R}}_{n_jr_j}\boldsymbol{p}^{r_j}_{\mathrm{PARS,Alt}} \tag{6.40}$$

$$\hat{\boldsymbol{y}}_{\mathrm{pars}_j} = \boldsymbol{R}^{\intercal}_{en_j}\left(\hat{\boldsymbol{p}}^e_{eb} - \boldsymbol{p}^e_{er_j}\right) \tag{6.41}$$

$$\boldsymbol{H}_{\mathrm{pos}_j} = \boldsymbol{R}^{\intercal}_{en_j} \tag{6.42}$$

$$\boldsymbol{H}_{\mathrm{calib}_j} = \hat{\boldsymbol{R}}_{n_jr_j}\boldsymbol{S}\left(\hat{\boldsymbol{R}}^{\intercal}_{er_j}\left(\hat{\boldsymbol{p}}^e_{eb} - \boldsymbol{p}^e_{er_j}\right)\right). \tag{6.43}$$

The resulting measurement matrix becomes

$$\boldsymbol{H}_{\mathrm{pars}} = \begin{pmatrix} \boldsymbol{H}_{\mathrm{pos}_1} & \mathbf{0}_{3\times12} & \boldsymbol{H}_{\mathrm{calib}_1} & & & \mathbf{0}_{3\times3(m-1)} \\ \vdots & \vdots & & \ddots & & \vdots \\ \boldsymbol{H}_{\mathrm{pos}_j} & \mathbf{0}_{3\times12} & \mathbf{0}_{3\times3(j-1)} & & \boldsymbol{H}_{\mathrm{calib}_j} & \mathbf{0}_{3\times3(m-j-1)} \\ \vdots & \vdots & & & & \ddots \\ \boldsymbol{H}_{\mathrm{pos}_m} & \mathbf{0}_{3\times12} & & \mathbf{0}_{3\times3(m-1)} & & \boldsymbol{H}_{\mathrm{calib}_m} \end{pmatrix} \in \mathbb{R}^{3m\times(15+3m)}. \tag{6.44}$$

The intermediate calculation between Eq. (6.38) and Eq. (6.39) can be found in Appendix C.2 (the expanded and reformulated version of Section 6.1.2). The position estimate from GNSS-aided INS and the PARS measurement correspond to $\boldsymbol{p}^e_{eb}$ and $\boldsymbol{p}^{r_j}_{r_jb}$ (i.e. $\boldsymbol{p}^{r_j}_{\mathrm{PARS,Alt}}$), respectively. $\boldsymbol{R}^{e}_{n_j}{}^{\intercal}$ and $\boldsymbol{p}^e_{er_j}$ are considered known, since these can be computed from the antenna locations of the ground station surveyed. Furthermore, the covariance of the original PARS measurement $\rho_{y_j}$, $\psi_{y_j}$ and $\gamma_{y_j}$ is

$$\boldsymbol{\mathcal{R}}_{\mathrm{PARS,Alt}} = \mathrm{diag}(\mathbb{E}[\varepsilon^2_\rho], \mathbb{E}[\varepsilon^2_\psi], \mathbb{E}[\varepsilon^2_\gamma]) \tag{6.45}$$

and the covariance of $\boldsymbol{p}^{r_j}_{\text{PARS,Alt}}$ can be computed using

$$\boldsymbol{\mathcal{R}}^{r_j}_{\text{PARS,Alt}} = \boldsymbol{M}_{\text{PARS,Alt}_j} \boldsymbol{\mathcal{R}}_{\text{PARS,Alt}} \boldsymbol{M}_{\text{PARS,Alt}_j}{}^{\intercal}. \tag{6.46}$$

Here, $\boldsymbol{\mathcal{R}}_{\text{PARS,Alt}}$ given in cylindrical coordinates is converted to $\boldsymbol{\mathcal{R}}^{r_j}_{\text{PARS,Alt}}$ in Cartesian coordinates [47, Ch. 1.6]. $\boldsymbol{M}_{\text{PARS,Alt}_j}$ was computed similarly with Section 4.2.3. $\boldsymbol{M}_{\text{PARS,Alt}_j}$ is a Jacobian matrix of $\boldsymbol{p}^{r_j}_{\text{PARS,Alt}}$ with respect to the noise $\boldsymbol{\varepsilon}_{\text{PARS,Alt}} = (\varepsilon_\rho, \varepsilon_\psi, \varepsilon_\gamma)^\intercal$:

$$\boldsymbol{M}_{\text{PARS,Alt}_j} = \frac{\partial \boldsymbol{p}^{r_j}_{\text{PARS,Alt}}}{\partial \boldsymbol{\varepsilon}_{\text{PARS,Alt}}} = \begin{pmatrix} m_{11} & m_{12} & m_{13} \\ m_{21} & m_{22} & m_{23} \\ 0 & 0 & 1 \end{pmatrix}, \tag{6.47}$$

with

$$\begin{aligned} m_{11} &= \frac{\cos(\psi_{y_j})\rho_{y_j}}{\bar{\rho_{y_j}}} & m_{12} &= -\sin(\psi_{y_j})\bar{\rho_{y_j}} \\ m_{13} &= -\frac{\cos(\psi_{y_j})\gamma_{y_j}}{\bar{\rho_{y_j}}} & m_{21} &= \frac{\sin(\psi_{y_j})\rho_{y_j}}{\bar{\rho_{y_j}}} \\ m_{22} &= \cos(\psi_{y_j})\bar{\rho_{y_j}} & m_{23} &= -\frac{\sin(\psi_{y_j})\gamma_{y_j}}{\bar{\rho_{y_j}}}. \end{aligned}$$

In addition, the covariance can be transformed from $\{r_j\}$ frame to $\{n_j\}$ frame by taking

$$\boldsymbol{\mathcal{R}}^{n_j}_{\text{PARS,Alt}} = \boldsymbol{R}_{n_j r_j} \boldsymbol{M}_{\text{PARS,Alt}_j} \boldsymbol{\mathcal{R}}_{\text{PARS,Alt}} \boldsymbol{M}^\intercal_{\text{PARS,Alt}_j} \boldsymbol{R}^\intercal_{n_j r_j} \tag{6.48}$$

as Eq. (6.40)–Eq. (6.44) in the $\{n_j\}$ frame.

### 6.2.6 Measurement model (mode 2: PARS + Barometer)

To avoid the noise issue, the vertical measurement in Eq. (3.7) was replaced by an altitude measurement based on barometer in [24]. However, since the barometer measures the altitude from the reference surface perpendicular to the tangent line of the Earth's curvature, using the barometer altitude directly in the local NED frame induces errors when the flight distance of the UAV becomes longer since this formulation does not take into account the curvature of the Earth. Therefore, in this paper, the barometer altitude as a replacement of the PARS vertical component was treated separately from the PARS measurements to include the curvature of the Earth.

#### PARS

A measurement of the horizontal range ($\bar{\rho}_{y_j}$) was computed by approximating the elevation angle ($\alpha_j$) using a trigonometric relation, similarly to Eq. (4.19)

$$\bar{\rho}_{y_j} = \rho_{y_j} \cos \alpha_j \tag{6.49}$$

where

$$\cos \alpha_j = \frac{\boldsymbol{p}^e_{eb} \cdot \boldsymbol{p}^e_{er_j}}{\|\boldsymbol{p}^e_{eb}\|_2 \|\boldsymbol{p}^e_{er_j}\|_2}. \tag{6.50}$$

The horizontal components of Cartesian PARS position measurements can be expressed as

$$\begin{aligned} \boldsymbol{y}^{r_j}_{\text{PARS}} &= \begin{pmatrix} \bar{\rho}_{y_j} \cos \psi_{y_j} \\ \bar{\rho}_{y_j} \sin \psi_{y_j} \end{pmatrix}, \\ &= \begin{pmatrix} 1 & 0 & 0 \\ 0 & 1 & 0 \end{pmatrix} \boldsymbol{R}^{\mathsf{T}}_{n_j r_j} \boldsymbol{R}^{\mathsf{T}}_{en_j} \left( \boldsymbol{p}^e_{eb} - \boldsymbol{p}^e_{er_j} \right). \end{aligned} \tag{6.51}$$

By using the relation $\boldsymbol{p}^e_{eb} = \hat{\boldsymbol{p}}^e_{eb} + \delta \boldsymbol{p}^e_{eb}$, the estimate measurement is given as

$$\hat{\boldsymbol{y}}^{r_j}_{\text{PARS}} = \begin{pmatrix} 1 & 0 & 0 \\ 0 & 1 & 0 \end{pmatrix} \hat{\boldsymbol{R}}^{\mathsf{T}}_{n_j r_j} \boldsymbol{R}^{\mathsf{T}}_{en_j} \left( \hat{\boldsymbol{p}}^e_{eb} - \boldsymbol{p}^e_{er_j} \right), \tag{6.52}$$

while the Jacobian matrix of $\boldsymbol{y}^{r_j}_{\text{PARS}}$ with respect to $\delta \boldsymbol{p}^e_{eb}$ can be found by differentiating Eq. (6.52)

$$\left. \frac{\partial \boldsymbol{y}^{r_j}_{\text{PARS}}}{\partial \delta \boldsymbol{p}^e_{eb}} \right|_{\delta \boldsymbol{x} = \mathbf{0}_{2\times(15+3m)}} = \underbrace{\begin{pmatrix} 1 & 0 & 0 \\ 0 & 1 & 0 \end{pmatrix}}_{\boldsymbol{\Pi}} \underbrace{\hat{\boldsymbol{R}}^{\mathsf{T}}_{n_j r_j} \boldsymbol{R}_{en_j}{}^{\mathsf{T}}}_{\hat{\boldsymbol{R}}^{\mathsf{T}}_{er_j}} \in \mathbb{R}^{2\times 3}. \tag{6.53}$$

Hence, the measurement matrix becomes

$$\boldsymbol{H}_{\text{PARS}} = (\boldsymbol{\Pi} \hat{\boldsymbol{R}}^{\mathsf{T}}_{er_j} \; \mathbf{0}_{2\times 3} \; \mathbf{0}_{2\times 3} \; \mathbf{0}_{2\times 3} \; \mathbf{0}_{2\times 3} \; \mathbf{0}_{2\times 3m}) \in \mathbb{R}^{2\times(15+3m)}. \tag{6.54}$$

Furthermore, the covariance of $\boldsymbol{y}^{r_j}_{\text{PARS}}$ can be computed using

$$\mathcal{R}^{r_j}_{\text{PARS}} = \boldsymbol{M}_{\text{PARS}_j} \mathcal{R}_{\text{PARS}} \boldsymbol{M}_{\text{PARS}_j}{}^{\mathsf{T}} \tag{6.55}$$

where

$$\mathcal{R}_{\text{PARS}} = \text{diag}(\mathbb{E}[\varepsilon^2_\rho], \mathbb{E}[\varepsilon^2_\psi]). \tag{6.56}$$

Here, $\mathcal{R}_{\text{PARS}}$ given in cylindrical coordinates is converted to $\mathcal{R}^{r_j}_{\text{PARS}}$ in Cartesian coordinates [47, Ch. 1.6]. $\boldsymbol{M}_{\text{PARS}_j}$ is a Jacobian matrix of $\boldsymbol{y}^{r_j}_{\text{PARS}}$ with respect to the noise $\boldsymbol{\varepsilon}_{\text{PARS}} = (\varepsilon_\rho, \varepsilon_\psi)$:

$$\boldsymbol{M}_{\text{PARS}_j} = \frac{\partial \boldsymbol{y}^{r_j}_{\text{PARS}}}{\partial \boldsymbol{\varepsilon}_{\text{PARS}}} = \begin{pmatrix} m_{11} & m_{12} \\ m_{21} & m_{22} \end{pmatrix} \tag{6.57}$$

with

$$\begin{aligned} m_{11} &= \frac{\cos(\psi_{y_j}) \rho_{y_j}}{\bar{\rho}_{y_j}} & m_{12} &= -\sin(\psi_{y_j}) \bar{\rho}_{y_j} \\ m_{21} &= \frac{\sin(\psi_{y_j}) \rho_{y_j}}{\bar{\rho}_{y_j}} & m_{22} &= \cos(\psi_{y_j}) \bar{\rho}_{y_j}. \end{aligned}$$

In a practical implementation $\hat{\boldsymbol{p}}^e_{eb}$ is used instead of $\boldsymbol{p}^e_{eb}$ in Eq. (6.50) such that

$$\bar{\rho}_{y_j} \approx \rho_{y_j} \frac{\hat{\boldsymbol{p}}^e_{eb} \cdot \boldsymbol{p}^e_{er_j}}{\|\hat{\boldsymbol{p}}^e_{eb}\|_2 \|\boldsymbol{p}^e_{er_j}\|_2}, \tag{6.58}$$

which is valid for small $\|\delta \boldsymbol{p}^e_{eb}\|_2$.

**Barometer**

This is the extended version of the barometer measurement model in Section 4.2.4. Using Eq. (3.17), atmospheric pressure measurements from barometer can be converted to the altitude of UAV from the sea level [5]

$$\gamma_y = \frac{T_0}{K_t} \left[ \left( \frac{P_b}{P_0} \right)^{-(\frac{R_t K_t}{g_0})} - 1 \right]$$

Then the barometer measurement is simply

$$y_{\text{baro}} = \gamma_y.$$

The barometric altitude measurement $y_{\text{baro}}$ can then be related to the position using

$$y_{\text{baro}} = \|\hat{\boldsymbol{p}}^e_{eb} + \delta \boldsymbol{p}^e_{eb} - \boldsymbol{p}^e_{eS}\|_2 + b_\gamma + \varepsilon_\gamma \tag{6.59}$$

where $\boldsymbol{p}^e_{eS}$ denotes the ECEF position of the geoid (approximate Earth's surface) below the UAV position [6], $b_\gamma$ represent the barometers altitude bias and $\varepsilon_\gamma$ is the measurement noise. The Jacobian matrix of $y_{\text{baro}}$ with respect to $\delta \boldsymbol{p}^e_{eb}$ can be computed by differentiating Eq. (6.59)

$$\left.\frac{\partial y_{\text{baro}}}{\partial \delta \boldsymbol{p}^e_{eb}}\right|_{\delta \boldsymbol{p}^e_{eb} = \boldsymbol{0}_{3\times 1}} = \underbrace{\frac{(\hat{\boldsymbol{p}}^e_{eb} - \boldsymbol{p}^e_{eS})^\intercal}{\|\hat{\boldsymbol{p}}^e_{eb} - \boldsymbol{p}^e_{eS}\|}}_{\boldsymbol{H}_{\text{alt}}} \in \mathbb{R}^{1\times 3} \tag{6.60}$$

such that the measurement matrix becomes

$$\boldsymbol{H}_{\text{baro}} = (\boldsymbol{H}_{\text{alt}}\ \boldsymbol{0}_{1\times 3}\ \boldsymbol{0}_{1\times 3}\ \boldsymbol{0}_{1\times 3}\ \boldsymbol{0}_{1\times 3}\ \boldsymbol{0}_{1\times 3m}) \in \mathbb{R}^{1\times(15+3m)} \tag{6.61}$$

and the measurement covariance matrix is simply

$$\boldsymbol{\mathcal{R}}_{\text{baro}} = \mathbb{E}[\varepsilon_\gamma^2]. \tag{6.62}$$

**Multiplicative extended Kalman Filter**

Using the motion model and the measurement models presented in Section 6.2.4, 6.2.6 and 6.2.5, MEKF is propagated. The procedure is similar for both mode 1 and mode 2.

[5] See Section 3.4.2 for details.
[6] See Section 3.4.1 for details.

### 6.2.7 Overview

An overview of the in-flight calibration navigation system is given in Fig. 6.7.

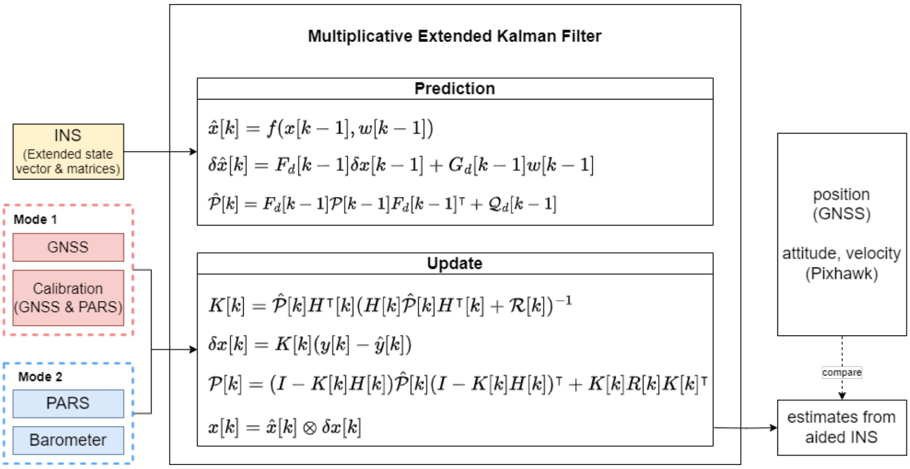


Figure 6.7: In-flight calibration navigation system overview

### 6.2.8 Practical Aspects

In this work, we used the field test data from Raudstein 2020 (described in Section 5.2.2). Please note that the data from *both the first and the second* ground antennas was used as the PARS measurements. The details of the UAV equipment used for the field test are the same as Section 5.1.

### 6.2.9 Results and Discussion

Offline calculations were carried out using the data to verify the navigation system presented in Section 6.2.3. In the offline calculations, rough estimates of the first and the second antenna orientation measured by a compass were used as an initial state:

$$\mathbf{\Theta}_{\mathrm{PARS}_1} = (\phi_{r_1}, \theta_{r_1}, \psi_{r_1}) = (0^\circ, 0^\circ, -65.5^\circ) \tag{6.63}$$

$$\mathbf{\Theta}_{\mathrm{PARS}_2} = (\phi_{r_2}, \theta_{r_2}, \psi_{r_2}) = (0^\circ, 0^\circ, 26.7^\circ). \tag{6.64}$$

Numerical values for the covariance matrices $\boldsymbol{Q}$ and $\boldsymbol{R}_\star$, and the parameters for Eq. (3.17) can be found in the Appendix C.3. The $\chi^2_\alpha = 7.815$ was chosen as the outlier rejection threshold.

The GNSS measurements were made available between 1000 s-1200 s. This means that before 1000 s, the INS used PARS measurements with the rough estimates of the antenna orientations from Eq. (6.63) and Eq. (6.64) as an aid (Mode 2).

Once the GNSS measurements became available, the INS switched to use GNSS measurements and calibration of the antenna mounting angles started (Mode 1). After GNSS outage at 1200 s, the calibration stopped, and the INS switched back to solely use PARS measurements with calibrated mounting angles (Mode 2 again).

Figure 6.8 shows the antenna orientation estimates in Euler angles. The calibration algorithm successfully estimated the antenna mounting angles fairly quickly (by 1050 s) using the position estimates from the GNSS-aided INS, even though the initial estimates contain approximately 10° of errors.

Figure 6.9 presents the position, velocity and attitude estimates from the aided-INS. The solutions from aided-INS are denoted as *Calibration MEKF (ECEF)*, and shown with orange lines.

In Figure 6.9a and Figure 6.9b, the attitude and the velocity from aided-INS are compared to the heading reference (AHRS) and the velocity from the autopilot (Pixhawk). The autopilot solutions are denoted as *pixhawk: ahrs* and *pixhawk: vel3d* respectively, and shown with blue lines in the figures. Considering that the Pixhawk uses relatively low-cost sensors, its solution is not sufficiently accurate to be regarded as a ground truth. However, as it provides attitude and velocity solutions which are independent from the aided-INS, and is a well-established navigation solution for closed-loop flight, it is considered as an appropriate reference. The attitude and velocity estimates did not change significantly between before and after the calibration.

Figure 6.9c and Figure 6.9d evaluates the position estimate from the aided-INS by comparing it to RTK-GNSS solution, where Figure 6.9e shows the transition part of Figure 6.9d. The RTK-GNSS solution was denoted as *rtk: pos3d*, and shown with blue lines in the figures. As RTK-GNSS solution has centimeter-level accuracy, it is sufficient to be considered as a ground truth. A significant change between before and after the calibration can be seen in the position estimate plot. The orange line (aided-INS) is shifted from the blue-line (RTK-GNSS) when using the rough estimates of antenna orientation, while the orange line fits well with the blue line when using the accurate orientation estimates.

Table 6.3, 6.4, and 6.5 show mean-error (ME), absolute mean-error (AME), standard deviation (STD) and root mean square error (RMSE) statistics of the aided-INS estimates for before (0 s-1000 s), during (1000 s-1200 s) and after (1200 s-2625 s) the calibration, denoted as *PARS/INS: Pre calib.*, *GNSS/INS: Mid. calib.* and *PARS/INS: After calib.* respectively, using the autopilot solution as a reference. Essentially, the values before and after the calibration are from PARS-aided (and barometer-aided) INS, while the values during calibration are from GNSS-aided INS. While the attitude and velocity statistics did not change much before and after the calibration, the position statistics improved significantly. As barometer measurements aided the altitude, the calibration did not affect the position statistics in the Down direction.

In addition to the situation considered above with mounting angles precisely calibrated in the middle of the flight, we also considered a situation that PARS-aided INS uses fixed approximate mounting angles with 0° for pitch and roll and ±2° − 3° error in yaw angle

$$\mathbf{\Theta}_{\mathrm{PARS}_1} = (0^\circ,\ 0^\circ,\ -77^\circ)$$
$$\mathbf{\Theta}_{\mathrm{PARS}_2} = (0^\circ,\ 0^\circ,\ 19^\circ).$$

throughout the entire flight without calibration, while the calibrated yaw angles for the first and the second ground antennas were −74.927° and 16.627° respectively. The statistics from this additional situation using fixed approximate mounting angles are compared with the statistics with calibrated mounting angles in Table 6.6. The statistics with fixed mounting was computed over the period 1200 s-2625 s (equivalent to the duration of after calibration) to directly compare the statistics with precisely calibrated mounting. The attitude, velocity and position statistics are denoted as *Attitude*, *Velocity* and *Position* respectively, with an extra label indicating fixed mounting or calibrated mounting. The calibrated mounting gave slightly better accuracy than the fixed approximate mounting, but the difference was not significant. It seems that the transition from inaccurate initial mounting to precise mounting during the online calibration induced some errors.

Figure 6.10 compares attitude, velocity and position error plots between the two different situations with the precisely calibrated mounting angles and with the fixed approximate mounting angles. Errors at the beginning and at the end of the position error plots are relatively large, as the UAV was too close to the ground antenna and sometimes flew outside of the effective 90° frustum coverage by the antenna. A spike in the North direction of the velocity error plot appeared at 1000 s when the INS switches from PARS-aided to GNSS-aided. For the period 1200 s-2625 s, the error plots behaved in a similar manner.

### 6.2.10 Conclusion

In this paper, the previously presented calibration algorithm, which estimates ground antenna orientation for the PARS, was implemented with aided-INS. We applied the calibration algorithm with aided-INS to data obtained from a field test and performed offline calculations. The aided-INS switched between PARS- and GNSS-aided INS depending on the availability of GNSS measurements. The algorithm successfully estimated the mounting angles of multiple PARS ground antennas in the middle of flight when GNSS measurements were available, and the accuracy of position estimates improved significantly. As a future work, we want to implement the extended aided-INS with calibration in the onboard embedded system and test it in the field.

| | | Roll [°] | Pitch [°] | Yaw [°] | Norm [°] |
|---|---|---|---|---|---|
| PARS+ Baro/INS: Pre calib. | ME: | -0.62 | 0.88 | -11.42 | 11.47 |
| | AME: | 1.98 | 1.65 | 17.80 | 17.99 |
| | STD: | 2.73 | 1.94 | 18.00 | 18.31 |
| | RMSE: | 2.80 | 2.13 | 21.31 | 21.60 |
| PARS+ GNSS/INS: Mid. calib. | ME: | -2.95 | 0.24 | -14.13 | 14.44 |
| | AME: | 3.08 | 1.14 | 14.25 | 14.62 |
| | STD: | 1.67 | 1.38 | 12.46 | 12.64 |
| | RMSE: | 3.39 | 1.40 | 18.84 | 19.19 |
| PARS+ Baro/INS: After calib. | ME: | -2.68 | 0.97 | 5.26 | 5.98 |
| | AME: | 2.84 | 2.17 | 13.44 | 13.90 |
| | STD: | 2.08 | 2.74 | 15.81 | 16.18 |
| | RMSE: | 3.39 | 2.91 | 16.66 | 17.25 |

Table 6.3: Attitude error statistics before (top), during (middle) and after (bottom) calibration

| | | North [m/s] | East [m/s] | Down [m/s] | Norm [m/s] |
|---|---|---|---|---|---|
| PARS+ Baro/INS: Pre calib. | ME: | -0.46 | -0.12 | 0.05 | 0.48 |
| | AME: | 1.59 | 2.00 | 0.13 | 2.55 |
| | STD: | 1.91 | 2.33 | 0.22 | 3.02 |
| | RMSE: | 1.96 | 2.34 | 0.22 | 3.06 |
| PARS+ GNSS/INS: Mid. calib. | ME: | 0.09 | -0.10 | -0.02 | 0.14 |
| | AME: | 0.34 | 0.21 | 0.07 | 0.41 |
| | STD: | 1.57 | 0.33 | 0.09 | 1.61 |
| | RMSE: | 1.57 | 0.35 | 0.09 | 1.61 |
| PARS+ Baro/INS: After calib. | ME: | 0.00 | 0.03 | 0.04 | 0.05 |
| | AME: | 0.41 | 0.40 | 0.10 | 0.58 |
| | STD: | 0.65 | 0.61 | 0.15 | 0.90 |
| | RMSE: | 0.65 | 0.61 | 0.16 | 0.91 |

Table 6.4: Velocity error statistics before (top), during (middle) and after (bottom) calibration

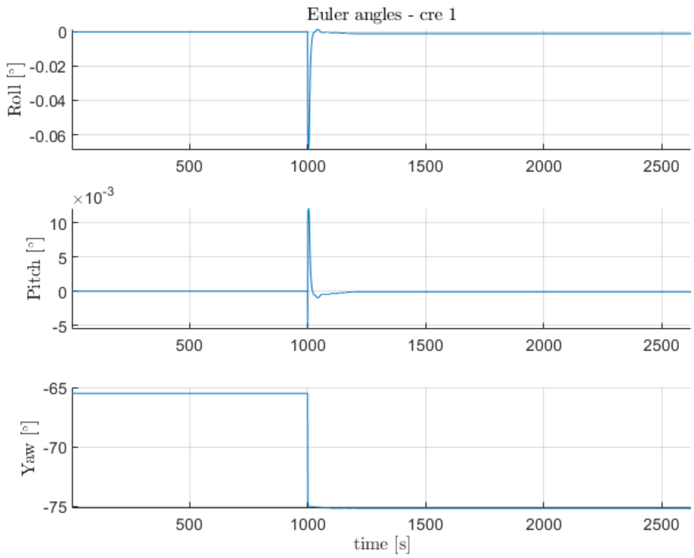


(a) The first antenna with $\psi_{r_1} = -65.5°$

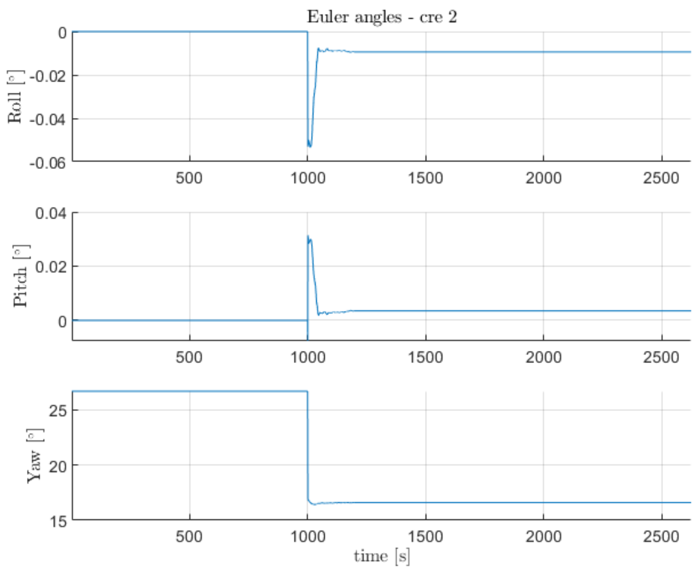


(b) The second antenna with $\psi_{r_2} = 26.7°$

Figure 6.8: Euler angles of antenna orientations

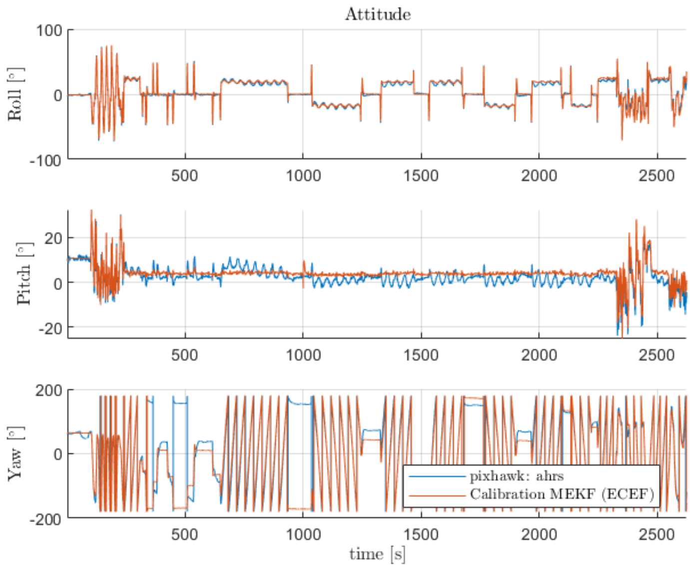


(a) Attitude compared to autopilot reference

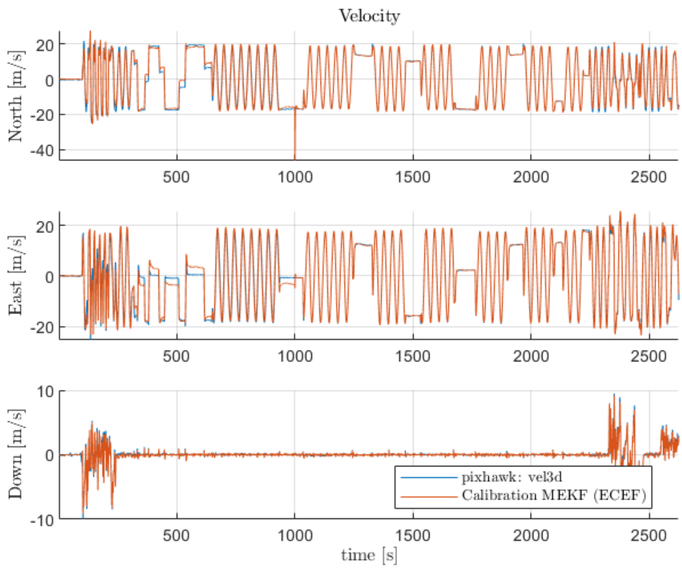


(b) Velocity compared to autopilot reference

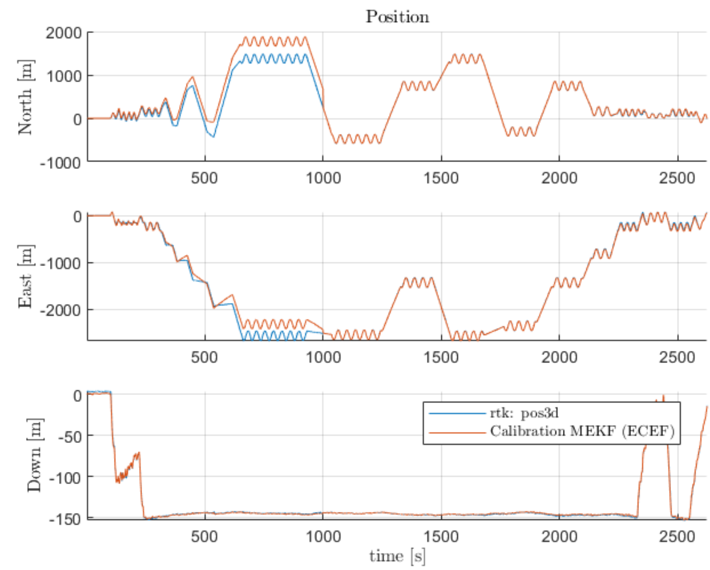


(c) Position compared to RTK-GNSS reference in 1D

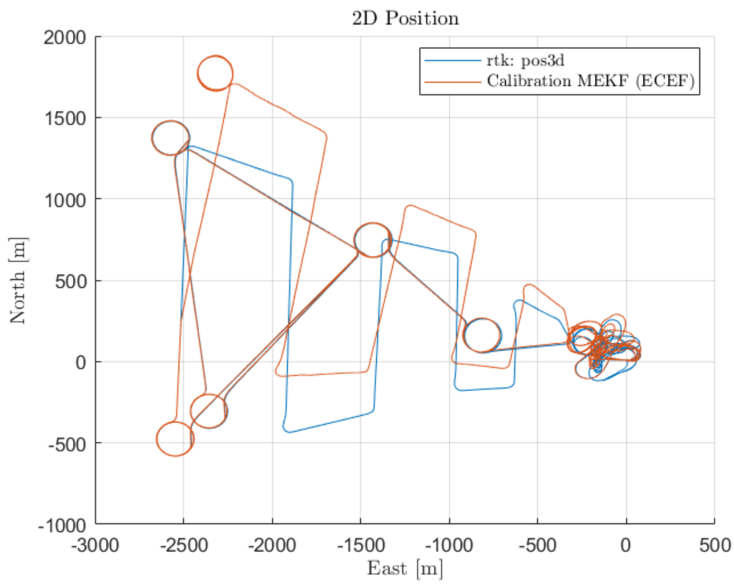


(d) Position compared to RTK-GNSS reference in 2D

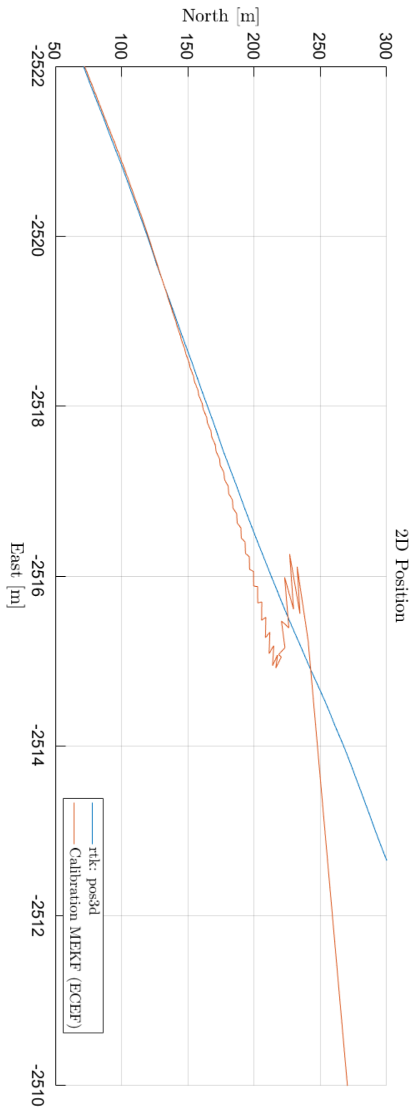


(e) Position during transition compared to RTK-GNSS reference in 2D

Figure 6.9: Attitude, Velocity and Position plots of the UAV

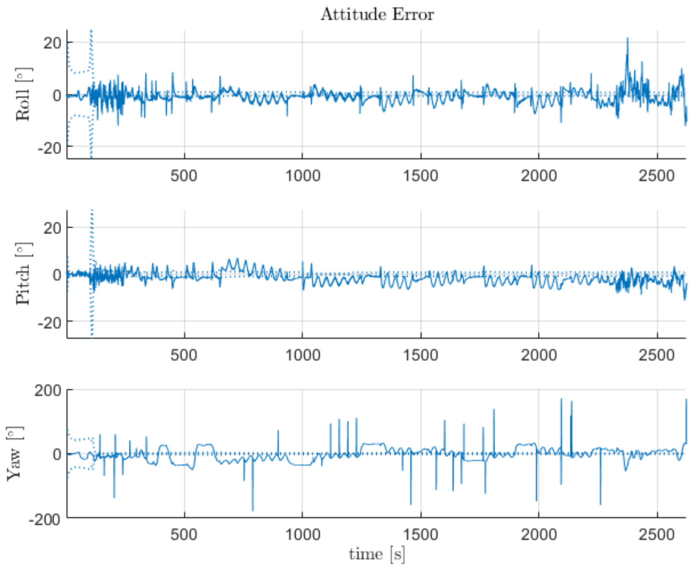


(a) Attitude error with calibrated mounting

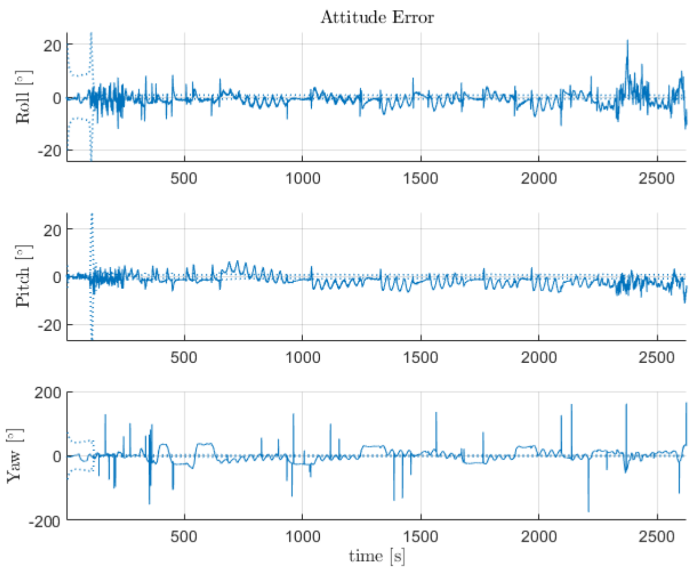


(b) Attitude error with fixed mounting

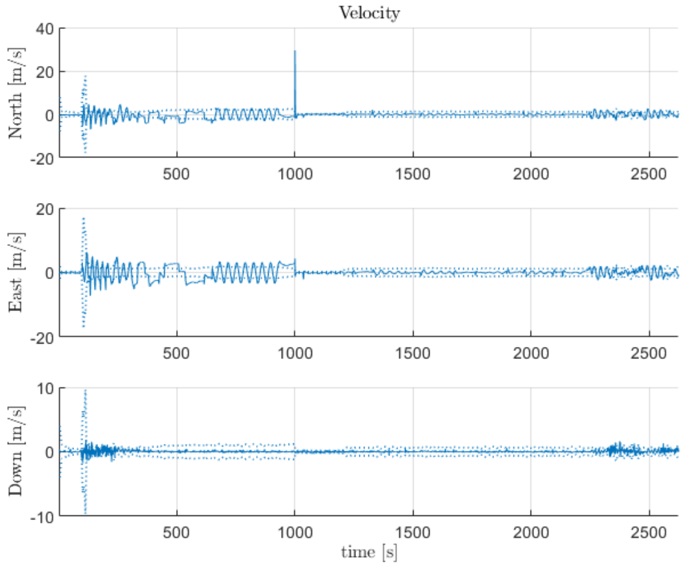


(c) Velocity error with calibrated mounting

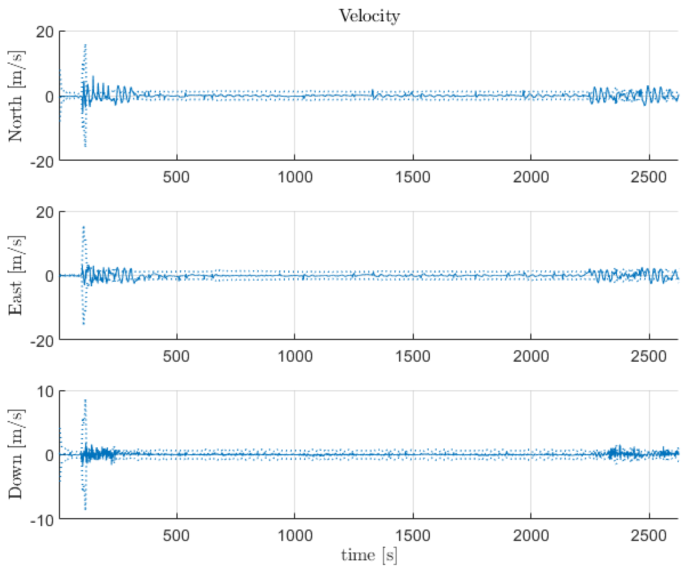


(d) Velocity error with fixed mounting

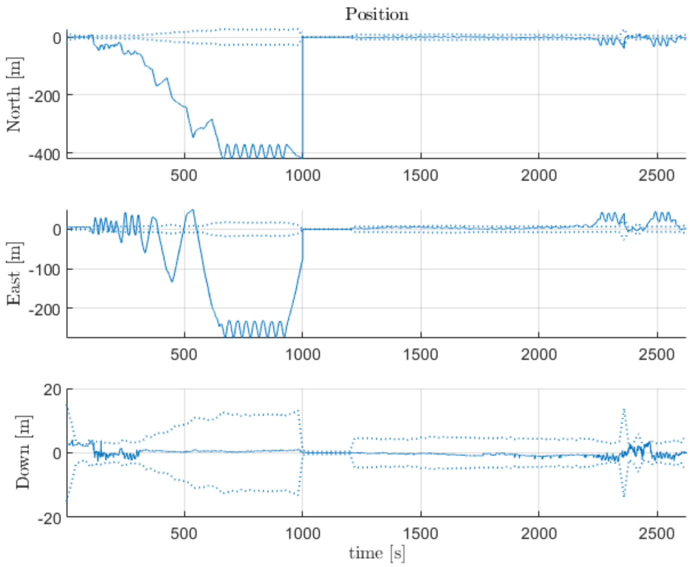


(e) Position error with calibrated mounting

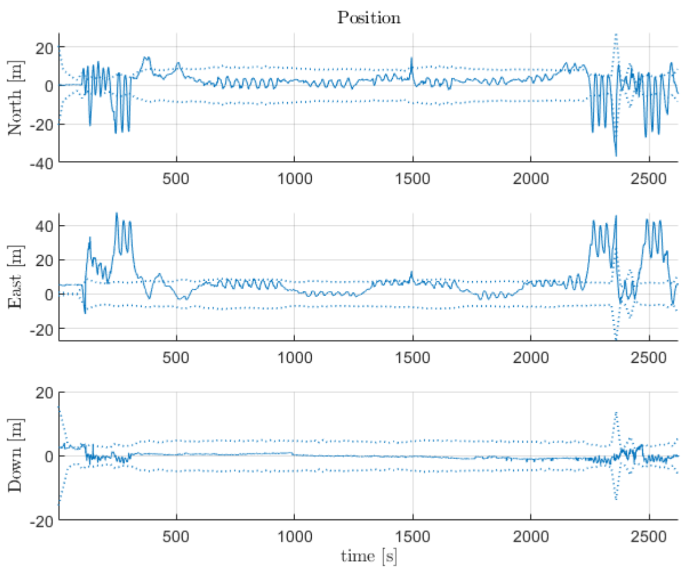


(f) Position error with fixed mounting

Figure 6.10: Error plots w.r.t the autopilot (attitude, velocity) and RTK-GNSS (position) reference

| | | North [m] | East [m] | Down [m] | Norm [m] |
|---|---|---|---|---|---|
| PARS+ Baro/INS: Pre calib. | ME: | -223.19 | -101.28 | 0.58 | 245.09 |
| | AME: | 223.37 | 112.03 | 0.82 | 249.89 |
| | STD: | 159.97 | 114.99 | 0.94 | 197.01 |
| | RMSE: | 274.59 | 153.23 | 1.10 | 314.46 |
| PARS+ GNSS/INS: Mid. calib. | ME: | -0.02 | -0.01 | 0.01 | 0.03 |
| | AME: | 0.14 | 0.06 | 0.03 | 0.16 |
| | STD: | 0.45 | 0.10 | 0.05 | 0.47 |
| | RMSE: | 0.45 | 0.10 | 0.05 | 0.47 |
| PARS+ Baro/INS: After calib. | ME: | -2.98 | 7.79 | -0.47 | 8.35 |
| | AME: | 3.96 | 7.94 | 0.67 | 8.90 |
| | STD: | 6.94 | 10.36 | 0.74 | 12.49 |
| | RMSE: | 7.55 | 12.96 | 0.87 | 15.03 |

Table 6.5: Position error statistics before (top) during (middle) and after (bottom) calibration

| | | Roll [°] | Pitch [°] | Yaw [°] | Norm [°] |
|---|---|---|---|---|---|
| Attitude: Calibrated | ME: | -2.68 | 0.97 | 5.26 | 5.98 |
| | AME: | 2.84 | 2.17 | 13.44 | 13.90 |
| | STD: | 2.08 | 2.74 | 15.81 | 16.18 |
| | RMSE: | 3.39 | 2.91 | 16.66 | 17.25 |
| Attitude: Fixed | ME: | -2.69 | 0.95 | 5.28 | 6.01 |
| | AME: | 2.85 | 2.17 | 13.46 | 13.93 |
| | STD: | 2.08 | 2.75 | 15.79 | 16.17 |
| | RMSE: | 3.41 | 2.91 | 16.65 | 17.25 |
| | | North [m/s] | East [m/s] | Down [m/s] | Norm [m/s] |
| Velocity: Calibrated | ME: | 0.00 | 0.03 | 0.04 | 0.05 |
| | AME: | 0.41 | 0.40 | 0.10 | 0.58 |
| | STD: | 0.65 | 0.61 | 0.15 | 0.90 |
| | RMSE: | 0.65 | 0.61 | 0.16 | 0.91 |
| Velocity: Fixed | ME: | -0.01 | 0.03 | 0.04 | 0.05 |
| | AME: | 0.44 | 0.39 | 0.10 | 0.60 |
| | STD: | 0.74 | 0.62 | 0.15 | 0.97 |
| | RMSE: | 0.74 | 0.62 | 0.16 | 0.98 |
| | | North [m] | East [m] | Down [m] | Norm [m] |
| Position: Calibrated | ME: | -2.98 | 7.79 | -0.47 | 8.35 |
| | AME: | 3.96 | 7.94 | 0.67 | 8.90 |
| | STD: | 6.94 | 10.36 | 0.74 | 12.49 |
| | RMSE: | 7.55 | 12.96 | 0.87 | 15.03 |
| Position: Fixed | ME: | 1.36 | 8.20 | -0.45 | 8.32 |
| | AME: | 4.67 | 8.67 | 0.65 | 9.86 |
| | STD: | 6.72 | 10.74 | 0.73 | 12.69 |
| | RMSE: | 6.85 | 13.51 | 0.85 | 15.18 |

Table 6.6: Error statistics comparison between calibrated mounting (top) and fixed approximate mounting (bottom)

## 6.3 Implementation of the in-flight calibration

### 6.3.1 Introduction

In this work, the previously presented in-flight calibration algorithm in Section 6.2 was implemented in the DUNE unified navigation environment [57] for real-time operation. This implementation was verified using replay data collected from field tests and validated by comparing the result with RTK-GNSS measurement and Pixhawk autopilot solution as ground truth.

### 6.3.2 Positioning

The positioning techniques that formulate the navigation system in this work are INS (Section 3.1), RTK GNSS (Section 3.2), PARS (Section 3.3) and barometer (Section 3.4). Please note that RTK GNSS **aided** INS when available and the calibration mode (Section 6.2.5) was activated. The RTK GNSS measurements were aslo used as ground truth to examine the performance of the PARS and barometer-aided INS.

### 6.3.3 Navigation system

The navigation system implemented in this paper is essentially an aided INS presented in Section 6.2.

Fundamentally, the INS is aided using two modes. The first mode performs the calibration of the ground antenna orientation using the algorithm presented in Section 6.2. Here, both PARS and GNSS aid the INS, and the calibration algorithm uses the position estimates from the GNSS-aided INS as ground truth. The second mode is PARS and barometer-aided INS, which is the normal GNSS-free navigation. Sec. 6.3.6 and Sec. 6.3.5 describe mode 1 and mode 2, respectively.

As *a single PARS ground antenna was used* (i.e. $m = 1$), the index $j$ is omitted for convenience (i.e. $\{n\}$-frame in the rest of this section means $\{n_j\}$-frame.), and thus the navigation system is slightly different from the one in Section 6.2 in terms of the size of the state vector and the matrices. As this work is a practical implementation, the discrete versions of the equations INS are presented here.

### 6.3.4 Navigation system model

**Nominal system kinematics.**

The nominal state estimate is given as

$$\hat{\boldsymbol{x}} = (\hat{\boldsymbol{p}}^e_{eb},\ \hat{\boldsymbol{v}}^e_{eb},\ \hat{\boldsymbol{q}}^e_b,\ \hat{\boldsymbol{b}}^b_{\text{acc}},\ \hat{\boldsymbol{b}}^b_{\text{ars}},\ \boldsymbol{q}^n_r)^\intercal \in \mathbb{R}^{1\times 20}. \tag{6.65}$$

This is the $m = 1$ version of Eq. (6.26).

The nominal state is propagated using the following kinematic model based on the IMU measurement model and strapdown equations presented in Section 3.1:

$$\hat{\boldsymbol{\omega}}^b_{eb} = \boldsymbol{\omega}^b_{\text{IMU}} - \hat{\boldsymbol{b}}^b_{\text{ars}} - \hat{\boldsymbol{R}}^{\mathsf{T}}_{eb}\boldsymbol{\omega}^e_{ie} \tag{6.66a}$$

$$\Delta\boldsymbol{q}^e_b = \begin{pmatrix} \cos\left(\frac{T_s}{2}\cdot\|\hat{\boldsymbol{\omega}}^b_{eb}\|_2\right) \\ \sin\left(\frac{T_s}{2}\cdot\|\hat{\boldsymbol{\omega}}^b_{eb}\|_2\right)\cdot\frac{\hat{\boldsymbol{\omega}}^b_{eb}}{\|\hat{\boldsymbol{\omega}}^b_{eb}\|_2} \end{pmatrix} \tag{6.66b}$$

$$\hat{\boldsymbol{q}}^e_b \leftarrow \boldsymbol{q}^e_b \otimes \Delta\boldsymbol{q}^e_b \tag{6.66c}$$

$$\hat{\boldsymbol{R}}_{eb} = \boldsymbol{R}_{eb}(\hat{\boldsymbol{q}}^e_b), \quad \text{using (2.12)} \tag{6.66d}$$

$$\bar{\boldsymbol{R}}_{eb} = \left(\boldsymbol{R}_{eb} + \boldsymbol{R}_{eb,\text{prev}}\right)/2 \tag{6.66e}$$

$$\hat{\boldsymbol{f}}^b_{ib} = \boldsymbol{f}^b_{\text{IMU}} - \hat{\boldsymbol{b}}^b_{\text{acc}} \tag{6.66f}$$

$$\hat{\boldsymbol{a}}^e_{eb} = -2\boldsymbol{S}\left(\boldsymbol{\omega}^e_{ie}\right)\hat{\boldsymbol{v}}^e_{eb} + \bar{\boldsymbol{R}}_{eb}\hat{\boldsymbol{f}}^b_{ib} + \boldsymbol{g}^e_b \tag{6.66g}$$

$$\hat{\boldsymbol{v}}^e_{eb} \leftarrow \hat{\boldsymbol{v}}^e_{eb} + T_s\cdot\hat{\boldsymbol{a}}^e_{eb} \tag{6.66h}$$

$$\hat{\boldsymbol{p}}^e_{eb} \leftarrow \hat{\boldsymbol{p}}^e_{eb} + T_s\cdot\hat{\boldsymbol{v}}^e_{eb} + \frac{T_s^2}{2}\cdot\hat{\boldsymbol{a}}^e_{eb} \tag{6.66i}$$

$$\hat{\boldsymbol{b}}^b_{\text{acc}} \leftarrow e^{-T_s\cdot\boldsymbol{T}^{-1}_{\text{acc}}}\cdot\hat{\boldsymbol{b}}^b_{\text{acc}} \tag{6.66j}$$

$$\hat{\boldsymbol{b}}^b_{\text{ars}} \leftarrow e^{-T_s\cdot\boldsymbol{T}^{-1}_{\text{ars}}}\cdot\hat{\boldsymbol{b}}^b_{\text{ars}} \tag{6.66k}$$

$$\boldsymbol{R}_{eb,\text{prev}} = \hat{\boldsymbol{R}}_{eb}. \tag{6.66l}$$

similar to [38, Ch. 5]. This is the discretised and $m = 1$ version of Eq. (6.27). The derivative of $\boldsymbol{q}^n_r$ is zero, as the ground antenna is stationary.

**Error-state system kinematics.**

The error state is given as

$$\delta\boldsymbol{x} = (\delta\boldsymbol{p}^e_{eb},\ \delta\boldsymbol{v}^e_{eb},\ \delta\boldsymbol{a}^e_b,\ \delta\boldsymbol{b}^b_{acc},\ \delta\boldsymbol{b}^b_{ars},\ \delta\boldsymbol{a}^n_r)^{\mathsf{T}} \in \mathbb{R}^{18}. \tag{6.67}$$

This is the $m = 1$ version of Eq. (6.29). The continuous-time linearized error state system model is

$$\delta\dot{\boldsymbol{x}} = \boldsymbol{F}(t)\delta\boldsymbol{x} + \boldsymbol{G}(t)\boldsymbol{w} \tag{6.68}$$

where the Jacobian matrices $\boldsymbol{F}$ and $\boldsymbol{G}$, and the process covariance matrix $\boldsymbol{Q}$ based on the process noise $\boldsymbol{w}$ are given in Appendix C.1 (Please note that $m = 1$ in this case).

### 6.3.5 Measurement model (mode 1)

When GNSS measurements are available, GNSS aids the INS, and the calibration of the PARS ground antenna mounting presented in Chapter 6.1 is performed using the position estimate from the GNSS-aided INS as ground truth. See Section 6.2.5 for details (Please note that $m = 1$ in this case.).

### 6.3.6 Measurement model (mode 2)

When GNSS is unavailable, PARS and barometer aided the INS in the horizontal and vertical directions, respectively. The barometer altitude as a replacement for the PARS vertical component was treated separately from the PARS measurements to include the effect of the Earth's curvature. See Section 6.2.6 for details (Please note that $m = 1$ in this case.).

### 6.3.7 Results and Discussion

In this work, we used the field test data from Raudstein 2019 (described in Section 5.2.1) and Bleik 2022 (described in Section 5.2.3, jamming-free data was used in this work). Figure 6.11 indicates the flight paths with ground antenna positions. The details of the UAV equipment used for the field test are the same as Section 5.1. Before the field test, the position of the ground antenna ($\boldsymbol{p}^e_{er}$) was measured using GNSS, and the initial angles of the ground antenna mounting were measured by a compass.

The navigation system presented in this paper was implemented in DUNE unified navigation environment [57] for real-time operation in the fields. The presented algorithm was written in C++ using the mathematical libraries provided by DUNE. The implementation in DUNE was verified using the replay data obtained from the field tests. The numerical values for the process and measurement covariance matrices $\boldsymbol{Q}$ and $\boldsymbol{R}_\star$ (i.e. $\varepsilon_\star \sim \mathcal{N}(0, \sigma^2_\star)$) are in Appendix C.3.

**Calibration of ground antenna orientation**

The initial estimate of the ground antenna orientation was assumed to contain ±10° error

$$\boldsymbol{\Theta}_{\mathrm{PARS}_R} = (\phi_r\ , \theta_r\ , \psi_r) = (0^\circ\ , 0^\circ\ , -116^\circ) \tag{6.69}$$

$$\boldsymbol{\Theta}_{\mathrm{PARS}_B} = (\phi_a\ , \theta_a\ , \psi_a) = (0^\circ\ , 0^\circ\ , -47^\circ), \tag{6.70}$$

where the subscript $R$ and $B$ denote Raudstein and Bleik locations, respectively.

The calibration mode (i.e. mode 1) was enabled in the middle of the flight, approximately for 150 s. In other words, our navigation system (aided-INS) used mode 2 from the start of the flight and switched to mode 1, then switched back to mode 2 after the calibration mode is disabled 150 s later.

Figures 6.12–6.13 present the results of the in-flight calibration operation, for Raudstein and Bleik respectively. Figure 6.12a and Figure 6.13a show that the ground antenna orientation was estimated successfully and converged to +10° in the yaw angle. In Figure 6.12b and Figure 6.13b, the NED position estimate from the aided-INS is compared to the RTK-GNSS as ground-truth. In the North and East direction, the dotted blue line (the aided-INS) shifts to match the dotted orange line (RTK-GNSS) after the calibration starts. The 2D plot in Figure 6.12c

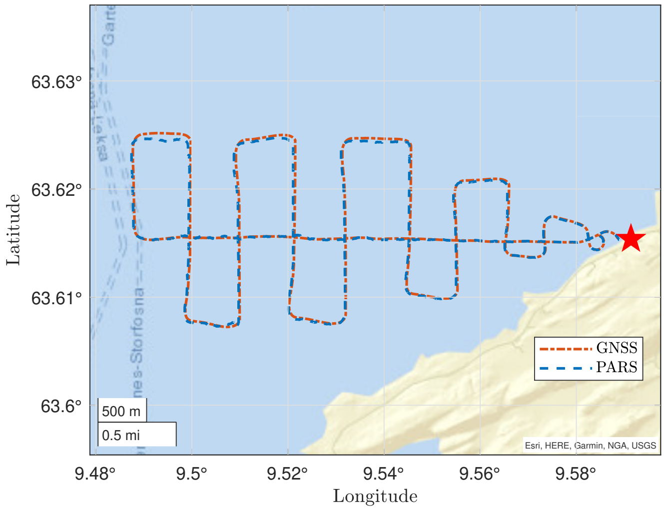


(a) Raudstein

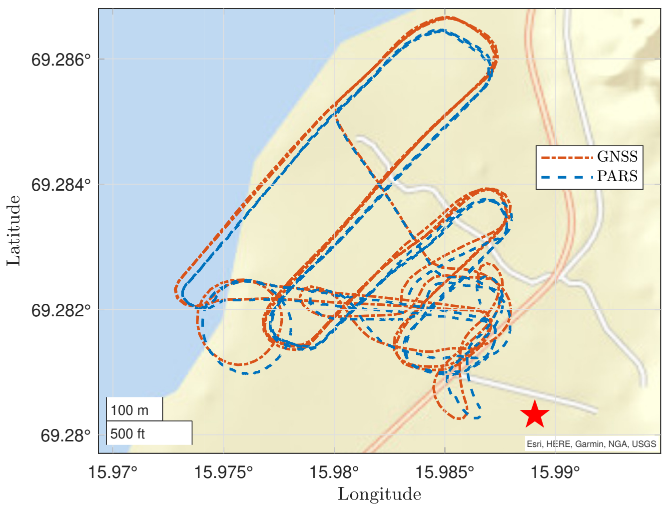


(b) Bleik

Figure 6.11: Flight path of the UAV with ground antenna positions indicated

and Figure 6.13c shows the improvement in the position estimate more clearly. In the Down direction, except for the calibration period, the dotted blue line (the aided-INS) is shifted from the dotted orange line (RTK-GNSS) due to the bias in the barometer altitude. During the calibration, as the RTK-GNSS is aiding the INS, the Down position matches with the ground truth. In Figure 6.12d and Figure 6.13d, the NED position error improved significantly in the North and East directions.

To ensure safety in shared airspace, it is important that the vertical bias does not propagate in the horizontal bias. However, in the current formulation, the bias in the altitude measurement affects the horizontal position estimate through the horizontal range computation in Eq. (4.18). As the bias in the barometer altitude changes depending on the altitude, it is difficult to compensate for with a fixed offset. For a better estimate of barometer bias, we need a smarter algorithm.

**Approximate mounting**

In addition to the situation considered in Section 6.3.7 with in-flight calibration, we also considered a situation in which the aided-INS uses a fixed approximate ground antenna mounting with $\pm 1^\circ$ error throughout the entire flight without calibration. We used the Raudstein replay data and the same initial angle, as in [26]:

$$\boldsymbol{\Theta}_{\mathrm{PARS}_R} = (0^\circ,\ 0^\circ,\ -106^\circ).$$

where this paper propagated the system dynamics in the ECEF frame, while [26] used the local NED frame.

Figure 6.14 shows the result from the approximate mounting. The NED position error plot in Figure 6.14a can be compared with Fig.15 in [26]. In the North and East direction, the position error plots behave similarly. However, in the Down direction, the error plot in Fig.15 in [26] has a clear inclination as the distance from the ground antenna increases, while Figure 6.14a does not. Since the barometer measures altitude from the reference surface perpendicular to the tangent line of the earth curvature, using the barometer altitude directly in the local NED frame induces errors as explained in [26]. Although the use of the ECEF frame could solve this issue, the position estimate in the Down direction has a slightly larger mean error (considering barometer altitude bias by approximately 10 m).

### 6.3.8 Conclusion

In this paper, the previously presented in-flight calibration algorithm which estimates the ground antenna orientation for the PARS was implemented in DUNE unified navigation environment for real-time operation. The algorithm is integrated with the aided-inertial navigation system (aided-INS), and the INS equations are propagated in the Earth Fixed Earth Centred (ECEF) frame, while the previous implementation used the local North East Down (NED) frame. We conducted field tests using a single ground antenna at Raudstein and Bleik to collect replay data to validate the implementation. The recorded replay data included IMU, RTK-GNSS, PARS, and Pixhawk autopilot (with barometer) measurements. The estimates from the implemented navigation system were verified by comparing them with RTK-GNSS measurements and Pixhawk autopilot solutions as ground truth.

The calibration mode was enabled for approximately 150 s in the middle of the flights, and the position estimate improved significantly after the calibration by estimating the precise orientation of the ground antenna. In addition, the result showed that the propagation of navigation equations in the ECEF frame, instead of the local NED frame, is beneficial to overcome the error induced in the vertical position estimate presented previously.

In future work, we want to add barometer bias estimation to the implementation and conduct flights in the fields using the navigation solutions from DUNE in the control loop of the autopilot.

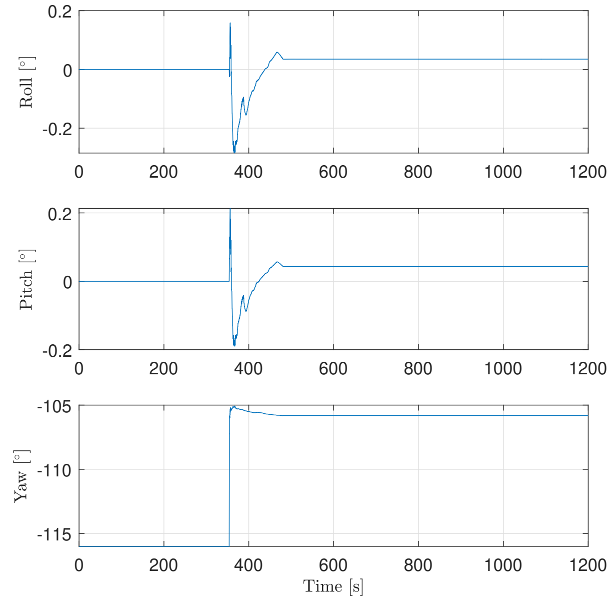


(a) Attitude of the ground antenna

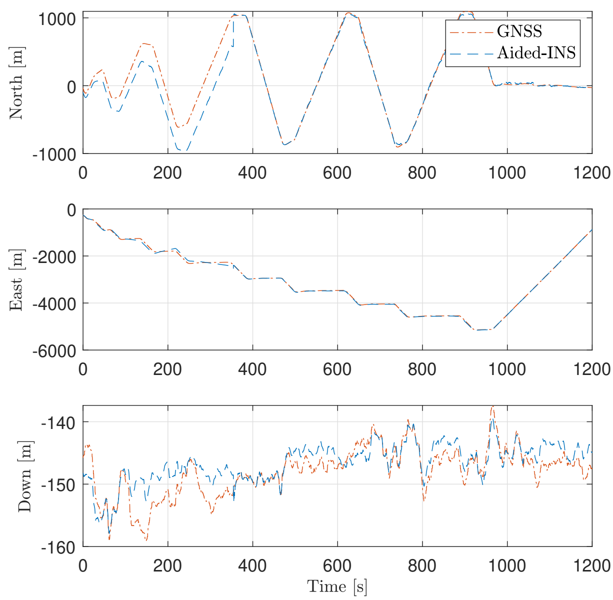


(b) NED position with RTK-GNSS reference in 1D

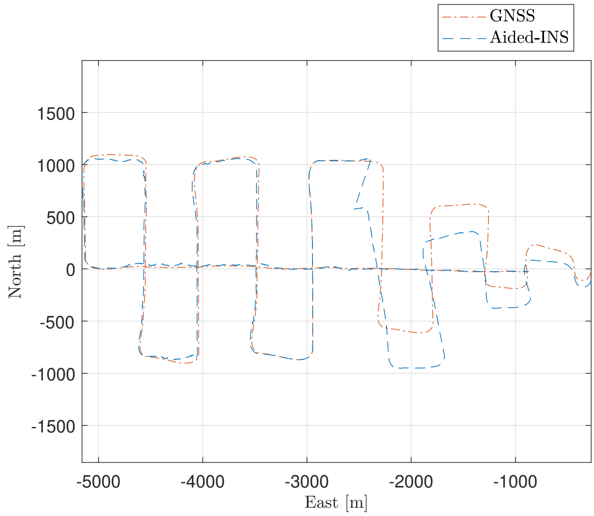


(c) NE position with RTK-GNSS reference in 2D

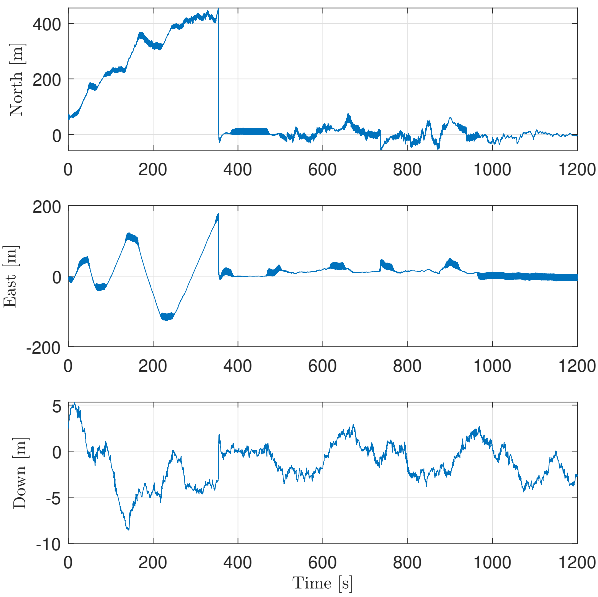


(d) NED position error w.r.t RTK-GNSS reference

Figure 6.12: Calibrated mounting (Raudstein)

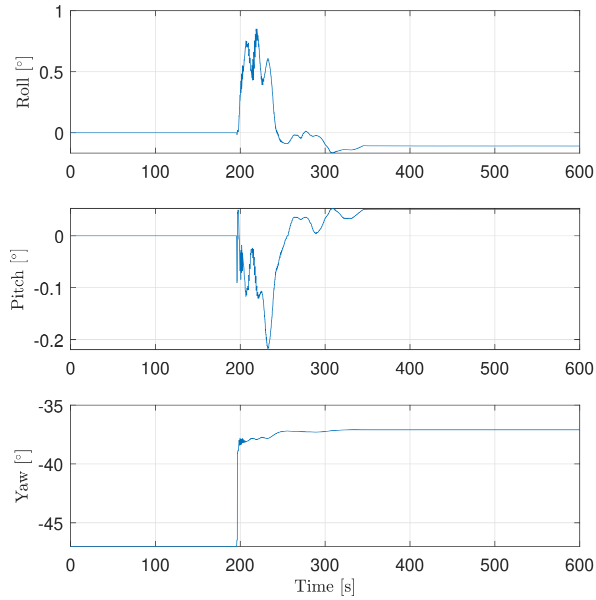


(a) Attitude of the ground antenna

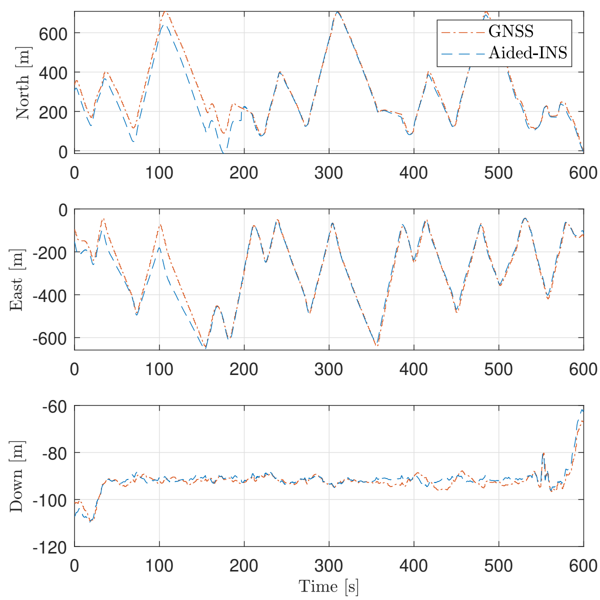


(b) NED position with RTK-GNSS reference in 1D

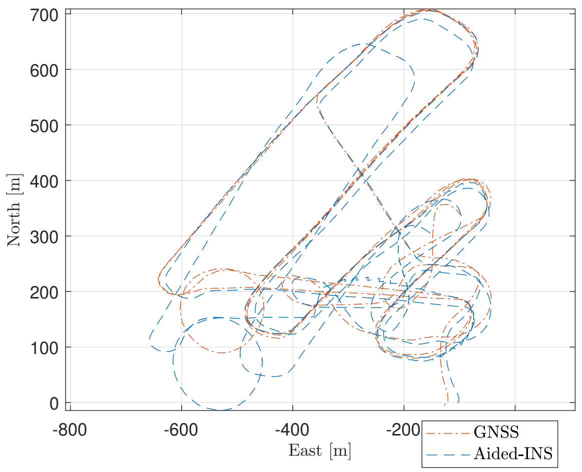


(c) NE position with RTK-GNSS reference in 2D

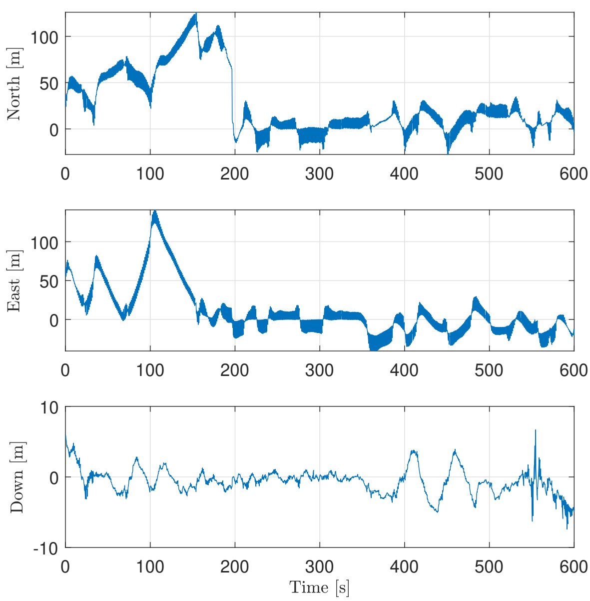


(d) NED position error w.r.t RTK-GNSS reference

Figure 6.13: Calibrated mounting (Bleik)

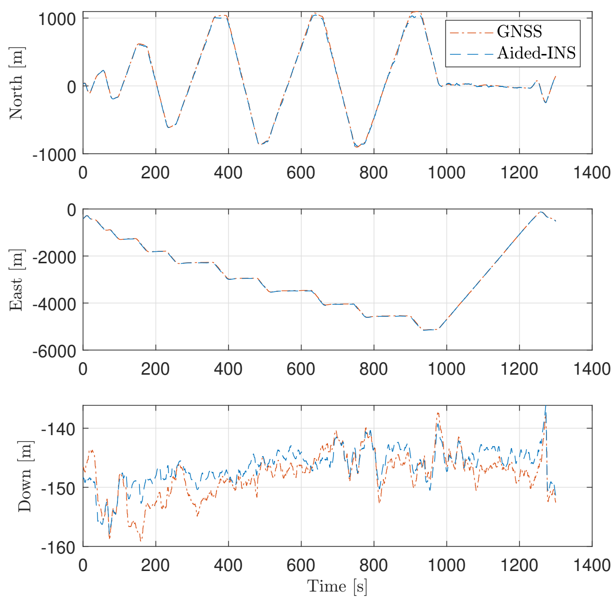


(a) NED position with RTK-GNSS reference in 1D

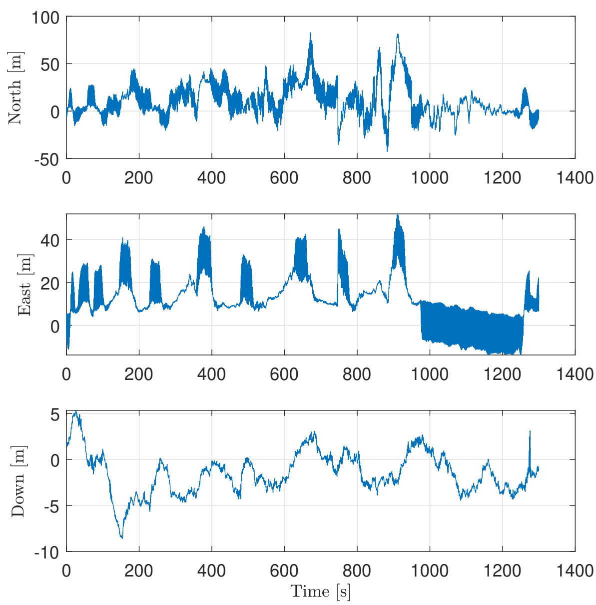


(b) NED position error w.r.t RTK-GNSS reference

Figure 6.14: Approximate mounting (Raudstein)

# 7 Noise mitigation in elevation angle

As presented in [22], one of the disadvantages of PARS is a multipath problem. When PARS finds a position using a direction of arrival (DoA) algorithm, the elevation angle measurement suffers from noise due to radio reflection from water surfaces. The reflected signal affects the DoA algorithm and causes clutter. The main idea of this chapter is to address problem by using the non-linear update of barometer altitude (Section 7.1), using PDAF incorporating multiple PARS measurements from to find a true one (Section 7.2), or using the alternative of the noisy elevation angle (Section 7.3).

This chapter is based on the following papers:

- Mika Okuhara, Torleiv Håland Bryne, Kristoffer Gryte, and Tor Arne Johansen. Phased array radio and barometric navigation system for UAVs: A nonlinear measurement update approach. Internal Report, 2021
- Mika Okuhara, Torleiv Håland Bryne, Kristoffer Gryte, and Tor Arne Johansen. Phased array radio navigation system on UAVs: Multi hypothesis filter for noise mitigation. Internal Report, 2023
- Mika Okuhara, Torleiv Håland Bryne, Kristoffer Gryte, and Tor Arne Johansen. Elevation angle redundancy from barometric altitude in multipath-affected phased array radio navigation of UAVs. In *2024 International Conference on Unmanned Aircraft Systems (ICUAS)*, 2024. Submitted

## 7.1 Nonlinear barometric measurement update

### 7.1.1 Introduction

The main idea of this work is to make further refinements to the MEKF-based PARS- and barometer-aided INS navigation system by including the effect of Earth's curvature into consideration for a long-distance flight.

Barometer altitude was used as a replacement of the PARS vertical measurement in this work. A similar approach (described in Section 4.2.3) was used in [22, 25] but the PARS and the altitude measurements were formulated in a one measurement model in the local radio frame. In this way, the Earth's curvature is neglected, as the altitude measurement is directly used in the local radio frame, although the barometer measures the altitude from the geoid in the direction perpendicular to the tangent line of the Earth's surface. Therefore, in this work, PARS and barometer-based measurements were formulated in two independent measurement models to deal with the altitude effectively.

### 7.1.2 Positioning

The positioning techniques that formulate the navigation system in this work are INS (Section 3.1), PARS (Section 3.3) and barometer (Section 3.4). Please note that RTK-GNSS (Section 3.2) did not aid INS. The RTK-GNSS measurements were used as ground truth to examine the performance of the PARS and barometer-aided INS.

### 7.1.3 The Navigation System

The difference between the navigation system in this work and the one described in Chapter 4 is the measurement model (Section 4.2). The main focus of this section is comparing the two PARS measurement models: *PARS with previous approach* (Section 4.2.3) and *PARS with new approach*. Please note that the measurement model for RTK-GNSS (Section 4.2.1) was NOT used in this section as RTK-GNSS did not aid INS in this work.

The system model (Section 4.1), pre-launch calibration (Section 4.3), the outlier rejection (Section 4.4) and MEKF (Section 4.5) are the same as Chapter 4.

**Measurement model with previous approach**

The previous approach from [22] is the one in Section 4.2.3.

The measurement of the horizontal range ($\bar{\rho}_m$) was computed using Eq. (4.18) (to prevent the noise in elevation angle measurement from affecting the horizontal positioning)

$$\bar{\rho}_y = \sqrt{\rho_y^2 - \gamma_y^2}$$

and the Cartesian PARS position measurement is

$$\boldsymbol{y}^r_{\text{PARS,Alt}} = \begin{pmatrix} \bar{\rho}_y \cos(\psi_y) \\ \bar{\rho}_y \sin(\psi_y) \\ -\gamma_y \end{pmatrix}$$

which is Eq. (4.20).

Please note that this approach is not ideal for long-distance flights. As the barometer measures the altitude from geoid in the direction perpendicular to the tangent line of the Earth curvature, using the barometer altitude directly in the $\{r\}$-frame induces errors. Therefore, in this work, the barometer altitude as a replacement of the PARS vertical component was treated separately from the PARS measurements to include the Earth's curvature into consideration.

**Measurement model with new approach**

One possible way is formulating the measurement model in spherical coordinates as Titterton did in [69, Ch. 13.6.2.2]:

$$\boldsymbol{y}^r_{\text{PARS}} = \begin{pmatrix} \rho_y \\ \psi_y \\ \gamma_y \end{pmatrix} \tag{7.1}$$

where[1]

$$\rho_y = \|\boldsymbol{p}^e_{eb} - \boldsymbol{p}^e_{er}\|_2 \tag{7.2}$$

$$\psi_y = \tan^{-1}\left(\frac{\boldsymbol{p}^r_{rb,y}}{\boldsymbol{p}^r_{rb,x}}\right) \tag{7.3}$$

$$\gamma_y = \|\boldsymbol{p}^e_{eb} - \boldsymbol{p}^e_{eS}\|_2. \tag{7.4}$$

In this way, the measurements are not regulated in the $\{r\}$-frame. However, as Eq. (7.3) contains $\tan^{-1}$, the linearization of the equations induces errors due to its high non-linearity. Therefore, we used a hybrid approach to treat these measurements:

- PARS measurement model was formulated in Cartesian coordinate, which is essentially the $\{r\}$-frame, to avoid the linearization issue.
- Barometer measurement model was formulated *independently* from the PARS measurement model to treat the altitude in the $\{e\}$-frame.

**PARS** The PARS measurement model presented here is the two-dimensional version of Section 4.2.2 (omitting the vertical component). The horizontal components of Cartesian PARS measurements are

$$\boldsymbol{y}^r_{\text{PARS,2D}} = \begin{pmatrix} \bar{\rho_y} \cos\psi_y \\ \bar{\rho_y} \sin\psi_y \end{pmatrix} \tag{7.5}$$

where the measurement of the horizontal range ($\bar{\rho}_y$) was computed using Eq. (4.19) by approximating the elevation angle ($\alpha$) as shown in Figure 4.1:

$$\bar{\rho}_y = \rho_y \cos\alpha \tag{7.6}$$

whereas

$$\cos\alpha = \frac{\boldsymbol{p}^e_{eb} \cdot \boldsymbol{p}^e_{er}}{\|\boldsymbol{p}^e_{eb}\|_2 \|\boldsymbol{p}^e_{er}\|_2}. \tag{7.7}$$

[1]Details about $\boldsymbol{p}^e_{eS}$ is in Section 3.4.

In a practical implementation, $\hat{\boldsymbol{p}}^e_{eb}$ is used instead of $\boldsymbol{p}^e_{eb}$ in Eq. (7.7) such that

$$\bar{\rho}_y \approx \rho_y \frac{\hat{\boldsymbol{p}}^e_{eb} \cdot \boldsymbol{p}^e_{er}}{\|\hat{\boldsymbol{p}}^e_{eb}\|_2 \|\boldsymbol{p}^e_{er}\|_2} \tag{7.8}$$

which is valid for small $\|\delta \boldsymbol{p}^e_{eb}\|_2$.

The horizontal position measurement ($\boldsymbol{y}^r_{\text{PARS,2D}}$) can be related to the UAV position ($\boldsymbol{p}^e_{eb}$) by

$$\boldsymbol{y}^r_{\text{PARS,2D}} = \begin{pmatrix} 1 & 0 & 0 \\ 0 & 1 & 0 \end{pmatrix} \boldsymbol{R}^\top_{nr} \boldsymbol{R}^\top_{en} (\boldsymbol{p}^e_{eb} - \boldsymbol{p}^e_{er}). \tag{7.9}$$

Therefore, using the relation $\boldsymbol{p}^e_{eb} = \hat{\boldsymbol{p}}^e_{eb} + \delta \boldsymbol{p}^e_{eb}$, the estimate measurement is given as

$$\hat{\boldsymbol{y}}^r_{\text{PARS,2D}} = \begin{pmatrix} 1 & 0 & 0 \\ 0 & 1 & 0 \end{pmatrix} \boldsymbol{R}^\top_{nr} \boldsymbol{R}^\top_{en} (\hat{\boldsymbol{p}}^e_{eb} - \boldsymbol{p}^e_{er}) \tag{7.10}$$

The Jacobian matrix of $\boldsymbol{y}^r_{\text{PARS}}$ with respect to $\delta \boldsymbol{p}^e_{eb}$ can be found by differentiating Eq. (7.9)

$$\left. \frac{\partial \boldsymbol{y}^r_{\text{PARS,2D}}}{\partial \delta \boldsymbol{p}^e_{eb}} \right|_{\delta \boldsymbol{p}^e_{eb} = \boldsymbol{0}_{3\times 1}} = \underbrace{\begin{pmatrix} 1 & 0 & 0 \\ 0 & 1 & 0 \end{pmatrix}}_{\boldsymbol{\Pi}} \underbrace{\boldsymbol{R}^\top_{nr} \boldsymbol{R}^\top_{en}}_{\boldsymbol{R}^\top_{er}} \in \mathbb{R}^{2\times 3}. \tag{7.11}$$

Hence, the measurement matrix becomes

$$\boldsymbol{H}_{\text{PARS,2D}} = (\boldsymbol{\Pi} \boldsymbol{R}^\top_{er} \; \boldsymbol{0}_{2\times 3} \; \boldsymbol{0}_{2\times 3} \; \boldsymbol{0}_{2\times 3} \; \boldsymbol{0}_{2\times 3}) \in \mathbb{R}^{2\times 15}. \tag{7.12}$$

Furthermore, the covariance matrix of $\boldsymbol{y}^r_{\text{PARS,2D}}$ was computed using

$$\boldsymbol{\mathcal{R}}^r_{\text{PARS,2D}} = \boldsymbol{M}_{\text{PARS,2D}} \boldsymbol{\mathcal{R}}_{\text{PARS,2D}} \boldsymbol{M}^\top_{\text{PARS,2D}} \tag{7.13}$$

where

$$\boldsymbol{\mathcal{R}}_{\text{PARS,2D}} = \text{diag}(\mathbb{E}[\varepsilon^2_\rho], \mathbb{E}[\varepsilon^2_\psi]). \tag{7.14}$$

Here, $\boldsymbol{\mathcal{R}}_{\text{PARS,2D}}$ given in spherical coordinates is converted to $\boldsymbol{\mathcal{R}}^r_{\text{PARS,2D}}$ in Cartesian coordinates [47, Ch. 1.6]. $\boldsymbol{M}_{\text{PARS,2D}}$ is a Jacobian matrix of $\boldsymbol{y}^r_{\text{PARS,2D}}$ with respect to the noise $\boldsymbol{\varepsilon}_{\text{PARS,2D}} = (\varepsilon_\rho, \varepsilon_\psi)$:

$$\boldsymbol{M}_{\text{PARS,2D}} = \frac{\partial \boldsymbol{y}^r_{\text{PARS,2D}}}{\partial \boldsymbol{\varepsilon}_{\text{PARS,2D}}} = \begin{pmatrix} m_{11} & m_{12} \\ m_{21} & m_{22} \end{pmatrix}, \tag{7.15}$$

with

$$m_{11} = \frac{\cos(\psi_y)\rho_y}{\bar{\rho}_y} \qquad m_{12} = -\sin(\psi_y)\bar{\rho}_y$$

$$m_{21} = \frac{\sin(\psi_y)\rho_y}{\bar{\rho}_y} \qquad m_{22} = \cos(\psi_y)\bar{\rho}_y$$

**Barometer** The barometer measurement model is the same as Section 4.2.4.

Please note that Eq. (4.31)

$$y_{\text{baro}} = \|\boldsymbol{p}^e_{eb} - \boldsymbol{p}^e_{eS}\|_2 + b_\gamma + \varepsilon_\gamma$$

is nonlinear, linearization errors might effect.

### 7.1.4 Results and Discussion

In this work, we used Raudstein 2020 field test data (described in Section 5.2.2). Please note that the data from *only the first* ground antenna was used as the PARS measurements. The details of the UAV equipment used for the field test are the same as Section 5.1. The position of the ground antenna, $\boldsymbol{p}^e_{er}$, was measured using GNSS before the field test. Before performing the offline calculation of the PARS-aided INS proposed in this paper, we ran the calibration presented in Chapter 6 to obtain the precise estimate of the PARS ground antenna orientation (i.e. $\hat{\boldsymbol{R}}_{nr}$) using the RTK-GNSS measurements. The $\chi^2_\alpha = 7.815$ was chosen as the outlier rejection threshold.

The attitude, velocity and position estimates from the PARS- and barometer-aided INS were compared to the estimates from RTK-GNSS-aided INS (used as ground truth), and the errors between them were computed. Figure 7.1 compares the attitude, velocity and position error plots between the previous and new approaches. Table 7.1 presents the mean error (ME), the absolute mean error (AME), standard deviation (STD) and root mean square error (RMSE) of the attitude, the velocity and the position estimation errors. The attitude and velocity errors between the previous and new approaches do not have much difference, while the the position error has differences. The new approach gave larger error than the previous approach in all the North, East and Down directions. Comparing Figures 7.1e–7.1f, the new approach gave large errors when the UAV is close to the ground station. This can be because the approximation of the angle $\alpha$ by Eq. (7.7) (the geometry is shown in Figure 4.1) is not very accurate when the range between the UAV and the ground station is short, although the formulation of the new approach can incorporate the Earth's curvature into the measurement model and this is beneficial when the range between the UAV and the ground station is long.

### 7.1.5 Conclusion

This paper made modifications to the MEKF-based aided INS using the PARS and barometer measurements to incorporate the effect of Earth's curvature into consideration. Starting from the conventional approach, which uses barometer-based altitude to avoid noisy vertical measurement in PARS, a new approach was suggested to deal with the PARS and the barometer measurements independently. Effectively, the PARS and barometer measurements were updated non-linearly

| | | Roll [°] | Pitch [°] | Yaw [°] | Norm [°] |
|---|---|---|---|---|---|
| Attitude: New | ME: | -0.94 | -2.51 | 4.54 | 5.27 |
| | AME: | 2.20 | 2.62 | 12.58 | 13.04 |
| | STD: | 2.79 | 1.85 | 15.32 | 15.68 |
| | RMSE: | 2.95 | 3.12 | 15.98 | 16.55 |
| Attitude: Previous | ME: | -2.64 | 0.99 | 4.77 | 5.55 |
| | AME: | 2.79 | 2.19 | 13.26 | 13.73 |
| | STD: | 2.07 | 2.75 | 15.78 | 16.15 |
| | RMSE: | 3.36 | 2.93 | 16.49 | 17.08 |
| | | North [m/s] | East [m/s] | Down [m/s] | Norm [m/s] |
| Velocity: New | ME: | 0.02 | 0.04 | 0.04 | 0.05 |
| | AME: | 0.49 | 0.39 | 0.10 | 0.63 |
| | STD: | 0.72 | 0.66 | 0.16 | 0.99 |
| | RMSE: | 0.72 | 0.66 | 0.16 | 0.99 |
| Velocity: Previous | ME: | 0.01 | -0.09 | 0.01 | 0.09 |
| | AME: | 0.35 | 0.26 | 0.09 | 0.44 |
| | STD: | 0.48 | 0.35 | 0.14 | 0.61 |
| | RMSE: | 0.48 | 0.36 | 0.14 | 0.62 |
| | | North [m] | East [m] | Down [m] | Norm [m] |
| Position: New | ME: | -2.51 | 9.54 | -0.47 | 9.88 |
| | AME: | 7.54 | 9.72 | 0.68 | 12.32 |
| | STD: | 9.85 | 11.05 | 0.75 | 14.82 |
| | RMSE: | 10.16 | 14.60 | 0.89 | 17.81 |
| Position: Previous | ME: | 2.53 | -2.46 | 0.27 | 3.54 |
| | AME: | 7.17 | 4.15 | 1.20 | 8.37 |
| | STD: | 8.27 | 4.43 | 1.65 | 9.53 |
| | RMSE: | 8.65 | 5.07 | 1.67 | 10.16 |

Table 7.1: Error statistics comparison between old and new approaches

in the MEKF. The new approach was compared to the conventional approach through offline calculation, using dataset obtained from a field test with using RTK-GNSS aided INS position estimates as ground truth. Through the comparison, we found that the formulation of the new approach can effectively incorporate Earth's curvature, but induces errors when the distance from the ground station is too short due to the approximation of elevation angle.

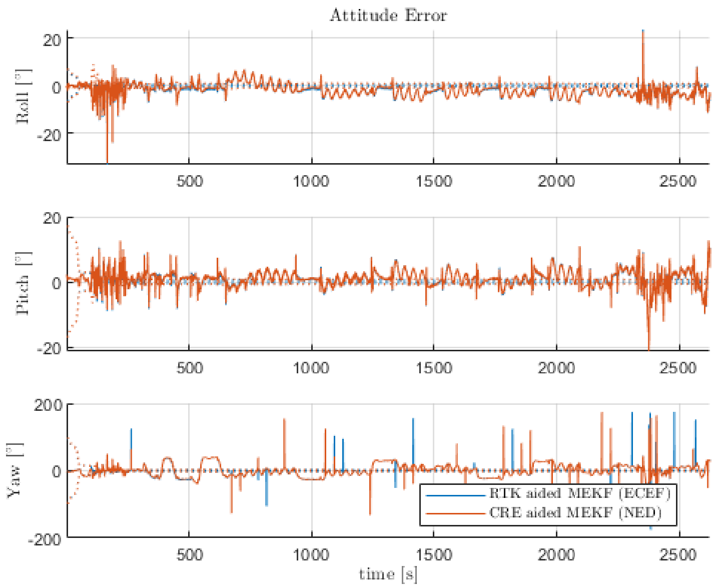


(a) Attitude error with the previous approach

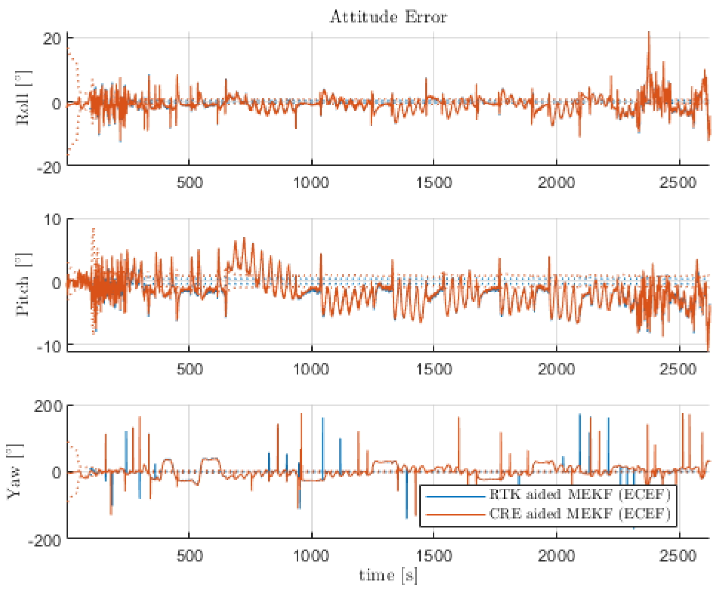


(b) Attitude error with the new approach

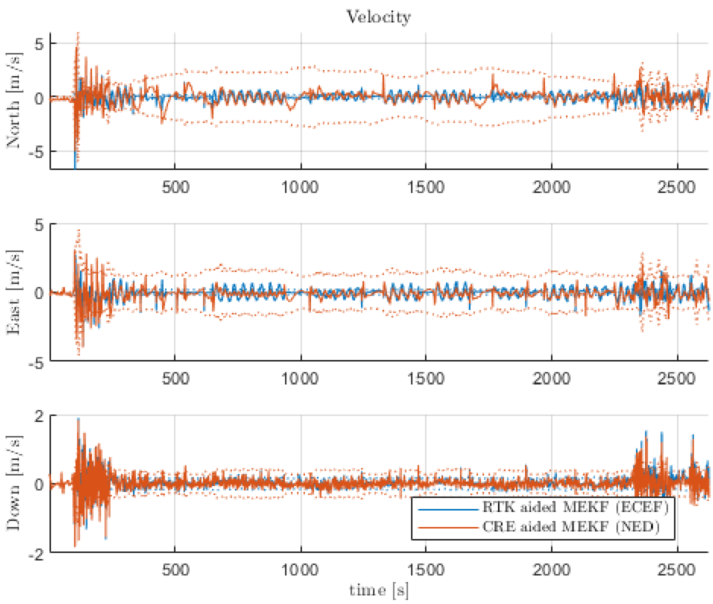

(c) Velocity error with the previous approach

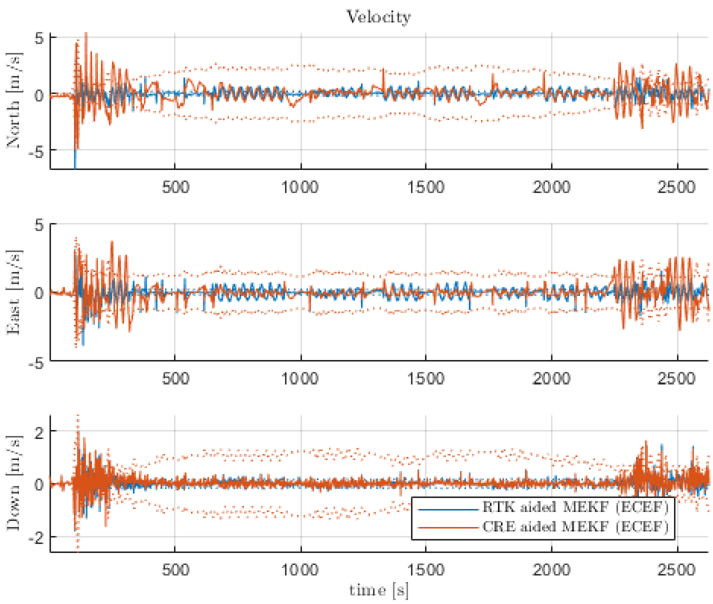

(d) Velocity error with the new approach

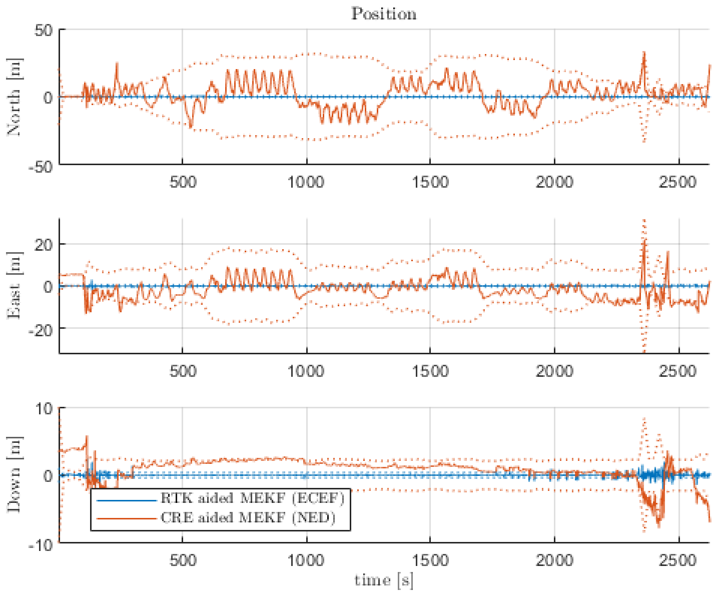


(e) Position error with the previous approach

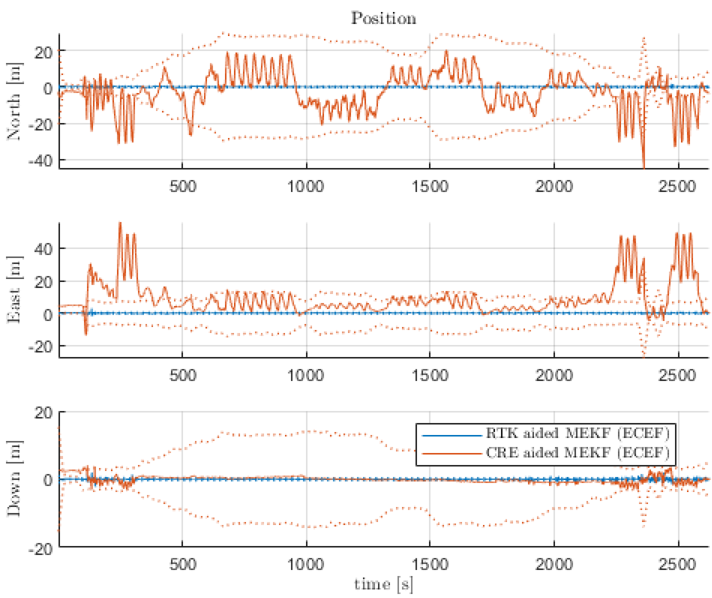


(f) Position error with the new approach

Figure 7.1: Error plots w.r.t the autopilot (attitude, velocity) and RTK-GNSS (position) reference

## 7.2 Multi Hypothesis Filter for Noise Mitigation

### 7.2.1 Introduction

In this work, multiple position measurements (including clutter) were extracted from the PARS vector file created by the DoA algorithm, and the PDAF was applied using the extracted multiple measurements to overcome the multipath problem in the elevation angle assuming that one of the measurements is true and the rest is clutter. The position estimate from the PDAF was compared with the previously implemented MEKF.

### 7.2.2 Positioning

The positioning techniques that formulate the navigation system in this work are INS (Section 3.1) and PARS (Section 3.3). Please note that the barometer (Section 3.4) and RTK-GNSS (Section 3.2) did not aid INS. The RTK-GNSS measurements were used as ground truth to examine the performance of the PARS-aided INS.

### 7.2.3 Navigation System

The navigation system presented in this work is PARS-aided INS using MEKF integrated with PDAF to incorporate multiple PARS measurements at each time step.

The difference from the navigation system presented in Chapter 4 and the one in this section is that:

1. PDAF makes changes to the correction step of MEKF (Section 4.5).
2. Only the PARS measurement model (Section 4.2.2) from Section 4.2 was used.

The system model (Section 4.1), pre-launch calibration (Section 4.3) and the outlier rejection (Section 4.4) are the same as Chapter 4. Please note that in the context of PDAF, outlier rejection (Section 4.4) is called *gating*.

### 7.2.4 Probabilistic Data Association Filter (PDAF)

In PDAF, the prediction step is the same as the standard Kalman filters and the difference is in the update step. When multiple measurements exit at time-step $k$, PDAF updates the state for each measurement and produces a Gaussian mixture, known as hypotheses. Then PDAF approximates the Gaussian mixture as a single Gaussian by computing *weighted* mean and covariance.

More specifically, when we have $n_k$ measurements denoted by subscript $i = 1, 2, ..., n_k$, we get $n_k + 1$ hypotheses after measurement update as a Gaussian mixture, where $i = 0$ corresponds to no valid measurement. PDAF reduces the number of hypotheses from $n_k + 1$ to 1 by merging. In other words, the posterior is a sum of *weighted* Gaussian distributions corresponding to the multiple hypotheses.

#### Weight

The weight expressed as a probability score $p_i$ sum to unity

$$\sum_{i=0}^{n_k} p_{k,i} = 1 \tag{7.16}$$

where $p_0$ is allocated to the null hypothesis (i.e. no valid measurement), representing the probability that none of the other hypotheses are correct.

The weight $p_{k,i}$ is a normalized weight for hypothesis $i$ to make the sum unity. When $p_{k,i} \propto \tilde{p}_{k,i}$,

$$\tilde{p}_{k,i} = \begin{cases} \lambda(1 - P^D) & \text{if } i = 0 \\ P^D \mathcal{N}(\boldsymbol{z}_{k,i}; \hat{\boldsymbol{z}}_k, \boldsymbol{S}_k) & \text{if } i = 1, 2, \ldots, n_k \end{cases}$$

where $\lambda$ is a clutter rate, $P^D$ is a detection rate, $\boldsymbol{z}_{k,i} = \boldsymbol{y}^r_{\mathrm{PARS}}$ is a measurement, $\hat{\boldsymbol{z}}_k = \hat{\boldsymbol{y}}^r_{\mathrm{PARS}}$ is a predicted measurement, $\boldsymbol{S}_k$ is a predicted measurement covariance (or innovation covariance)

$$\boldsymbol{S}_k = \boldsymbol{H}_k \hat{\boldsymbol{\mathcal{P}}}_k \boldsymbol{H}_k^\intercal + \boldsymbol{\mathcal{R}}_{k,i}, \tag{7.17}$$

whereas $\hat{\boldsymbol{\mathcal{P}}}_k$ is a prior error covariance, $\boldsymbol{H}_k = \boldsymbol{H}_{\mathrm{PARS}}$ and $\boldsymbol{R}_{k,i} = \boldsymbol{\mathcal{R}}_{\mathrm{PARS}}$. The predicted measurement distribution is expressed as

$$\mathcal{N}(\boldsymbol{z}_{k,i}; \hat{\boldsymbol{z}}_k, \boldsymbol{S}_k) = \frac{1}{(2\pi)^{\frac{1}{2}} |\boldsymbol{S}_k|^{\frac{1}{2}}} \exp(-\frac{1}{2} \underbrace{(\boldsymbol{z}_{k,i} - \hat{\boldsymbol{z}}_k)^\intercal \boldsymbol{S}_k{}^{-1} (\boldsymbol{z}_{k,i} - \hat{\boldsymbol{z}}_k))}_{\boldsymbol{q}(\boldsymbol{z})}. \tag{7.18}$$

Finally, normalization is needed to compute $p_{k,i}$

$$p_{k,i} = \frac{\tilde{p}_{k,i}}{\sum_{i=0}^{n_k} \tilde{p}_{k,i}}. \tag{7.19}$$

#### Computation of posterior

With a mean $\boldsymbol{z}_{k,i}$ and a covariance $\boldsymbol{\mathcal{R}}_{k,i}$ for each measurement, a measurement matrix $\boldsymbol{H}_k$, a prior state vector (or a nominal state) $\hat{\boldsymbol{x}}_k$ and a prior error covariance $\hat{\boldsymbol{\mathcal{P}}}_k$, Kalman gain can be computed using

$$\boldsymbol{K}_{k,i} = \hat{\boldsymbol{\mathcal{P}}}_k \boldsymbol{H}_k^\intercal [\boldsymbol{H}_k \hat{\boldsymbol{\mathcal{P}}}_k \boldsymbol{H}_k^\intercal + \boldsymbol{\mathcal{R}}_{k,i}]^{-1} \tag{7.20}$$

then a posterior state vector can be updated using

$$\delta \boldsymbol{x} = \sum_{i=1}^{n_k} p_{k,i} \boldsymbol{K}_{k,i} (\boldsymbol{z}_{k,i} - \hat{\boldsymbol{z}}_k) \tag{7.21}$$

and a posterior error covariance can be updated using

$$\boldsymbol{\mathcal{P}}_k = \left[ \boldsymbol{I} - \left( \sum_{i=1}^{n_k} p_{k,i} \boldsymbol{K}_{k,i} \right) \boldsymbol{H}_k \right] \hat{\boldsymbol{\mathcal{P}}}_k + \sum_{i=1}^{n_k} p_{k,i} (\boldsymbol{x}_{k,i} - \boldsymbol{x}_k)(\boldsymbol{x}_{k,i} - \boldsymbol{x}_k)^\intercal \tag{7.22}$$

where

$$\boldsymbol{x}_{k,i} = \hat{\boldsymbol{x}}_k + \boldsymbol{K}_{k,i} (\boldsymbol{z}_{k,i} - \hat{\boldsymbol{z}}_k) \tag{7.23}$$

$$\tag{7.24}$$

Eq. (7.21) and Eq. (7.22) complete the update step and the reduction of the hypothesis at the same time.

### 7.2.5 Overview

An overview of the multi hypothesis filter is given in Fig. 7.2.

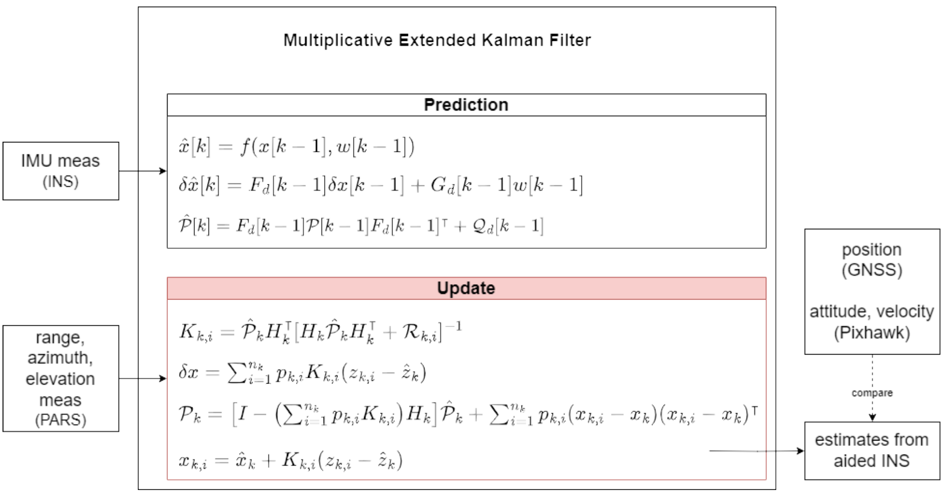


Figure 7.2: Multi hypothesis filter overview

### 7.2.6 Results and Discussion

In this work, we used the field test data from Raudstein 2020 (described in Section 5.2.2). Please note that the data from *only the first* ground antenna was used as the PARS measurements. The details of the UAV equipment used for the field test are the same as Section 5.1. The position of the ground antenna, $\boldsymbol{p}_{er}^{e}$, was measured using GNSS before the field test. Before performing the offline calculation of the PARS-aided INS proposed in this paper, we ran the calibration presented in Chapter 6 to obtain the precise estimate of the PARS ground antenna orientation (i.e. $\hat{\boldsymbol{R}}_{nr}$) using the RTK-GNSS measurements. Numerical values for the covariance matrices can be found in Appendix C.3. The $\chi_{\alpha}^{2} = 7.815$ was chosen as the outlier rejection threshold. The clutter rate was set $\lambda = 10^{-6}$, and the detection rate was set $P^{D} = 0.95$.

At each time step, **four** measurements were extracted from the PARS vector file and each measurement was named in order of the strength of the peaks. Figure 7.3 shows the extracted measurements for the PARS elevation angle, comparing with the GNSS measurement as ground truth. The measurements were extracted manually using duplicate code of the built-in software. The 1st peak (i.e. the strongest peak) is almost identical to the PARS elevation angle extracted by the built-in software automatically. This means that the PARS measurements used in the other work were essentially the strongest peak. The measurements from the second, third, and fourth peaks were much noisier than the strongest peak.

PDAF was applied using the four measurements extracted. Figure 7.4 compares the results from the PARS-aided INS between the standard MEKF presented in Section 4.5 and the PDAF presented in this paper. The orange line is the estimate from the PARS-aided INS and the blue line is the GNSS measurement shown as ground truth. The estimates from standard MEKF and the PDAF were almost identical. This means that PDAF mostly used the strongest peaks and rejected the other peaks or the weight assigned to the other peaks were very low. PDAF does not seem to solve the problem of noise in the elevation angle.

Figure 7.5 is the zoomed version of Figure 7.3a. The noise in the elevation angle has a sine-wave-like shape and does not have a sudden jump which is a sign of using measurements from wrong peaks. This may be because the assumption of PDAF is not true in this case.

When multipath occurs due to reflection, the reflected signal can disturb the true signal in two possible ways:

- In the first case, the reflected signal and the true signal do not sum up, and two (or more) peaks appear in the DoA algorithm. If the wrong peak (from the reflected signal) becomes stronger somehow, the wrong measurement will be reported.
- In the second case, the reflected and true signals sum up, and wave interference occurs.

Figure 7.5 indicates the second case. This means that the PDAF is not effective to eliminate the noise in the elevation angle, as the PDAF assumes the first case. The first case has been observed before, but the vector file was not recorded. Thus, PDAF could not be applied by extracting multiple measurements. To overcome the second case noise, we might have to consider changing the ground antenna design.

### 7.2.7 Conclusion

This paper applied the PDAF to overcome the multipath error in the elevation angle of the PARS.

We conducted a field test in the north of Agdenes outside of Trondheim and recorded the PARS vector file produced by the built-in DoA algorithm. Four positioning measurements were extracted from the PARS vector file in an order of the strength of peaks at each time step, and the PDAF assumed that one of the four measurements is true and the rest is clutter due to multipath.

The results showed that the PDAF mostly used the measurement from the strongest peak and the performances between the PDAF and the previously implemented standard Kalman filter did not differ much.

The reason can be that the assumption of the PDAF was not valid this time. The recorded PARS elevation measurement does not have a sudden jump which is an indication of choosing a measurement from a wrong peak, and instead, we can observe sine-wave-like noise. This means that the reflected signal did not cause clutter which appears as multiple peaks in the DoA algorithm (first case), instead, the reflected signal disturbed the true signal itself (second case). Although the first case (i.e. the PDAF assumption is valid) has been observed before, the second case (i.e. the PDAF assumption is not valid) was dominant in the experiment results we obtained this time. For the second case, the PDAF is not effective, and we need to consider changing the design of the ground antenna.

In future work, we want to apply the PDAF to the multipath problem from the first case if we succeed to record the data.

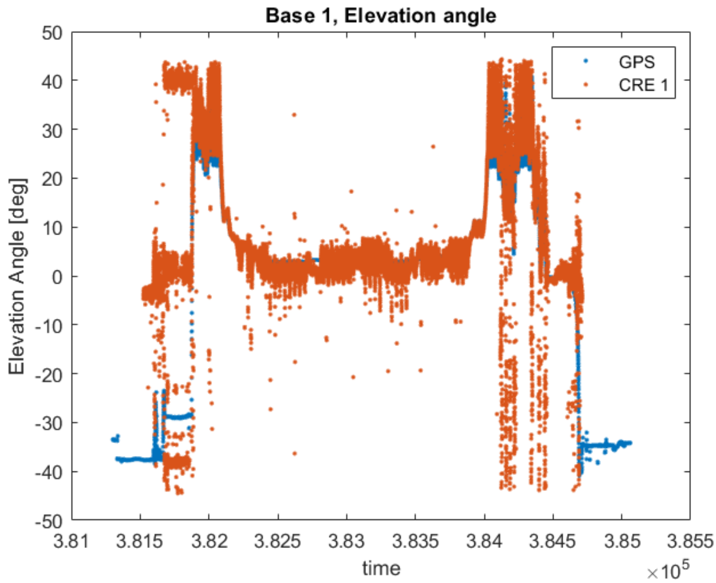


(a) The 1st (strongest) peak

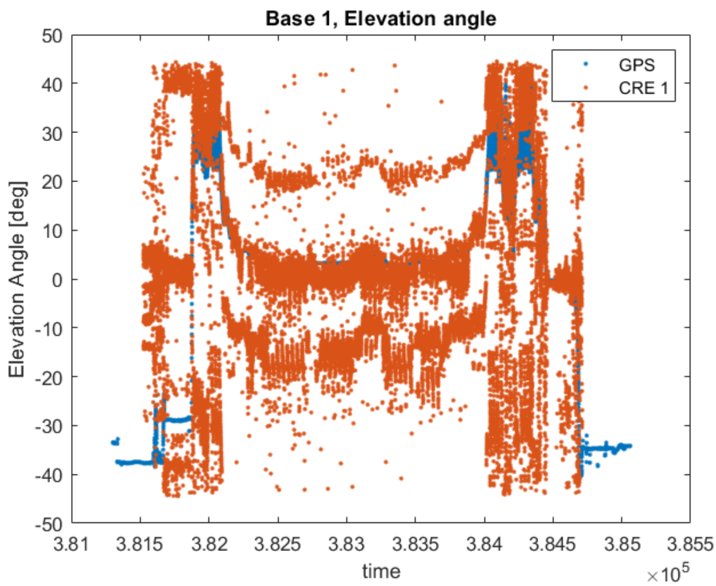


(b) The 2nd peak

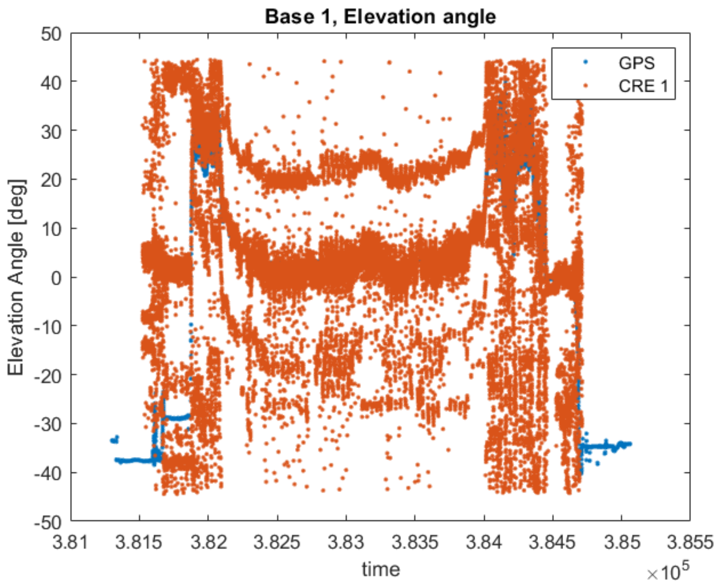


(c) The 3rd peak

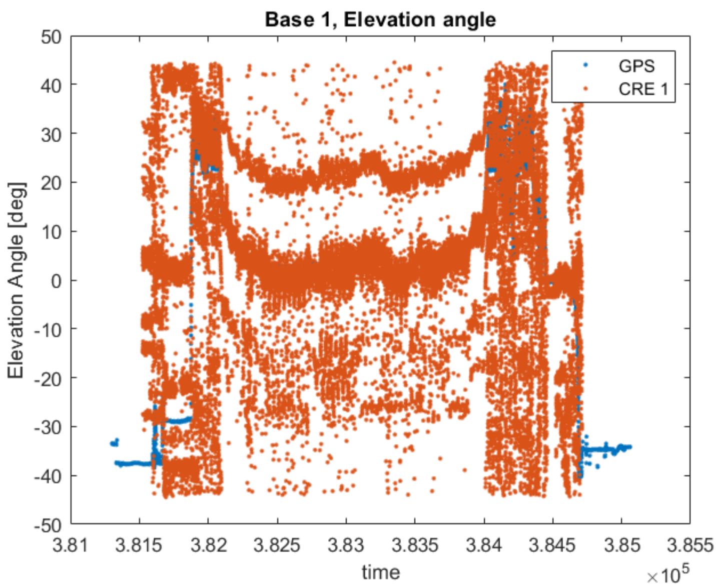


(d) The 4th peak

Figure 7.3: The extracted four elevation angles

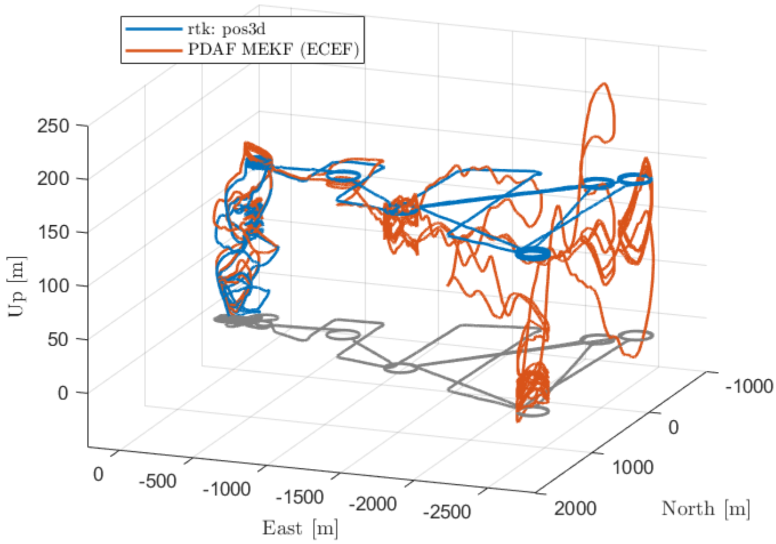


(a) Standard MEKF

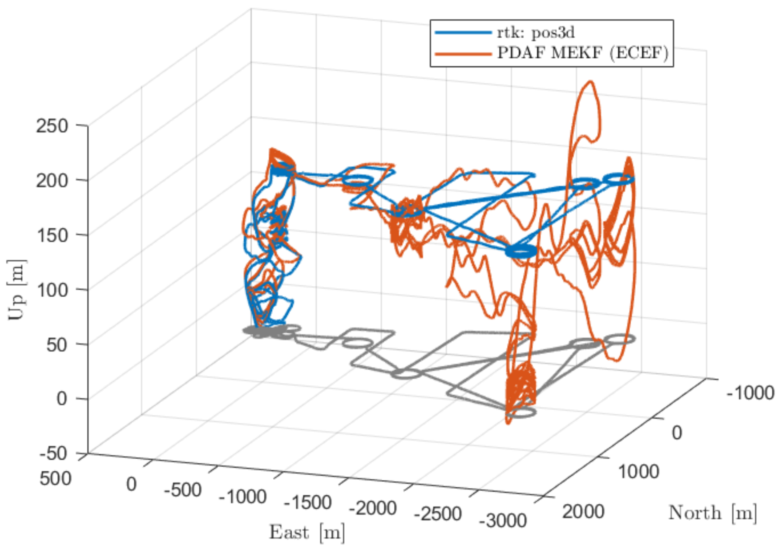


(b) PDAF

Figure 7.4: Position estimate from the PARS-aided INS comparing the standard MEKF and the PDAF

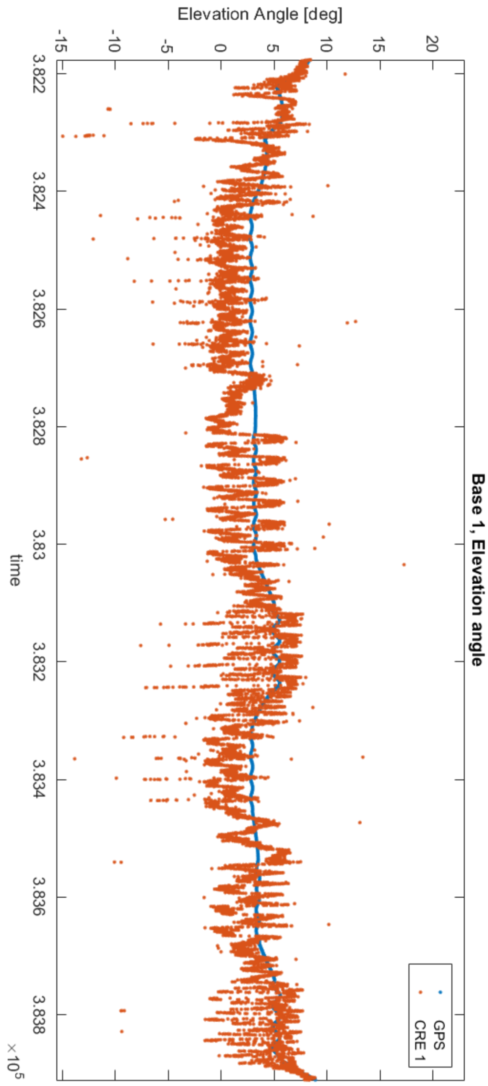


Figure 7.5: 1st peak elevation zoomed

## 7.3 Alternative elevation angle

### 7.3.1 Introduction

This work proposes an alternative to the uncertain and multipath-prone elevation angle during UAV navigation over horizontal surfaces, such as open water, by recalculating the elevation angle using redundant altitude information from an altimeter based on barometer, laser, or radar. The elevation angle is computed from the PARS range measurement, the barometer altitude measurement, and the effective Earth radius derived from the PARS ground radio position. This concept, similar to calculating the grazing angle in airborne radar reflections [70], addresses the unincorporated Earth curvature and inaccuracies of alternative elevation angle estimates previously unaddressed [32, 30, 33]. The recalculated elevation angle can mitigate these issues by incorporating the Earth's curvature and maintaining reasonable accuracy even when the UAV is close to the PARS ground antenna, avoiding manipulation of range measurements as in prior work [23, 24, 25, 26]. The performance of the recalculated angle is assessed through offline computation of PARS-aided INS using field test data.

### 7.3.2 Positioning

The positioning techniques that formulate the navigation system in this work are INS (Section 3.1), PARS (Section 3.3) and the barometer (Section 3.4). Please note that RTK-GNSS (Section 3.2) did not aid INS. The RTK-GNSS solution was used to provide the ground truth of the UAV position.

The PARS measurements are formulated in two ways:

- using the original elevation angle $\theta_u$ (measured by PARS), and
- using a recalculated grazing angle $\alpha_u$ based on the altitude (measured by a barometer) and the distance (measured by PARS), which is the main focus of this paper.

#### Raw PARS elevation angle formulation

The range $\rho_y$, azimuth $\psi_y$ and elevation $\theta_y$ measurement can be related to a Cartesian position measurement in the radio coordinate system $\{r\}$ using

$$\boldsymbol{y}^r_{\text{PARS}} = \begin{pmatrix} \rho_y \cos(\psi_y) \cos(\theta_y) \\ \rho_y \sin(\psi_y) \cos(\theta_y) \\ -\rho_y \sin(\theta_y)) \end{pmatrix}$$

which is same as Eq. (4.11).

**Recalculated elevation angle formulation based on barometric altitude and PARS range measurements**

A geometrical illustration of the elevation angle $\alpha_u$ is given in Figure 7.6. Considering the curved Earth model with an effective Earth radius $r_a$, the elevation angle $\alpha_u$ can be computed from the range $\rho_u$ and the altitude $\gamma_u$, from Section 3.4,

$$\alpha_u = \sin^{-1}\left(\frac{\gamma_u^2 + 2\gamma_u r_a - \rho_u^2}{2\rho_u r_a}\right). \tag{7.25}$$

is similar to the grazing angle calculation of [70, Ch. 2.6.1] in airborne radar reflection calculations. Using the (2.108) in [38, Ch. 2.4.1], the Earth radius at the PARS ground antenna $r_r$ is

$$r_r = \left(\frac{\cos^2(\psi_y)}{r_N} + \frac{\sin^2(\psi_y)}{r_E}\right)^{-1} \tag{7.26}$$

where $\psi_y$ is the PARS azimuth measurement in Eq. (3.9) compensated for any azimuth mounting offset of {r} about {n}, $r_N$ is the meridian (North-South) radius of curvature and $r_E$ is the normal/transverse (East-West) radius of curvature. The $r_N$ and $r_E$ are computed using

$$r_N(\mu_r) = \frac{r_0(1-e^2)}{1 - e^2\sin^2(\mu_r)^{3/2}} \tag{7.27}$$

$$r_E(\mu_r) = \frac{r_0}{\sqrt{1 - e^2\sin^2(\mu_r)}} \tag{7.28}$$

from the latitude of the PARS ground antenna $\mu_r$, which can be found from the known PARS ground antenna position $\boldsymbol{p}^e_{er}$. The equatorial radius $r_0$, as presented earlier, and the eccentricity of the ellipsoid $e = 0.0818191908425$ are the parameters of the WGS84 ellipsoid.

By assuming zero-mean Gaussian noise $\varepsilon_\alpha \sim \mathcal{N}(0, \sigma_\alpha^2)$, the measurement of the computed elevation angle $\alpha_u$, from the redundant altitude $\gamma_y$ and the range measurements $\rho_y$ is represented by

$$\alpha_y = \alpha_u + \varepsilon_\alpha. \tag{7.29}$$

Now having access to the redundant evaluation angle $\alpha_y$, the UAV recalculated position measurement can be given as

$$\boldsymbol{y}^r_{\text{PARS,recalc}} = \begin{pmatrix} \rho_y \cos(\psi_y)\cos(\alpha_y) \\ \rho_y \sin(\psi_y)\cos(\alpha_y) \\ -\rho_y \sin(\alpha_y) \end{pmatrix} \tag{7.30}$$

in the $\{r\}$ frame.

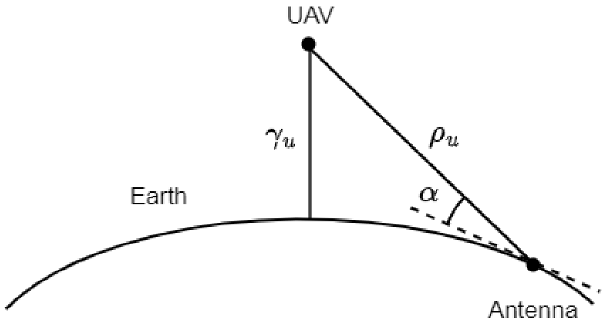


Figure 7.6: Grazing Angle geometry

**Motivating example**

We use a UAV flying from an airfield to an offshore installation as motivating example where the use of PARS can result in a multipath-corrupted elevation angle measurement due to reflections from the sea surface. We propose the case of flying from Ørland Airport in Norway (63°, 41′34.19″N, 9°36′8.39″E) to the Draugen oil field (64°21′11.42″N, 7°46′57.38″E) on the Norwegian continental shelf carrying some equipment needed offshore. The approximate surface distance between the two locations is $s_{\text{Ørland-Draugen}} = 115.462\,\text{km}$. The result depends on the choice of Earth approximation (spherical or ellipsoid). We used Eq. (7.26) in the surface distance calculation based on relevant formulae from [71]. The geometric range between an hypothetical base antenna at the airport and the helideck at the oil field is 115.467 km. The base antenna was assumed to be mounted on a mast 30 m above the mean sea level at Ørland. The helideck was placed 40 m above the mean sea level at the Draugen.

With this setup we get 0.503 m difference between the surface distance and the horizontal range component

$$\rho_{\text{hor}} = \sqrt{\rho_u^2 - \left(\boldsymbol{p}_{rb,D}^n\right)^2} \tag{7.31}$$

used in previous results [24, 23, 26] to handle the elevation angle multipath problem. However, assuming that the Earth is flat, using the negated down component of $\boldsymbol{p}_{rb,D}^n$ to represent the altitude at Draugen gives an altitude difference of 1113.995 m. Moreover, this is not an issue, since we do not trust the $\boldsymbol{p}_{rb,D}^n$ signal due to the multipath affecting the elevation. Recalculating the elevation angle

$$\alpha_{u_{\text{FlatEarth}}} \approx \sin^{-1}\left(\frac{h_{\text{Draugen}} - h_{\text{Ørland}}}{\rho_u}\right) \tag{7.32}$$

using a flat Earth assumption, where $h_{\text{Draugen}}$ is assumed measured by a barometer and $h_{\text{Ørland}}$ is known, results in an recalculated elevation angle of

$$\alpha_{u_{\text{FlatEarth}}} = 0.005\,086°. \tag{7.33}$$

The true elevation angle is however

$$\theta_u = -0.512\,419°. \tag{7.34}$$

Using Eq. (7.25), we get

$$\alpha_{u_{\text{CurvedEarth}}} = -0.512\,427°. \tag{7.35}$$

The resulting altitude error at Draugen using based on using Eq. (7.30) as a position sensor is −1042.905 m and 0.016 m, respectively when using Eq. (7.32) and Eq. (7.25) to calculate $\alpha_u$. In conclusion, beginning to be able to recalculate the elevation angle taking into account the curved Earth is vital for PARS-based navigation. Especially when the distances from the base radio to the UAV is large.

### 7.3.3 Navigation System

The difference between the navigation system in this work and the one described in Chapter 4 is the PARS measurement model.

The main focus of this section is comparing the two PARS measurement models: *PARS with elevation angle* and *PARS with redundant grazing/elevation angle* based on barometric altitude.

Please note that the measurement model for RTK-GNSS was not used in this section as RTK-GNSS did not aid INS in this work.

#### Measurement model: PARS with Elevation Angle

The model is same as the one in Section 4.2.2.

#### Measurement model: PARS with recalculated elevation angle

The measurement in Eq. (7.30) is mathematically similar to Eq. (4.11), and we just have to replace $\theta_y$ by $\alpha_y$. The $\hat{\boldsymbol{y}}^r_{\text{PARS}}$ and $\boldsymbol{H}_{\text{PARS}}$ are the same as Eq. (4.13) and Eq. (4.14).

We can obtain the measurement covariance matrix $\mathcal{R}_{\text{PARS}}$ by replacing $\varepsilon_\theta$ with $\varepsilon_\alpha$ in Eq. (4.15):

$$\mathcal{R}_{\text{PARS}} = \text{diag}(\mathbb{E}[\varepsilon_\rho^2], \mathbb{E}[\varepsilon_\psi^2], \mathbb{E}[\varepsilon_\alpha^2]). \tag{7.36}$$

where

$$\mathbb{E}[\varepsilon_\alpha^2] = \frac{1}{(\sqrt{1-\alpha_y})^2}\left(A^2\mathbb{E}[\varepsilon_\rho^2] + B^2\mathbb{E}[\varepsilon_\gamma^2]\right) \tag{7.37}$$

whereas

$$A = \frac{-2r_a\gamma_y - \gamma_y^2 + \rho_y^2}{2r_a\rho_y^2} \tag{7.38}$$

$$B = \frac{r_a + \gamma_y}{r_a\rho_y}, \tag{7.39}$$

following [47, Ch. 1.6]. The computation of $\mathcal{R}^r_{\text{PARS}}$ is the same as Eq. (4.16), and the Jacobian matrix $\boldsymbol{M}_{\text{PARS}}$ can be obtained by replacing $\theta_y$ with $\alpha_y$ in Eq. (4.17). The derivation of Eq. (7.37) is in Appendix D.

**Measurement model: Barometric altitude**

There is an option to also use the barometer measurement as direct aiding measurement Eq. (3.12) in addition to using it to calculating $\alpha_u$. The model is same as the one in Section 4.2.4.

### 7.3.4 Experimental Setup

In this work, we used the field test data from Raudstein 2020 (described in Section 5.2.2). Please note that the data from *only the first* ground antenna was used as the PARS measurements. The details of the UAV equipment used for the field test are the same as Section 5.1.

The position of the ground antenna, $\boldsymbol{p}^e_{er}$, was measured using GNSS before the field test. Before performing the offline calculation of the PARS-aided INS proposed in this paper, we ran the calibration presented in Chapter 6 to obtain the precise estimate of the PARS ground antenna orientation (i.e. $\hat{\boldsymbol{R}}_{nr}$) using the RTK-GNSS measurements.

### 7.3.5 Results and Discussion

We performed offline evaluation of the PARS-aided INS using either the raw PARS elevation angle measurement or the recalculated elevation angle based on altitude, range, and the Earth's radius, cf. Eqs. (7.25) to (7.28) proposed in this paper.

Figure 7.7 shows the PARS measurements used to aid the INS. Figure 7.7a compares the raw PARS elevation measurement with the calculated elevation angle Eq. (7.25). It can be observed that the recalculated elevation angle is free from multipath reflections from the ocean surface that strongly affect the raw PARS elevation angle measurement. Figure 7.7b compares the local PARS NED positions based on $\theta_y$, $\alpha_y$, and Section 7.3.2, Eq. (7.30), respectively. It is shown how the noise in the elevation angle manifests mainly in the Down direction, but also affects the North and East directions, compared to using the recalculated elevation angle in the aiding position measurement.

INS estimates are compared with the GNSS-RTK position reference in Figure 7.8. From Figure 7.8b, in comparison to Figure 7.8a, it is evident that vertical position estimates significantly improve using the recalculated elevation angle based on Eq. (7.25). This is further substantiated by Fig. 7.9, which shows the position estimation error along with the corresponding $3\sigma$ position error uncertainty (represented by dotted lines) provided by the MEKF. By comparing the statistics in Table 7.2 and Table 7.3, which include the mean error (ME), the absolute mean error (AME), the standard deviation (STD), and the root mean square error (RMSE) of the position estimation error, a significant improvement in the altitude estimates can be observed when using the proposed recalculated elevation angle before employing $\boldsymbol{p}_{rb}^{r}$ as an aiding measurement. The RMSE in altitude and for the total position is improved by 95.3 % and 87.1 %, respectively.

There is a smaller improvement in the altitude estimates when also incorporating the barometer as a range-like altitude aiding measurement, as presented in Section 3.4 and Section 4.2.4. This observation is supported by the position estimation error in Fig. 7.9 and the statistics provided in Tables 7.4 to 7.5. In this scenario, the results suggest that utilizing the Cartesian PARS position measurement, based on the recalculated elevation angle in conjunction with the barometer as aiding measurements, performs slightly worse compared to employing the raw elevation angle in the position calculation along with barometer aiding with respect to the lowest position RMSE, as seen by comparing Table 7.4 with Table 7.5. However, these differences are minor, with only a 32 cm difference in total position RMSE, indicating that it is still beneficial to avoid using the multipath-prone elevation measurement from PARS when flying over water, provided that the barometer pressure is well calibrated before takeoff. Notably, in the scenario where the raw elevation angle and the barometer serve as aiding measurements, there is an estimation error in the North direction outside the $3\sigma$ bounds shortly after takeoff. This suggests that this solution may result in a more inconsistent MEKF, compared to using the recalculated elevation angle, making covariance-based outlier rejection more challenging when using the raw elevation measurement.

In summary, considering both the estimation error and the consistency, the best estimation performance is achieved by using the recalculated elevation based on redundant altitude information alongside the barometer as a direct altitude aiding measurement.

### 7.3.6 Conclusion

This paper presented a novel approach for improving the accuracy of UAV positioning by utilizing a recalculated elevation angle in a PARS-aided INS based on redundant altitude information. The proposed method addresses the inherent issues in elevation angle measurements caused by multipath reflections. By integrating the recalculated elevation angle, which is derived from PARS range

| | North [m] | East [m] | Down [m] | Norm [m] |
|---|---|---|---|---|
| ME: | 2.90 | 2.96 | -56.72 | 56.88 |
| AME: | 6.22 | 4.36 | 58.17 | 58.66 |
| STD: | 7.32 | 4.94 | 61.07 | 61.70 |
| RMSE: | 7.87 | 5.76 | 83.35 | 83.92 |

Table 7.2: Position error statistics with position measurement based on raw PARS elevation

| | North [m] | East [m] | Down [m] | Norm [m] |
|---|---|---|---|---|
| ME: | 3.89 | -0.57 | 2.07 | 4.44 |
| AME: | 7.14 | 3.46 | 3.01 | 8.49 |
| STD: | 8.11 | 4.52 | 3.36 | 9.88 |
| RMSE: | 8.99 | 4.56 | 3.95 | 10.83 |

Table 7.3: Position error statistics with position measurement based on recalculated elevation angle

| | North [m] | East [m] | Down [m] | Norm [m] |
|---|---|---|---|---|
| ME: | 3.32 | 1.51 | 0.63 | 3.70 |
| AME: | 6.56 | 3.95 | 0.72 | 7.69 |
| STD: | 7.28 | 5.26 | 0.98 | 9.04 |
| RMSE: | 8.00 | 5.47 | 1.16 | 9.76 |

Table 7.4: Position error statistics with position measurement based on raw PARS elevation + barometer used as aiding measurements

measurements, barometer altitude, and the effective Earth radius, our approach effectively incorporates the Earth's curvature into the positioning calculations, offering a more reliable alternative to the traditional elevation angle. In addition we avoid estimation errors due to multipath corrupted elevation angle measurements when flying over water or other reflective surfaces.

The performance of the recalculated elevation angle was assessed through offline computations using field test data. The results demonstrated a significant reduction in aiding sensor colored noise and an overall improvement in the positioning accuracy of the UAV, especially vertically, where the majority of the noise from elevation angle measurements was observed.

This result highlights the potential of the recalculated elevation angle as a more reliable option for UAV navigation, providing an effective alternative to the noisy elevation angle in the presented application.

| | **North** [m] | **East** [m] | **Down** [m] | **Norm** [m] |
|---|---|---|---|---|
| ME: | 3.92 | -0.48 | 0.66 | 4.00 |
| AME: | 7.21 | 3.44 | 0.75 | 8.02 |
| STD: | 7.93 | 4.64 | 1.01 | 9.25 |
| RMSE: | 8.85 | 4.67 | 1.21 | 10.08 |

Table 7.5: Position error statistics with position measurement based on recalculated elevation angle + barometer used as aiding measurements

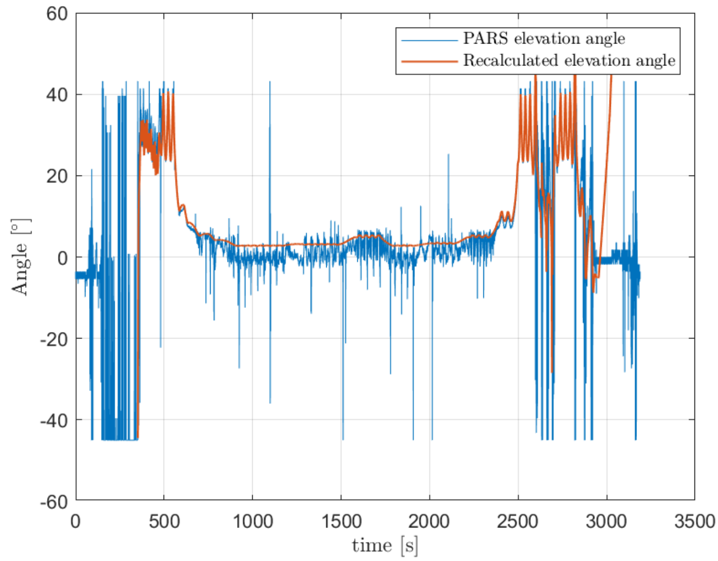


(a) Elevation measurements

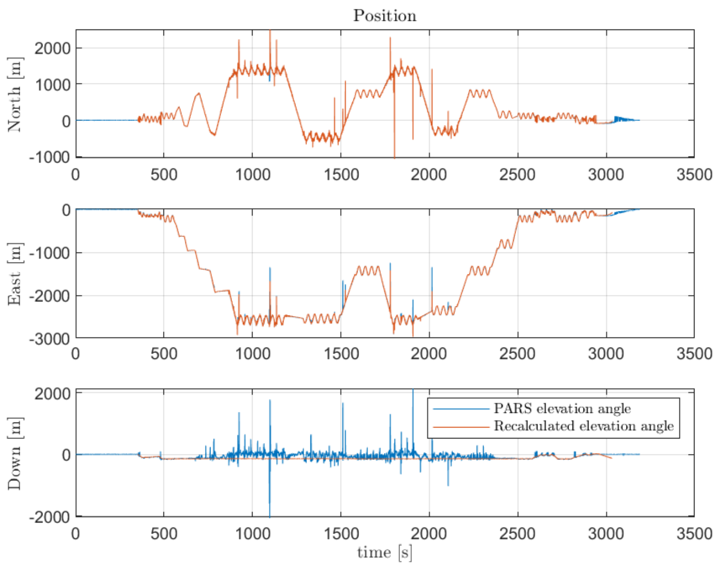


(b) PARS Position measurement including measurement outliers

Figure 7.7: Comparison of PARS and recalculated elevation angles and their effect of the Cartesian, $\boldsymbol{p}_{rb}^{r}$.

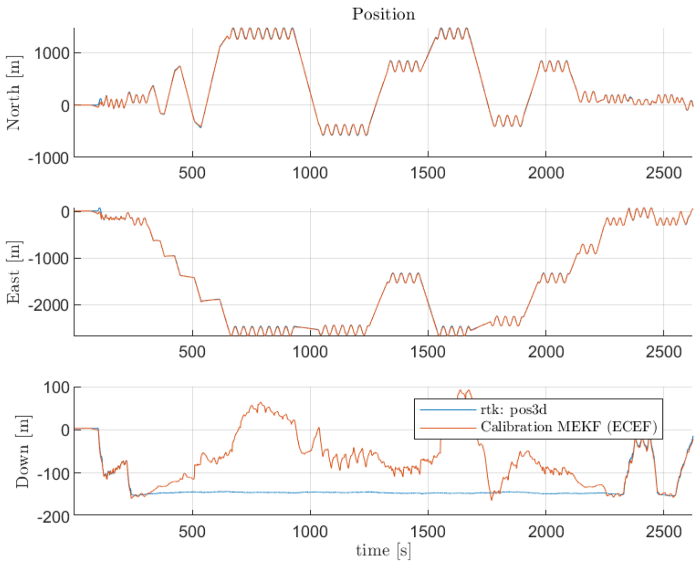


(a) using raw PARS elevation angle in the aiding measurement

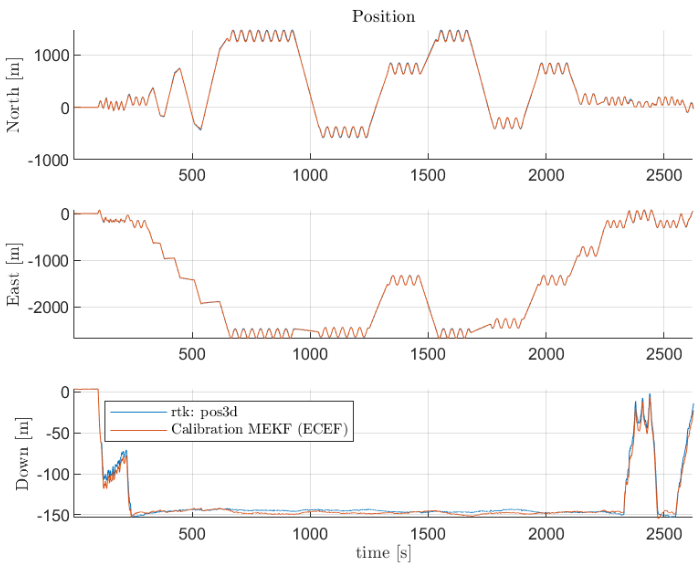


(b) using recalculated elevation angle in the aiding measurement

Figure 7.8: Aided-INS Position estimates in local NED coordinates compared to RTK-GNSS position

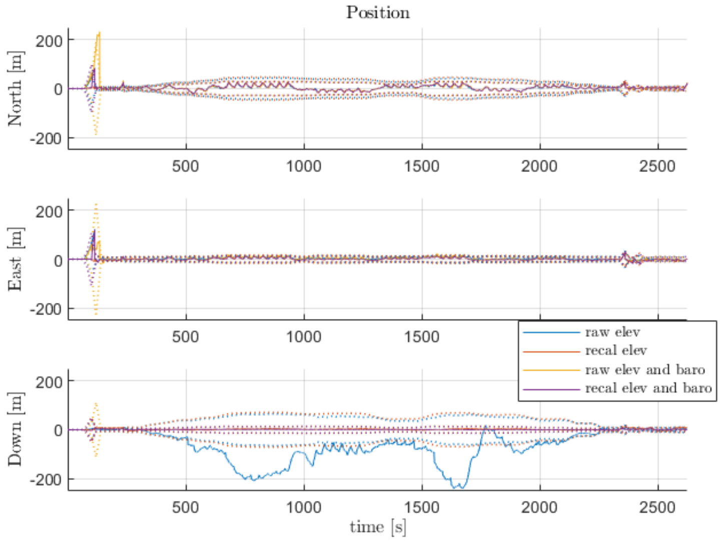


(a) position estimation error in NED coordinates

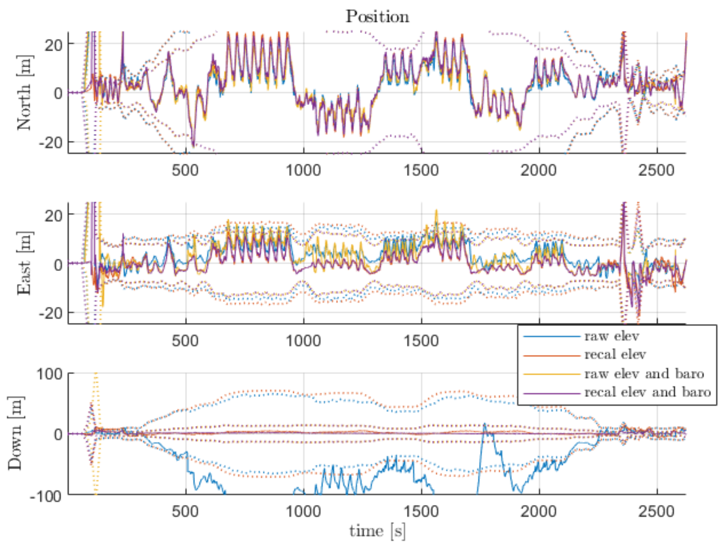


(b) position estimation error in NED coordinates - zoomed

Figure 7.9: Aided-INS position error compared to RTK-GNSS with $3\sigma$ estimation error (dotted lines). Four different INS aiding scenarios are presented. 1) Using the Cartesian PARS measurement with the raw PARS elevation angle. 2) Using the Cartesian PARS measurement with the recalculated elevation angle. 3) Using the Cartesian PARS measurement with the raw PARS elevation angle + the barometer as altitude measurement. 4) Using the Cartesian PARS measurement with the recalculated elevation angle + the barometer as altitude measurement

# 8 Jamming Detection

This chapter introduces an algorithm for jamming detection based on the Kalman filter (KF), as well as its incorporation into our navigation system. This chapter is based on on the paper

- Mika Okuhara, Torleiv Håland Bryne, Kristoffer Gryte, Oliver Hasler, and Tor Arne Johansen. UAV navigation during active GNSS jamming using phased-array-radio positioning. *NAVIGATION: Journal of the Institute of Navigation*, 2024. Submitted

## 8.1 Introduction

The natural next step is to ensure a safe handover from GNSS-aided to PARS-aided positioning in the event of GNSS RFI. The PNT solution from low-cost GNSS equipment is known to be degraded when the GNSS signal is exposed to jamming, shortly before the PNT solution is completely lost, [72]. It can potentially be critical if a faulty GNSS position is used by any aircraft onboard systems. Although standard consistency checks and integrity monitoring techniques would detect this as an outlier, early detection and classification of a jamming event would nevertheless be beneficial to enable a safe handover to another positioning system.

In the literature, jamming detection has been attempted using automatic gain control (AGC) and carrier-to-noise ratio (C/N0) as indicators, [73, 74, 75, 76]. AGC is an adaptive system where a variable gain amplifier adjusts the power of the incoming signal to optimize the signal dynamics for the analogue-to-digital converter (ADC) to minimize quantization losses, [72]. Without interference signals, the gain depends almost exclusively on thermal noise, and AGC adjusts the signal dynamics for variations in the received power due to the elevation of the satellite and/or different active antenna gain values. In the presence of interfering signals, AGC decreases its gain to match the maximum dynamics of the ADC, thus causing a reduction in the amplitude of the useful signal which might be lost. As the gain is expected to be stable under normal conditions (due to the slowly-varying nature of noise, temperature, and power supply voltage, etc.), sudden or large variations in the gain are useful indicators for interference detection, [77, 78].

C/N0 (in decibels per hertz (dB-Hz)) is a ratio between the received power and the thermal noise power spectral density at the input of the receiver. Although interference does not increase thermal noise, additional (non-thermal) noise generated by interference affects C/N0, as the ratio is estimated based on correlator outputs at the tracking stage. A compromised code/carrier tracking determines a reduction in the C/N0 level computed by the receiver. Indeed, the C/N0 reduction may be caused by several factors, not only interference, such as non-line-of-sight (NLOS) propagation of the signal, temporary signal outage, multipath fading effect, etc [72]. Although determining the source of the reduction from the sole observation of C/N0 is difficult, nevertheless, it is a powerful indicator of a critical condition occurring to a specific satellite signal, considering that C/N0 is observable for each tracked satellite and each signal/frequency band. The observation of the C/N0 level makes it possible to exclude signals from a set of satellites experiencing a C/N0 ratio below a certain threshold based on the fact that a low C/N0 ratio indicates a low quality tracking condition [79, 80, 81]. Thus, although not a stand-alone detection method, the variation in the C/N0 level can be used to assess the impact of interference on the quality of satellite signals. Having access to a C/N0 value for each tracked GNSS signal provides a significant advantage over AGC-based interference detection methods, especially when the receiver hardware is designed with a single AGC per GNSS band. Therefore, C/N0 facilitates more precise interference detection for low-cost receivers with only one AGC.

### Main Contribution

This work introduces a novel approach to GNSS jamming detection by leveraging a KF based algorithm combined with hypothesis testing. Unlike existing methods [82, 83, 84], our approach uniquely formulates the use of KF and hypothesis testing to detect jamming in UAV navigation systems using C/N0 measurements.

This work also contributes through the validation of our proposed detection algorithm with real-world experimental data, illustrating its practical utility. Integration with a PARS-aided INS offers an advancement in enhancing UAV navigation's resilience to jamming attacks. Our experimental evaluation, leveraging data from a comprehensive jamming event, indicates the algorithm's capability to detect jammed GNSS bands and assist in transitioning to PARS-aided navigation smoothly. This endeavor aims to support uninterrupted navigation, contributing to the operational safety and effectiveness of UAVs in environments susceptible to jamming.

### Organization

This chapter consists mainly of three sections: We collected GNSS data during jamming events with multiple scenarios and examined the influence of jamming in Section 8.2. Based on the results of the examination, we proposed and tested a KF-based jamming detection algorithm in Section 8.3. Then we integrated the jamming detection algorithm with the previously developed MEKF-based GNSS/PARS-aided INS and assessed its performance in Section 8.4.

## 8.2 Jamming Experiment

In this work, we used the dataset 3 described in Section 5.2.3. We participated in an open GNSS jamming event organised by the Norwegian Communications

Authority (Nkom), the Norwegian Public Roads Administration (NPRA), and the Norwegian Defence Research Establishment (FFI) at Bleik, Andøya, Norway on the 19$^{th}$-23$^{rd}$ September 2022.

In various jamming scenarios, we recorded data from low-cost, multi-frequency, multi-constellation GNSS receivers fixed on the ground. We also conducted multiple flights and recorded sensor measurements, using a fixed-wing UAV equipped with a GNSS receiver (the same as the one on the ground), an inertial measurement unit (IMU), a Pixhawk autopilot, and a PARS radio module used as telemetry and for redundant positioning. All results are obtained with standard and publicly available products and firmware.

The locations of a jammer, ground GNSS receivers, and UAV start point are indicated in Figure 8.1. The jammer was 1154 m and 429 m away from the ground receivers and the start position of the UAV, respectively.

In this section, the measurements reported by the GNSS receivers during the jamming event are presented and examined.

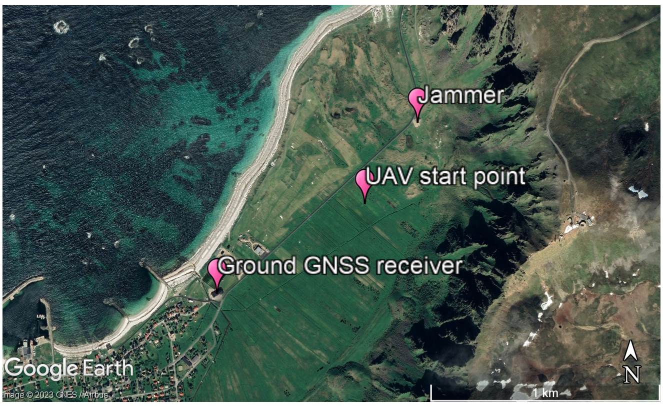


Figure 8.1: Jamming location

### 8.2.1 Jamming sessions

To examine the influence of jamming on the GNSS measurements, we used data from "Pyramid" and "Ramp" jamming tests conducted on the 20$^{th}$ September 2022. Table 8.1 and Table 8.2 show the summary of the "Pyramid" and "Ramp" jamming scenarios.

The "Pyramid" test was performed from 16:30:01 to 17:32:59 local time with constant jamming power at 10 W with a change in the number of jammed bands approximately every 3 min. Data from the "Pyramid" test were collected from **the receiver on the UAV**.

The "Ramp" test was conducted from 09:20:00 to 12:40:10 local time with six sessions depending on the type of jamming (either continuous wave (CW) or pseudorandom noise (PRN)) and which frequency bands were jammed, where the duration of each session was 25 min10 s. The jamming power increased from 2 nW to 20 W (i.e. 100 dB change) and then decreased from 20 W to 2 nW in the 2 dB step with minimum 10 s dwell time in each session. The jammed GNSS data from the "Ramp" test was collected from **the ground receivers**.

| Start | End | Jammed bands |
|---|---|---|
| 16:30:01 | 16:33:00 | E5b |
| 16:35:01 | 16:38:00 | E5b, L5 |
| 16:40:01 | 16:40:55 | E5b, L5 |
| 16:40:55 | 16:43:00 | E5b, L5, G2 |
| 16:45:01 | 16:47:59 | E5b, L5, G2, L2 |
| 16:50:00 | 16:50:10 | E5b, L5, G2, L2 |
| 16:50:10 | 16:52:59 | E5b, L5, G2, L2, B1 |
| 16:55:00 | 16:57:59 | E5b, L5, G2, L2, B1, G1 |
| 17:00:00 | 17:02:59 | E5b, L5, G2, L2, B1, G1, L1 |
| 17:04:59 | 17:07:59 | E5b, L5, G2, L2, B1, G1 |
| 17:10:00 | 17:12:59 | E5b, L5, G2, L2, B1 |
| 17:15:00 | 17:17:59 | E5b, L5, G2, L2 |
| 17:20:00 | 17:22:59 | E5b, L5, G2 |
| 17:25:00 | 17:27:59 | E5b, L5 |
| 17:30:00 | 17:32:59 | E5b |

Table 8.1: Pyramid jamming

| Start | End | Jammed bands | |
|---|---|---|---|
| 09:20:00 | 09:45:10 | L1 CW | Ramp 1 |
| 09:50:00 | 10:15:10 | L1 PRN | Ramp 2 |
| 10:20:00 | 10:45:10 | L1, G1, L2, L5 CW | Ramp 3 |
| 10:50:00 | 11:15:10 | L1, G1, L2, L5 PRN | Ramp 4 |
| 11:45:00 | 12:10:10 | L1, L5, E5b CW | Ramp 5 |
| 12:15:00 | 12:40:10 | L2, L5, G2, E5b CW | Ramp 6 |

Table 8.2: Ramp jamming

### 8.2.2 Equipment

In addition to the information on the general architecture of our equipment given in Section 5.1, the equipment used in this field test had the following additional specifications. Figure 8.2 gives a visual insight into the equipment.

#### Ground GNSS receiver

In addition to logging the data from the GNSS receiver on the UAV, we also logged data from data from the ZED-F9P and ZED-F9T ublox GNSS receivers **on the ground** on a Raspberry Pi single board computer through a SenTiBoard sensor interface and timing board, [55].

#### Software

The PARS-aided INS, from [25, 26], is implemented in DUNE unified navigation environment [57] running on the single-board computer for real-time operation of UAV in the field. The position estimate from the PARS-aided INS was used in closed-loop UAV flights when the GNSS measurements became invalid during the jamming tests.

#### Ground station

A ground station was set up in the indicated place labelled "UAV start point" in Figure 8.1.

### 8.2.3 Results

The gains from programmable gain amplifier (PGA) in AGC, and estimated C/N0 in the "Pyramid" and the "Ramp" tests are shown in Figures 8.4–8.10. The colour difference of the C/N0 plots shows different satellites. The shaded areas in Figure 8.4 indicate the active jamming periods during the "Pyramid" test. Please refer to Table 8.1 to look up which bands are experiencing jamming. For the "Ramp" data in Figures 8.5–8.10, the change in jamming power is indicated by vertical dotted lines with a 20dB power attenuation step. Different GNSS frequency bands were jammed in different "Ramp" tests (6 scenarios), as in Table 8.2. The NE plot is shown on a map in Figure 8.4f (overview) and Figure 8.4g (zoomed) with the PGA variation indicated by colour.

In addition to PGA gain and C/N0, the UAV position during the "Pyramid" test is shown in Figure 8.4. Please note that *block 1* and *block 2* in the PGA and spectrum figures indicate navigation frequency band blocks, corresponding to "Upper L-Band" and "Lower L-Band" in Figure 8.3.

Moreover, the spectrum of the GNSS signals in the frequency domain during the "Ramp" test is shown in Figures 8.5–8.10.

#### Pyramid tests - UAV-based logging

Figure 8.4a shows sudden and frequent changes in the PGA gain, which indicates interference with the GNSS signal. The PGA gain oscillated frequently not only when jamming was active (i.e. in the shaded area), but also when the jamming

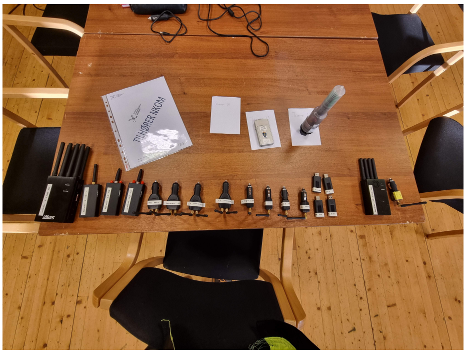

(a) Jammers

(b) Ground GNSS receiver

(c) Skywalker X8

(d) ground station with PARS antenna

Figure 8.2: Equipment used in the jamming event at Bleik in 2022

was not active (i.e. in the non-shaded areas). However, significant drops occurred most of the time when the jamming became active.

Figures 8.4b–8.4e clearly show significant drops or complete loss of the C/N0 estimate during the active jamming. Exceptionally, the GPS L1 band does not appear to be affected when this band was targeted, whereas the Galileo E1 and GPS L2 bands show a clear loss, although the jammer did not target these bands. It seems that other bands with similar frequencies were also affected by the jamming, even though they were not targeted.

Figures 8.4h–8.4g show that the UAV position reported by the UAV GNSS receiver degraded significantly when the PGA gain was low. The error in the degraded GNSS position was approximately 25 km maximum.

**Ramp tests - ground-based logging**

Through all the "Ramp scenarios, the PGA gain remained almost constant until the jamming power attenuation dropped to 40 dB (i.e. the jamming power became

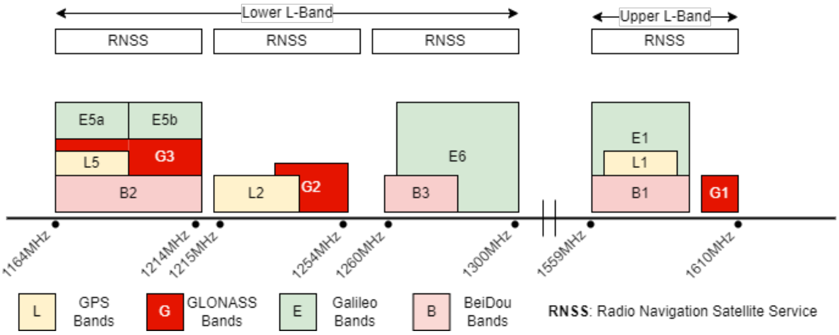

Figure 8.3: GPS, GLONASS, Galileo and BeiDou navigational frequency bands

stronger). Once the power attenuation decreased below 40 dB, the PGA gain started to gradually vary as the jamming power altered, as in Figures 8.5a–8.10a.

Overall, C/N0 ratio varied similarly to the PGA gain, seeing from Figures 8.5b–8.5e to Figures 8.10b–8.10e. The jamming effect appeared when the jamming power attenuation was below 40 dB, and the C/N0 ratio varied as the power attenuation altered. In some cases, jamming with less than 20 dB power attenuation caused a complete loss of the C/N0 ratio estimate.

For the "Ramp 1" and "Ramp 2" test scenarios (Figure 8.5 and Figure 8.6), the PGA gain of the block 1 frequency band varied, while that of the block 2 frequency band remained constant. This result matches the fact that the jammer aimed at the GPS L1 band only. However, not only the GPS L1 but also the Galileo E1, the BeiDou B1, and GLONASS G1 bands experienced the jamming effect, probably because these bands share a similar frequency range.

For the "Ramp 3" and "Ramp 4" test scenarios (Figure 8.7 and Figure 8.8), the jammer aimed at the GPS L1, L2, L5 and GLONASS G1 bands, so both frequency band blocks were affected. In addition to the aimed bands, the Galileo E1 E5b, the BeiDou B1, B2, and the GLONASS G2 bands were also affected because their frequency ranges are close to the aimed ones.

For the "Ramp 5" test scenario (Figure 8.9), the jammer aimed at the GPS L1, L5 and the Galileo E5b bands, so both frequency blocks are affected. In addition to the aimed bands, the BeiDou B2 (Close to GPS L5 and Galileo E5b), the Galileo E1 and the GLONASS G1 (Close to GPS L1) bands were also affected.

For the "Ramp 6" test scenario (Figure 8.10), the jammer aimed at the GPS L2, L5, the Galileo E5b and the GLONASS G2 bands, so mainly the frequency block 2 was affected. In addition to the aimed bands, the BeiDou B2 band was also affected (close to GPS L5 and Galileo E5b).

The subfigures (f) and (g) in Figures 8.5–8.10 show that the spectrum of the GNSS signal was skewed under the influence of jamming due to AGC adjustment. The effect of jamming appeared when the jamming power attenuation was below 40 dB, similar to the PGA gain and C/N0.

Comparing the C/N0 variations and the time-varying spectrum in "Ramp 1" and "Ramp 2" (Figure 8.5 and Figure 8.6) or "Ramp 3" and "Ramp 4" (Figure 8.7 and Figure 8.8), the effect of the PRN jammer seems stronger than the CW jammer.

### 8.2.4 Discussion

The results showed that GNSS jamming can be detected from decrements in PGA gain. Similarly, GNSS frequency bands experiencing jamming can be identified by complete losses or decrements in C/N0 ratios. Jamming detection can be activated when the PGA and C/N0 become below thresholds. As the UAV position plot in Figure 8.4g shows, the GNSS receiver provided a decent UAV position even with lower PGA gain to some extent. This result indicated that the observation of PGA gain enables early detection of jamming before the PNT solution degrades.

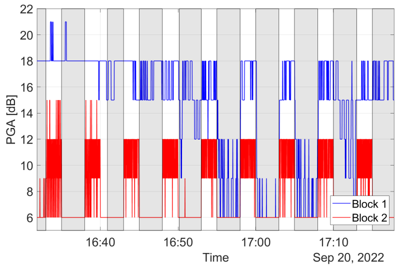


(a) PGA gain

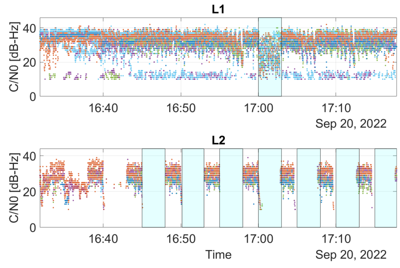


(b) GPS

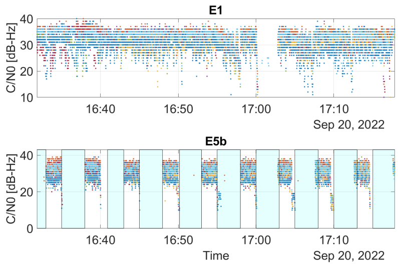


(c) Galileo

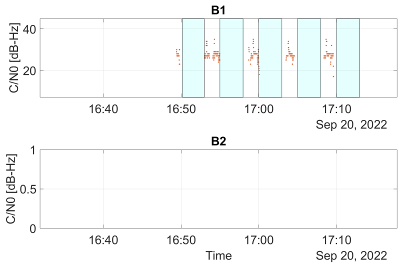


(d) BeiDou

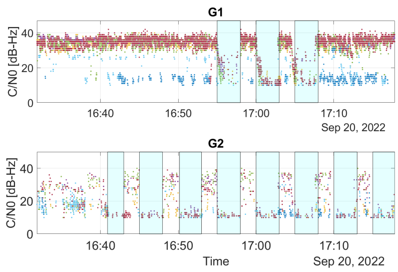


(e) GLONASS

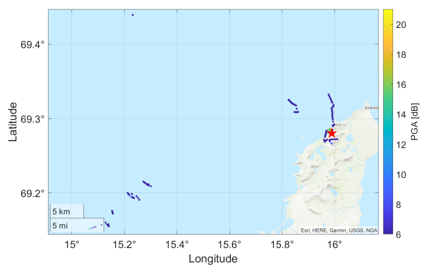


(f) UAV position (overview)

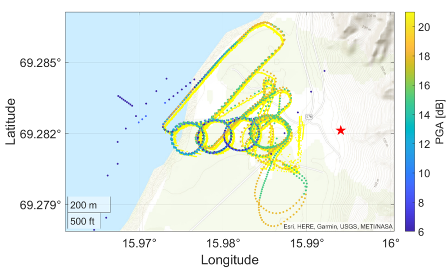


(g) UAV position (zoomed).
The yellow dots below are the PARS position to indicate the true UAV position without the jamming effect.

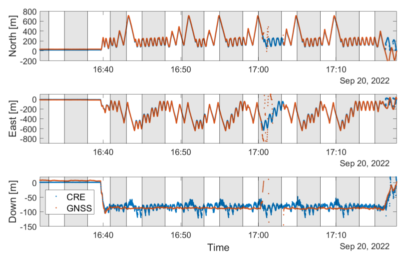


(h) UAV position (NED) from GNSS (red line) with the PARS position as reference (blue line).

Figure 8.4: "Pyramid" test.

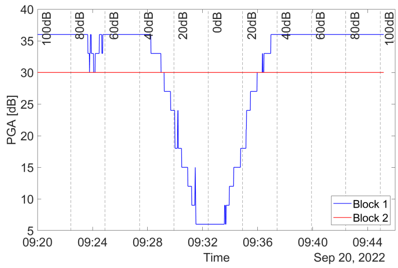


(a) PGA gain

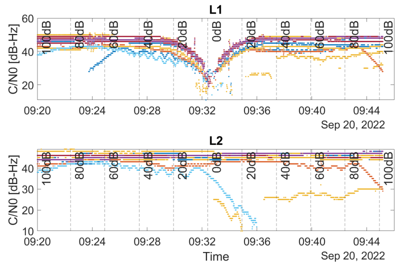


(b) GPS

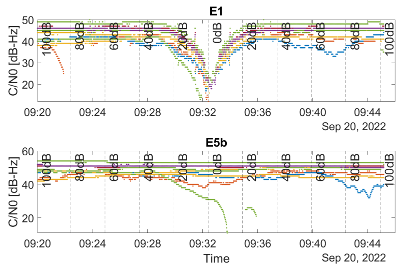


(c) Galileo

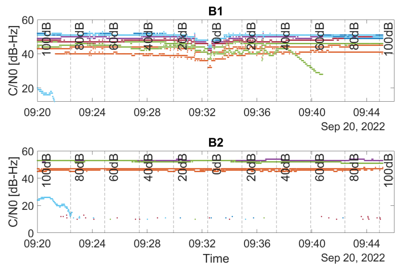


(d) BeiDou

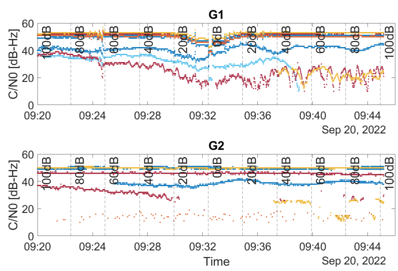


(e) GLONASS

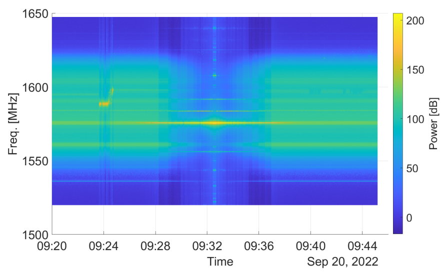


(f) Spectrum (block 1)

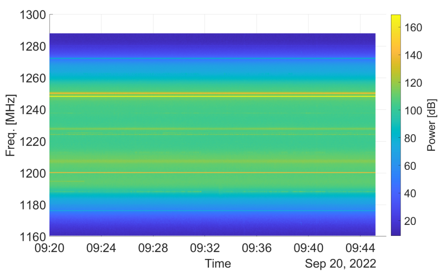


(g) Spectrum (block 2)

Figure 8.5: "Ramp 1" test

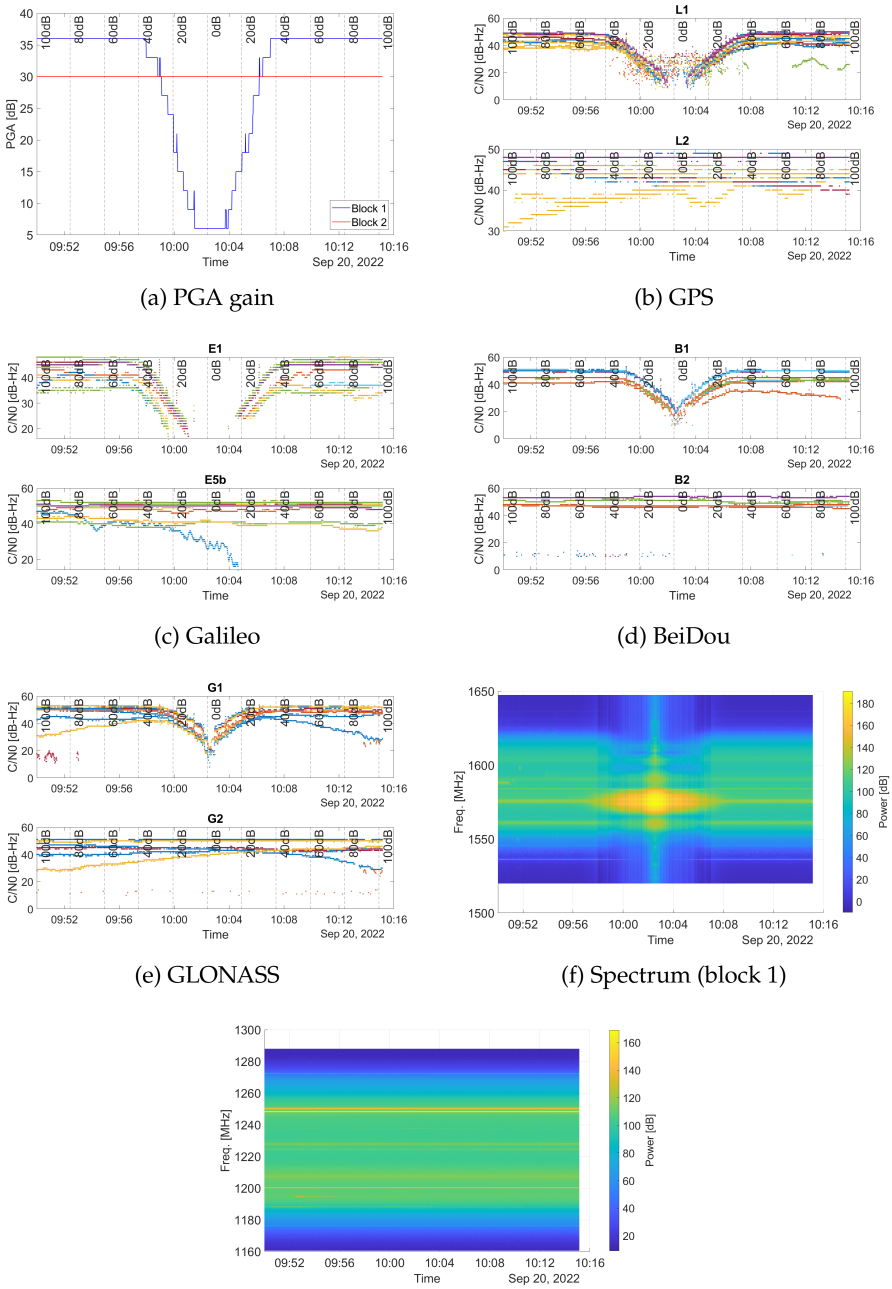


(a) PGA gain

(b) GPS

(c) Galileo

(d) BeiDou

(e) GLONASS

(f) Spectrum (block 1)

(g) Spectrum (block 2)

Figure 8.6: "Ramp 2" test

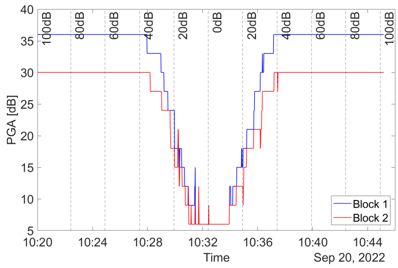


(a) PGA gain

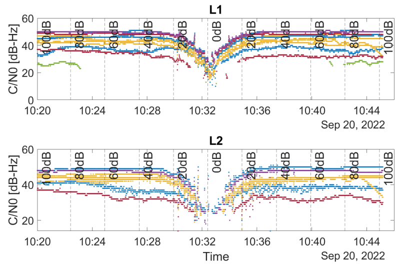


(b) GPS

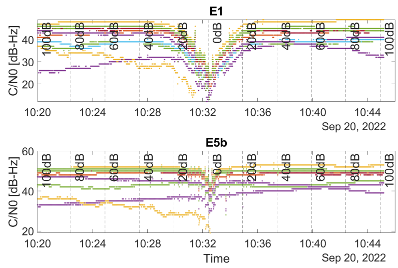


(c) Galileo

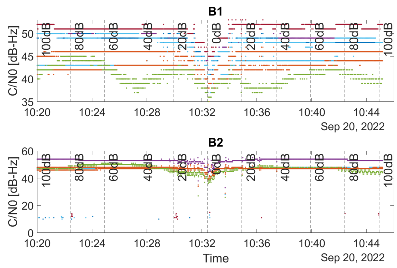


(d) BeiDou

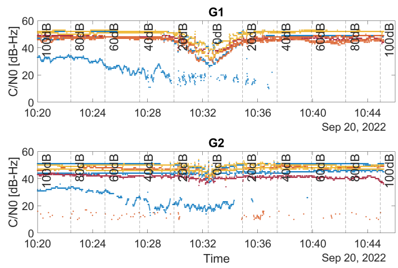


(e) GLONASS

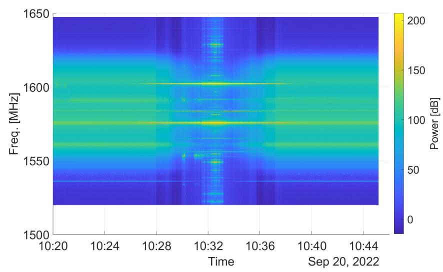


(f) Spectrum (block 1)

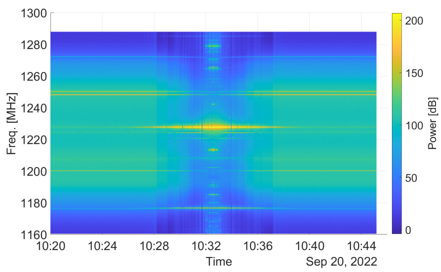


(g) Spectrum (block 2)

Figure 8.7: "Ramp 3" test

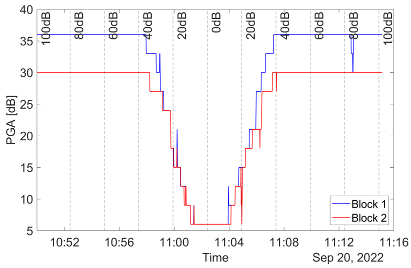


(a) PGA gain

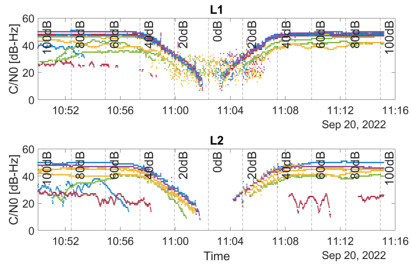


(b) GPS

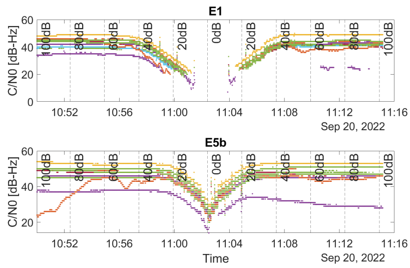


(c) Galileo

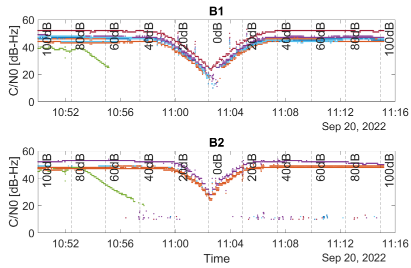


(d) BeiDou

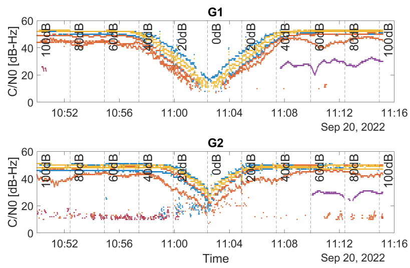


(e) GLONASS

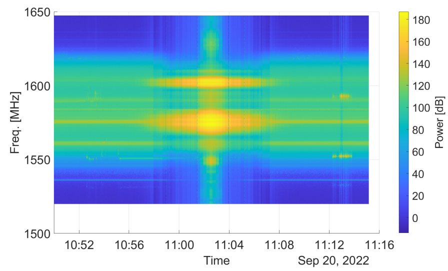


(f) Spectrum (block 1)

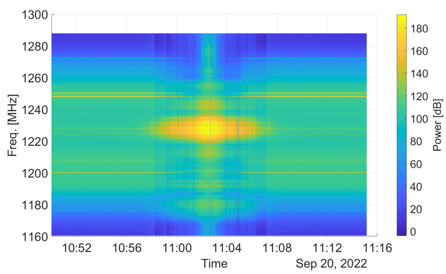


(g) Spectrum (block 2)

Figure 8.8: "Ramp 4" test

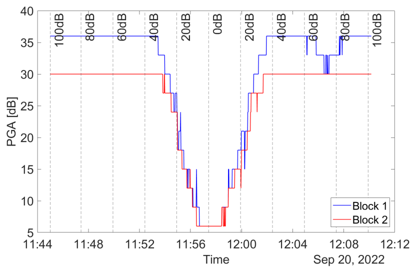


(a) PGA gain

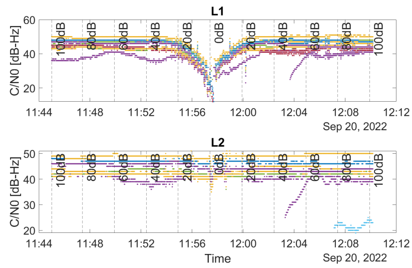


(b) GPS

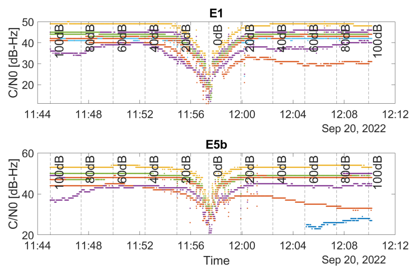


(c) Galileo

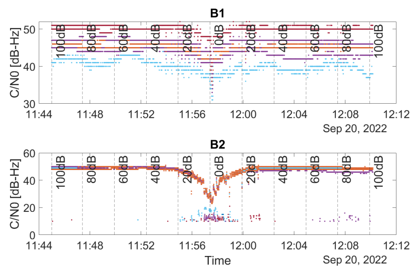


(d) BeiDou

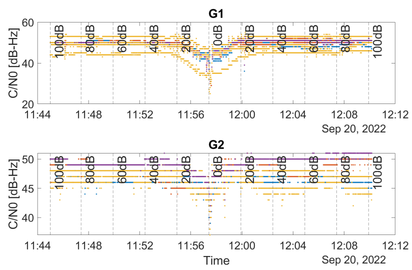


(e) GLONASS

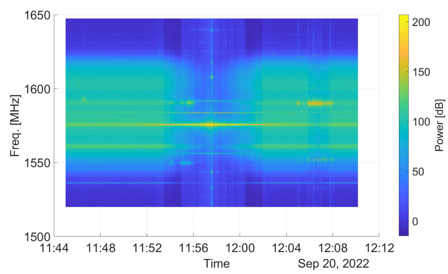


(f) Spectrum (block 1)

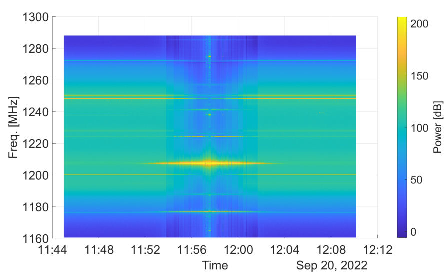


(g) Spectrum (block 2)

Figure 8.9: "Ramp 5" test

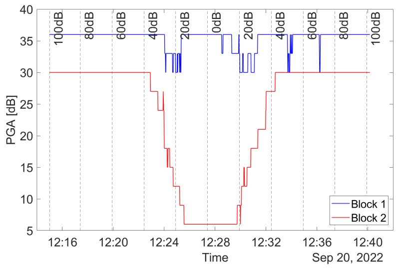


(a) PGA gain

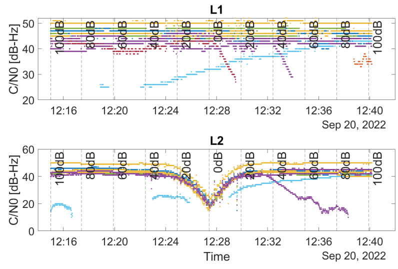


(b) GPS

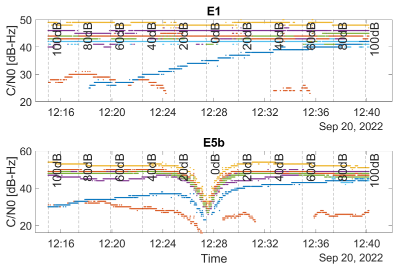


(c) Galileo

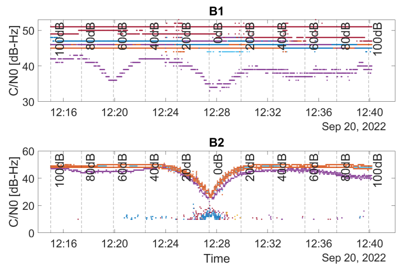


(d) BeiDou

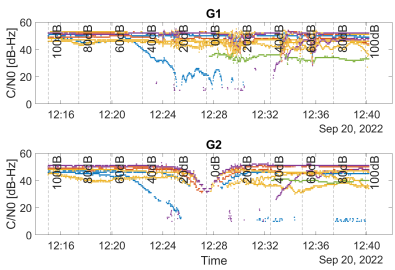


(e) GLONASS

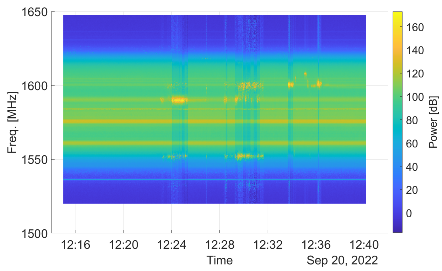


(f) Spectrum (block 1)

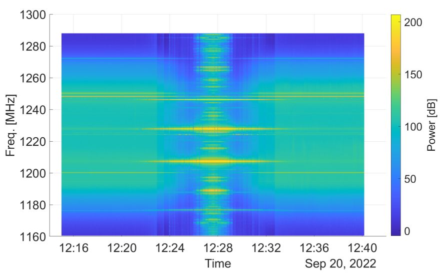


(g) Spectrum (block 2)

Figure 8.10: "Ramp 6" test

## 8.3 Jamming Detection

Based on the findings in Sec. 8.2, we propose a jamming detection methodology in this section. Essentially, our jamming detection algorithm estimates the mean and variance of C/N0 measurements using a KF and applies hypothesis testing by comparing a test static and a threshold computed from the estimated state and variance.

The first subsection (8.3.1) presents the system and measurement models fed into the KF detailed in the Appendix E.1, and the second subsection (8.3.2) explains how the hypothesis testing was applied for the jamming detection. The detection algorithm was tested using the "Pyramid" jamming data, and the last two subsections 8.3.3 and 8.3.4 present and discuss the results.

### 8.3.1 Estimate the mean and variance of C/N0

#### System Model

The dynamics of C/N0 under jamming conditions is modelled using the Gauss-Markov process in our KF formulation. This choice is motivated by the Gauss-Markov model's ability to represent the time-correlated nature of C/N0 variations [85], particularly in environments affected by jamming. The model captures the slow-varying characteristics of C/N0, which is effective for predicting its future states amidst jamming interference.

The parameters of the Gauss-Markov model were carefully selected based on empirical data. The tuning of these parameters was guided by an extensive analysis of experimental data collected during jamming scenarios, ensuring that the model accurately reflects the real-world behaviour of C/N0 dynamics:

$$\underbrace{\begin{bmatrix} \dot{x_1} \\ \dot{x_2} \end{bmatrix}}_{\dot{\boldsymbol{x}}} = \underbrace{\begin{bmatrix} -\frac{1}{T_{\text{nom}}} & 0 \\ 0 & -\frac{1}{T_{\text{dr}}} \end{bmatrix}}_{\boldsymbol{F}} \underbrace{\begin{bmatrix} x_1 \\ x_2 \end{bmatrix}}_{\boldsymbol{x}} + \underbrace{\begin{bmatrix} 1 & 0 \\ 0 & 1 \end{bmatrix}}_{\boldsymbol{G}} \underbrace{\begin{bmatrix} w_{\text{nom}} \\ w_{\text{dr}} \end{bmatrix}}_{\boldsymbol{w}} \tag{8.1}$$

Here, $\boldsymbol{x}$ represents the state vector of the model, comprising the normal power level ($x_1$) and the drift ($x_2$): The normal power level ($x_1$) captures the average of C/N0 under normal conduction without interference, while the the drift ($x_2$) captures the fluctuation in C/N0 due to interference.

$$\boldsymbol{x} = \begin{bmatrix} x_1 \\ x_2 \end{bmatrix} = \begin{bmatrix} \text{Normal power level} \\ \text{Drift} \end{bmatrix}$$

The state transition matrix $\boldsymbol{F}$ represents the dynamics of the system, where $T_{\text{nom}}$ and $T_{\text{dr}}$ are the time constants for the nominal and drift states, respectively. The entries of $\boldsymbol{F}$ are the negative inverses of these time constants, indicating exponential decay in each state variable. This reflects how each state variable evolves overtime, gradually losing its influence unless acted upon by external forces or inputs.

The matrix $\boldsymbol{G}$ is used to scale the process noise vector $\boldsymbol{w}$, allowing the noise to affect each state variable differently.

The vector $\boldsymbol{w}$ represents the process noise in the system, with $w_{\text{nom}}$ and $w_{\text{dr}}$ being the noise components for the nominal and drift states, respectively. These noise components are modelled as zero-mean Gaussian random variables with variances $\sigma^2_{\text{nom}}$ and $\sigma^2_{\text{dr}}$, indicating the uncertainty in the system dynamics:

$$w_{\text{nom}} \sim \mathcal{N}(0, \sigma^2_{\text{nom}}) \tag{8.2}$$

$$w_{\text{dr}} \sim \mathcal{N}(0, \sigma^2_{\text{dr}}) \tag{8.3}$$

The equations above can also be expressed as a Gaussian random variable with zero mean and covariance matrix $\boldsymbol{Q}$:

$$\boldsymbol{w} \sim \mathcal{N}(0, \boldsymbol{Q}) \tag{8.4}$$

The matrix $\boldsymbol{Q}$ (i.e. process noise matrix) is typically constructed as a diagonal matrix with the variances of the noise components as its diagonal elements:

$$\boldsymbol{Q} = \begin{bmatrix} \sigma^2_{\text{nom}} & 0 \\ 0 & \sigma^2_{\text{dr}} \end{bmatrix} \tag{8.5}$$

**Measurement Model**

The following equation defines the measurement model, where $y$ is the observed measurement. It is a linear combination of the state variables plus measurement noise $\varepsilon$. The matrix $\boldsymbol{H}$ indicates how each state variable contributes to the measurement.

$$y = \underbrace{\begin{bmatrix} 1 & 1 \end{bmatrix}}_{\boldsymbol{H}} \underbrace{\begin{bmatrix} x_1 \\ x_2 \end{bmatrix}}_{\boldsymbol{x}} + \varepsilon \tag{8.6}$$

$$= \underbrace{x_1 + x_2}_{\hat{y}} + \varepsilon \tag{8.7}$$

The measurement noise $\varepsilon$ is also assumed to be a Gaussian random variable with zero mean and covariance matrix $\mathcal{R}$:

$$\varepsilon \sim \mathcal{N}(0, \mathcal{R})$$

The matrix $\mathcal{R}$ (i.e. measurement noise matrix) represents the uncertainty in the measurements and is given by:

$$\mathcal{R} = \begin{bmatrix} \sigma^2_{\text{mea}} \end{bmatrix}$$

**Outlier rejection**

To maintain the integrity of the estimation, an outlier rejection process in Section 4.4 was incorporated.

### 8.3.2 Neyman-Pearson Hypothesis Testing

We treat the jamming detection as a *binary hypothesis* problem to choose among two competing hypotheses: the *null hypothesis* $\mathcal{H}_0$ (i.e. jamming inactive) and the *alternative hypothesis* $\mathcal{H}_1$ (i.e. jamming active)

$$\mathcal{H}_0 : x[n] = s[n] + w[n] \qquad n = 0, 1, ..., N-1 \tag{8.8}$$

$$\mathcal{H}_1 : x[n] = s[n] - d[n] + w[n] \qquad n = 0, 1, ..., N-1 \tag{8.9}$$

where $N$ is the number of samples, $s[n]$ is a signal under normal operation, $d[n]$ is disturbance due to jamming, and $w[n]$ is white Gaussian noise with variance $\sigma^2$ [1] :

$$s[n] = S = 0 \tag{8.10}$$

$$d[n] = -D < 0 \tag{8.11}$$

$$w[n] \sim \mathcal{N}(0, \sigma^2) \tag{8.12}$$

Thus, Eq. (8.8) and Eq. (8.9) can also be written as

$$\mathcal{H}_0 : \boldsymbol{x} \sim \mathcal{N}(\boldsymbol{0}, \sigma^2 \boldsymbol{I}) \tag{8.13}$$

$$\mathcal{H}_1 : \boldsymbol{x} \sim \mathcal{N}(-D\boldsymbol{1}, \sigma^2 \boldsymbol{I}). \tag{8.14}$$

where $\boldsymbol{I}$ is an identity matrix, and $\boldsymbol{1}$ is the vector of all ones.

Following [86], we apply the Neyman-Pearson (NP) theorem and decide $\mathcal{H}_1$, if

$$\underbrace{\frac{1}{N}\sum_{n=0}^{N-1} x[n]}_{T(x)} < \gamma' \tag{8.15}$$

where $T(x)$ is a test static, and $\gamma'$ is a threshold. The general explanation on the NP theorem is in Appendix E.3.

From the probability of a false alarm

$$P_{FA} = 1 - Q\left(\frac{\gamma'}{\sqrt{\sigma^2/N}}\right), \tag{8.16}$$

[1] The drift state $x_2$ in Eq. (8.1) corresponds to $x[n]$ in Eq. (8.8) and Eq. (8.9). As the drift state $x_2$ is supposed be 0 under normal condition (i.e. no jamming), $s[n] = 0$. The disturbance $d[n]$ is negative, as we expect C/N0 values drop if jamming is active.

we can find the threshold

$$\gamma' = \sqrt{\frac{\sigma^2}{N}} Q^{-1}(1 - P_{FA}), \tag{8.17}$$

where $Q$ denotes the *right-tail probability* or the *complementary cumulative distribution function (CDF)*, and $Q^{-1}$ is an inverse of $Q$. More details about the function $Q$ is in the Appendix E.4.

Detailed derivation for Eq. (8.15)-Eq. (8.17) is in Appendix E.5.

### 8.3.3 Results

The jamming detection algorithm described in the previous two sections (8.3.1) and (8.3.2) was implemented and tested using the data obtained from the "Pyramid" jamming test.

The numerical values for the matrices $\boldsymbol{F}$, $\boldsymbol{Q}$, and $\mathcal{R}$ are in Appendix E.2. The $\chi_\alpha = 3.841$ was chosen as the outlier rejection threshold. The probability of a false alarm was set $P_{FA} = 10^{-3}$. The number of samples was set $N = 10$. The threshold $\gamma'$ was computed from Eq. (8.17). $T(x)$ was computed from the drift state from the KF averaged over 10 iteration (as $N = 10$). The $\sigma$ used the variance of the drift state from the KF. The initial state of the KF used the following values:

$$\boldsymbol{x} = \begin{bmatrix} 30 \\ 0 \end{bmatrix}$$
$$\boldsymbol{P} = \begin{bmatrix} 5^2 & 0 \\ 0 & 5^2 \end{bmatrix}.$$

The jamming detection algorithm was applied to each band and the result is shown in Figure 8.11.

The nominal state stays at the mean of the C/N0 measurements even during the jamming-active period, and instead the drift state mainly captures the behaviour of jamming effect.

The detection flag shown by the red line switches between 0 and 1, indicating that jamming is not detected when the flag is 0 (i.e. $\mathcal{H}_0$ was chosen) and jamming is detected when the flag is 1 (i.e. $\mathcal{H}_1$ was chosen).

### 8.3.4 Discussion

The proposed algorithm detected jamming in two cases:

1. when the test static became less than the threshold (i.e. $T(x) < \gamma'$)
2. when no C/N0 measurements exist

The first case is clear and straightforward from the hypothesis testing described in section 8.3.2. The second case must also be considered, as the algorithm must be able to detect jamming even when the C/N0 measurements disappear completely, so that the drift state cannot capture the characteristic of the jamming behaviour.

In Figure 8.11a and Figure 8.11g, the test static decreases to less than the threshold when the C/N0 values drop significantly, and the jamming was detected successfully. Figure 8.11b - Figure 8.11f show that jamming is also detected successfully in the absence of C/N0 measurements. In Figure 8.11h, the detection flag is noisy because a large proportion of the C / N0 measurements of the G2 band are missing and the available measurements are sparsely distributed. A similar behaviour of the noisy flag can also be seen in Figures 8.11a–8.11c and Figure 8.11g.

[2] The plots have two axes: one for C/N0 (blue) and one for the detection flag (red). The blue dots are C/N0 measurements from the "Pyramid" jamming session. The nominal (black line) and drift (green line) states from KF are plotted on top of the C/N0 measurements. The threshold $\gamma'$ is shown by the blue line. Please note that only the detection flag shown by the red line uses the red axis on the right side, and the rest (C/N0 measurements, nominal and drift states from KF, threshold) uses the blue axis on the left side.

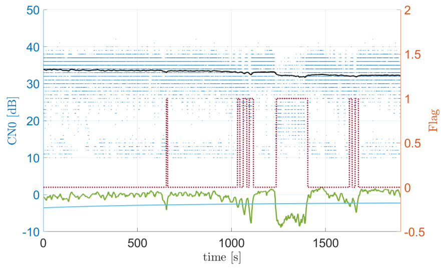


(a) GPS L1

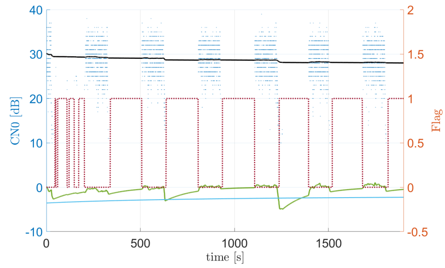


(b) GPS L2

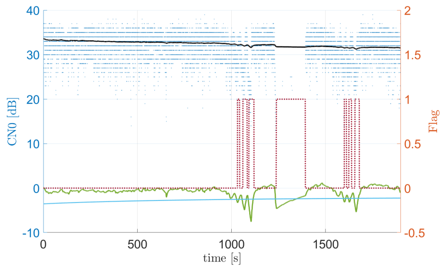


(c) Galileo E1

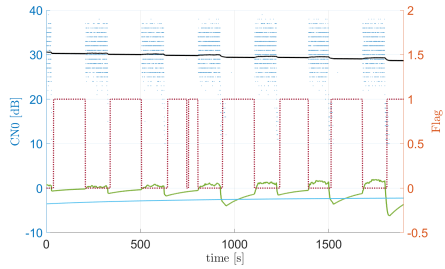


(d) Galileo E5b

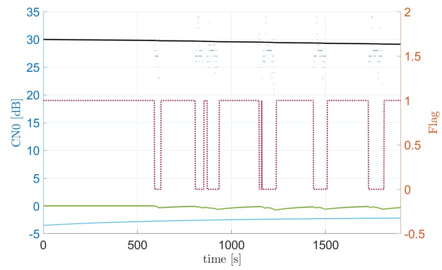


(e) BeiDou B1

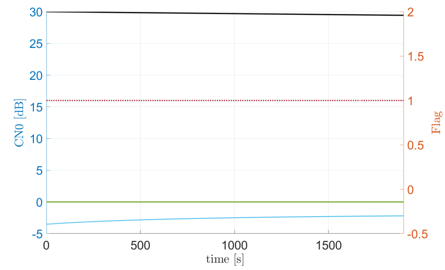


(f) BeiDou B2

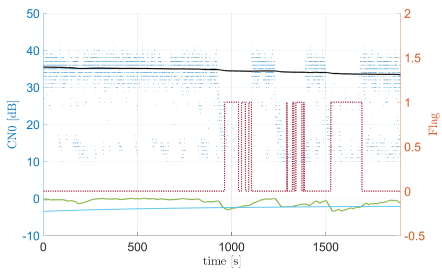


(g) GLONASS G1

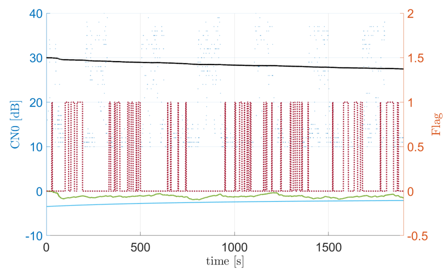


(h) GLONASS G2

Figure 8.11: Jamming detection [2]

## 8.4 Integration with aided-INS

The jamming detection algorithm formulated and tested in Section 8.3 was integrated with the previously developed MEKF-based INS aided by GNSS, PARS, and barometer (in Chapter 4). Before performing the offline calculation of the PARS-aided INS proposed in this paper, we ran the calibration presented in Chapter 6 to obtain a precise estimate of the PARS ground antenna orientation (i.e. $\hat{\boldsymbol{R}}_{nr}$) using the (jamming-free) RTK-GNSS measurements.

The detection algorithm identifies which GNSS bands are jammed and which are not, and sends flags for each band to indicate whether jamming is active or not. When the UAV operates under detected jamming, the aided-INS stops using a position estimated by jammed bands and switches to use a position estimated by only jamming-free bands. If all the bands are jammed, the aided-INS stops using GNSS a position, and switches to use a position from the PARS.

### 8.4.1 Overview

An overview of the aided-INS integrated with jamming detection is given in Fig. 8.12.

### 8.4.2 Results

We performed offline computation using the experimental data to test the aided-INS integrated with jamming detection using the "Pyramid" dataset. To enable aided-INS to avoid using position estimates affected by jammed bands, we prepared the following data sets in table 8.3 according to the "Pyramid" session using RTKLIB [87]. Each data set has a number that we call *Aid-Mode*. The datasets with aid modes 2-4 were produced by removing the corresponding bands from the original dataset containing all bands with aid mode 1. Their NED plots are in Figure 8.13.

| Aid-Mode | Aid measurement |
|---|---|
| 1 | GNSS all bands used |
| 2 | GNSS L1 L2 E1 B1 G1 G2 used |
| 3 | GNSS L1 E1 B1 G1 used |
| 4 | GNSS E1 used |
| 5 | PARS |

Table 8.3: Aid-Modes

[3] We employed a radio positioning aided INS where the aiding has three options. 1) using the GNSS position from the receiver if GNSS interference is not detected, 2) using GNSS positions calculated from raw GNSS observations from each respective GNSS band and 3) using aiding from PARS. The raw GNSS observations also include the C/N0 which is used as input to the jamming detection.

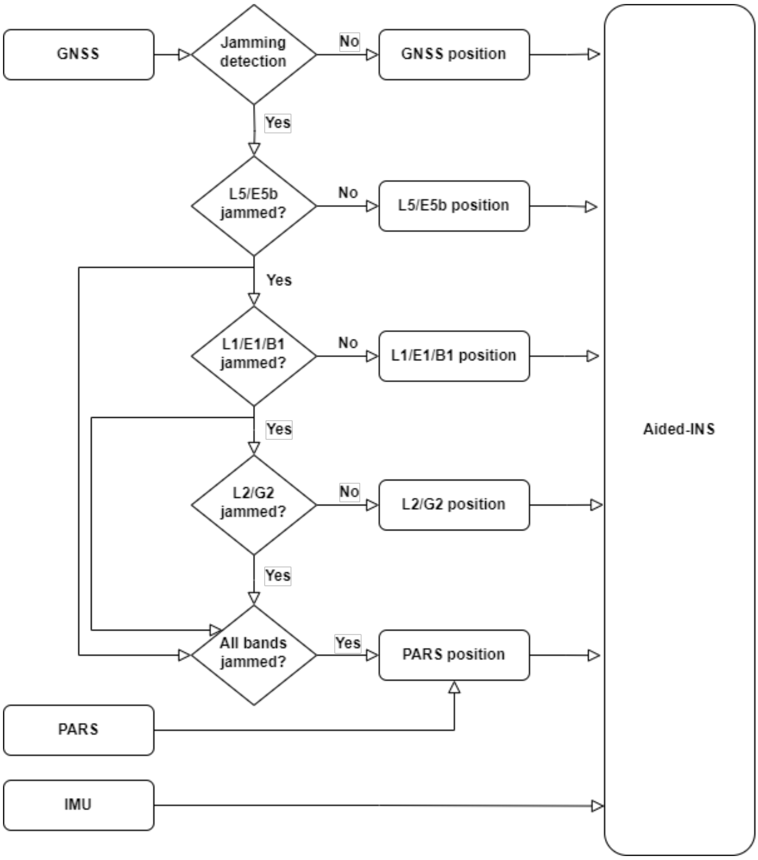


Figure 8.12: Overview of the aided INS integrated with jamming detection[3]

The quality of the GNSS data appeared to be poor even in nominal condition (i.e. no jamming). The jamming affected the timing record of the IMU, GNSS, and PARS measurements and some IMU measurements were missing. To be able to run the offline calculation of the aided-INS, we filled in the missing IMU measurements by interpolation, and manually aligned the timing of the multiple sensor measurements.

Figure 8.14 shows the flags for each mode, and Figure 8.15 shows the performance of the aided-INS using the GNSS measurements excluding jammed bands, or the PARS measurements. Aid mode plot was added to Figure 8.15a, Figure 8.15c and Figure 8.15d to indicate which dataset was used to aid the INS. In Figure 8.15a, the position estimate from the aided INS (red line) is plotted in the North, East, Down directions, with the PARS (blue line) and the barometer measurements (yellow line, in Down direction only) [4] as a reference. Similarly, in Figure 8.15b, the

[4]When PARS aided the INS, the barometer measurement from PixHawk autopilot aided the vertical

position estimate (red line) is compared with PARS (blue line). In Figure 8.15c and Figure 8.15d, the attitude and the velocity from the aided INS are compared to the heading reference (AHRS) and the velocity from the autopilot (Pixhawk).

Figure 8.16 plots the errors found by subtracting the estimates from the reference. The dotted lines are the $3\sigma$ lines to indicate the uncertainty boundary. Based on the error found in Figure 8.16, Table 8.4 shows the mean error (ME), absolute mean error (AME), standard deviation (STD), and root mean square error (RMSE) statistics of the aided-INS estimates.

| | **North** [m] | **East** [m] | **Down** [m] | **Norm** [m] |
|---|---|---|---|---|
| ME: | -2.49 | 4.21 | 1.26 | 5.05 |
| AME: | 5.06 | 7.42 | 8.32 | 12.24 |
| STD: | 6.49 | 9.92 | 10.51 | 15.84 |
| RMSE: | 6.95 | 10.77 | 10.59 | 16.63 |
| | **North** [m/s] | **East** [m/s] | **Down** [m/s] | **Norm** [m/s] |
| ME: | 0.05 | -0.04 | 0.06 | 0.08 |
| AME: | 0.66 | 0.95 | 0.27 | 1.19 |
| STD: | 0.88 | 1.21 | 0.35 | 1.54 |
| RMSE: | 0.88 | 1.21 | 0.35 | 1.54 |
| | **Roll** [°] | **Pitch** [°] | **Yaw** [°] | **Norm** [°] |
| ME: | -0.34 | -4.40 | 9.47 | 10.45 |
| AME: | 4.28 | 4.68 | 23.31 | 24.15 |
| STD: | 5.28 | 3.41 | 25.50 | 26.26 |
| RMSE: | 5.29 | 5.56 | 27.20 | 28.27 |

Table 8.4: Error statistics

### 8.4.3 Discussion

Although manual adjustment of sensor timing and compensation for missing data was required, the aided-INS produced estimates with reasonable accuracy using data sets affected by jamming. When most of the bands were jammed in the middle of the flight, the aided-INS switched to PARS and successfully avoided using the GNSS measurements containing significantly large error (which can be seen in Figure 8.4h around 17:00).

position of the INS as in [30]. Although the estimate from INS (redline) and the barometer measurement (yellow line) are plotted with the PARS measurement (blue line) in the Down plot of Figure 8.15a, the PARS measurement did not aid the vertical position of the INS.

As the timing errors of the multiple sensors were manually compensated, the misalignment of the sensor timing caused more error in the statistics than the previous results in [30], especially in the yaw angle. However, this may also be due to the jamming effect on the attitude estimate from the Pixhawk autopilot.

As mentioned in [30], the elevation angle of the PARS is subject to errors due to the radio-wave reflection from the ground surface, the barometer measurement aided the vertical position of the INS while PARS aided the horizontal position. Figure 8.15a clearly shows how the error in the PARS elevation appears in the Down direction. The PARS measurement in Down direction is wavy, but it looks like it is oscillating around the mean which follows the barometric measurement.

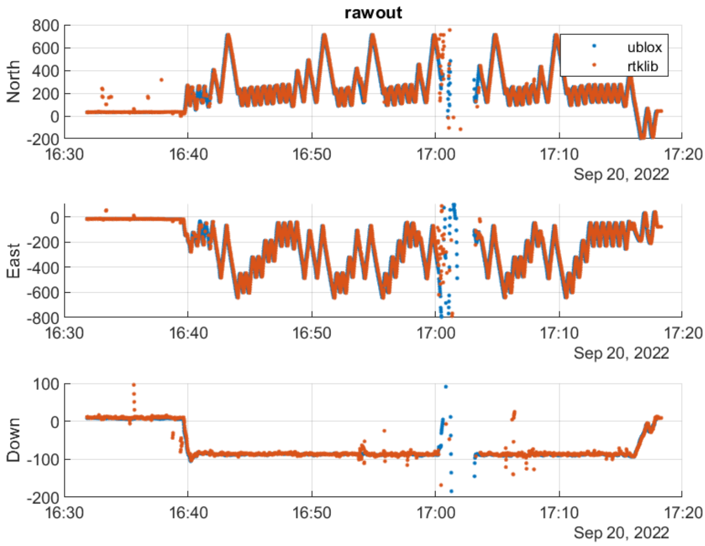


(a) Mode 1

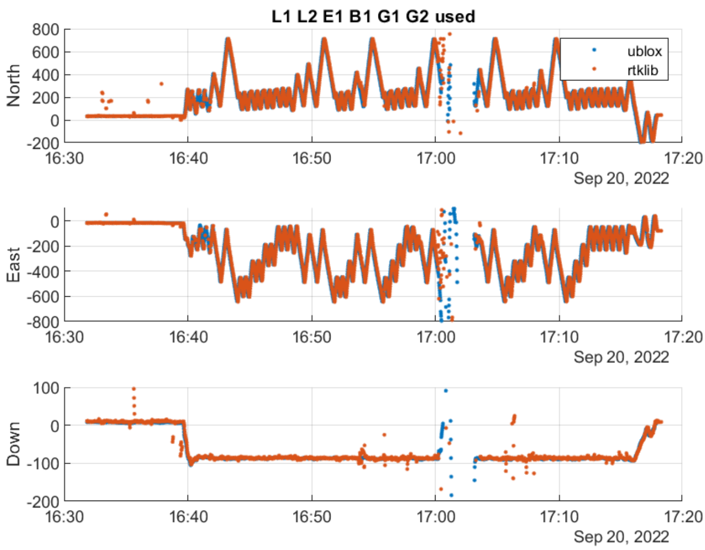


(b) Mode 2

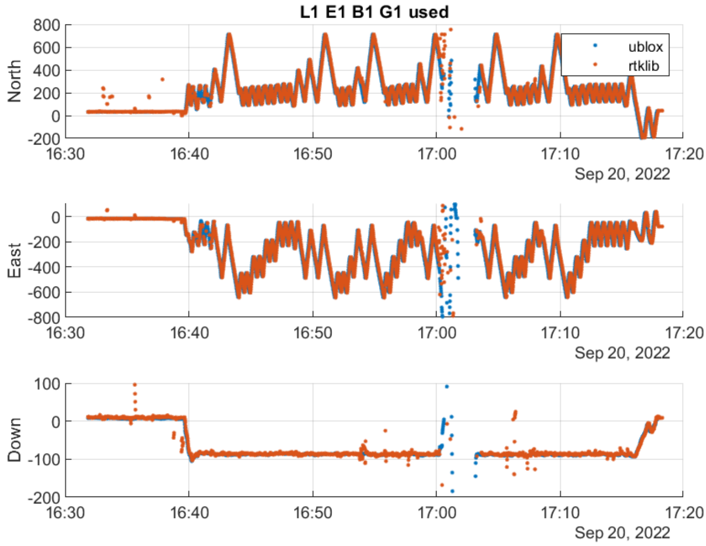


(c) Mode 3

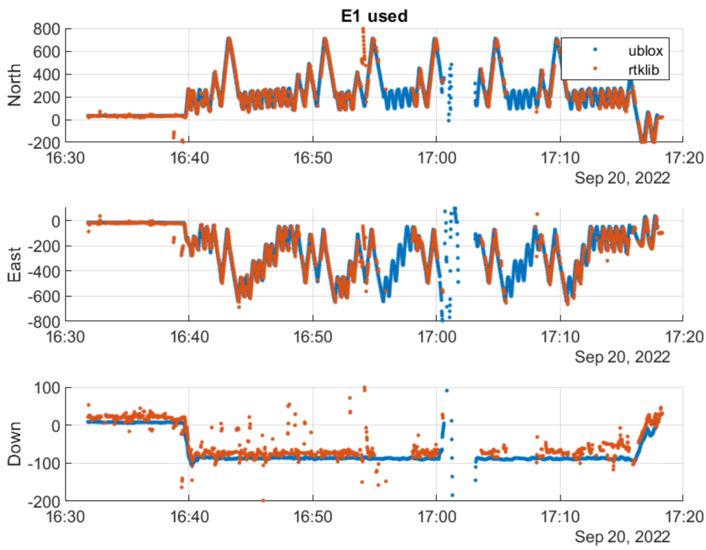


(d) Mode 4

Figure 8.13: Extracted GNSS position plot (NED) per mode

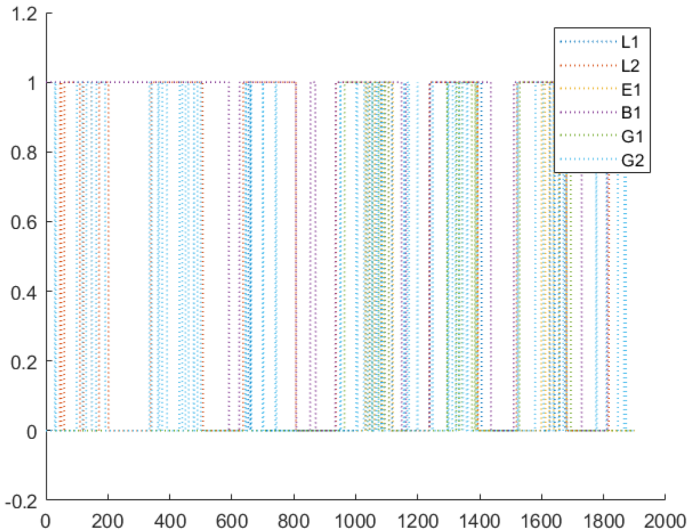


(a) Mode 2

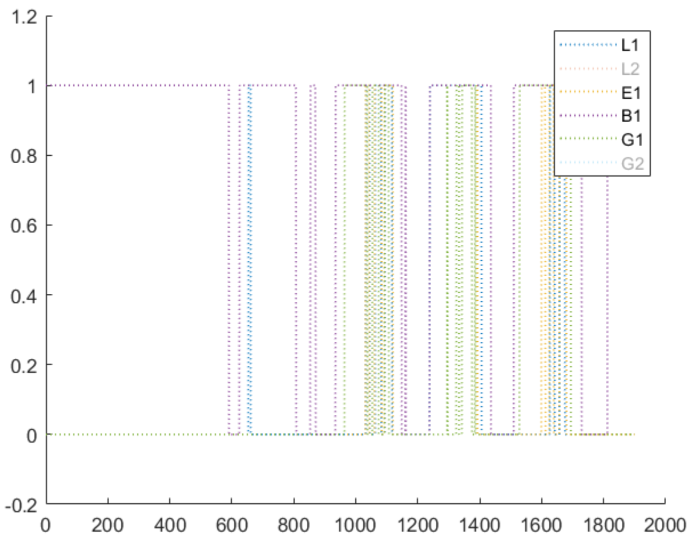


(b) Mode 3

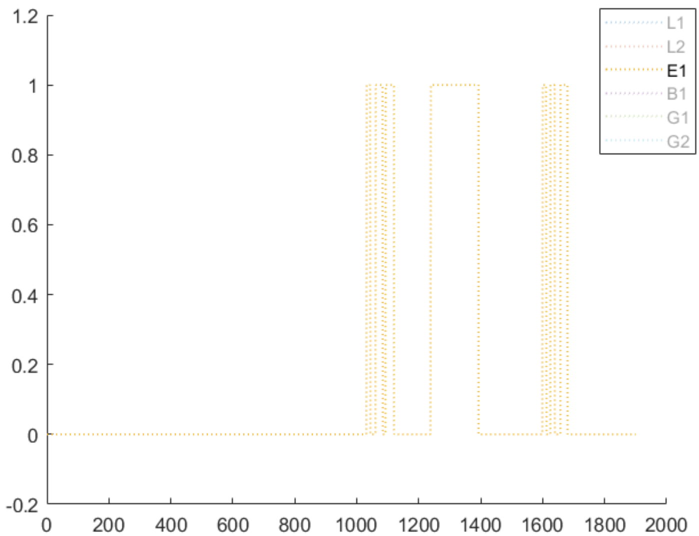


(c) Mode 4

Figure 8.14: Flags of the bands used in each mode

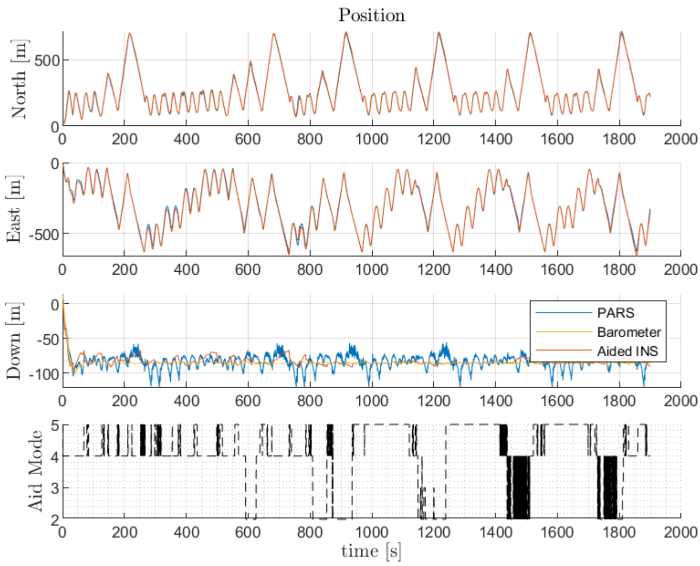


(a) Position - NED

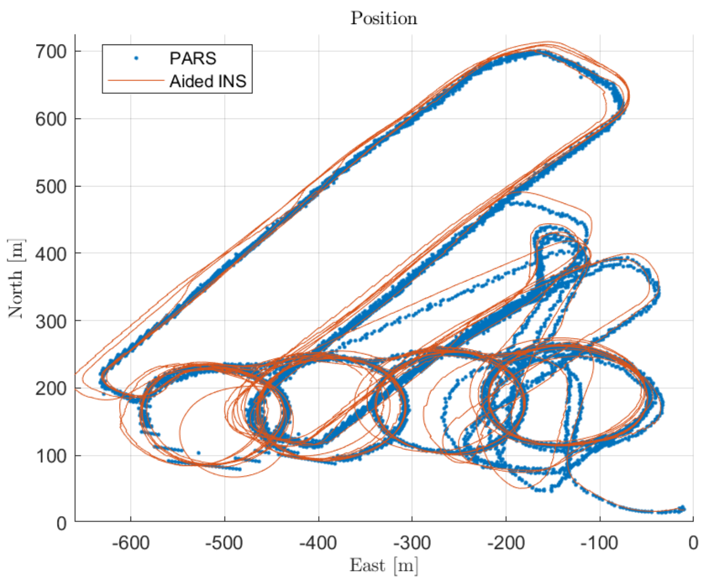


(b) Position - NE

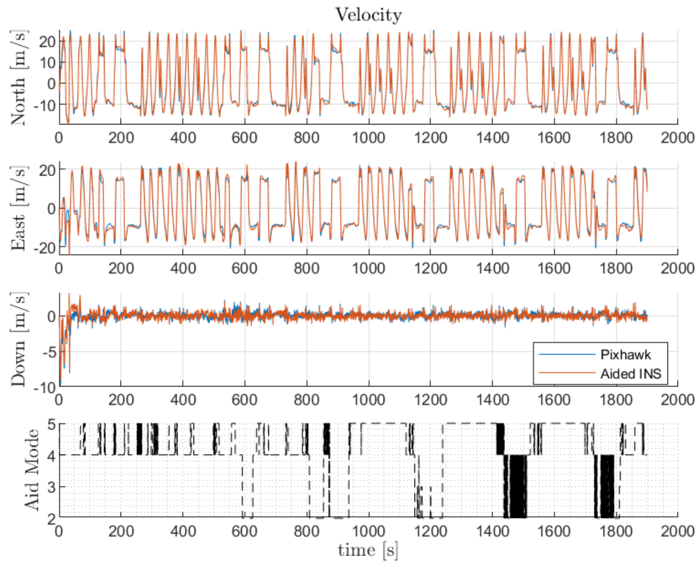


(c) Velocity

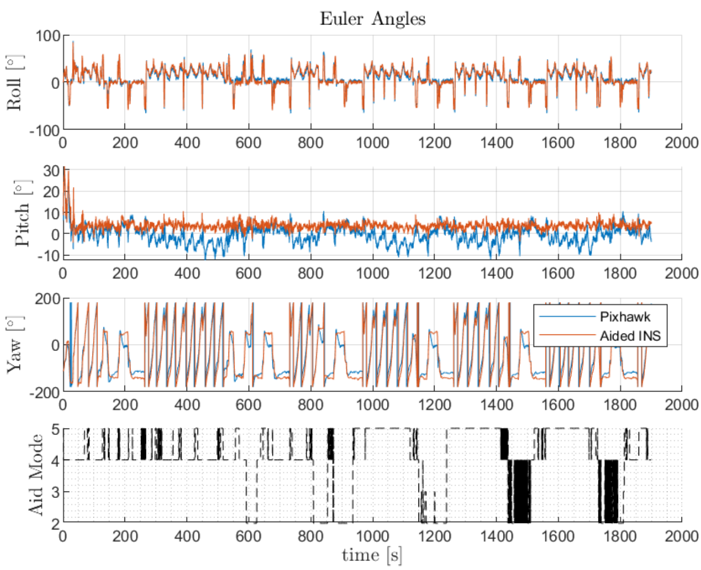


(d) Attitude

Figure 8.15: Aided INS

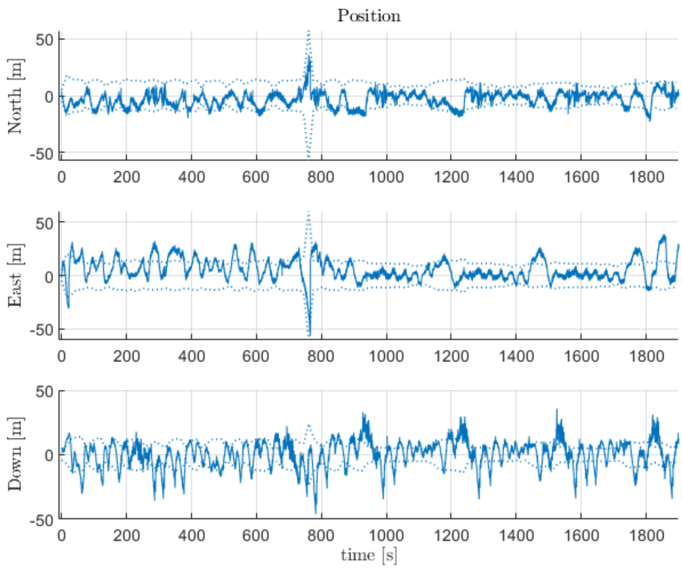


(a) Position error

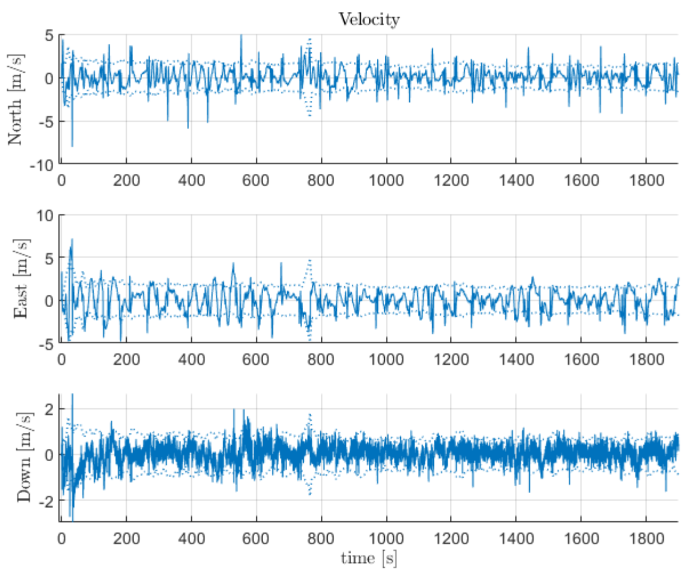


(b) Velocity error

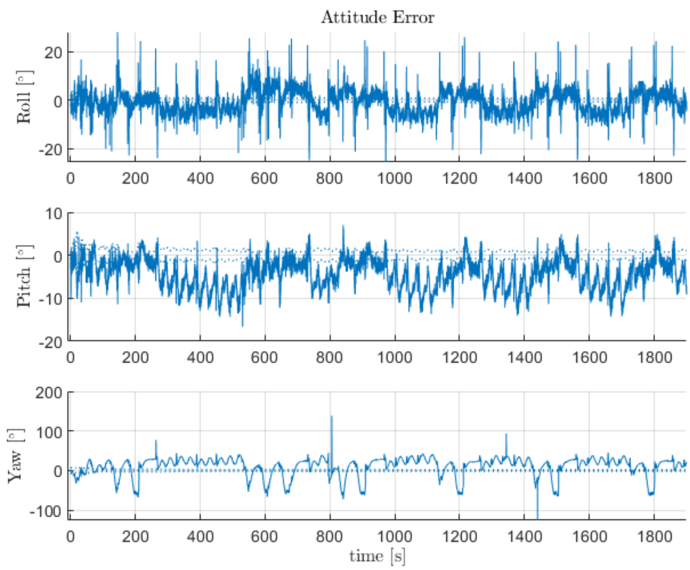


(c) attitude error

Figure 8.16: Aided INS Error

## 8.5 Conclusion

In this study, we collected global navigation satellite system (GNSS) data in various jamming scenarios using GNSS receivers on the ground and on an unmanned aerial vehicle (UAV) during jamming events in a controlled field experiment, and examined the influence of jamming on the GNSS data. The results indicated that the gains from the programmable gain amplifier (PGA) in automatic gain control (AGC) and carrier-to-noise ratio (C/N0) measurements are effective indicators of jamming. We then developed a KF algorithm for early detection of GNSS jamming and identification of jammed GNSS frequency bands, and tested it using the jamming-affected GNSS data. Finally, we extended the previous work on the phased array radio system (PARS)-aided inertial navigation system (INS), as an alternative positioning solution to GNSS-aided INS, by integrating the jamming detection algorithm with aided-INS to enable a safe handover either

1. from GNSS using all the available frequency bands to GNSS using only jamming-free frequency bands if only some of the frequency bands are jammed, or

2. from GNSS-based to PARS-based positioning if all the available frequency bands are affected by jamming.

The INS successfully switched between jamming-unaffected GNSS and PARS to avoid using critically degraded measurements for aiding. However, we found that the jamming also affected the timing of the GNSS measurements. The timing error affected the synchronisation between multiple sensors by introducing time lags and caused some missing sensor measurements. As a result, we needed to post-process the data in order to perform the off-line calculation of the aided INS. In the future, we would like to develop a real-time strategy to avoid or compensate for the effect of jamming on the synchronisation of the measurements to operate UAVs safely in a jammed environment.

# 9 Conclusion Remarks

This thesis has presented a study on enhancing the accuracy and reliability of UAV navigation through the application of the PARS and various filtering techniques. The core focus was on overcoming the limitations of GNSS in environments susceptible to interference or jamming, thereby providing a robust alternative or complementary navigation solution.

More specifically, this thesis addressed the three main critical challenges that PARS has, as presented in Chapter 1:

**C1** As PARS measures the UAV position relative to the local ground antenna frame, calibration of the PARS ground antenna's orientation becomes necessary each time it is relocated. Previous approaches, relying on manual measurements with a GNSS receiver and a compass, or manual alignment with GNSS positions, become increasingly inaccurate over longer distances from the ground radio, highlighting the need for an automated pose estimation method.

**C2** The issue of multipath interference arises when the PARS elevation angle measurements are distorted by noise resulting from radio signal reflections off water surfaces. This interference compromises the accuracy of positional determinations made through the DoA algorithm [22].

**C3** The transition from GNSS-aided to PARS-aided positioning in scenarios of GNSS RFI is critical, necessitating an early detection mechanism for a reliable system handover. The degradation in the PNT solution just before complete signal loss makes early jamming detection critical for operational safety.

and made key contributions to the challenges:

## Contributions

### For C1

- The implementation of a Multiplicative Extended Kalman Filter (MEKF)-based calibration algorithm marked a significant advancement in the estimation of the orientation of ground antennas for PARS. Field tests validated the algorithm's effectiveness, revealing consistent antenna orientation estimations across different flights and proving its robustness in calibrating antenna orientation. (⇒ **Section 6.1**)
- Further studies integrated the calibration algorithm with an aided-INS, demonstrating substantial improvements in position estimate accuracy. The

integration enabled in-flight calibration whenever reliable GNSS is available. (⇒ **Section 6.2**)

- Following that, the extended INS with in-flight calibration algorithm was implemented on UAVs' onboard embedded systems using DUNE unified navigation environment for real-time operation. (⇒ **Section 6.3**)

**For C2**

- We proposed non-linear update of barometer altitude as a solution to the multipath problem. This method was suggested to effectively incorporate the Earth's curvature into the measurement update of the MEKF. Although this method is effective when the UAV is far from the ground station, we found out that the method induces errors when the UAV is close to the ground station due to the estimation of alternative elevation angles. (⇒ **Section 7.1**)
- We employed the PDAF to distinguish true signals from noise . This method was suggested under the assumption that the true elevation exists in the clutter of the measurements. Although this method is effective if the true signal is not interfered by other reflected signals (which appear as clutter measurements), we found out that actually the true signal is interfered by other reflected signals and the noise in the elevation angle measurement exhibits a wavy shape. (⇒ **Section 7.2**)
- We proposed a recalculated elevation angle based on redundant altitude information in PARS-aided INS as a novel approach to mitigate the effects of multipath reflections on elevation angle measurements. The results proved that the recalculated elevation angle can successfully replace the elevation angle with noise mitigation. (⇒ **Section 7.3**)

**For C3**

- We examined the influence of jamming on the GNSS data collected in various jamming scenarios in a controlled field experiment. The results showed that the gains from the PGA in AGC and C/N0 measurements are effective indicators of jamming. (⇒ **Section 8.2**)
- We developed a Kalman-Filter based algorithm for early detection of GNSS jamming and identification of jammed GNSS frequency bands. The results showed that the jamming detection algorithm can detect jamming when it is active for each GNSS frequency band. (⇒ **Section 8.3**)
- We extended the previous work on PARS-aided INS, as an alternative positioning solution to GNSS-aided INS, by integrating the jamming detection algorithm with aided-INS to enable a safe handover either

1. from GNSS using all the available frequency bands to GNSS using only jamming-free frequency bands if only some of the frequency bands are jammed, or
2. from GNSS-based to PARS-based positioning if all the available GNSS frequency bands are affected by jamming.

The INS successfully switched between GNSS and PARS to avoid using critically degraded measurements for aiding under jamming conditions. However, we found that the jamming also affected the timing of the GNSS measurements. The timing error affected the synchronisation between multiple sensors by introducing time lags and caused some missing sensor measurements. As a result, we needed to post-process the data in order to perform the off-line calculation of the aided INS. (⇒ **Section 8.4**)

## Future Work

The findings from this thesis open several avenues for future research:

### For C1

- **Fully GNSS-free Navigation Systems:** The proposed calibration algorithm is promising, but cannot be used if reliable GNSS measurements are not available, for at least the initial part of a flight. It is worth exploring calibration using INS or additional PARS, rather than relying on GNSS, with the aim of achieving a fully GNSS-independent navigation system that ensures operational integrity in GNSS-denied environments.

- **Barometer Bias Estimation:** The barometer bias was manually compensated using a constant value in both offline calculations and real-time implementation, although the barometer bias varies gradually with time and altitude. Integration of barometer bias estimation into the PARS-aided INS framework further refines altitude measurements and improve overall navigation accuracy.

### For C2

- **Multipath Error Mitigation:** The detailed mechanism and effects of interference between the true signal and the reflected signals are unknown. Further research into multipath error and its mitigation, with a particular focus on scenarios where the reflected signals interfere with the original signal, may indicate the possibility of removing the noise from the elevation angle itself rather than calculating an alternative elevation angle.

- **Antenna Design Modifications:** In addition to approaching multipath mitigation from the algorithm/software side, another option is to investigate modifications to the ground antenna design to enhance its resilience to multipath interference and improve signal reception quality. Mitigating the interference between the true and reflected signals may only be achieved by changing the hardware design.

**For C3**

- **Real-time Jamming Adaptation:** The result exhibited that the jamming also affects the timing of the GNSS measurements. We propose to develop real-time strategies to compensate for the effects of jamming on synchronisation between multiple sensors, ensuring safe UAV operations under jammed conditions.

# Appendix A

## A.1 Direction of Arrival

PARS positioning is a method of navigation that uses the phase difference of radio signals from a network of fixed antennas to determine the position of a receiver. This technology uses the principle of phase interferometry, allowing for high-precision location tracking over large distances.

PARS operates by transmitting radio signals from multiple fixed antennas. The phase difference between these signals as received by a mobile unit is then measured. Since the phase difference varies with the position of the receiver, it can be used to calculate the receiver's precise location relative to the antennas. This is known as the DoA problem.

In this section, we consider the simplest linear antenna and consider only the azimuth angle $\psi$. Here, we have two sets of antennas:

1. transmitting antennas on the UAV, denoted by a subscript $t$
2. receiving antennas on the ground, denoted by a subscript $r$

At simplest, the architecture of PARS is foundational on a uniform linear array comprising $D$ antennas. The (transmitting) antennas are evenly spaced at $d_{\mathbf{t}}$. The direction of transmission, denoted $\psi_{\mathbf{t}}$, is modulated by a phase shift given to each antenna [88]. The essence of transmission involves a time delay $\delta_\tau$ that introduces a consistent phase shift across the antenna array. This principle is visualised in Fig. A.1, leading to the relation:

$$\sin(\psi_{\mathbf{t}}) = \frac{\delta_\tau c}{d_{\mathbf{t}}}, \tag{A.1}$$

where $c = f\lambda$ signifies the wave speed, formulated as the product of frequency $f$ and wavelength $\lambda$. The phase shift $\phi$, given by the time delay $\delta_\tau$, is calculable as

$$\phi = 2\pi f \delta_\tau \tag{A.2}$$

which represents the phase shift in radians resulting from the time delay.
Hence, the expression for $\psi_{\mathbf{t}}$ is refined to:

$$\psi_{\mathbf{t}} = \arcsin\left(\frac{\phi\lambda}{2\pi d_{\mathbf{t}}}\right). \tag{A.3}$$

Conversely, the challenge is to deduce the direction $\psi_{\mathbf{r}}$ of an incoming signal by observing the phase shift at different antennas within the array, which is the DoA problem [44, 45]. The DoA problem for estimating $\psi_r$ [89] can be solved by e.g. MUSIC [90], ESPRIT [91] and SAMV [92]

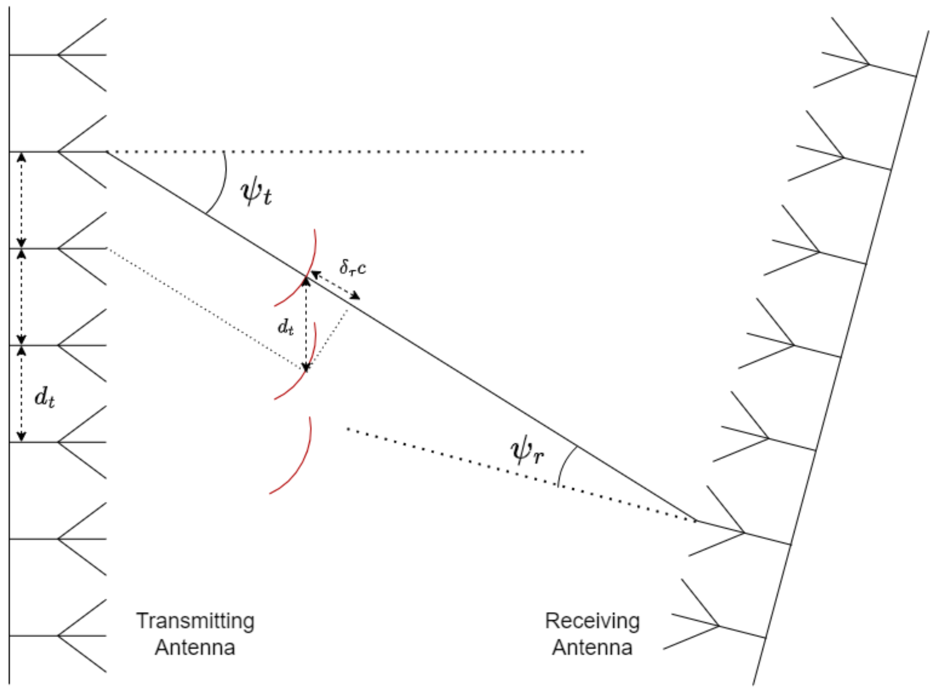


Figure A.1: Phased Array

# Appendix B

## B.1 MEKF error-state kinematics

The derivation of position error, ACC bias error, and ARS bias error kinematics in the error-states of MEKF is straightforward. Consequently, we will focus solely on demonstrating the derivation for the kinematics of velocity and attitude errors as presented below.

### B.1.1 Velocity error

$$\begin{aligned}\dot{\boldsymbol{v}}^e_{eb} &= -2\boldsymbol{S}(\boldsymbol{\omega}^e_{ie})\boldsymbol{v}^e_{eb} + \boldsymbol{R}_{eb}\boldsymbol{f}^b_{ib} + \boldsymbol{g}^e_b \\ &= -2\boldsymbol{S}(\boldsymbol{\omega}^e_{ie})(\hat{\boldsymbol{v}}^e_{eb} + \delta\boldsymbol{v}^e_{eb}) \\ &\quad + \hat{\boldsymbol{R}}_{eb}(\boldsymbol{I}_3 + \boldsymbol{S}(\delta\boldsymbol{a}))(\underbrace{\boldsymbol{f}^b_{\text{IMU}} - \hat{\boldsymbol{b}}^b_{acc}}_{\hat{\boldsymbol{f}}^b_{ib}} + \underbrace{-\delta\boldsymbol{b}^b_{acc} - \boldsymbol{\varepsilon}^b_{acc}}_{\delta\boldsymbol{f}}) + \boldsymbol{g}^e_b\end{aligned} \tag{B.1}$$

$$\begin{aligned}&= \underbrace{-2\boldsymbol{S}(\boldsymbol{\omega}^e_{ie})\hat{\boldsymbol{v}}^e_{eb} + \hat{\boldsymbol{R}}_{eb}\hat{\boldsymbol{f}}^b_{ib} + \boldsymbol{g}^e_b}_{\dot{\hat{\boldsymbol{v}}}^e_{eb}} \\ &\quad + \underbrace{-2\boldsymbol{S}(\boldsymbol{\omega}^e_{ie})\delta\boldsymbol{v}^e_{eb} + \hat{\boldsymbol{R}}_{eb}\boldsymbol{S}(\delta\boldsymbol{a})\hat{\boldsymbol{f}}^b_{ib} + \hat{\boldsymbol{R}}_{eb}(\boldsymbol{I}_3 + \boldsymbol{S}(\delta\boldsymbol{a}))\delta\boldsymbol{f}}_{\delta\dot{\boldsymbol{v}}^e_{eb}}\end{aligned} \tag{B.2}$$

where [1]

$$\boldsymbol{v}^e_{eb} = \hat{\boldsymbol{v}}^e_{eb} + \delta\boldsymbol{v}^e_{eb} \tag{B.3}$$

$$\boldsymbol{R}_{eb} \approx \hat{\boldsymbol{R}}_{eb}(\boldsymbol{I}_3 + \boldsymbol{S}(\delta\boldsymbol{a})) \tag{B.4}$$

$$\boldsymbol{f}^b_{\text{IMU}} = \boldsymbol{f}^b_{ib} + \hat{\boldsymbol{b}}^b_{acc} + \delta\boldsymbol{b}^b_{acc} + \boldsymbol{\varepsilon}^b_{acc}. \tag{B.5}$$

From Eq. (B.2) [2]

$$\dot{\hat{\boldsymbol{v}}}^e_{eb} = -2\boldsymbol{S}(\boldsymbol{\omega}^e_{ie})\hat{\boldsymbol{v}}^e_{eb} + \hat{\boldsymbol{R}}_{eb}\hat{\boldsymbol{f}}^b_{ib} + \boldsymbol{g}^e_b \tag{B.6}$$

and [3]

$$\delta\dot{\boldsymbol{v}}^e_{eb} = -2\boldsymbol{S}(\boldsymbol{\omega}^e_{ie})\delta\boldsymbol{v}^e_{eb} + \hat{\boldsymbol{R}}_{eb}\boldsymbol{S}(\delta\boldsymbol{a})\hat{\boldsymbol{f}}^b_{ib} + \hat{\boldsymbol{R}}_{eb}(\boldsymbol{I}_3 + \boldsymbol{S}(\delta\boldsymbol{a}))\delta\boldsymbol{f} \tag{B.7}$$

$$= -2\boldsymbol{S}(\boldsymbol{\omega}^e_{ie})\delta\boldsymbol{v}^e_{eb} - \hat{\boldsymbol{R}}_{eb}\boldsymbol{S}(\hat{\boldsymbol{f}}^b_{ib})\delta\boldsymbol{a} + \hat{\boldsymbol{R}}_{eb}\delta\boldsymbol{f} + \underbrace{\hat{\boldsymbol{R}}_{eb}\boldsymbol{S}(\delta\boldsymbol{a})\delta\boldsymbol{f}}_{\approx 0} \tag{B.8}$$

Assuming that the product of error-states is close to zero,

$$\delta\dot{\boldsymbol{v}}^e_{eb} \approx -2\boldsymbol{S}(\boldsymbol{\omega}^e_{ie})\delta\boldsymbol{v}^e_{eb} \underbrace{-\hat{\boldsymbol{R}}_{eb}\boldsymbol{S}(\boldsymbol{f}^b_{\text{IMU}} - \hat{\boldsymbol{b}}^b_{acc})}_{\boldsymbol{V}_a}\delta\boldsymbol{a} \underbrace{-\hat{\boldsymbol{R}}_{eb}}_{\boldsymbol{V}_{\text{acc}}}\delta\boldsymbol{b}^b_{acc} - \hat{\boldsymbol{R}}_{eb}\boldsymbol{\varepsilon}^b_{acc}. \tag{B.9}$$

[1] Eq. (B.5) is equivalent to Eq. (3.1).
[2] Eq. (B.6) is equivalent to Eq. (4.3b).
[3] Note that $\boldsymbol{S}(\boldsymbol{a})\boldsymbol{b} = -\boldsymbol{S}(\boldsymbol{b})\boldsymbol{a}$.

### B.1.2 Attitude error

Starting from a true quaternion,

$$\boldsymbol{q}_b^e = \hat{\boldsymbol{q}}_b^e \otimes \delta \boldsymbol{q}_b^e \tag{B.10}$$

$$\Rightarrow \delta \boldsymbol{q}_b^e = (\hat{\boldsymbol{q}}_b^e)^* \otimes \boldsymbol{q}_b^e. \tag{B.11}$$

Differentiating Eq. (B.11),

$$\delta \dot{\boldsymbol{q}}_b^e = \underbrace{(\dot{\hat{\boldsymbol{q}}}_b^e)^* \otimes \boldsymbol{q}_b^e}_{\text{I}} + \underbrace{(\hat{\boldsymbol{q}}_b^e)^* \otimes \dot{\boldsymbol{q}}_b^e}_{\text{II}}. \tag{B.12}$$

Then, we have [4]

$$\dot{\boldsymbol{q}}_b^e = \frac{1}{2}\boldsymbol{q}_b^e \otimes \begin{bmatrix} 0 \\ \hat{\boldsymbol{\omega}}_{eb}^b + \delta\boldsymbol{\omega}_{eb}^b \end{bmatrix} \tag{B.13}$$

$$\dot{\hat{\boldsymbol{q}}}_b^e = \frac{1}{2}\hat{\boldsymbol{q}}_b^e \otimes \begin{bmatrix} 0 \\ \hat{\boldsymbol{\omega}}_{eb}^b \end{bmatrix} \tag{B.14}$$

$$\Rightarrow (\dot{\hat{\boldsymbol{q}}}_b^e)^* = -\frac{1}{2}\begin{bmatrix} 0 \\ \hat{\boldsymbol{\omega}}_{eb}^b \end{bmatrix} \otimes (\hat{\boldsymbol{q}}_b^e)^* \tag{B.15}$$

Substituting Eq. (B.13) and Eq. (B.15) into Eq. (B.12) using Eq. (B.11) yields

$$\text{I} = (\dot{\hat{\boldsymbol{q}}}_b^e)^* \otimes \boldsymbol{q}_b^e \tag{B.16}$$

$$= -\frac{1}{2}\begin{bmatrix} 0 \\ \hat{\boldsymbol{\omega}}_{eb}^b \end{bmatrix} \otimes \underbrace{(\hat{\boldsymbol{q}}_b^e)^* \otimes \boldsymbol{q}_b^e}_{\delta \boldsymbol{q}_b^e} \tag{B.17}$$

$$\text{II} = (\hat{\boldsymbol{q}}_b^e)^* \otimes \dot{\boldsymbol{q}}_b^e \tag{B.18}$$

$$= \frac{1}{2}\underbrace{(\hat{\boldsymbol{q}}_b^e)^* \otimes \boldsymbol{q}_b^e}_{\delta \boldsymbol{q}_b^e} \otimes \begin{bmatrix} 0 \\ \hat{\boldsymbol{\omega}}_{eb}^b + \delta\boldsymbol{\omega}_{eb}^b \end{bmatrix} \tag{B.19}$$

$$\delta \dot{\boldsymbol{q}}_b^e = \text{I} + \text{II} \tag{B.20}$$

$$= -\frac{1}{2}\begin{bmatrix} 0 \\ \hat{\boldsymbol{\omega}}_{eb}^b \end{bmatrix} \otimes \delta \boldsymbol{q}_b^e + \frac{1}{2}\delta \boldsymbol{q}_b^e \otimes \begin{bmatrix} 0 \\ \hat{\boldsymbol{\omega}}_{eb}^b + \delta\boldsymbol{\omega}_{eb}^b \end{bmatrix} \tag{B.21}$$

$$= -\frac{1}{2}\begin{bmatrix} 0 & -(\hat{\boldsymbol{\omega}}_{eb}^b)^\intercal \\ \hat{\boldsymbol{\omega}}_{eb}^b & \boldsymbol{S}(\hat{\boldsymbol{\omega}}_{eb}^b) \end{bmatrix} \delta \boldsymbol{q}_b^e + \frac{1}{2}\begin{bmatrix} 0 & -(\hat{\boldsymbol{\omega}}_{eb}^b + \delta\boldsymbol{\omega}_{eb}^b)^\intercal \\ \hat{\boldsymbol{\omega}}_{eb}^b + \delta\boldsymbol{\omega}_{eb}^b & -\boldsymbol{S}(\hat{\boldsymbol{\omega}}_{eb}^b + \delta\boldsymbol{\omega}_{eb}^b) \end{bmatrix} \delta \boldsymbol{q}_b^e \tag{B.22}$$

$$= \frac{1}{2}\begin{bmatrix} 0 & -(\delta\boldsymbol{\omega}_{eb}^b)^\intercal \\ \delta\boldsymbol{\omega}_{eb}^b & -2\boldsymbol{S}(\hat{\boldsymbol{\omega}}_{eb}^b) - \boldsymbol{S}(\delta\boldsymbol{\omega}_{eb}^b) \end{bmatrix} \delta \boldsymbol{q}_b^e \tag{B.23}$$

$$= \frac{1}{2}\left(\boldsymbol{\Omega}(\delta\boldsymbol{\omega}_{eb}^b) + \bar{\boldsymbol{\Gamma}}(\hat{\boldsymbol{\omega}}_{eb}^b)\right) \delta \boldsymbol{q}_b^e \tag{B.24}$$

[4] Eq. (B.14) is equivalent to Eq. (4.3c)

where

$$\bar{\mathbf{\Gamma}}(\hat{\boldsymbol{\omega}}_{eb}^{b}) = \mathbf{\Omega}(\hat{\boldsymbol{\omega}}_{eb}^{b} + \delta\boldsymbol{\omega}_{eb}^{b}) - \mathbf{\Gamma}(\hat{\boldsymbol{\omega}}_{eb}^{b}) \tag{B.25}$$

$$= \begin{bmatrix} 0 & \mathbf{0}_{1\times 3} \\ \mathbf{0}_{3\times 1} & -2\boldsymbol{S}(\hat{\boldsymbol{\omega}}_{eb}^{b}) \end{bmatrix}. \tag{B.26}$$

We can write Eq. (B.24) as

$$\begin{bmatrix} \delta\dot{q}_s \\ \delta\dot{\boldsymbol{q}}_v \end{bmatrix} = \frac{1}{2}\begin{bmatrix} 0 & -(\delta\boldsymbol{\omega}_{eb}^{b})^{\top} \\ \delta\boldsymbol{\omega}_{eb}^{b} & -\boldsymbol{S}(\delta\boldsymbol{\omega}_{eb}^{b}) \end{bmatrix}\begin{bmatrix} \delta q_s \\ \delta\boldsymbol{q}_v \end{bmatrix} + \frac{1}{2}\begin{bmatrix} 0 & \mathbf{0}_{1\times 3} \\ \mathbf{0}_{3\times 1} & -2\boldsymbol{S}(\hat{\boldsymbol{\omega}}_{eb}^{b}) \end{bmatrix}\begin{bmatrix} \delta q_s \\ \delta\boldsymbol{q}_v \end{bmatrix} \tag{B.27}$$

and

$$\delta\dot{q}_s = -\frac{1}{2}(\delta\boldsymbol{\omega}_{eb}^{b})^{\top}\delta\boldsymbol{q}_v \tag{B.28}$$

$$\delta\dot{\boldsymbol{q}}_v = \frac{1}{2}\left(\delta q_s\delta\boldsymbol{\omega}_{eb}^{b} - \boldsymbol{S}(\delta\boldsymbol{\omega}_{eb}^{b})\delta\boldsymbol{q}_v - 2\boldsymbol{S}(\hat{\boldsymbol{\omega}}_{eb}^{b})\delta\boldsymbol{q}_v\right) \tag{B.29}$$

From Eq. (2.11), we have

$$\delta\boldsymbol{a}_{\text{mrp}} \equiv \left(\frac{\delta\boldsymbol{q}_v}{1+\delta q_s}\right) \equiv \frac{\delta\boldsymbol{a}}{4} \tag{B.30}$$

and differentiating Eq. (B.30) gives

$$\delta\dot{\boldsymbol{a}}_{\text{mrp}} = \frac{\delta\dot{\boldsymbol{q}}_v}{1+\delta q_s} - \frac{\delta\dot{q}_s\delta\boldsymbol{q}_v}{(1+\delta q_s)^2} \tag{B.31}$$

Then, substituting Eq. (B.28) and Eq. (B.29) into Eq. (B.31) yields [5]

$$\delta\dot{\boldsymbol{a}}_{\text{mrp}} = \frac{1}{4}\Big(-2\underbrace{\boldsymbol{S}(\delta\boldsymbol{\omega}_{eb}^{b})\delta\boldsymbol{a}_{\text{mrp}}}_{\approx 0} - 4\boldsymbol{S}(\hat{\boldsymbol{\omega}}_{eb}^{b})\delta\boldsymbol{a}_{\text{mrp}} + (1 - \underbrace{\delta\boldsymbol{a}_{\text{mrp}}\delta\boldsymbol{a}_{\text{mrp}}^{\top}}_{\approx 0})\delta\boldsymbol{\omega}_{eb}^{b}\Big) + \frac{1}{2}\underbrace{\left((\delta\boldsymbol{\omega}_{eb}^{b})^{\top}\delta\boldsymbol{a}_{\text{mrp}}\right)\delta\boldsymbol{a}_{\text{mrp}}}_{\approx 0}. \tag{B.32}$$

Then, assuming the products of error-states are close to zero, and as $\delta\boldsymbol{a} = 4\delta\boldsymbol{a}_{\text{mrp}}$,

$$\delta\dot{\boldsymbol{a}} = 4\delta\dot{\boldsymbol{a}}_{\text{mrp}} \tag{B.33}$$

$$= -4\boldsymbol{S}(\hat{\boldsymbol{\omega}}_{eb}^{b})\delta\boldsymbol{a}_{\text{mrp}} + \delta\boldsymbol{\omega}_{eb}^{b} \tag{B.34}$$

$$= \underbrace{-\boldsymbol{S}(\boldsymbol{\omega}_{\text{IMU}}^{b} - \hat{\boldsymbol{b}}_{\text{ars}}^{b} - \boldsymbol{R}_{eb}^{\top}\boldsymbol{\omega}_{ie}^{e})}_{\boldsymbol{A}_a}\delta\boldsymbol{a} - \delta\boldsymbol{b}_{\text{ars}}^{b} - \boldsymbol{\varepsilon}_{\text{ars}}^{b}. \tag{B.35}$$

[5] See [93] for details.

where [6]

$$\boldsymbol{\omega}^b_{\text{IMU}} = \boldsymbol{\omega}^b_{ib} + \hat{\boldsymbol{b}}^b_{\text{ars}} + \delta\boldsymbol{b}^b_{\text{ars}} + \varepsilon^b_{\text{ars}} \tag{B.36}$$

and

$$\begin{aligned}
\boldsymbol{\omega}^e_{eb} &= \boldsymbol{\omega}^b_{ib} - \boldsymbol{R}^\intercal_{eb}\boldsymbol{\omega}^e_{ie} && \text{(B.37)}\\
&= (\boldsymbol{\omega}^b_{\text{IMU}} - \hat{\boldsymbol{b}}^b_{\text{ars}} - \delta\boldsymbol{b}^b_{\text{ars}} - \varepsilon^b_{\text{ars}}) - \boldsymbol{R}^\intercal_{eb}\boldsymbol{\omega}^e_{ie} && \text{(B.38)}\\
&= \underbrace{(\boldsymbol{\omega}^b_{\text{IMU}} - \hat{\boldsymbol{b}}^b_{\text{ars}} - \boldsymbol{R}^\intercal_{eb}\boldsymbol{\omega}^e_{ie})}_{\hat{\boldsymbol{\omega}}^e_{eb}} \underbrace{-\delta\boldsymbol{b}^b_{\text{ars}} - \varepsilon^b_{\text{ars}}}_{\delta\boldsymbol{\omega}^e_{eb}}. && \text{(B.39)}
\end{aligned}$$

## B.2 Jacobean matrices (Original)

The Jacobean matrices of the error-state system equation are given as

$$\boldsymbol{F} = \begin{pmatrix} \mathbf{0}_{3\times3} & \boldsymbol{I}_3 & \mathbf{0}_{3\times3} & \mathbf{0}_{3\times3} & \mathbf{0}_{3\times3} \\ \mathbf{0}_{3\times3} & -2\boldsymbol{S}(\boldsymbol{\omega}^e_{ie}) & \boldsymbol{V}_a & \boldsymbol{V}_{acc} & \mathbf{0}_{3\times3} \\ \mathbf{0}_{3\times3} & \mathbf{0}_{3\times3} & \boldsymbol{A}_a & \mathbf{0}_{3\times3} & \boldsymbol{A}_{ars} \\ \mathbf{0}_{3\times3} & \mathbf{0}_{3\times3} & \mathbf{0}_{3\times3} & -\boldsymbol{T}^{-1}_{acc} & \mathbf{0}_{3\times3} \\ \mathbf{0}_{3\times3} & \mathbf{0}_{3\times3} & \mathbf{0}_{3\times3} & \mathbf{0}_{3\times3} & -\boldsymbol{T}^{-1}_{ars} \end{pmatrix} \in \mathbb{R}^{15\times15} \tag{B.40}$$

$$\boldsymbol{G} = \begin{pmatrix} \mathbf{0}_{3\times3} & \mathbf{0}_{3\times3} & \mathbf{0}_{3\times3} & \mathbf{0}_{3\times3} \\ -\boldsymbol{R}_{eb}(\boldsymbol{q}^e_b) & \mathbf{0}_{3\times3} & \mathbf{0}_{3\times3} & \mathbf{0}_{3\times3} \\ \mathbf{0}_{3\times3} & -\boldsymbol{I}_3 & \mathbf{0}_{3\times3} & \mathbf{0}_{3\times3} \\ \mathbf{0}_{3\times3} & \mathbf{0}_{3\times3} & \boldsymbol{I}_3 & \mathbf{0}_3 \\ \mathbf{0}_{3\times3} & \mathbf{0}_{3\times3} & \mathbf{0}_{3\times3} & \boldsymbol{I}_3 \end{pmatrix} \in \mathbb{R}^{15\times12} \tag{B.41}$$

where

$$\begin{aligned}
\boldsymbol{V}_a &= -\hat{\boldsymbol{R}}_{eb}(\boldsymbol{q}^e_b)\boldsymbol{S}(\boldsymbol{f}^b_{\text{IMU}} - \hat{\boldsymbol{b}}^b_{acc}) \\
\boldsymbol{V}_{\text{acc}} &= -\hat{\boldsymbol{R}}_{eb}(\boldsymbol{q}^e_b) \\
\boldsymbol{A}_a &= -\boldsymbol{S}\left(\boldsymbol{\omega}^b_{\text{IMU}} - \hat{\boldsymbol{b}}^b_{ars} - \hat{\boldsymbol{R}}^\intercal_{eb}\boldsymbol{\omega}^e_{ie}\right) \\
\boldsymbol{A}_{\text{ars}} &= -\boldsymbol{I}_3.
\end{aligned}$$

The process noise effecting the velocity, orientation and bias estimates error $\boldsymbol{w} = (\varepsilon^\intercal_{\text{acc}}, \varepsilon^\intercal_{\text{ars}}, \varepsilon^\intercal_{b_{\text{acc}}}, \varepsilon^\intercal_{b_{\text{ars}}})^\intercal$ are modeled by white Gaussian processes. The total spectral density is given as

$$\boldsymbol{Q} = \begin{pmatrix} \boldsymbol{V}_\epsilon & \mathbf{0}_{3\times3} & \mathbf{0}_{3\times3} & \mathbf{0}_{3\times3} \\ \mathbf{0}_{3\times3} & \boldsymbol{\Theta}_\epsilon & \mathbf{0}_{3\times3} & \mathbf{0}_{3\times3} \\ \mathbf{0}_{3\times3} & \mathbf{0}_{3\times3} & \boldsymbol{A}_\epsilon & \mathbf{0}_{3\times3} \\ \mathbf{0}_{3\times3} & \mathbf{0}_{3\times3} & \mathbf{0}_{3\times3} & \boldsymbol{\Omega}_\epsilon \end{pmatrix} \in \mathbb{R}^{12\times12} \tag{B.42}$$

[6] Eq. (B.36) is equivalent to Eq. (3.2).

where

$$\boldsymbol{V}_\epsilon = \sigma^2_{\text{acc}} \boldsymbol{I}_3 \quad [\text{m}^2\,\text{s}^{-3}] \tag{B.43}$$
$$\boldsymbol{\Theta}_\epsilon = \sigma^2_{\text{ars}} \boldsymbol{I}_3 \quad [\text{rad}^2\,\text{s}^{-1}] \tag{B.44}$$
$$\boldsymbol{A}_\epsilon = \sigma^2_{b_{\text{acc}}} \boldsymbol{I}_3 \quad [\text{m}^2\,\text{s}^{-5}] \tag{B.45}$$
$$\boldsymbol{\Omega}_\epsilon = \sigma^2_{b_{\text{ars}}} \boldsymbol{I}_3 \quad [\text{rad}^2\,\text{s}^{-3}] \tag{B.46}$$

and the received spectral densities are calculated

$$\sigma^2_\star = \mathbb{E}[\varepsilon_\star(t)\varepsilon^\intercal_\star(\tau)]. \tag{B.47}$$

## B.3 Pre-calibration equation derivation

### B.3.1 Accelerometer

$$\boldsymbol{y}_{\text{acc}} = \boldsymbol{f}^b_{\text{IMU}} \tag{B.48}$$
$$\approx -\boldsymbol{R}^T_{eb}\boldsymbol{g}^e_b + \boldsymbol{b}^b_{\text{acc}} + \varepsilon^b_{\text{acc}} \tag{B.49}$$
$$= -(\hat{\boldsymbol{R}}_{eb}(\boldsymbol{I}_3 + \boldsymbol{S}(\boldsymbol{\delta a})))^T \boldsymbol{g}^e_b + \hat{\boldsymbol{b}}^b_{\text{acc}} + \boldsymbol{\delta b}^b_{\text{acc}} + \varepsilon^b_{\text{acc}} \tag{B.50}$$
$$= -\hat{\boldsymbol{R}}^T_{eb}\boldsymbol{g}^e_b + \boldsymbol{S}(\boldsymbol{\delta a})\hat{\boldsymbol{R}}^T_{eb}\boldsymbol{g}^e_b + \hat{\boldsymbol{b}}^b_{\text{acc}} + \boldsymbol{\delta b}^b_{\text{acc}} + \varepsilon^b_{\text{acc}} \tag{B.51}$$
$$= -\hat{\boldsymbol{R}}^T_{eb}\boldsymbol{g}^e_b + \boldsymbol{S}(-\hat{\boldsymbol{R}}^T_{eb}\boldsymbol{g}^e_b)\boldsymbol{\delta a} + \hat{\boldsymbol{b}}^b_{\text{acc}} + \boldsymbol{\delta b}^b_{\text{acc}} + \varepsilon^b_{\text{acc}} \tag{B.52}$$
$$\Rightarrow \hat{\boldsymbol{y}}_{\text{acc}} = -\hat{\boldsymbol{R}}^T_{eb}\boldsymbol{g}^e_b + \hat{\boldsymbol{b}}^b_{\text{acc}} \tag{B.53}$$
$$\Rightarrow \boldsymbol{H}_{\text{acc}} = \begin{bmatrix} \boldsymbol{0}_{3\times3} & \boldsymbol{0}_{3\times3} & -\boldsymbol{S}(\hat{\boldsymbol{R}}^\intercal_{eb}\boldsymbol{g}^e_b) & \boldsymbol{I}_3 & \boldsymbol{0}_{3\times3} \end{bmatrix} \tag{B.54}$$

### B.3.2 Angular rate sensor

$$\boldsymbol{y}_{\text{ars}} = \boldsymbol{\omega}^b_{\text{IMU}} \tag{B.55}$$
$$\approx \boldsymbol{R}^\intercal_{eb}\boldsymbol{\omega}^e_{ie} + \boldsymbol{b}^b_{ars} + \varepsilon^b_{ars} \tag{B.56}$$
$$= \boldsymbol{R}^\intercal_{eb}\boldsymbol{\omega}^e_{ie} + \hat{\boldsymbol{b}}^b_{\text{ars}} + \boldsymbol{\delta b}^b_{\text{ars}} + \varepsilon^b_{ars} \tag{B.57}$$
$$\Rightarrow \hat{\boldsymbol{y}}_{\text{ars}} = \hat{\boldsymbol{b}}^b_{\text{ars}} \tag{B.58}$$
$$\Rightarrow \boldsymbol{H}_{\text{ars}} = \begin{bmatrix} \boldsymbol{0}_{3\times3} & \boldsymbol{0}_{3\times3} & \boldsymbol{0}_{3\times3} & \boldsymbol{0}_{3\times3} & \boldsymbol{I}_3 \end{bmatrix} \tag{B.59}$$

## B.4 Discretization of $F$ and $Q$

As in [85, Section 3.9], the discrete versions of $\boldsymbol{F}$ and $\boldsymbol{Q}$ ( i.e. $\boldsymbol{F}_d$ and $\boldsymbol{Q}_d$ ) were determined using the Van Loan method [49]. As we only have measurements at discrete times $t_k, t_{k+1}, t_{k+2}$... (i.e. $y$ in the measurement model described by (8.6)), we will be primarily interested in the solution of the system model described by (8.1) at the corresponding times (i.e. the system model is continuous-time random process).

Analytical methods for determining $\boldsymbol{F}_d$ and $\boldsymbol{Q}_d$ work well for systems with only a few elements in the state vector. Nonetheless, the state vector's dimensionality can become so extensive that deriving explicit expressions for $\boldsymbol{F}_d$ and $\boldsymbol{Q}_d$ is unfeasible. A numerical method for these large-scale systems, developed by C. F. van Loan [7], is particularly well-suited for implementation in MATLAB. Following the continuous-time model specified by (8.1), the van Loan method is as follows:

1. Begin with the formation of a $2n \times 2n$ matrix, designated as $\boldsymbol{A}$ ($n$ is the dimension of $\boldsymbol{x}$ and $\Delta t$ is the $(t_k, t_{k+1})$ interval).

$$\boldsymbol{A} = \begin{bmatrix} -\boldsymbol{F} & \boldsymbol{G}\boldsymbol{Q}\boldsymbol{G}^\top \\ \boldsymbol{0} & \boldsymbol{F}^\top \end{bmatrix} \Delta t$$

2. Using MATLAB (or another software), calculate $e^{\boldsymbol{A}}$ and denote it as $\boldsymbol{B}$.

$$\boldsymbol{B} = \text{expm}(\boldsymbol{A}) = \begin{bmatrix} \dots & \boldsymbol{F}_d^{-1}\boldsymbol{Q}_d \\ \boldsymbol{0} & \boldsymbol{F}_d^\top \end{bmatrix}$$

   (The upper-left quadrant of $\boldsymbol{B}$ is not of interest.)

3. The transpose of the bottom-right quadrant of $\boldsymbol{B}$ is $\boldsymbol{F}_d$.

$$\boldsymbol{F}_d = \text{transpose of bottom-right quadrant of } \boldsymbol{B}$$

4. Finally, $\boldsymbol{Q}_d$ is computed as a matrix product:

$$\boldsymbol{Q}_d = \boldsymbol{F}_d \text{ [upper-right quadrant of } \boldsymbol{B}]$$

# Appendix C

## C.1 Jacobean matrices (extended)

The Jacobean matrices of the error-state system equation presented here are the extended version of Appendix B.2:

$$\boldsymbol{F} = \begin{pmatrix} \mathbf{0}_{3\times3} & \boldsymbol{I}_3 & \mathbf{0}_{3\times3} & \mathbf{0}_{3\times3} & \mathbf{0}_{3\times3} & \mathbf{0}_{3\times3m} \\ \mathbf{0}_{3\times3} & -2\boldsymbol{S}(\boldsymbol{\omega}_{ie}^{e}) & \boldsymbol{V}_a & \boldsymbol{V}_{acc} & \mathbf{0}_{3\times3} & \mathbf{0}_{3\times3m} \\ \mathbf{0}_{3\times3} & \mathbf{0}_{3\times3} & \boldsymbol{A}_a & \mathbf{0}_{3\times3} & \boldsymbol{A}_{ars} & \mathbf{0}_{3\times3m} \\ \mathbf{0}_{3\times3} & \mathbf{0}_{3\times3} & \mathbf{0}_{3\times3} & -\boldsymbol{T}_{acc}^{-1} & \mathbf{0}_{3\times3} & \mathbf{0}_{3\times3m} \\ \mathbf{0}_{3\times3} & \mathbf{0}_{3\times3} & \mathbf{0}_{3\times3} & \mathbf{0}_{3\times3} & -\boldsymbol{T}_{ars}^{-1} & \mathbf{0}_{3\times3m} \\ \mathbf{0}_{3m\times3} & \mathbf{0}_{3m\times3} & \mathbf{0}_{3m\times3} & \mathbf{0}_{3m\times3} & \mathbf{0}_{3m\times3} & \mathbf{0}_{3m\times3m} \end{pmatrix} \in \mathbb{R}^{(15+3m)\times(15+3m)} \tag{C.1}$$

$$\boldsymbol{G} = \begin{pmatrix} \mathbf{0}_{3\times3} & \mathbf{0}_{3\times3} & \mathbf{0}_{3\times3} & \mathbf{0}_{3\times3} & \mathbf{0}_{3\times3m} \\ -\boldsymbol{R}_b^e(\boldsymbol{q}_b^e) & \mathbf{0}_{3\times3} & \mathbf{0}_{3\times3} & \mathbf{0}_{3\times3} & \mathbf{0}_{3\times3m} \\ \mathbf{0}_{3\times3} & -\boldsymbol{I}_3 & \mathbf{0}_{3\times3} & \mathbf{0}_{3\times3} & \mathbf{0}_{3\times3m} \\ \mathbf{0}_{3\times3} & \mathbf{0}_{3\times3} & \boldsymbol{I}_3 & \mathbf{0}_3 & \mathbf{0}_{3\times3m} \\ \mathbf{0}_{3\times3} & \mathbf{0}_{3\times3} & \mathbf{0}_{3\times3} & \boldsymbol{I}_3 & \mathbf{0}_{3\times3m} \\ \mathbf{0}_{3m\times3} & \mathbf{0}_{3m\times3} & \mathbf{0}_{3m\times3} & \mathbf{0}_{3m\times3} & \mathbf{0}_{3m\times3m} \end{pmatrix} \in \mathbb{R}^{(15+3m)\times(12+3m)} \tag{C.2}$$

where

$$\begin{aligned} \boldsymbol{V}_a &= -\hat{\boldsymbol{R}}_b^e(q_b^e)\boldsymbol{S}(\boldsymbol{f}_{\text{IMU}}^b - \hat{\boldsymbol{b}}_{acc}^b) \\ \boldsymbol{V}_{\text{acc}} &= -\hat{\boldsymbol{R}}_b^e(q_b^e) \\ \boldsymbol{A}_a &= -\boldsymbol{S}\left(\boldsymbol{\omega}_{\text{IMU}}^b - \hat{\boldsymbol{b}}_{ars}^b - \hat{\boldsymbol{R}}_{eb}^\intercal \boldsymbol{\omega}_{ie}^e\right) \\ \boldsymbol{A}_{\text{ars}} &= -\boldsymbol{I}_3. \end{aligned}$$

The process noise effecting the velocity, orientation and bias estimates error $\boldsymbol{w} = (\varepsilon_{\text{acc}}^\intercal, \varepsilon_{\text{ars}}^\intercal, \varepsilon_{b_{\text{acc}}}^\intercal, \varepsilon_{b_{\text{ars}}}^\intercal, \varepsilon_{\delta a_1}^\intercal, \ldots, \varepsilon_{\delta a_m}^\intercal)^\intercal$ are modeled by white Gaussian processes. The total spectral density is given as

$$\boldsymbol{Q} = \begin{pmatrix} \boldsymbol{V}_\epsilon & \mathbf{0}_{3\times3} & \mathbf{0}_{3\times3} & \mathbf{0}_{3\times3} & \mathbf{0}_{3\times3m} \\ \mathbf{0}_{3\times3} & \boldsymbol{\Theta}_\epsilon & \mathbf{0}_{3\times3} & \mathbf{0}_{3\times3} & \mathbf{0}_{3\times3m} \\ \mathbf{0}_{3\times3} & \mathbf{0}_{3\times3} & \boldsymbol{A}_\epsilon & \mathbf{0}_{3\times3} & \mathbf{0}_{3\times3m} \\ \mathbf{0}_{3\times3} & \mathbf{0}_{3\times3} & \mathbf{0}_{3\times3} & \boldsymbol{\Omega}_\epsilon & \mathbf{0}_{3\times3m} \\ \mathbf{0}_{3m\times3} & \mathbf{0}_{3m\times3} & \mathbf{0}_{3m\times3} & \mathbf{0}_{3m\times3} & \boldsymbol{C}_\epsilon \end{pmatrix} \in \mathbb{R}^{(12+3m)\times(12+3m)} \tag{C.3}$$

where

$$\boldsymbol{V}_\epsilon = \sigma^2_{\text{acc}} \boldsymbol{I}_3 \quad [\text{m}^2\,\text{s}^{-3}] \tag{C.4}$$
$$\boldsymbol{\Theta}_\epsilon = \sigma^2_{\text{ars}} \boldsymbol{I}_3 \quad [\text{rad}^2\,\text{s}^{-1}] \tag{C.5}$$
$$\boldsymbol{A}_\epsilon = \sigma^2_{b_{\text{acc}}} \boldsymbol{I}_3 \quad [\text{m}^2\,\text{s}^{-5}] \tag{C.6}$$
$$\boldsymbol{\Omega}_\epsilon = \sigma^2_{b_{\text{ars}}} \boldsymbol{I}_3 \quad [\text{rad}^2\,\text{s}^{-3}] \tag{C.7}$$
$$\boldsymbol{C}_\epsilon = \sigma^2_{a_{\text{calib}}} \boldsymbol{I}_m \quad [\text{rad}^2\,\text{s}^{-1}]. \tag{C.8}$$

and the receive spectral densities are calculated

$$\sigma^2_\star = \mathbb{E}[\varepsilon_\star(t)\varepsilon^\intercal_\star(\tau)]. \tag{C.9}$$

## C.2 Calibration algorithm

The measurement model is formulated based on the following relationship between the UAV position ($\boldsymbol{p}^e_{eb}$), the ground station position ($\boldsymbol{p}^e_{er_j}$) and UAV PARS position relative to the ground radio ($\boldsymbol{p}^{r_j}_{r_jb}$):

$$\boldsymbol{p}^e_{eb} = \boldsymbol{p}^e_{er_j} + \boldsymbol{R}^e_{n_j}\boldsymbol{R}^{n_j}_{r_j}\boldsymbol{p}^{r_j}_{r_jb}. \tag{C.10}$$

Firstly, moving $\boldsymbol{p}^e_{er_j}$ from RHS to LHS yields

$$\boldsymbol{p}^e_{eb} - \boldsymbol{p}^e_{er_j} = \boldsymbol{R}^e_{n_j}\boldsymbol{R}^{n_j}_{r_j}\boldsymbol{p}^{r_j}_{r_jb}. \tag{C.11}$$

By multiplying both sides by $\boldsymbol{R}^\intercal_{en_j}$ and using $\boldsymbol{R}_{n_jr_j} = \hat{\boldsymbol{R}}_{n_jr_j}(\boldsymbol{I}_3 + \boldsymbol{S}(\delta\boldsymbol{a}))$,

$$\boldsymbol{R}^\intercal_{en_j}(\boldsymbol{p}^e_{eb} - \boldsymbol{p}^e_{er_j}) = \boldsymbol{R}^\intercal_{en_j}\boldsymbol{R}_{en_j}\boldsymbol{R}_{n_jr_j}\boldsymbol{p}^{r_j}_{r_jb} \tag{C.12}$$
$$= \hat{\boldsymbol{R}}_{n_jr_j}(\boldsymbol{I}_3 + \boldsymbol{S}(\delta\boldsymbol{a}))\boldsymbol{p}^{r_j}_{r_jb} \tag{C.13}$$
$$= \hat{\boldsymbol{R}}_{n_jr_j}\boldsymbol{p}^{r_j}_{r_jb} + \hat{\boldsymbol{R}}_{n_jr_j}\boldsymbol{S}(\delta\boldsymbol{a})\boldsymbol{p}^{r_j}_{r_jb}. \tag{C.14}$$

Swapping cross product between $\boldsymbol{p}^{r_j}_{r_jb}$ and $\delta\boldsymbol{a}$ yields

$$\boldsymbol{R}^\intercal_{en_j}(\boldsymbol{p}^e_{eb} - \boldsymbol{p}^e_{er_j}) = \hat{\boldsymbol{R}}_{n_jr_j}\boldsymbol{p}^{r_j}_{r_jb} - \hat{\boldsymbol{R}}_{n_jr_j}\boldsymbol{S}(\boldsymbol{p}^{r_j}_{r_jb})\delta\boldsymbol{a}^{n_j}_{r_j}, \tag{C.15}$$

and by moving the $\delta\boldsymbol{a}$ from the left to right side,

$$\hat{\boldsymbol{R}}_{n_jr_j}\boldsymbol{p}^{r_j}_{r_jb} = \boldsymbol{R}^e_{n_j}{}^\intercal(\boldsymbol{p}^e_{eb} - \boldsymbol{p}^e_{er_j}) + \hat{\boldsymbol{R}}^{n_j}_{r_j}\boldsymbol{S}\left(\boldsymbol{p}^{r_j}_{r_jb}\right)\delta\boldsymbol{a}^{n_j}_{r_j}. \tag{C.16}$$

Finally, by substituting $\boldsymbol{p}^e_{eb} = \hat{\boldsymbol{p}}^e_{eb} + \delta\boldsymbol{p}^e_{eb}$, the final equation is formulated:

$$\underbrace{\hat{\boldsymbol{R}}^{n_j}_{r_j}\boldsymbol{p}^{r_j}_{r_jb}}_{\boldsymbol{y}_{\text{pars}_j}} = \underbrace{\boldsymbol{R}^\intercal_{en_j}\left(\hat{\boldsymbol{p}}^e_{eb} - \boldsymbol{p}^e_{er_j}\right)}_{\hat{\boldsymbol{y}}_{\text{pars}_j}} + \underbrace{\boldsymbol{R}^\intercal_{en_j}}_{\boldsymbol{H}_{\text{pos}_j}}\delta\boldsymbol{p} + \underbrace{\hat{\boldsymbol{R}}^{n_j}_{r_j}\boldsymbol{S}\left(\boldsymbol{p}^{r_j}_{r_jb}\right)}_{\boldsymbol{H}_{\text{calib}_j}}\delta\boldsymbol{a}^{n_j}_{r_j} \tag{C.17}$$

**PARS measurement equation validation**

$$\begin{aligned}
\boldsymbol{p}_{eb}^{e} &= \boldsymbol{p}_{er_j}^{e} + \boldsymbol{R}_{en_j}\boldsymbol{R}_{n_jr_j}\boldsymbol{p}_{r_jb}^{r_j},\\
\Rightarrow \hat{\boldsymbol{p}}_{eb}^{e} + \delta\boldsymbol{p} - \boldsymbol{p}_{er_j}^{e} &= \boldsymbol{R}_{en_j}\hat{\boldsymbol{R}}_{n_jr_j}\left(\boldsymbol{I}_3 + \boldsymbol{S}(\delta\boldsymbol{a}_{r_1}^{n_1})\right)\boldsymbol{p}_{r_jb}^{r_j},\\
\Rightarrow \boldsymbol{R}_{en_j}^{\mathsf{T}}\left(\hat{\boldsymbol{p}}_{eb}^{e} + \delta\boldsymbol{p} - \boldsymbol{p}_{er_j}^{e}\right) &= \hat{\boldsymbol{R}}_{r_j}^{n_j}\left(\boldsymbol{I}_3 + \boldsymbol{S}(\delta\boldsymbol{a}_{r_1}^{n_1})\right)\boldsymbol{p}_{r_jb}^{r_j},\\
\Rightarrow \boldsymbol{R}_{en_j}^{\mathsf{T}}\left(\hat{\boldsymbol{p}}_{eb}^{e} + \delta\boldsymbol{p} - \boldsymbol{p}_{er_j}^{e}\right) &= \hat{\boldsymbol{R}}_{r_j}^{n_j}\boldsymbol{p}_{r_jb}^{r_j} + \hat{\boldsymbol{R}}_{r_j}^{n_j}\boldsymbol{S}(\delta\boldsymbol{a}_{r_1}^{n_1})\boldsymbol{p}_{r_jb}^{r_j},\\
\Rightarrow \boldsymbol{R}_{en_j}^{\mathsf{T}}\left(\hat{\boldsymbol{p}}_{eb}^{e} + \delta\boldsymbol{p} - \boldsymbol{p}_{er_j}^{e}\right) &= \hat{\boldsymbol{R}}_{r_j}^{n_j}\boldsymbol{p}_{r_jb}^{r_j} - \hat{\boldsymbol{R}}_{r_j}^{n_j}\boldsymbol{S}(\boldsymbol{p}_{r_jb}^{r_j})\delta\boldsymbol{a}_{r_1}^{n_1}\\
\Rightarrow \underbrace{\hat{\boldsymbol{R}}_{r_j}^{n_j}\boldsymbol{p}_{r_jb}^{r_j}}_{\boldsymbol{y}_{\mathrm{pars}_j}} &= \underbrace{\boldsymbol{R}_{en_j}^{\mathsf{T}}\left(\hat{\boldsymbol{p}}_{eb}^{e} - \boldsymbol{p}_{er_j}^{e}\right)}_{\hat{\boldsymbol{y}}_{\mathrm{pars}_j}} + \underbrace{\boldsymbol{R}_{en_j}^{\mathsf{T}}}_{\boldsymbol{H}_{\mathrm{pos}_j}}\delta\boldsymbol{p} + \underbrace{\hat{\boldsymbol{R}}_{r_j}^{n_j}\boldsymbol{S}(\boldsymbol{p}_{r_jb}^{r_j})}_{\boldsymbol{H}_{\mathrm{calib}_j}}\delta\boldsymbol{a}_{r_1}^{n_1}\\
\Rightarrow \underbrace{\hat{\boldsymbol{R}}_{r_j}^{n_j}\boldsymbol{p}_{r_jb}^{r_j}}_{\boldsymbol{y}_{\mathrm{pars}_j}} &\approx \underbrace{\boldsymbol{R}_{en_j}^{\mathsf{T}}\left(\hat{\boldsymbol{p}}_{eb}^{e} - \boldsymbol{p}_{er_j}^{e}\right)}_{\hat{\boldsymbol{y}}_{\mathrm{pars}_j}} + \underbrace{\boldsymbol{R}_{en_j}^{\mathsf{T}}}_{\boldsymbol{H}_{\mathrm{pos}_j}}\delta\boldsymbol{p} + \underbrace{\hat{\boldsymbol{R}}_{r_j}^{n_j}\boldsymbol{S}\left(\hat{\boldsymbol{R}}_{er_j}^{\mathsf{T}}\left(\hat{\boldsymbol{p}}_{eb}^{e} - \boldsymbol{p}_{er_j}^{e}\right)\right)}_{\boldsymbol{H}_{\mathrm{calib}_j}}\delta\boldsymbol{a}_{r_1}^{n_1}
\end{aligned} \tag{C.18}$$

where $\boldsymbol{p}_{r_jb}^{r_j} \approx \hat{\boldsymbol{R}}_{er_j}^{\mathsf{T}}\left(\hat{\boldsymbol{p}}_{eb}^{e} - \boldsymbol{p}_{er_j}^{e}\right)$ inside $\boldsymbol{H}_{\mathrm{calib}_j}$ and $\hat{\boldsymbol{R}}_{er_j} = \hat{\boldsymbol{R}}_{en_j}\hat{\boldsymbol{R}}_{n_jr_j}$.

## C.3 Numerical values

Numerical values for the matrices $\boldsymbol{Q}$ and $\boldsymbol{R}_{\star}$ were set as

$$\begin{aligned}
\sigma_{\mathrm{acc}} &= 47.85\,\mathrm{m\,s^{-1.5}}\\
\sigma_{\mathrm{ars}} &= 5.35\times10^{-7}\,\mathrm{rad\,s^{-0.5}}\\
\sigma_{b_{\mathrm{acc}}} &= 4.91\times10^{-3}\,\mathrm{m\,s^{-2.5}}\\
\sigma_{b_{\mathrm{ars}}} &= 1.74\times10^{-7}\,\mathrm{rad\,s^{-1.5}}\\
\sigma_{\mathrm{calib}} &= 0\,\mathrm{rad\,s^{-0.5}},
\end{aligned}$$

where $\sigma_{\mathrm{calib}}$ is zero because the antennas are stationary, and

$$\begin{aligned}
\sigma_{\rho} &= 15\,\mathrm{m} & \sigma_{\mathrm{gnss},x} &= 0.2\,\mathrm{m}\\
\sigma_{\psi} &= 2^{\circ} & \sigma_{\mathrm{gnss},y} &= 0.2\,\mathrm{m}\\
\sigma_{\mathrm{baro}} &= 5\,\mathrm{m} & \sigma_{\mathrm{gnss},z} &= 0.4\,\mathrm{m}\\
\sigma_{\mathrm{alt}} &= 5\,\mathrm{m}.
\end{aligned}$$

The parameters for (3.17) were chosen to be

$$
\begin{aligned}
P_0 &= 10\,040\,\mathrm{Pa} \\
T_0 &= 280.15\,\mathrm{K} \\
R_t &= 287.7\,\mathrm{J\,kg^{-1}\,K^{-1}} \\
K_t &= 6.5 \times 10^{-3}\,\mathrm{K\,m^{-1}} \\
g_0 &= 9.807\,\mathrm{m\,s^{-2}}.
\end{aligned}
$$

The numerical values for $R_t$, $K_t$ and $g_0$ were chosen from [38, Ch. 6.2.1], and $P_0$ and $T_0$ are based on the local temperature and atmospheric pressure on the field test day.

# Appendix D

## D.1 Linearization of arcsin

Linearizing the arcsin function with two variables involves a slightly more complex approach since arcsin inherently operates on a single argument. However, if we're dealing with a scenario where arcsin is applied to a function of two variables, say $f(x, y)$, then we would linearize $\arcsin(f(x, y))$ around a point $(x_0, y_0)$.

We linearize $\arcsin(f(x, y))$ around a point $(x_0, y_0)$, where $f(x, y)$ is a function that maps $x, y$ to a value within the domain of arcsin, that is, $[-1, 1]$. The first-order Taylor expansion for a function of two variables is:

$$g(x, y) \approx g(x_0, y_0) + \left.\frac{\partial g}{\partial x}\right|_{(x_0, y_0)} \cdot (x - x_0) + \left.\frac{\partial g}{\partial y}\right|_{(x_0, y_0)} \cdot (y - y_0) \tag{D.1}$$

For $g(x, y) = \arcsin(f(x, y))$, this becomes:

$$\begin{aligned} \arcsin(f(x, y)) \approx{}& \arcsin(f(x_0, y_0)) + \\ & \left.\frac{\partial \arcsin(f(x, y))}{\partial x}\right|_{(x_0, y_0)} \cdot (x - x_0) + \left.\frac{\partial \arcsin(f(x, y))}{\partial y}\right|_{(x_0, y_0)} \cdot (y - y_0) \end{aligned} \tag{D.2}$$

The partial derivatives of $\arcsin(f(x, y))$ with respect to $x$ and $y$ are obtained through the chain rule:

$$\frac{\partial \arcsin(f(x, y))}{\partial x} = \frac{1}{\sqrt{1 - f(x, y)^2}} \cdot \frac{\partial f(x, y)}{\partial x} \tag{D.3}$$

$$\frac{\partial \arcsin(f(x, y))}{\partial y} = \frac{1}{\sqrt{1 - f(x, y)^2}} \cdot \frac{\partial f(x, y)}{\partial y} \tag{D.4}$$

Substituting these back into the approximation gives:

$$\begin{aligned} \arcsin(f(x, y)) \approx{}& \arcsin(f(x_0, y_0)) + \frac{1}{\sqrt{1 - f(x_0, y_0)^2}} \\ & \left( \left.\frac{\partial f(x, y)}{\partial x}\right|_{(x_0, y_0)} \cdot (x - x_0) + \left.\frac{\partial f(x, y)}{\partial y}\right|_{(x_0, y_0)} \cdot (y - y_0) \right) \end{aligned} \tag{D.5}$$

This formula linearizes $\arcsin(f(x, y))$ around $(x_0, y_0)$, provided $f(x, y)$ is known and its partial derivatives can be computed. This approach is useful for approximating the behavior of arcsin applied to multivariable functions near specific points, simplifying the analysis of systems modeled by such functions.

## D.2 Grazing angle uncertainty

### D.2.1 Problem setting

We have

$$\rho_m = \rho + \tilde{\rho} \tag{D.6}$$

$$\gamma_m = \gamma + \tilde{\gamma} \tag{D.7}$$

where $\rho_m$ and $\gamma_m$ are measurements, $\rho$ and $\gamma$ are true values, and $\tilde{\rho}$ and $\tilde{\gamma}$ are the Gaussian errors with zero mean with standard deviations $\sigma_\rho$ and $\sigma_\gamma$.

Then, the grazing angle $\alpha_m = \alpha + \tilde{\alpha}$ is given by

$$\alpha_m = \arcsin \frac{\gamma_m^2 + 2\gamma_m r_a + \rho_m^2}{2\rho_m r_a} \tag{D.8}$$

where $r_a$ is the Earth radius, $\alpha$ is a true value and $\tilde{\alpha}$ is an error with zero mean with standard deviation $\sigma_\alpha$.

### D.2.2 Express $\tilde{\alpha}(\tilde{\rho}, \tilde{\gamma})$

We apply the first-order Taylor expansion with two variables (D.5) to our problem (i.e. we linearize (D.8) here.).

Given the function

$$f(\gamma, \rho) = \frac{\gamma^2 + 2\gamma r_a + \rho^2}{2\rho r_a} \tag{D.9}$$

linearizing $\arcsin(f(\gamma, \rho))$ around a specific point $(\gamma_m, \rho_m)$:

$$\arcsin(f(\gamma, \rho)) \approx \arcsin(f(\gamma_m, \rho_m)) + \frac{1}{\sqrt{1 - f(\gamma_m, \rho_m)^2}} \left( \left.\frac{\partial f}{\partial \gamma}\right|_{(\gamma_m, \rho_m)} \cdot (\gamma - \gamma_m) + \left.\frac{\partial f}{\partial \rho}\right|_{(\gamma_m, \rho_m)} \cdot (\rho - \rho_m) \right) \tag{D.10}$$

The partial derivatives of $f(\gamma, \rho)$ are as follows:

1. With respect to $\gamma$:

$$\frac{\partial f}{\partial \gamma} = \frac{r_a + \gamma}{r_a \rho} \tag{D.11}$$

2. With respect to $\rho$:

$$\frac{\partial f}{\partial \rho} = \frac{-2r_a\gamma - \gamma^2 + \rho^2}{2r_a\rho^2} \tag{D.12}$$

Substituting (D.11) and (D.12) into (D.10),

$$\underbrace{\arcsin(f(\gamma,\rho))}_{\alpha} \approx \underbrace{\arcsin(f(\gamma_m,\rho_m))}_{\alpha_m} +$$

$$\underbrace{\frac{1}{\sqrt{1-f(\gamma_m,\rho_m)^2}}}_{\sqrt{1-\alpha_m^2}} \left( \underbrace{\frac{r_a+\gamma_m}{r_a\rho_m}}_{B} \cdot \underbrace{(\gamma-\gamma_m)}_{-\tilde{\gamma}} + \underbrace{\frac{-2r_a\gamma_m-\gamma_m^2+\rho_m^2}{2r_a\rho_m^2}}_{A} \cdot \underbrace{(\rho-\rho_m)}_{-\tilde{\rho}} \right). \tag{D.13}$$

Therefore,

$$\underbrace{\alpha_m - \tilde{\alpha}}_{\alpha} \approx \alpha_m + \frac{1}{\sqrt{1-\alpha_m^2}}\left(-A\tilde{\rho} - B\tilde{\gamma}\right) \tag{D.14}$$

$$\tilde{\alpha} \approx \frac{1}{\sqrt{1-\alpha_m^2}}\left(A\tilde{\rho} + B\tilde{\gamma}\right). \tag{D.15}$$

The uncertainty in $\alpha$ is expressed by the uncertainties in $\rho$ and $\gamma$.

### D.2.3 Variance of $\tilde{\alpha}$

From (D.15),

$$\mathbb{E}[\tilde{\alpha}] = 0 \tag{D.16}$$

$$\mathbb{V}[\tilde{\alpha}] = \left(\frac{1}{\sqrt{1-\alpha_m^2}}\right)^2 \left(A^2\mathbb{V}[\tilde{\rho}] + B^2\mathbb{V}[\tilde{\gamma}]\right), \tag{D.17}$$

as $\tilde{\alpha}$ is zero-mean Gaussian with standard deviation $\sigma_\alpha$, and the general variance rule says,

$$\mathbb{V}[aX + bY] = a^2\mathbb{V}[X] + b^2\mathbb{V}[Y] \tag{D.18}$$

# Appendix E

## E.1 Kalman Filter

The Kalman Filter is a recursive algorithm used for estimating the state of a linear dynamic system from a series of noisy measurements. It operates in two fundamental steps: prediction and correction.

### Prediction

In the prediction step, the Kalman Filter predicts the state of the system in the next time step. The prediction consists of two parts:

1. Predict the state estimate using the current state estimate and the system model:
$$\hat{\boldsymbol{x}}[k+1] = \boldsymbol{F}_d[k]\boldsymbol{x}[k] + \boldsymbol{G}[k]\boldsymbol{w}[k]$$
where $\boldsymbol{F}_d[k]$ is the discretized version of state transition model $\boldsymbol{F}$ [1], $\boldsymbol{G}[k]$ is the control-input model, and $\boldsymbol{w}[k]$ is the control vector representing process noise or external inputs.

2. Update the estimate covariance:
$$\hat{\boldsymbol{P}}[k+1] = \boldsymbol{F}_d[k]\boldsymbol{P}[k]\boldsymbol{F}_d[k]^\intercal + \boldsymbol{Q}_d[k]$$
where $\boldsymbol{P}[k]$ is the prior estimate covariance, and $\boldsymbol{Q}_d[k]$ is the discretized version of process noise covariance matrix $\boldsymbol{Q}$ [2].

### Correction

The correction step, also known as measurement update, adjusts the predicted state estimate using the actual measurement at that time. This step involves:

1. Compute the Kalman gain:
$$\boldsymbol{K}[k] = \hat{\boldsymbol{P}}[k+1]\boldsymbol{H}[k]^\intercal(\boldsymbol{H}[k]\hat{\boldsymbol{P}}[k+1]\boldsymbol{H}[k]^\intercal + \mathcal{R}[k])^{-1}$$
where $\boldsymbol{H}[k]$ is the observation model, and $\mathcal{R}[k]$ is the measurement noise covariance matrix.

2. Update the state estimate:
$$\boldsymbol{x}[k+1] = \hat{\boldsymbol{x}}[k+1] + \boldsymbol{K}[k](\boldsymbol{y}[k] - \boldsymbol{H}[k]\hat{\boldsymbol{x}}[k+1])$$
where $\boldsymbol{y}[k]$ is the measurement vector.

[1] Discretization of $F$ is in Appendix B.4.
[2] Discretization of $Q$ is in Appendix B.4.

3. Update the estimate covariance:

$$\boldsymbol{P}[k+1] = (\boldsymbol{I} - \boldsymbol{K}[k]\boldsymbol{H}[k])\hat{\boldsymbol{P}}[k+1]$$

These two steps, prediction and correction, are repeated recursively to provide a real-time estimate of the system's state.

## E.2 Numerical values

The state transition matrix $\boldsymbol{F}$, the process noise matrix $\boldsymbol{Q}$ and the measurement noise matrix $\boldsymbol{\mathcal{R}}$ are defined as follows:

$$\boldsymbol{F} = \begin{bmatrix} -\frac{1}{T_{\text{nom}}} & 0 \\ 0 & -\frac{1}{T_{\text{dr}}} \end{bmatrix}$$
$$\boldsymbol{Q} = \begin{bmatrix} \sigma_{\text{nom}}^2 & 0 \\ 0 & \sigma_{\text{dr}}^2 \end{bmatrix}$$
$$\boldsymbol{\mathcal{R}} = \begin{bmatrix} \sigma_{\text{mea}}^2 \end{bmatrix}$$

The numerical values for these parameters are given by:

$$\begin{aligned} T_{\text{nom}} &= 50000 \\ T_{\text{dr}} &= 70 \\ \sigma_{\text{nom}} &= 0.05 \\ \sigma_{\text{dr}} &= 1 \\ \sigma_{\text{mea}} &= 10 \end{aligned}$$

It should be noted that the zero values for $T_{\text{dr}}$, $T_{\text{nom}}$, $\sigma_{\text{dr}}$, and $\sigma_{\text{nom}}$ are placeholders and should be replaced with actual values based on the specific application and system characteristics.

## E.3 Neyman-Pearson theorem

By maximising $P_D$ (the probability of detection) for a given $P_{FA} = \alpha$ (the probability of false), decide $\mathcal{H}_1$, if

$$\boldsymbol{L}(x) = \frac{p(\boldsymbol{x}; \mathcal{H}_1)}{p(\boldsymbol{x}; \mathcal{H}_0)} > \gamma \tag{E.1}$$

where the threshold $\gamma$ is fround from

$$P_{FA} = \int_{\{\boldsymbol{x}:\boldsymbol{L}(\boldsymbol{x})>\gamma\}} p(\boldsymbol{x}; \mathcal{H}_0)\, dx = \alpha \tag{E.2}$$

The expression $\boldsymbol{L}(x)$ is referred to as the *likelihood ratio*. It represents, for each $\boldsymbol{x}$, the probability of $\mathcal{H}_1$ relative to the probability of $\mathcal{H}_0$. The complete procedure described in (E.1) is known as the *likelihood ratio test (LRT)*. For more details and the proof of the NP theorem, see [86].

## E.4 Gaussian right-tail probability

The Gaussian probability density function (PDF) (also known as the normal PDF) for a scalar random variable $x$ is described by

$$p(x) = \frac{1}{\sqrt{2\pi\sigma^2}} \exp\left[-\frac{1}{2\sigma^2}(x-\mu)^2\right]$$

where $\mu$ is the mean and $\sigma^2$ is the variance of $x$.

For the cases where $\mu = 0$ and $\sigma^2 = 1$, the PDF is known as a *standard normal PDF*. Its CDF is given by

$$\Phi(x) = \int_{-\infty}^{x} \frac{1}{\sqrt{2\pi}} \exp\left(-\frac{1}{2}t^2\right) dt.$$

An alternative representation, often called the *right-tail probability* or the *complementary CDF*, which denotes the probability of a value exceeding a specified threshold, is expressed as $Q(x) = 1 - \Phi(x)$, where

$$Q(x) = \int_{x}^{\infty} \frac{1}{\sqrt{2\pi}} \exp\left(-\frac{1}{2}t^2\right) dt.$$

## E.5 Derivation of test static and threshold

Following (8.13) and (8.14), we apply the NP theorem [3] and decide $\mathcal{H}_1$, if

$$\frac{\frac{1}{(2\pi\sigma^2)^{\frac{N}{2}}} \exp\left[-\frac{1}{2\sigma^2}\sum_{n=0}^{N-1}(x[n]-(-D))^2\right]}{\frac{1}{(2\pi\sigma^2)^{\frac{N}{2}}} \exp\left[-\frac{1}{2\sigma^2}\sum_{n=0}^{N-1}(x[n])^2\right]} > \gamma. \tag{E.3}$$

Taking the logarithm of both sides results in

$$-\frac{D}{\sigma^2}\sum_{n=0}^{N-1} x[n] - \frac{ND^2}{2\sigma^2} > \ln\gamma \tag{E.4}$$

which simplifies to

$$\underbrace{\frac{1}{N}\sum_{n=0}^{N-1} x[n]}_{T(x)} < \underbrace{-\frac{\sigma^2}{ND}\ln\gamma - \frac{D}{2}}_{\gamma'} \tag{E.5}$$

where the test static

$$T(x) = \frac{1}{N}\sum_{n=0}^{N-1} x[n] \tag{E.6}$$

[3] See Appendix E.3.

is Gaussian under each hypothesis

$$T(x) \sim \begin{cases} \mathcal{N}(0, \frac{\sigma^2}{N}) & \text{under } \mathcal{H}_0 \\ \mathcal{N}(-D, \frac{\sigma^2}{N}) & \text{under } \mathcal{H}_1. \end{cases}$$

We then have the probability of a false alarm

$$P_{FA} = \Pr\{T(x) < \gamma'; \mathcal{H}_0\} \tag{E.7}$$

$$= 1 - Q\left(\frac{\gamma'}{\sqrt{\sigma^2/N}}\right) \tag{E.8}$$

where $Q$ denotes the *right-tail probability* or the *complementary CDF*. [4] Given that $1 - Q$ represents a CDF and increases monotonically, the function $Q$, in contrast, decreases monotonically. Consequently, $Q$ has an inverse, which is designated as $Q^{-1}$. By arranging (E.8), the threshold is found from

$$\gamma' = \sqrt{\frac{\sigma^2}{N}} Q^{-1}(1 - P_{FA}). \tag{E.9}$$

[4] See Appendix E.4

# References

[1] Y. Bar-Shalom, P. K. Willett, and X. Tian. *Tracking and Data Fusion: A Handbook of Algorithm*. YBS Publishing, 2011.

[2] J. M. Hansen, T. A. Johansen, and T. I. Fossen. Tightly coupled integrated inertial and real-time-kinematic positioning approach using nonlinear observer. In *American Control Conference*, pages 1–8, 2016.

[3] J. M. Hansen, T. I. Fossen, and T. A. Johansen. Nonlinear observer design for gnss-aided inertial navigation systems with time-delayed gnss measurements. *Control Engineering Practice*, 60:39–50, 2017.

[4] K. C. Yeh and C.-H. Liu. Radio wave scintillations in the ionosphere. *Proceedings of the IEEE*, 70(4):324–360, 1982.

[5] Aron Pinker and Charles Smith. Vulnerability of the GPS signal to jamming. *GPS Solutions*, 3(2):19–27, 1999.

[6] Andrew J. Kerns, Daniel P. Shepard, Jahshan A. Bhatti, and Todd E. Humphreys. Unmanned aircraft capture and control via GPS spoofing. *Journal of Field Robotics*, 31(4):617–636, 2014.

[7] D. Schmidt, K. Radke, S. Camtepe, E. Foo, and M. Ren. A survey and analysis of the gnss spoofing threat and countermeasures. *ACM Computing Surveys (CSUR)*, 48(4):1–31, 5 2016.

[8] Greg Jaffe and Thomas Erdbrink. Iran says it downed u.s. stealth drone; pentagon acknowledges aircraft downing. The Washington Post, December 2011. Accessed: 2024-03-19.

[9] P. Karasz. Europe billed galileo as its answer to gps. it's been mostly down for days. The New York Times, July 2019. https://www.nytimes.com/2019/07/16/world/europe/galileo-european-gps.html.

[10] Christian Forster, Matia Pizzoli, and Davide Scaramuzza. Svo: Fast semi-direct monocular visual odometry. In *2014 IEEE International Conference on Robotics and Automation (ICRA)*, pages 15–22. IEEE, 2014.

[11] A. I. Mourikis and S. I. Roumeliotis. A multi-state constraint kalman filter for vision-aided inertial navigation. In *Proceedings IEEE International Conference on Robotics and Automation*, pages 3565–3572, Roma, Italy, April 2007. IEEE.

[12] Huan Wang, Zhengjie Wang, Quanpan Liu, and Yulong Gao. Multi-features visual odometry for indoor mapping of uav. In *2020 3rd International Conference on Unmanned Systems (ICUS)*, pages 203–208. IEEE, 2020.

[13] Xinghui Zhu, Yongzhen Chen, Xiaodong Zhang, Zhiwei Zhang, and Baoquan Ren. Feature matching for indoor-oriented visual odometry. In *2022 International Conference on Networking and Network Applications (NaNA)*, pages 253–258. IEEE, 2022.

[14] Jakob Engel, Thomas Schöps, and Daniel Cremers. Lsd-slam: Large-scale direct monocular slam. In *European Conference on Computer Vision (ECCV)*, pages 834–849, Zurich, Switzerland, 2014. Springer.

[15] R. Mur-Artal, J. M. M. Montiel, and J. D. Tardos. Orb-slam: A versatile and accurate monocular slam system. *IEEE Transactions on Robotics*, 31(5):1147–1163, 2015.

[16] Pingrui Huang. Vision-based slam for uavs in dynamic environments. *Highlights in Science, Engineering and Technology*, 70, 2023.

[17] Taiyuan Ma, Yafei Wang, Zili Wang, Xulei Liu, and Huimin Zhang. Asd-slam: A novel adaptive-scale descriptor learning for visual slam. *2020 IEEE Intelligent Vehicles Symposium (IV)*, pages 809–816, 2020.

[18] F. Gustafsson. Particle filter theory and practice with positioning applications. *IEEE Aerospace and Electronic Systems Magazine*, pages 53–82, 2010.

[19] Sinan Gezici, Zhi Tian, Georgios B. Giannakis, Hisashi Kobayashi, Andreas F. Molisch, H. Vincent Poor, and Zafer Sahinoglu. Localization via ultra-wideband radios: A look at positioning aspects for future sensor networks. *IEEE Signal Processing Magazine*, 22(4):70–84, 2005.

[20] M. R. Mahfouz, C. Zhang, B. C. Merkl, M. J. Kuhn, and A. E. Fathy. Investigation of high-accuracy indoor 3-d positioning using uwb technology. *IEEE Transactions on Microwave Theory and Techniques*, 56(6):1316–1330, June 2008.

[21] J. Djugash, B. Hamner, and S. Roth. Navigating with ranging radios: Five data sets with ground truth. *Journal of Field Robotics*, 26(9):689–695, 2009.

[22] S. M. Albrektsen, A Sœgrov, and T. A. Johansen. Navigation of uav using phased array radio. In *Workshop on Research, Education and Development of Unmanned Aerial Systems (RED UAS)*, pages 138–143, 3 2017.

[23] S. M. Albrektsen, T. H. Bryne, and T. A. Johansen. Phased array radio system aided inertial navigation for unmanned aerial vehicles. In *Proc. of the IEEE Aerospace Conference*, pages 1–11, Big Sky, Montana, March 3–10 2018.

[24] S. M. Albrektsen, T. H. Bryne, and T. A. Johansen. Robust and secure uav navigation using gnss, phased-array radiosystem and inertial sensor fusion. In *2nd IEEE Conference on Control Technology and Applications*, pages 1338–1345, Copenhagen, Denmark, Aug. 21–24 2018.

[25] K. Gryte, T. H. Bryne, S. M. Albrektsen, and T. A. Johansen. Field test results of gnss-denied inertial navigation aided by phased-array radio systems for uavs. In *2019 International Conference on Unmanned Aircraft Systems (ICUAS)*, pages 1398–1406, 2019.

[26] K Gryte, T. H. Bryne, and T. A. Johansen. Unmanned aircraft flight control aided by phased-array radio navigation. *Journal of Field Robotics*, pages 1–20, 12 2020.

[27] V. E. Hovstein, A. Sægrov, and T. A. Johansen. Experiences with coastal and maritime uas blos operation with phased-array antenna digital payload data link. In *Proc. International Conference Unmanned Aircraft Systems (ICUAS)*, pages 262–266, May 2014.

[28] Joan Solà. Quaternion kinematics for the error-state kalman filter, Submitted on 3 Nov 2017 2017.

[29] F. Landis Markley. Attitude error representation for kalman filtering. *Journal of Guidance, Control, and Dynamics*, 26(2):311–317, 3 2003.

[30] Mika Okuhara, Torleiv Håland Bryne, Kristoffer Gryte, and Tor Arne Johansen. Phased array radio navigation system on UAVs: In-flight calibration. *Journal of Intelligent & Robotic Systems*, 109(3):51, 2023.

[31] Mika Okuhara, Torleiv Håland Bryne, Kristoffer Gryte, Oliver Hasler, and Tor Arne Johansen. UAV navigation during active GNSS jamming using phased-array-radio positioning. *NAVIGATION: Journal of the Institute of Navigation*, 2024. Submitted.

[32] Mika Okuhara, Torleiv Håland Bryne, Kristoffer Gryte, and Tor Arne Johansen. Phased array radio navigation system on UAVs: GNSS-based calibration in the field. In *2021 International Conference on Unmanned Aircraft Systems (ICUAS)*, pages 210–218, 2021.

[33] Mika Okuhara, Torleiv Håland Bryne, Kristoffer Gryte, and Tor Arne Johansen. Phased array radio navigation system on UAVs: Real-time implementation of in-flight calibration. *IFAC-PapersOnLine*, 56(2):1152–1159, 2023. 22nd IFAC World Congress.

[34] Mika Okuhara, Torleiv Håland Bryne, Kristoffer Gryte, and Tor Arne Johansen. Elevation angle redundancy from barometric altitude in multipath-affected phased array radio navigation of UAVs. In *2024 International Conference on Unmanned Aircraft Systems (ICUAS)*, 2024. Submitted.

[35] Mika Okuhara, Torleiv Håland Bryne, Kristoffer Gryte, and Tor Arne Johansen. Phased array radio and barometric navigation system for UAVs: A nonlinear measurement update approach. Internal Report, 2021.

[36] Mika Okuhara, Torleiv Håland Bryne, Kristoffer Gryte, and Tor Arne Johansen. Phased array radio navigation system on UAVs: Multi hypothesis filter for noise mitigation. Internal Report, 2023.

[37] J. A. Farrell. *Aided Navigation: GPS with High Rate Sensors*. McGraw-Hill, 2008.

[38] P. D. Groves. *Principles of GNSS, Inertial, and Multisensor Integrated Navigation Systems*. Artech House, 2nd edition, 2013.

[39] Kenneth Gade. *Inertial Navigation – Theory and Applications*. Doctral dissertation, Norwegian University of Science and Technology (NTNU), January 2018.

[40] Bernhard Hofmann-Wellenhof, Herbert Lichtenegger, and Elmar Wasle. *GNSS – Global Navigation Satellite Systems: GPS, GLONASS, Galileo, and more*. Springer, 2008.

[41] Alfred Leick, Lev Rapoport, and Dmitry Tatarnikov. *GPS Satellite Surveying*. Wiley, 4 edition, 2015.

[42] E. D. Kaplan and C. J. Hegarty. *Understanding GPS/GNSS - Principles and Applications*. Artech House, 2017.

[43] Pratap Misra and Per Enge. *Global Positioning System: Signals, Measurements, and Performance*. Ganga-Jamuna Press, 2 edition, 2006.

[44] P.-J. Chung, M. Viberg, and J. Yu. Chapter 14 - doa estimation methods and algorithms. In A. M. Zoubir, M. Viberg, R. Chellappa, and S. Theodoridis, editors, *Academic Press Library in Signal Processing: Volume 3*, volume 3 of *Academic Press Library in Signal Processing*, pages 599–650. Elsevier, 2014.

[45] M. Haardt, M. Pesavento, F. Roemer, and M. N. E. Korso. Chapter 15 - subspace methods and exploitation of special array structures. In A. M. Zoubir, M. Viberg, R. Chellappa, and S. Theodoridis, editors, *Academic Press Library in Signal Processing: Volume 3*, volume 3 of *Academic Press Library in Signal Processing*, pages 651–717. Elsevier, 2014.

[46] S.I. Roumeliotis, G.S. Sukhatme, and G.A. Bekey. Circumventing dynamic modeling: Evaluation of the error-state kalman filter applied to mobile robot localization. In *IEEE International Conference on Robotics and Automation*, pages 1656–1663, Detroit, Michigan, May 10-15 1999.

[47] Yaakov Bar-Shalom and Xiao-Rong Li. *Multitarget-Multisensor Tracking: Principles and Techniques*. YBS Publishing, Storrs, CT, 1995.

[48] Fredrik Gustafsson. *Statistical Sensor Fusion*. Studentlitteratur, Lund, SWE, 2nd edition, 2012.

[49] C. F. van Loan. Computing integrals involving the matrix exponential. *IEEE Trans. Automatic Control*, AC–23(3):395–404, 1978.

[50] Lorenz Meier, Dominik Honegger, and Marc Pollefeys. Px4: A node-based multithreaded open source robotics framework for deeply embedded platforms. *Proceedings - IEEE International Conference on Robotics and Automation*, pages 6235–6240, 2015.

[51] ArduPilot Development Team. Ardupilot. http://ardupilot.org, 2009–2018.

[52] Honeywell. 3-axis digital compass IC HMC5883L, 02 2013.

[53] Measurement Specialties. MS5611-01BA03 barometric pressure sensor, 09 2015.

[54] Sensonor. STIM300 inertial measurement unit, 04 2013.

[55] Sigurd M. Albrektsen and Tor A. Johansen. User-configurable timing and navigation for UAVs. *Sensors*, 18(8):1–27, 2018.

[56] Hard Kernel. User manual odroid-XU4, 2015.

[57] José Pinto, Paulo S Dias, Ricardo Martins, Joao Fortuna, Eduardo Marques, and Joao Sousa. The lsts toolchain for networked vehicle systems. In *2013 MTS/IEEE OCEANS-Bergen*, pages 1–9. IEEE, 2013.

[58] A. S. Ferreira, J. Pinto, P. Dias, and J. B. de Sousa. The lsts software toolchain for persistent maritime operations applied through vehicular adhoc networks. In *Unmanned Aircraft Systems (ICUAS), 2017 International Conference on*, pages 609–616. IEEE, 2017.

[59] P. S. Dias, S. L. Fraga, R. M. Gomes, G. M. Goncalves, F. L. Pereira, J. Pinto, and J. B. Sousa. Neptus - a framework to support multiple vehicle operation. In *Europe Oceans 2005*, volume 2, pages 963–968. IEEE, 2005.

[60] F. M. Mirzaei and S. I. Roumeliotis. A kalman filter-based algorithm for imu-camera calibration: Observability analysis and performance evaluation. *IEEE Transactions on Robotics*, 24(5):1143–1156, 2008.

[61] Jonathan Kelly and Gaurav Sukhatme. Visual-inertial sensor fusion: Localization, mapping and sensor-to-sensor self-calibration. *I. J. Robotic Res.*, 30:56–79, 01 2011.

[62] Michael Bloesch, Michael Burri, Sammy Omari, Marco Hutter, and Roland Siegwart. Iterated extended kalman filter based visual-inertial odometry using direct photometric feedback. *The International Journal of Robotics Research*, 36(10):1053–1072, 2017.

[63] Guobin Chang. Fast two-position initial alignment for sins using velocity plus angular rate measurements. *Advances in Space Research*, 56(7):1331 – 1342, 2015.

[64] Jianwei Liu and Tao Zhao. In-flight alignment method of navigation system based on microelectromechanical systems sensor measurement. *International Journal of Distributed Sensor Networks*, 15(4), 2019.

[65] Jiazhen Lu, Chaohua Lei, Yanqiang Yang, and Ming Liu. In-motion initial alignment and positioning with ins/cns/odo integrated navigation system for lunar rovers. *Advances in Space Research*, 59(12):3070 – 3079, 2017.

[66] Wanli Li, Wenqi Wu, Jinling Wang, and Meiping Wu. A novel backtracking navigation scheme for autonomous underwater vehicles. *Measurement*, 47:496 – 504, 2014.

[67] Kang Gao, Shunqing Ren, Xijun Chen, and Zhenhuan Wang. An optimization-based initial alignment and calibration algorithm of land-vehicle sins in-motion. *Sensors*, 18(7):2081, 6 2018.

[68] Zhenglong Lu, Jie Li, Xi Zhang, Kaiqiang Feng, Xiaokai Wei, Debiao Zhang, Jing Mi, and Yang Liu. A new in-flight alignment method with an application to the low-cost sins/gps integrated navigation system. *Sensors*, 20(2):512, 1 2020.

[69] David H. Titterton and John L. Weston. *Strapdown inertial navigation technology*. Institution of Electrical Engineers and American Institute of Aeronautics and Astronautics, Stevenage, 2nd edition, 2004.

[70] James Ward. Space-time adaptive processing for airborne radar. Technical Report (TP) 1015, Lincoln Laboratory Massachusetts Institute of Technology (MiT), 12 1994.

[71] Kenneth Gade. A non-singular horizontal position representation. *The Journal of Navigation*, 63(3):395—417, 2010.

[72] Fabio Dovis. *GNSS interference threats and countermeasures*. GNSS technology and applications series. Artech House, Boston, 2015.

[73] Beatrice Motella, Marco Pini, and Fabio Dovis. Investigation on the effect of strong out-of-band signals on global navigation satellite systems receivers. *GPS Solutions*, 12:77–86, 01 2008.

[74] Erik Axell, Fredrik Marsten Eklöf, Peter Johansson, Mikael Alexandersson, and Dennis Akos. Jamming detection in gnss receivers: Performance evaluation of field trials. *Navigation*, 62, 03 2015.

[75] Salomon Honkala, Sarang Thombre, Martti Kirkko-Jaakkola, Hein Zelle, Henk Veerman, Anders E. Wallin, Erik F. Dierikx, Sanna Kaasalainen, Stefan Söderholm, and Heidi Kuusniemi. Performance of egnss-based timing in various threat conditions. *IEEE Transactions on Instrumentation and Measurement*, 69(5):2287–2299, 2020.

[76] Nicholas Spens, Dong-Kyeong Lee, Filip Nedelkov, and Dennis Akos. Detecting gnss jamming and spoofing on android devices. *NAVIGATION: Journal of the Institute of Navigation*, 69(3), 2022.

[77] Frédéric Bastide, Dennis M. Akos, Christophe Macabiau, and Benoît Roturier. Automatic gain control (agc) as an interference assessment tool. *Proceedings of the 16th International Technical Meeting of the Satellite Division of The Institute of Navigation (ION GPS/GNSS 2003)*, pages 2042–2053, 2003.

[78] Oscar Isoz, Dennis Akos, Tore Lindgren, Chih-Cheng Sun, and Shau-Shiun Jan. Assessment of gps l1/galileo e1 interference monitoring system for the airport environment. *Proceedings of the 24th International Technical Meeting of the Satellite Division of The Institute of Navigation (ION GNSS 2011)*, pages 1920–1930, 2011.

[79] Paul D.Groves. Gps signal-to-noise measurement in weak signal and high-interference environments. *Journal of the institute of navigation*, 52:83–94, 2005.

[80] Emanuela Falletti, Marco Pini, and Letizia Lo Presti. Low complexity carrier-to-noise ratio estimators for gnss digital receivers. *IEEE Transactions on Aerospace and Electronic Systems*, 47:420–437, 2011.

[81] Johannes van der Merwe, Fabio Garzia, Alexander Rügamer, Santiago Urquijo, David Contreras Franco, and Wolfgang Felber. Wide-band interference mitigation in gnss receivers using sub-band automatic gain control. *Sensors*, 22:679, 01 2022.

[82] Chotipong Sakorn and P. Supnithi. Calculating agc and c/n0 thresholds of mobile for jamming detection. In *2021 18th International Conference on Electrical Engineering/Electronics, Computer, Telecommunications and Information Technology (ECTI-CON)*, pages 268–271, 2021.

[83] D. Borio and C. Gioia. Real-time jamming detection using the sum-of-squares paradigm. In *2015 International Conference on Location and GNSS (ICL-GNSS)*, pages 1–6, 2015.

[84] F. Dimc, M. Bazec, D. Borio, C. Gioia, G. Baldini, and Marco Basso. An experimental evaluation of low-cost gnss jamming sensors. *Annual of Navigation*, 64:93–109, 2017.

[85] Robert Grover Brown and Patrick Y. C. Hwang. *Introduction to Random Signals and Applied Kalman Filtering*. John Wiley & Sons, Inc., Hoboken, New Jersey, fourth edition, 2012.

[86] S.M. Kay. *Fundamentals of Statistical Signal Processing: Detection theory*. Fundamentals of Statistical Si. Prentice-Hall PTR, 1998.

[87] Version 2.4.2. Available online at http://www.rtklib.com, Last updated: 29.04.2013.

[88] T. Maruyama, K. Kihira, and H. Miyashita. *Phased Arrays*, chapter 37, pages 1113–1162. Springer Singapore, 2016.

[89] H. Krim and M. Viberg. Two decades of array signal processing research: the parametric approach. *IEEE Signal Processing Magazine*, 13(4):67–94, 7 1996.

[90] R. Schmidt. Multiple emitter location and signal parameter estimation. *IEEE Transactions on Antennas and Propagation*, 34(3):276–280, 3 1986.

[91] R. Roy and T. Kailath. ESPRIT-estimation of signal parameters via rotational invariance techniques. *IEEE Transactions on Acoustics, Speech, and Signal Processing*, 37(7):984–995, Jul 1989.

[92] H. Abeida, Q. Zhang, J. Li, and N. Merabtine. Iterative sparse asymptotic minimum variance based approaches for array processing. *IEEE Transactions on Signal Processing*, 61(4):933–944, 2013.

[93] A. B. Younes, D. Mortari, J. D. Turner, and J. L. Junkins. Attitude error kinematics. *Journal of Guidance, Control, and Dynamics*, 37(1), 2014.

ISBN 978-82-326-8122-8 (printed ver.)
ISBN 978-82-326-8121-1 (electronic ver.)
ISSN 1503-8181 (printed ver.)
ISSN 2703-8084 (online ver.)

NTNU
Norwegian University of
Science and Technology